

VOLUME 36

JULY 1958

NUMBER 7

# Canadian Journal of Physics

*Editor: H. E. DUCKWORTH*

*Associate Editors:*

- L. G. ELLIOTT, *Atomic Energy of Canada, Ltd., Chalk River*
- J. S. FOSTER, *McGill University*
- G. HERZBERG, *National Research Council of Canada*
- L. LEPRINCE-RINGUET, *Ecole Polytechnique, Paris*
- B. W. SARGENT, *Queen's University*
- G. M. VOLKOFF, *University of British Columbia*
- W. H. WATSON, *University of Toronto*
- G. A. WOONTON, *McGill University*

*Published by THE NATIONAL RESEARCH COUNCIL  
OTTAWA CANADA*

## CANADIAN JOURNAL OF PHYSICS

(Formerly Section A, Canadian Journal of Research)

Under the authority of the Chairman of the Committee of the Privy Council on Scientific and Industrial Research, the National Research Council issues THE CANADIAN JOURNAL OF PHYSICS and five other journals devoted to the publication, in English or French, of the results of original scientific research. Matters of general policy concerning these journals are the responsibility of a joint Editorial Board consisting of: members representing the National Research Council of Canada; the Editors of the Journals; and members representing the Royal Society of Canada and four other scientific societies.

### EDITORIAL BOARD

#### Representatives of the National Research Council

A. Gauthier, *University of Montreal*  
R. B. Miller, *University of Alberta*

H. G. Thode, *McMaster University*  
D. L. Thomson, *McGill University*

#### Editors of the Journals

D. L. Bailey, *University of Toronto*  
T. W. M. Cameron, *Macdonald College*  
H. E. Duckworth, *McMaster University*

K. A. C. Elliott, *Montreal Neurological Institute*  
Léo Marion, *National Research Council*  
R. G. E. Murray, *University of Western Ontario*

#### Representatives of Societies

D. L. Bailey, *University of Toronto*  
Royal Society of Canada  
T. W. M. Cameron, *Macdonald College*  
Royal Society of Canada  
H. E. Duckworth, *McMaster University*  
Royal Society of Canada  
Canadian Association of Physicists

K. A. C. Elliott, *Montreal Neurological Institute*  
Canadian Physiological Society  
P. R. Gendron, *University of Ottawa*  
Chemical Institute of Canada  
R. G. E. Murray, *University of Western Ontario*  
Canadian Society of Microbiologists  
T. Thorvaldson, *University of Saskatchewan*  
Royal Society of Canada

#### Ex officio

Léo Marion (Editor-in-Chief), *National Research Council*  
J. B. Marshall (Administration and Awards), *National Research Council*

---

*Manuscripts for publication should be submitted to Dr. H. E. Duckworth, Editor, Canadian Journal of Physics, Hamilton College, McMaster University, Hamilton, Ontario.*

(For instructions on preparation of copy, see **Notes to Contributors** (inside back cover).)

*Proof, correspondence concerning proof, and orders for reprints should be sent to the Manager, Editorial Office (Research Journals), Division of Administration and Awards, National Research Council, Ottawa 2, Canada.*

*Subscriptions, renewals, requests for single or back numbers, and all remittances should be sent to Division of Administration and Awards, National Research Council, Ottawa 2, Canada. Remittances should be made payable to the Receiver General of Canada, credit National Research Council.*

The journals published, frequency of publication, and prices are:

Canadian Journal of Biochemistry and Physiology	Monthly	\$3.00 a year
Canadian Journal of Botany	Bimonthly	\$4.00 a year
Canadian Journal of Chemistry	Monthly	\$5.00 a year
Canadian Journal of Microbiology	Bimonthly	\$3.00 a year
Canadian Journal of Physics	Monthly	\$4.00 a year
Canadian Journal of Zoology	Bimonthly	\$3.00 a year

The price of regular single numbers of all journals is 75 cents.





# Canadian Journal of Physics

*Issued by THE NATIONAL RESEARCH COUNCIL OF CANADA*

---

VOLUME 36

JULY 1958

NUMBER 7

---

## A COSMIC RAY INCREASE RELATED TO SOLAR ACTIVITY<sup>1</sup>

J. KATZMAN

### ABSTRACT

An increase in the intensity of cosmic ray particles of minimum momentum at Ottawa, Canada, of  $4.5 \times 10^9$  ev/c was observed with telescopes of solid angles  $11.5 \times 10^{-4}$  and  $26.0 \times 10^{-4}$  steradians with increase of solar activity. A large increase in cosmic ray activity for the period September 1956 to February 1957 was observed to accompany a large and sustained increase in solar activity as determined by means of the critical frequency of the F-2 layer.

### INTRODUCTION

The cosmic ray intensity in the atmosphere of the earth changes with time and is related in some complicated manner to the solar activity. Also the variations are greatest for particles of smallest rigidities. In the day to day variations, the nucleon component shows a high negative correlation with atmospheric pressure (Simpson 1957) but for the meson component the correlation is not consistently high. This is due to the fact that the meson is radioactive.

Telescopes of small solid angle follow more truly changes in the primary spectrum than telescopes of large solid angle, since the change of mass of air with decreasing zenith angle can be neglected. If an absorber of sufficient mass is used then particles of low energy will not be detected. This eliminates particles that are greatly influenced by changes in the magnetic field surrounding the earth and by changes in atmospheric conditions.

An experiment was set up at Ottawa, Canada ( $45.4^\circ$  N. lat.,  $75.6^\circ$  W. long.) to study the variations in intensity of particles coming from a small portion of the sky by means of very small solid angle telescopes with 96 inches of lead absorber. The minimum energy of a primary particle from which a secondary can be detected in such a telescope is about 7 Bev and the average effective primary energy would be greater than 30 Bev.

### EXPERIMENTAL ARRANGEMENT

Four trays each containing four brass Geiger counters of 1 inch outside

<sup>1</sup>Manuscript received March 20, 1958.

Contribution from the Division of Pure Physics, National Research Council, Ottawa, Canada.

Issued as N.R.C. No. 4776.

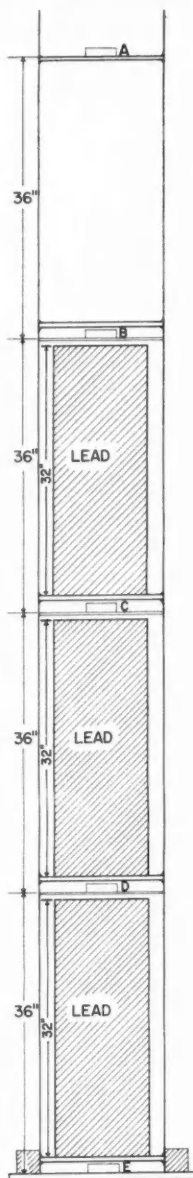


FIG. 1.

diameter and approximately 4 inches sensitive length were arranged to make two telescopes of three trays each. The trays are held in a welded angle-iron rack capable of supporting a large mass of lead on an area  $12 \times 12$  inches (Fig. 1). Trays can be placed at any of the positions *A*, *B*, *C*, *D*, *E* and telescopes *ADE*, *BDE*, *CDE* are labelled No. 1, No. 2, No. 3. The solid angles of these telescopes are  $6.5 \times 10^{-4}$ ,  $11.5 \times 10^{-4}$ ,  $26.0 \times 10^{-4}$  steradians respectively. Triple coincidences only are recorded on a 20-pen Esterline-Angus recorder and on electromechanical registers that are read every day. The electronics are composed of standard units that are in use at the Cosmic Ray Laboratory at Ottawa and have proved dependable over a period of eight years. All pulses are checked once a week and the high voltage is checked every day of the year.

The experiment was assembled in November 1954 with trays placed in positions *B*, *C*, *D*, *E*, with 4 inches of lead over *E* and 4 inches around three sides. The absorber was increased to 10, 20, 48, and finally 96 inches of lead. Thus for the period 21 December 1954 to 21 December 1955 telescopes No. 2 and No. 3 were operated with 96 inches of lead. The tray in position *D* was displaced to obtain the accidental and shower rate, which was found to be 0.02 counts per hour for a period of 30 days. In the latter part of January 1956 8 inches of lead was taken from below position *B* and placed above, and the tray in *C* was placed in position *A*. Triple coincidences were recorded for telescopes No. 1 and No. 2 for the period 25 January 1956 to 19 February 1957 when the tray at *A* was replaced in position *C*. The experiment was stopped 9 July 1957 to make necessary changes.

#### RESULTS

The monthly mean uncorrected rates for telescopes No. 1, No. 2, and No. 3, together with the critical frequency of the F-2 layer (Mc/sec), the mean daily planetary index  $K_p$ , the flux of the 10.7 cm radiation from the corona of the sun, and the mean monthly sunspot numbers  $\bar{R}$  are shown in Table I and Fig. 2. It can be seen that for the year 1955 there is no correlation between the sun's activity and the rate of the telescopes No. 2 and No. 3 that were in operation, whereas the correlation between telescope No. 2 and the critical frequency of the F-2 layer for the period February 1956 to July 1957 when the experiment was stopped is remarkable. However, no correlation exists between the rate of the narrower angle telescope No. 1 and  $f_0F-2$ .

#### DISCUSSION OF RESULTS

It has been recognized for some time that terrestrial effects such as magnetic disturbances, the aurora polaris, ionospheric storms, radio propagation, sudden increases in cosmic ray intensities, and other terrestrial phenomena arise as the result of electromagnetic or corpuscular radiations emitted by an active sun. The ionization of the F-2 layer is known to change with the 11-year solar cycle. Bartels (1950) demonstrated a 27-day variation in the noon values of the critical frequency of the F-2 layer for Huancayo, Peru. Covington (1957)

TABLE I

1955						
Month	No. 3 Counts/hr	No. 2 Counts/hr	$f_0F-2^{(1)}$	$K_p^{(2)}$	Flux <sup>(3)</sup>	$\bar{R}$
Jan.	1.43	0.57	3.60	15.90	83.1	23.1
Feb.	1.40	0.54	3.88	18.10	81.3	20.8
Mar.	1.48	0.60	3.50	19.71	74.5	4.9
Apr.	1.46	0.59	3.69	18.90	77.2	11.3
May	1.51	0.59	4.26	15.68	82.7	28.9
June	1.59	0.63	4.36	15.83	88.8	31.7
July	1.55	0.58	4.43	13.68	87.3	26.7
Aug.	1.50	0.59	4.40	14.32	90.6	40.7
Sept.	1.51	0.59	4.68	18.50	94.8	42.7
Oct.	1.55	0.56	5.53	15.74	111.1	58.5
Nov.	1.45	0.55	5.58	16.83	128.5	89.2
Dec.	1.62	0.66	5.57	13.23	132.3	76.9

1956						
Month	No. 2 Counts/hr	No. 1 Counts/hr	$f_0F-2$	$K_p$	Flux	$\bar{R}$
Jan.	0.61	0.31	5.49	22.19	139	70.5
Feb.	0.64	0.34	6.11	18.55	166	122.6
Mar.	0.64	0.34	7.10	22.13	160	115.5
Apr.	0.61	0.31	6.33	25.03	166	104.5
May	0.65	0.33	7.05	23.42	163	136.0
June	0.62	0.31	5.80	22.63	154	116.7
July	0.59	0.30	5.85	19.16	163	128.5
Aug.	0.68	0.29	6.29	18.97	194	171.1
Sept.	0.85	0.31	7.50	19.77	200	182.2
Oct.	1.06	0.28	8.78	18.42	200	160.8
Nov.	1.09	0.32	9.26	24.53	247	202.7
Dec.	1.03	0.32	8.94	16.61	249	185.5

1957						
Month	No. 2 Counts/hr	No. 1 Counts/hr	$f_0F-2$	$K_p$	Flux	$\bar{R}$
Jan.	0.97	0.29	8.61	19.61	228	152.3
Feb.		0.31 <sup>(4)</sup>				
No. 3						
Month	No. 2					
Feb.	2.45 <sup>(5)</sup>	1.01	8.73	20.79	185	116.8
Mar.	1.78	0.62	8.31	25.65	197	157.0
Apr.	1.70	0.63	6.65	24.57	200	175.0
May	1.69	0.67	6.67	17.61	208	165.0
June	1.59	0.61	6.28	22.30	252	206.0
July	1.61	0.62	6.26	18.19	218	194.0

(1) Critical frequency of the F-2 layer in Mc/sec. Data supplied by Defence Research Telecommunications Establishment, Defence Research Board, Ottawa, Ontario, Canada.

(2) Geomagnetic planetary index, daily average for the month.

(3) Solar flux in watts/m<sup>2</sup>/cycles/sec (bandwidth  $\times 10^{-22}$ ). Data supplied by Mr. A. E. Covington, National Research Council, Ottawa, Ontario, Canada.

(4) Average rate for the first 19 days of the month.

(5) Average rate for the last 8 days of the month.

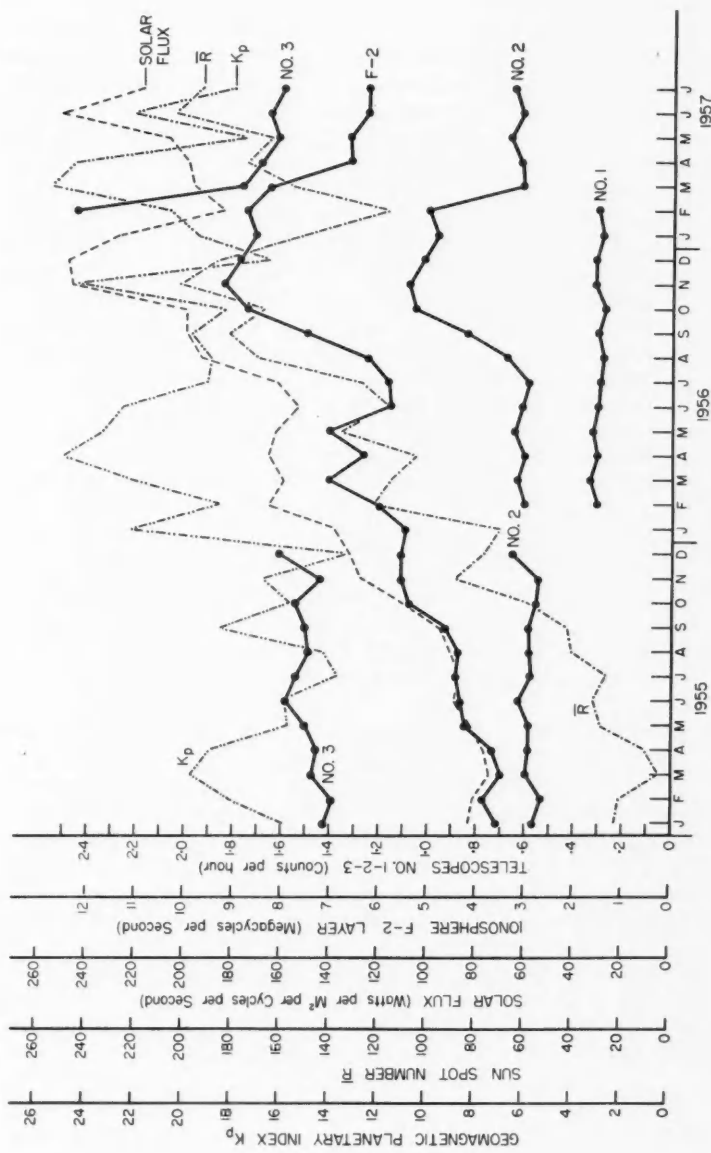


FIG. 2.

found that the solar noise (10.7 cm radiation) varies with the solar cycle and considers that the 10.7 cm radio wave may be an index of solar ultraviolet radiation. If the ionization of the F-2 layer is caused by ultraviolet radiation from the sun, it would be expected to vary as the flux of the 10.7 cm radiation. The agreement is very good up to February 1957 (Fig. 2), when the sunspot number and the 10.7 cm flux increased sharply but the critical frequency of the F-2 layer dropped just as sharply. Hence, if the 10.7 cm flux is an index of the solar ultraviolet radiation, then the ionization of the F-2 layer for short periods in a solar cycle must be caused by some agent other than the ultraviolet. Davies (1956) and Landmark (1956) found evidence of a corpuscular emission from the sun during the solar eclipse of 30 June 1954. If changes in the critical frequency were due to ultraviolet radiation only, then the world-wide fluctuations would be in unison; this, however, is not the case (Table II). It is to be noted that the greatest increase was at Ottawa. Hence there exists an agent other than the ultraviolet radiation that causes ionization of the F-2 layer over Ottawa, Canada.

TABLE II  
THE MEAN CRITICAL FREQUENCY OF THE F-2 LAYER IN MC/SEC

Station	June 1953 to May 1954	June 1956 to May 1957	% Increase	Geomagnetic	
Resolute	3.53	5.88	67.0	82.9° N.	289.3°
Churchill*	3.79	6.34	67.0	68.7° N.	322.7°
Ottawa	3.63	7.62	110.0	56.8° N.	351.4°
White Sands	4.47	8.28	85.0	41.2° N.	316.5°
Huancayo	5.95	9.81	65.0	0.6° S.	353.8°

\*Average for 9 months only; December, January, and February data are not complete for 1953-1954.

Telescopes No. 1 and No. 2 do not show the same increase in intensity. The two telescopes differ in only two respects.

- (1) The solid angle of No. 2 is bigger than that of No. 1 by approximately a factor two and both telescopes are of extremely small solid angle.
- (2) There were 8 inches of lead above the top tray of No. 2 and no lead above No. 1.

To determine whether the lead above No. 2 had any effect on the rate the lead was replaced below the top tray of No. 2 on 8 February 1957. The rate for No. 2 was  $1.23 \pm 0.07$  counts per hour for 10 days before 8 February 1957 and  $1.03 \pm 0.07$  for 10 days after the lead was replaced below the top tray. The rates for No. 1 for the same periods were  $0.35 \pm 0.04$  and  $0.30 \pm 0.04$ . Hence the lead above the top tray of No. 2 did not in any manner contribute to the observed increase.

The positive correlation that has been found cannot be attributed to particles arriving directly from the sun if they are of the same energy as those emitted from the sun during the solar flare of 23 February 1956. Telescopes No. 1 and No. 2 were in operation at that time. There was no indication whatsoever of an increase in intensity as monitored by these telescopes, whereas the

neutron monitor showed a very large increase and another telescope with 13 inches of lead showed a small increase (Rose and Katzman 1956).

Forbush (1954) showed the existence of a negative correlation between the sunspot numbers and the cosmic ray intensity of the low end of the energy spectrum for the years 1937 to 1952. This is also true for the present solar cycle (Rose and Fenton 1958). However, telescopes No. 2 and No. 3 showed an increase in intensity with increase of solar activity (Table III).

TABLE III  
COUNTS PER HOUR

	Feb.-July 1955	Feb.-July 1957	% Increase
Telescope No. 2	0.59	0.69	11.7
Telescope No. 3	1.50	1.73	11.5
Barometer, mb	1002.25	1002.86	

Morrison (1956) has suggested that clouds of ionized gas move outward from the sun carrying magnetic fields which would shield incident galactic cosmic ray particles from the earth, and that this accounts for the observed decrease in cosmic ray intensity with increased activity of the sun. Nagashima (1951) postulated that a geoelectric field may be responsible for the decrease. Neither of these mechanisms nor the geocentric model as developed by Parker (1956) can explain the observed increase of the cosmic ray intensity with the sun's activity, if the cosmic ray spectrum is constant.

Alfvén (1950) has shown that the periodic orbits of charged particles in the solar magnetic field can be affected by storm-producing streams emanating from the sun. Thus particles in these orbits if accelerated would leave the periodic orbits and enter orbits that come from infinity and strike the earth thus causing an increase in intensity. However, this does not explain the anomaly that the telescope of smaller solid angle showed no increase. Officer and Eccles (1955) also found an anomaly with zenith angles less than five degrees in their study of the penetrating component of extensive air showers. It is difficult at present to understand how so small a difference in solid angle can shift the acceptance of particles to a high energy in the spectrum. However, if this effect is not fortuitous it points to the fact that as the zenith is approached the energy of the particles rises steeply and therefore is not influenced by magnetic fields surrounding the earth. It also indicates that the active sun in some manner caused an increase in particles of a definite energy band for a short period (Neher 1957).

#### CONCLUSIONS

An increase in cosmic ray intensity with increase in solar activity has been indicated. It will be necessary to explore the phenomenon in greater detail before any definite conclusions can be drawn as regards the mechanism of the increase in intensity. The experiment is being continued and expanded so that

the variation of cosmic ray intensity very close to the zenith can be studied more fully.

#### ACKNOWLEDGMENTS

The writer wishes to thank Mr. A. E. Summers and Mr. O. Poulin for their assistance in the construction and the assembly of the apparatus and the other members of the Cosmic Ray Group for their assistance in the recording of the daily readings.

#### REFERENCES

- ALFVÉN, H. 1950. *Cosmical electrodynamics* (Clarendon Press, Oxford).  
BARTELS, J. 1950. *J. Atmos. Terr. Phys.* **1**, 2.  
COVINGTON, A. E. 1957. *J. Roy. Astro. Soc. Canada*, **51**, 298.  
DAVIES, K. 1956. *J. Atmos. Terr. Phys.* **6**, 40 (Special Supplement).  
FENTON, A. G., FENTON, K. B., and ROSE, D. C. 1958. *Can. J. Phys.* This issue.  
FORBUSH, S. E. 1954. *J. Geophys. Res.* **59**, 525.  
LANDMARK, B. 1956. *J. Atmos. Terr. Phys.* **6**, 54 (Special Supplement).  
MORRISON, P. 1956. *Phys. Rev.* **101**, 1397.  
NAGASHIMA, K. 1951. *J. Geomag. Geoelectr. (Japan)* **3**, 100.  
NEHER, H. V. 1957. *Phys. Rev.* **107**, 588.  
OFFICER, V. C. and ECCLES, P. J. 1955. *Aust. J. Phys.* **8**, 136.  
PARKER, E. N. 1956. *Phys. Rev.* **103**, 1518.  
ROSE, D. C. and KATZMAN, J. 1956. *Can. J. Phys.* **34**, 884.  
SIMPSON, J. A. 1957. *Proc. Natl. Acad. Sci. U.S.* **43**, 42.

# CALCULATION OF THE THERMAL CONDUCTIVITY OF POROUS MEDIA<sup>1</sup>

WILLIAM WOODSIDE

## ABSTRACT

The problem of determining the effective thermal conductivities of porous and other composite materials from the conductivities and volume fractions of their constituents is examined. An approximate equation is derived for the case of a cubic lattice of identical spherical particles in a medium having properties different from those of the particles. This equation is applied to the calculation of the thermal conductivity of snow at different densities in the range 0.10 to 0.48 gm/cc. The effect of water vapor diffusion in snow under a temperature gradient is taken into account by adding a latent heat term to the conductivity value for dry air. Conductivity values for snow, calculated in this manner, are found to agree satisfactorily with experimental data. An equation due to Russell is also shown to give conductivity values for several cellular thermal insulating materials which are in good agreement with experimental values.

## INTRODUCTION

Although gases are the poorest heat conductors, by themselves they do not constitute the best heat insulators. If the linear dimensions of a gas-filled space exceed approximately 1 cm, convection makes a large contribution to the total heat transfer across the space. At high temperatures radiation also becomes important. The best heat insulators are therefore solids which contain a high percentage of gas (usually air) in such a way that the individual gas spaces are small enough that convective heat transfer across them is negligible. These include powders and porous and fibrous materials, e.g. silica aerogel, expanded cork, and mineral wool.

It would be advantageous if, in the design and manufacture of thermal insulating materials, the effective thermal conductivity of such composite gas-solid materials could be calculated from the properties and volume fractions of the component substances. Unfortunately the conductivity of a composite material of known composition cannot be arrived at by any simple law of addition of the conductivities of its components.

In the present paper, an equation due to Russell (1935) is applied to several dry cellular insulating materials. A further equation is developed for the thermal conductivity of a medium consisting of a gas in which uniform solid spherical particles are distributed. This is applied to the calculation of the conductivity of snow at different densities, taking into account the heat transfer through snow by vapor diffusion.

## PREVIOUS WORK

Gemant (1950) derived a formula for the thermal conductivity of moist soils in terms of moisture content, thermal conductivity of water, and the

<sup>1</sup>Manuscript received February 24, 1958.

Contribution from the Building Services Section, Division of Building Research, National Research Council, Ottawa, Canada.

Issued as N.R.C. No. 4777.

solid particles composing the soil. He considered a spherical grain of soil in contact with six neighbors, i.e. a cubic lattice of uniform spheres. This lattice leads to a porosity value of 47.6%. The closest possible packing arrangement for uniform spheres gives a porosity value of 26%. Porosity values for sandy soils lie between these two extremes, averaging approximately 37%. Gemant assumed the moisture to occupy wedge-shaped rings around the contact points between the spheres, the volume of these rings varying with the moisture content. He then calculated the resistance to heat flow of a unit cube surrounding the soil grain, water rings, and air spaces, assuming parallel heat flow and neglecting the thermal resistance of the air spaces. The resulting thermal conductivities of several soils with moisture contents ranging from 5 to 25% by volume showed surprisingly good agreement with experimental values taken from the literature. Recently Webb (1956) has criticized the neglect of the air-phase resistance and de Vries (1956) has criticized the assumption of parallel heat flow in Gemant's development. Both criticisms are of course valid, yet the close agreement between calculated and experimental conductivities encourages the application of similar approximate methods to other materials.

Russell (1935), in connection with the thermal conductivity of refractory brick, has derived the effective thermal conductivity of a dry porous material from the properties of its component gas and solid for a distribution of uniform pores of cubical shape arranged in a simple cubic lattice. He assumed parallel heat flow and neglected convection across the pores. Russell's equation is

$$(1) \quad \frac{k_s}{k} = 1 - P^{1/3} + \frac{P^{1/3}}{(k_g/k_s)P^{2/3} + 1 - P^{2/3}}$$

where the porosity  $P = (\rho_s - \rho)/(\rho_s - \rho_g)$  and  $0 < P \leq 1$ .  $k$ ,  $k_g$ , and  $k_s$  are the thermal conductivities of the composite, gas, and solid respectively, and  $\rho$ ,  $\rho_g$ , and  $\rho_s$  are the densities of the composite, gas, and solid respectively.

Maxwell (1873) and Rayleigh (1892) derived by rigorous analysis a formula for the electrical conductivity of a two-phase medium consisting of uniform spheres of one material arranged in cubic array in the second material. This has been extended by Burger (1915) to the case of ellipsoidal particles, and generalized by Eucken (1932) for the case of a multiple medium. De Vries (1952) has successfully applied this theory to the thermal conductivity of wet soils, i.e., three phases: air, water, and solid.

For the case of pores distributed in a solid the original formula of Maxwell and Rayleigh reads

$$(2) \quad \frac{k}{k_s} = \frac{1 - (1 - bk_g/k_s)P}{1 + (b - 1)P}$$

where  $b = 3k_s/(2k_s + k_g)$ , and porosity  $P = (\rho_s - \rho)/(\rho_s - \rho_g)$ . Eucken assumes that this equation is valid for values of  $P$  as high as 0.5 with good approximation. This equation has also been derived by Kerner (1956).

#### ANALYSIS

To determine the thermal conductivity of a medium consisting of a cubic

lattice of uniform solid spherical particles in a gas, the following assumptions are made: (i) the gas spaces are small enough that heat transfer by convection may be neglected; and (ii) the isotherms are planes perpendicular to the direction of heat flow.

The second assumption is only valid when  $k_s = k_g$ . The larger the value of the ratio  $k_s/k_g$ , the greater will be the errors introduced by this assumption. Thus the equation developed should give best results for materials whose values of  $k_s/k_g$  are close to unity.

Fig. 1 is a diagram of a unit cube containing one-eighth of a sphere. The general case is considered in that the spheres are not assumed to be in contact. For heat conduction purposes, this is a representative "atom" of a material consisting of uniform solid spheres distributed in a cubic lattice in a gas. Thus the thermal resistance of this cube to heat conduction in the direction shown equals the thermal resistivity of the composite material.

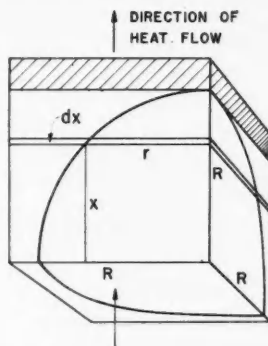


FIG. 1. Representative "atom" of a material consisting of uniform solid spheres distributed in a cubic lattice in a gas, used for calculation of thermal conductivity.

Let  $R$  denote the radius of the solid sphere.  $R$  will be an equivalent radius in the case of materials composed of nonuniform and/or nonspherical particles, e.g. snow. If  $S$  represents the ratio of volume of solid to total volume, then

$$S = 1 - P = \pi R^3 / 6$$

where  $0 \leq P \leq 1$ , and therefore

$$R = (6S/\pi)^{1/3}$$

where  $P$  is the porosity. The maximum value of  $R$  is unity, and hence the equation to be developed will only be applicable to granular materials having porosities greater than or equal to 47.6%. The value of  $S$  may be calculated from  $\rho$ ,  $\rho_s$ , and  $\rho_g$  since

$$S = (\rho - \rho_g)/(\rho_s - \rho_g).$$

In Fig. 1 the thermal resistance of the shaded layer composed wholly of gas is  $(1-R)/k_g$ . The thermal resistance of the composite gas-solid layer of thickness  $dx$  is, by the second assumption,

$$\frac{dx}{k_s \pi r^2 / 4 + k_g (1 - \pi r^2 / 4)}.$$

The total thermal resistance of the cube is therefore

$$\frac{1}{k} = \frac{1-R}{k_g} + \int_0^R \frac{dx}{k_s \pi r^2 / 4 + k_g (1 - \pi r^2 / 4)}.$$

Since  $r^2 = R^2 - x^2$  and  $R = (6S/\pi)^{1/3}$ , this results in

$$(3) \quad \frac{k_g}{k} = 1 - \left( \frac{6S}{\pi} \right)^{1/3} \left[ 1 - \left( \frac{a^2 - 1}{a} \right) \ln \left( \frac{a+1}{a-1} \right) \right]$$

where

$$a = \left[ 1 + \frac{4}{\pi(k_s/k_g - 1)(6S/\pi)^{2/3}} \right]^{1/2}, \quad S = \frac{\rho - \rho_g}{\rho_s - \rho_g}, \quad 0 \leq S \leq 0.5236.$$

It may be shown that when  $\rho = \rho_s$ , i.e. when  $S = 1$ ,  $k = k_s$ , and also that when  $\rho = \rho_g$ , i.e. when  $S = 0$ ,  $k = k_g$ . Thus the thermal conductivity  $k$  of a material of known density may be calculated if the densities and conductivities of its components are known and if it may be approximated by the above model. This formula may also be used to calculate the dielectric constant, electrical conductivity, and magnetic permeability of composite media.

If  $R = (6S/\pi)^{1/3} = 1$  is substituted into equation (3), the resulting equation is identical with the one derived and used by Webb (1956) for the calculation of the conductivity of dry soil. If the subscripts  $s$  and  $g$  are interchanged in equation (3) and the equation rearranged, it becomes the equation for the conductivity of a material consisting of uniform spherical pores distributed in a cubic lattice in a solid.

There are therefore three equations for the calculation of the thermal conductivity of a contingent medium (gas or solid) in which uniform particles (solid or gas) are distributed.

#### APPLICATION TO CELLULAR MATERIALS

Of the above equations, only equation (1) permits the porosity  $P$  to have any value between zero and unity. Equation (3) when applied to cellular materials (subscripts  $s$  and  $g$  interchanged) limits  $P$  to the range  $0 \leq P \leq 0.52$ , and equation (2) to the range  $0 \leq P \leq 0.50$ . Hence only equation (1) may be applied to the prediction of  $k$  for cellular materials since most cellular materials have porosities higher than 0.52. The conductivities of six materials calculated from equation (1) are compared with the experimental values, in Table I.

Pratt and Ball (1956) measured the thermal conductivity of a steel shot aggregate concrete and compared the measured value (13.8 B.t.u. in./hr ft<sup>2</sup> °F) with the theoretical estimate given by Maxwell's formula (equation (2)) above. The value of  $P$ , i.e. the fraction of the total volume occupied by the steel shot, was given as 0.56 and the calculated value of  $k$  was 11.8 B.t.u. in./hr ft<sup>2</sup> °F. The conductivity of this concrete may also be calculated from Russell's equation (1) where  $k_g$  now represents the conductivity of steel. This results in a value for  $k$  of 13.85 B.t.u. in./hr ft<sup>2</sup> °F in agreement with the experimental value. The value of  $k_s/k_g$  for this material is 0.0082.

TABLE I  
COMPARISON OF CALCULATED AND EXPERIMENTAL THERMAL CONDUCTIVITIES

Material	Density (lb/cu. ft)	Porosity (P)	$k_s/k_g$	Calc. cond. $k$	Measured cond. (B.t.u. in./hr ft <sup>2</sup> °F)
Cellular glass	9.0	0.944	34.7	0.402	0.402
Cellular rubber	4.9	0.946	12.3	0.260	0.28
Expanded ebonite	6.0	0.897	5.8	0.237	0.23
Expanded polystyrene*	2.0	0.971	5.4	0.191	0.220
Cellular cellulose acetate*	5.5	0.933	9.7	0.294	0.305
Cellular polyvinyl chloride*	3.5	0.961	6.5	0.206	0.23

\*Data for these materials taken from *Technical Data on Plastics*, Manufacturing Chemists' Association, Oct. 1952.

Thus Russell's equation results in calculated values for the thermal conductivity of certain composite materials which are in fair agreement with the measured values. Contrary to expectation the agreement does not appear to bear any simple relationship to the value of  $k_s/k_g$ .

#### APPLICATION TO SNOW

Snow is a powdery substance composed of ice crystals and air, and hence the above equations may be used for the calculation of its thermal conductivity at any density since the properties of ice and air are known. However, in snow and other moist materials, there is an additional mechanism by which heat may be transmitted. When a temperature gradient is imposed upon a layer of snow, a corresponding vapor pressure gradient is also set up. Thus water vapor may evaporate from one layer of ice crystals and condense on another. In so doing the heat removed from the first layer as latent heat of sublimation is transferred to the second layer. The water vapor traverses the air space between the two layers by a process of diffusion. Since this process occurs only in the air spaces between ice crystals, this second heat transfer mechanism may be accounted for by using an equivalent thermal conductivity for the air which includes a term representing the contribution of water vapor diffusion.

Yosida (1955) proposed that for the air in snow

$$(4) \quad k_{\text{eff.}} = k_{\text{air}} + a.D_0.L$$

where

$k_{\text{eff.}}$  = effective conductivity of air in snow, taking account of water vapor diffusion, cal/cm sec °C,

$k_{\text{air}}$  = thermal conductivity of dry air, cal/cm sec °C,

$a$  = rate of increase of vapor density of ice with temperature, g/cc °C,

$D_0$  = diffusion coefficient of water vapor through air, cm<sup>2</sup>/sec,

$L$  = latent heat of sublimation of ice, cal/g.

Yosida took the following values at 0° C,  $k_{\text{air}} = 5.3 \times 10^{-5}$ ,  $a = 0.39 \times 10^{-6}$ ,  $D_0 = 0.22$ , and  $L = 676$  in the units given above, to give a value for  $a.D_0.L$

of  $5.8 \times 10^{-5}$  cal/cm sec °C. Yosida concluded that the air in snow has an effective thermal conductivity twice its normal value.

Krischer (1941) has shown that the effective thermal conductivity of the air in the pores of a material whose pore walls are wetted, may be expressed by

$$(5) \quad k_{\text{eff.}} = k_{\text{air}} + \frac{D}{R_v T} \cdot \left( \frac{P}{P - P_v} \right) \frac{dP_v}{dT} \cdot L \quad \text{cal/cm sec °C}$$

where

$D$  = diffusion coefficient of water vapor through air, cm<sup>2</sup>/sec,

$R_v$  = gas constant of the water vapor, g-cm/g,

$T$  = absolute temperature, °K,

$P$  = air pressure, g/cm<sup>2</sup>,

$L$  = latent heat of evaporation, cal/g,

$P_v$  = partial pressure of water vapor, g/cm<sup>2</sup>.

Krischer experimentally studied the diffusion between the wetted walls of a greatly enlarged model of a pore, under the influence of temperature gradients. From his experiments the following value for the diffusion coefficient resulted,

$$D = \frac{239}{P} \left( \frac{T}{273} \right)^{2.3}.$$

Equation (5), when applied to the case of the air in snow, at 0° C gives  $k_{\text{eff.}} = k_{\text{air}} + 6.24 \times 10^{-5}$  cal/cm sec °C. Taking the latest value for  $k_{\text{air}}$  at 0° C as  $5.77 \times 10^{-5}$ ,

$$\begin{aligned} k_{\text{eff.}} &= 12.01 \times 10^{-5} \text{ cal/cm sec °C} \\ &= 0.029 \text{ B.t.u./hr ft °F}. \end{aligned}$$

The thermal conductivity of snow at 0° C and at various densities may now be calculated with the aid of equations (1), (2), and (3). The results are shown

TABLE II  
COMPARISON OF CALCULATED AND EXPERIMENTAL CONDUCTIVITIES OF SNOW

Thermal conductivity at 0° C, cal/cm sec °C				
Density of snow, g/cc	Mean of exp. values	Calculated from equation (3)	Calculated from equation (1)	Calculated from equation (2)
0.10	$0.155 \times 10^{-3}$	$0.238 \times 10^{-3}$	$0.211 \times 10^{-3}$	$0.160 \times 10^{-3}$
0.20	$0.330 \times 10^{-3}$	0.355	0.275	0.211
0.30	$0.595 \times 10^{-3}$	0.537	0.349	0.278
0.40	$1.04 \times 10^{-3}$	0.901	0.442	0.367

in Table II. In the calculations the following values were taken for  $\rho_s$ ,  $\rho_g$ ,  $k_s$ , and  $k_g$  at 0° C:

$\rho_s = \rho_{\text{ice}} = 0.917 \text{ g/cc}$ ,

$\rho_g = \rho_{\text{air}} = 0.0013 \text{ g/cc}$ ,

$k_s = k_{\text{ice}} = 5.33 \times 10^{-3} \text{ cal/cm sec °C}$  (Jakob 1949),

$k_g = k_{\text{eff.}} = 1.20 \times 10^{-4} \text{ cal/cm sec °C}$ .

The experimental values for the thermal conductivity of snow, which were averaged to give the values shown in the second column of Table II, are those of Kondrat'eva, Yosida, Abel's, Jansson, and Devaux. The experimental methods and results of these investigations are fully described by Yosida (1955) and Kondrat'eva (1954).

The values calculated from equation (3) agree with the experimental values much better than those calculated from equations (1) and (2) for the greater part of the above density range. Hence in the following, calculated values for the thermal conductivity of snow will refer to those calculated from equation (3).

The values of thermal conductivity shown in the fourth column of Table III are those calculated from equation (3) neglecting the contribution of water vapor diffusion to the heat transfer through snow, i.e. taking  $k_g = k_{at} = 0.577 \times 10^{-4}$  cal/cm sec °C. These values are thus the fictitious "pure" thermal conductivities which snow would possess at the densities shown, if there were no vapor diffusion mechanism. The last column of the table shows the percentage contribution to the thermal conductivity of snow made by this mechanism.

TABLE III  
CONTRIBUTION OF WATER VAPOR DIFFUSION TO  $k$  OF SNOW

Density, g/cc	$S = 1 - P$	Thermal conductivity cal/cm sec °C	Conductivity neglecting water vapor transfer cal/cm sec °C	% contribution of vapor transfer
0.10	0.1077	$0.238 \times 10^{-3}$	$0.125 \times 10^{-3}$	47.6
0.20	0.2171	0.355	0.192	45.9
0.30	0.3262	0.537	0.306	43.0
0.40	0.4355	0.901	0.576	36.0
0.45	0.4901	1.277	0.935	26.8
0.48	0.5228	1.666	1.445	13.2

The calculated thermal conductivity increases with density, the rate of increase being larger at the higher densities. The percentage contribution of vapor flow to the conductivity decreases as density increases. Both these results are caused by the fact that as density increases, the fraction of air present decreases.

At densities higher than 0.48 g/cc, i.e. at porosities lower than 47.7%, equation (3) cannot be applied to calculate thermal conductivities, since at the corresponding value of  $S (= 1 - P)$ , the value of  $R$  becomes unity, and the assumed solid spheres touch. The ice crystals in snow are not solid uniform spheres, but the agreement between the calculated and measured thermal conductivities indicates that they may be so represented for heat conduction purposes.

The above results are shown graphically in Fig. 2 where  $k$ , the thermal conductivity of snow, is plotted against its density  $\rho$ . The heavy full curve represents the variation of  $k$  with  $\rho$  calculated from equation (3), and the dashed curve the calculated variation omitting the vapor flow contribution.

The curves numbered 1 to 5 represent the experimental results of Kondrat'eva, Devaux, Jansson, Yosida, and Abel's. The results obtained by Abel's, expressed by the empirical relationship

$$k = 6.8\rho^2 \times 10^{-3} \text{ in c.g.s. units,}$$

appear to be the commonly accepted values. Since the agreement between the experimental results is poor, the agreement between the calculated and experimental results may be considered satisfactory.

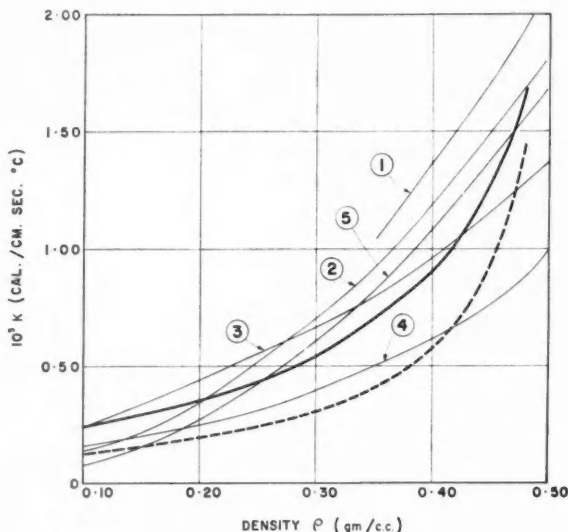


FIG. 2. Thermal conductivity of snow vs. snow density. Full curve: calculated. Dashed curve: calculated, omitting vapor flow contribution. Curves 1, 2, 3, 4, 5: empirical results of Kondrat'eva, Devaux, Jansson, Yosida, and Abel's respectively.

### CONCLUSION

The application of equation (3) to the calculation of the thermal conductivity of snow, taking into account vapor diffusion, was straightforward, since the air in snow is at all times effectively saturated with water vapor, so that  $P_s$  in equation (5) is the saturation water vapor pressure over ice. The application to moist porous materials would be more complicated since the vapor pressure conditions in this case are less well-defined.

### ACKNOWLEDGMENT

The author wishes to express his thanks to A. G. Wilson for useful discussions during the writing of this paper.

## REFERENCES

- BURGER, H. C. 1915. *Physik, Z.* **20**, 73.  
EUCKEN, A. 1932. *VDI Forschungsheft* 353, 16p.  
GEMANT, A. 1950. *J. Appl. Phys.* **21**, 21.  
JAKOB, M. 1949. *Heat transfer* (John Wiley & Sons Inc., New York).  
KERNER, E. H. 1956. *Proc. Phys. Soc. (London)*, B **69**, 802.  
KONDRAT'eva, A. S. 1954. Thermal conductivity of snow cover and physical processes caused by the temperature gradient. U.S. Army, Corps of Engineers, Snow, Ice and Permafrost Research Establishment, S.I.P.R.E. Translation No. 22, 13p.  
KRISCHER, O. 1941. *Wärme- u. Kältetech.* **43** (0), 2.  
MAXWELL, C. 1873. *Treatise on electricity and magnetism* Vol. I. (Oxford University Press, London), p. 365.  
PRATT, A. W. and BALL, J. M. E. 1956. *J. Inst. Heating Ventilating Engrs.* **24**, 201.  
RAYLEIGH, W. R. 1892. *Phil. Mag.* **5**, 481.  
RUSSELL, H. W. 1935. *J. Am. Ceram. Soc.* **18**, 1.  
VRIES, D. A. de. 1952. *Mededel. Landbouwhogeschool Wageningen.* **52**, 1.  
VRIES, D. A. de. 1956. *Nature,* **178**, 1074.  
WEBB, J. 1956. *Nature,* **177**, 989.  
YOSIDA, Z., et al. 1955. Physical studies on deposited snow and thermal properties. Institute of Low Temperature Science, Hokkaido University, Sapporo, Japan, Contributions from the Institute of Low Temperature Science, No. 7, p. 19.

## THE VARIATION OF SEA LEVEL COSMIC RAY INTENSITY BETWEEN 1954 AND 1957<sup>1</sup>

A. G. FENTON,<sup>2</sup> K. B. FENTON,<sup>3</sup> AND D. C. ROSE

### ABSTRACT

Results from neutron monitors and meson telescopes at Ottawa (geomagnetic latitude 57° N.) and Resolute (geomagnetic latitude 83° N.) are presented for the years 1954–57, a period of increasing solar activity. The results indicate that the sea level meson intensity at these latitudes decreased by 5–6% between April 1954 and December 1957. During the same period the intensity of the nucleonic component at these stations decreased by over 22%. Investigation of the relative response of the two types of recorder to transient decreases during this period indicates that the long term change in the intensity level cannot be explained completely as an accumulation of shorter transient decreases, which become more frequent at times of high solar activity. It is concluded that the transient decreases are superimposed upon the longer term changes, each being produced by a separate modulation process but ultimately controlled by the general level of solar activity. Significant differences are found in the shape of transient decreases observed at the Canadian stations, both between different components at the one station and the same component at different stations. These may be interpreted as due to a varying energy dependence from one transient decrease to another, and to anisotropy in the primary cosmic radiation at these times.

### INTRODUCTION

Convincing evidence that the intensity of cosmic radiation varies during the cycle of solar activity was first reported by Forbush (1954), using data obtained with Carnegie Model C ionization chambers. Forbush found a variation of almost 4% in the intensity during the period 1937–52, negatively correlated with the sunspot number. This 11-year variation has been discussed in relation to modulation theories which have been proposed by Morrison (1956), Parker (1956), and Singer (1957) in order to explain other cosmic ray variations controlled by the sun, such as the variation of the low energy cutoff for primary particles, the Forbush decreases, and the 27-day recurrences in cosmic ray intensity. The most recent modulation theories involve a constant galactic cosmic ray intensity spectrum that is modified as it approaches the earth, probably by disordered magnetic fields associated with plasma clouds of solar origin. When formulating and testing these hypotheses it is necessary to know whether the one type of mechanism is capable of explaining all the intensity changes observed or whether two or more processes are operative, each controlled by the general level of solar activity.

It is the purpose of this paper to present data on the variation of the intensities of both the meson and nucleonic components at Ottawa and Resolute since the solar minimum of 1954. It will be shown that the use of the two types of recorder at the one location permits conclusions concerning the relation

<sup>1</sup>Manuscript received April 1, 1958.

Contribution from the Division of Pure Physics, National Research Council, Ottawa, Canada.

Issued as N.R.C. No. 4789.

<sup>2</sup>Visiting scientist from the University of Tasmania.

<sup>3</sup>Now at the Enrico Fermi Institute for Nuclear Studies, University of Chicago.

of the 11-year changes to the more rapid transient changes observed in the cosmic ray intensities.

#### EQUIPMENT

The data were obtained from vertical counter telescopes and neutron monitors operated near sea level at Ottawa (geog. coord.  $45.4^{\circ}$  N. lat.,  $75.6^{\circ}$  W. long., geomag. lat.  $57^{\circ}$  N.) and at Resolute ( $74.7^{\circ}$  N. lat.,  $94.9^{\circ}$  W. long., geomag. lat.  $83^{\circ}$  N.). During the period considered several changes were made in the telescopes, resulting in changes in the counting rate; however, at these times other recorders were in operation and it was possible to obtain reliable normalizing factors, with the result that no significant errors are likely to remain in the records on account of these changes. In the case of the neutron monitors it was possible to correct for equipment changes by reference to the regular calibration tests against a neutron source.

A brief description of the equipment in use at present will now be given.

##### *A. Counter Telescopes*

The telescopes are of cubical geometry consisting of three trays each containing 24 all-metal counters covering an effective area approximately  $60 \times 60$  cm. The absorber (10 cm Pb) is located between the middle and bottom trays, the bottom tray being shielded also at the sides.

The Geiger counters are connected individually to triode preamplifiers which are coupled via germanium diodes to a common output cathode follower, one for each tray. It has been found that this circuit provides short pulses of adequate amplitude, while at the same time permitting the operation of the counters at a reduced charge per pulse, leading to a useful counter life of over two years.

The auxiliary coincidence, scaling, and power supply units are of a design proved to be highly reliable during operation over a number of years at the Cosmic Ray Laboratory.

Two methods of recording are used, namely, electromechanical registers and multi-pen operations recorders. The registers are read visually each day to provide a quick check on the performance of the equipment, and the pen recorder charts are used for the hourly intensities. One-minute time pips on the charts provide a time reference if required for determining onset times of solar flare increases.

In addition to the threefold (meson) component the coincidences between the top and middle trays are recorded, giving the wide angle total intensity.

Fig. 1 shows a schematic diagram of the circuit arrangement. Telescopes of this design are in operation at Resolute, Churchill, and Banff for the I.G.Y. program. The telescope in use at Ottawa differs a little from these in some details, owing to the fact that glass walled counters of a larger size were used, arranged to overlap each other but covering the area  $60 \times 60$  cm.

##### *B. Neutron Monitor*

The neutron monitors differ slightly from the design developed by Simpson, Fonger, and Treiman (1953). Larger counters and greater thicknesses of lead

are used, resulting in a higher counting rate per counter. As shown in Fig. 2, three counters are used, each measuring 27 in. effective length,  $2\frac{1}{2}$  in. in

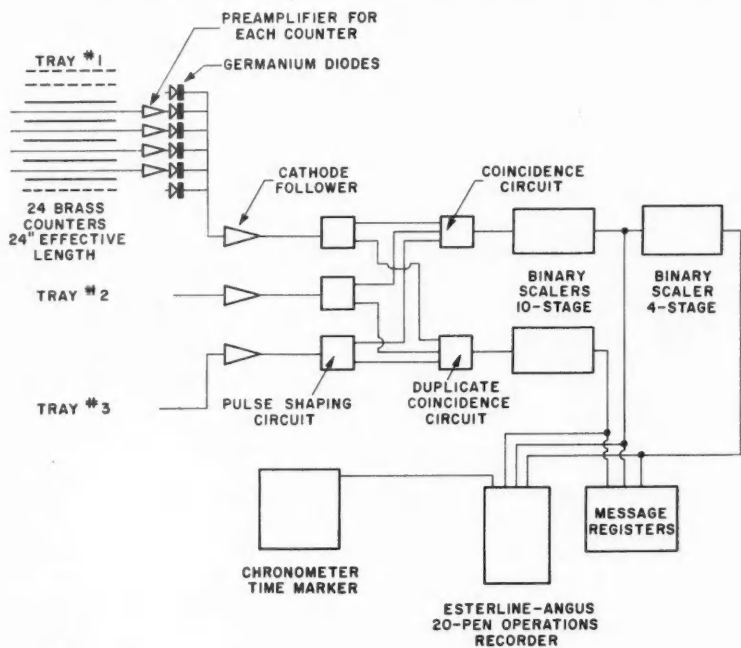
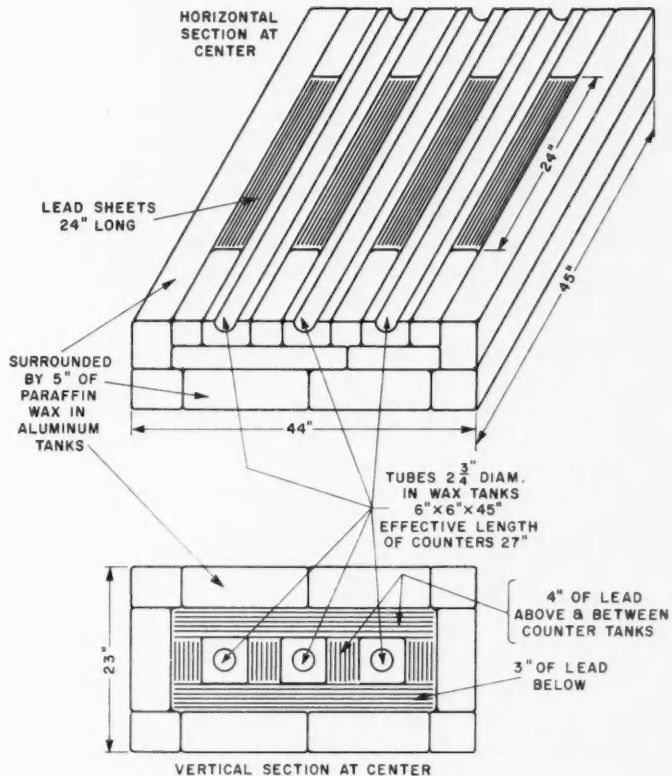


FIG. 1. Meson telescope.

diameter, made for us by Atomic Energy of Canada Ltd., at Chalk River. These are connected to three independent amplifiers and recording circuits, which enables a cross check on performance to be made by examining the ratios of the counts registered in the three channels. Thus it is possible to detect even minor changes in counting rate in one channel due to equipment faults, and also to fill in missing or faulty data in one channel from the other two.

This three-channel neutron monitor has been in operation since January 1956. Before that a two-counter monitor was used with slightly shorter counters. To be certain of a true normalization of the intensity the two monitors were operated together for a period of 3 months. Thus the sequence of calibrations referring to a standard neutron source can be carried back to April 1954. Apart from changing from the old to the new monitor only one other change was made, namely the replacement of the amplifiers by a better design in August 1955. This was done at a time of relatively little intensity change, and calibrations before and after the change were reasonably consistent. The earlier monitor showed a systematic change in sensitivity of a few

per cent (maximum 6%) for which corrections have been made. Calibrations of the later monitor show no systematic change, although the standard deviation of the individual calibrations is about twice that expected from the counting rates used in calibration. Considering all errors due to changes in the equipment and calibration uncertainties it is our belief that errors over the period April 1954 to December 1957 are of a random nature and are less than 1%.



### NEUTRON MONITOR

FIG. 2.

Fig. 2 gives the more important dimensions of the neutron monitor pile. The circuit consists of a preamplifier, amplifier, and pulse height discriminator of conventional design. The output is fed into a binary 6-stage scaler followed by a 4-stage scaler for each of the three channels. These record on message registers and the 20-pen operations recorder as shown in Fig. 1.

## ATMOSPHERIC CORRECTIONS AND DATA PROCESSING

The raw meson intensity data were corrected for atmospheric pressure according to a linear regression equation using the empirical coefficient  $\beta = -0.136\%$  per mb. A large seasonal variation remained in the pressure-corrected data. In the case of the Ottawa data this was practically removed by applying a further correction for the monthly mean surface temperature. It was noted that the monthly mean surface temperature in the continental climate of Ottawa is very consistent from year to year and follows closely an inverse plot of the cosmic ray data. A least squares analysis of monthly mean cosmic ray intensities (after correction for surface pressure) covering a two-year period of low solar activity gave a correlation coefficient  $r = 0.98 \pm 0.01$ . This is recognized as an arbitrary method of correcting for temperature but it appears to be justified by the close correlation, and was resorted to because there are no radiosonde flights at Ottawa. The temperature coefficient found in this way for the Ottawa data was  $-0.058 \pm 0.003\%$  per  $^{\circ}$ F. The Ottawa daily mean meson intensities were also corrected for surface temperature using the same coefficient, although this is a less reliable procedure than is the case for the correction of the monthly means. Surface temperature corrections for hourly values would be quite useless.

The Resolute data were corrected for atmospheric pressure, followed by correction for the height of the 200 mb level using radiosonde data obtained at this station (two flights per day). Both the monthly and daily mean values were corrected in this way, the coefficient obtained by least squares regression of the 1954-55 monthly mean data being  $-6.2 \pm 0.4\%$  per km. The corresponding correlation coefficient is  $0.95 \pm 0.02$ .

Neutron monitor data were corrected to a standard barometric pressure of 1010 mb using tables derived from the expression  $J = I \exp(\delta P/P_0)$ , where  $J$  is the pressure-corrected intensity,  $I$  is the uncorrected intensity,  $\delta P$  is the difference between the observed pressure,  $P$ , and the mean, viz.  $P - \bar{P}$ .  $\bar{P}$  is taken as 1010 mb and  $P_0$  is a constant, 136 mb, which corresponds to 138.7 gm/cm<sup>2</sup>. The current method of data processing involves the use of I.B.M. machines, and in this case the neutron pressure correction is made by using an expansion of the above exponential to three terms.

## RESULTS

Figs. 3 and 4 give the available information on the variation of the monthly average meson and nucleon intensities at Ottawa and Resolute during the period April 1954 to December 1957. To demonstrate the world-wide nature of the intensity changes the Hobart nucleon data have been included. In the figures the cosmic ray intensity data have been expressed as percentages below the value for the first month of each sequence, with the exception of the Resolute nucleon which has been normalized to Ottawa for October 1956. The data have been plotted on different vertical scales to avoid overlapping. The Zurich sunspot numbers and the sums of planetary magnetic disturbance  $K_p$  indices for each month are also shown, plotted inversely for comparison with the cosmic ray intensities.

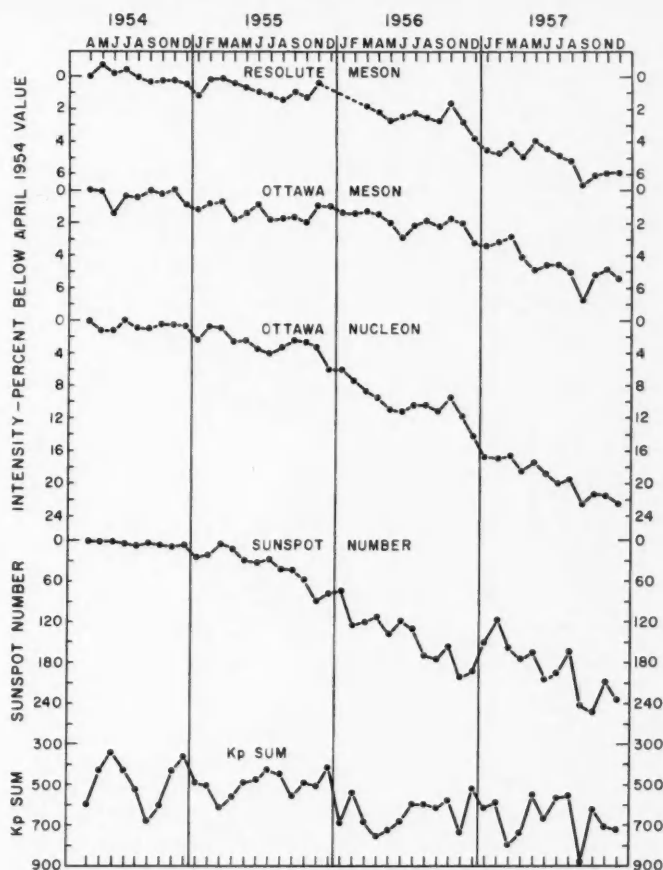


FIG. 3. Monthly mean meson and nucleon intensities, corrected for atmospheric effects and equipment changes, April 1954–December 1957, together with the corresponding Zurich sunspot numbers and the sums of the planetary geomagnetic disturbance index  $K_p$ .

As may be seen from Fig. 3 the Ottawa meson intensity decreased by about 5% during the period 1954–57, while the nucleonic component decreased by over 22%. The decrease in meson intensity at Resolute was about the same as at Ottawa, and the nucleonic component at Resolute for the shorter period October 1956 to December 1957 follows closely the corresponding section of the Ottawa nucleon intensity curve (Fig. 4).

It should be noted that the statistical fluctuations for the monthly averages of the cosmic ray intensities are considerably smaller than the fluctuations apparent in Figs. 3 and 4. The standard deviation for the meson data for 1 month is  $\pm 0.015\%$ , with  $\pm 0.025\%$  for the nucleon intensity data.

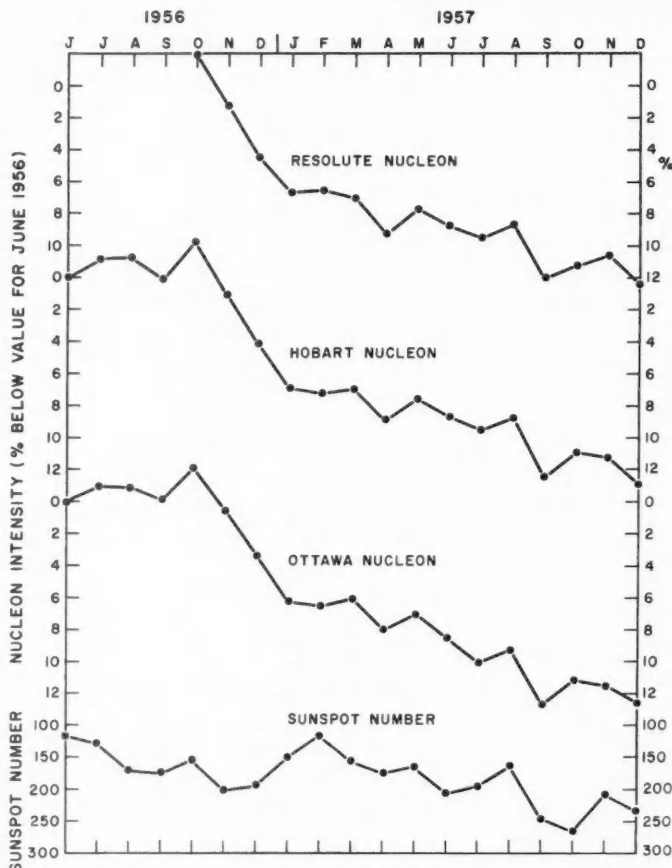


FIG. 4. Monthly mean nucleon intensities June 1956–December 1957. (The Resolute value for October 1956 has been normalized to Ottawa.)

The month to month intensity changes follow a similar trend from station to station, but statistically significant differences are observed.

Table I shows the monthly mean values of the nucleon and meson intensities (in scaled counts per hour) at Ottawa and Resolute for the period October 1956 to December 1957, when comparable data were available from both stations. Beside the columns for each component is the ratio of the Resolute to Ottawa intensities for each month, adjusted slightly to give a ratio of unity for the mean intensities over the complete period. The root mean square deviations of these ratios are respectively  $\pm 0.0069$  and  $\pm 0.0061$  for the nucleon and meson components. These are to be compared with the standard deviations due only to statistical variations in the counting rates, namely

0.0004 and 0.0002 respectively. Evidence has been presented by the Chicago group (Simpson, Fonger, and Treiman 1953) that correction of data from neutron monitors for barometric pressure is sufficient to remove intensity

TABLE I

MONTHLY MEAN VALUES OF THE NUCLEON AND MESON INTENSITIES (IN SCALED COUNTS PER HOUR) AT OTTAWA AND RESOLUTE FOR THE PERIOD OCTOBER 1956 TO DECEMBER 1957.  
(For ratio see text)

Month	Nucleon component			Meson component		
	Resolute (÷ 64)	Ottawa (÷ 64)	Ratio (R/O) (normalized)	Resolute (÷ 1024)	Ottawa (÷ 1024)	Ratio (R/O) (normalized)
<i>1956</i>						
Oct.	309.70	296.84	1.0035	56.57	52.64	1.0057
Nov.	299.67	289.17	0.9968	55.94	52.49	0.9973
Dec.	289.67	281.11	0.9911	55.36	51.82	0.9998
<i>1957</i>						
Jan.	282.94	272.75	0.9977	54.94	51.75	0.9936
Feb.	283.35	271.84	1.0025	54.86	51.88	0.9896
Mar.	281.80	273.27	0.9918	55.15	52.08	0.9910
Apr.	274.48	267.60	0.9865	54.74	51.40	0.9967
May	279.62	270.34	0.9948	55.31	50.95	1.0159
June	276.22	265.93	0.9990	55.03	51.11	1.0076
July	273.78	261.71	1.0062	54.80	51.12	1.0033
Aug.	276.46	264.09	1.0069	54.59	50.89	1.0039
Sept.	265.85	253.84	1.0073	53.70	49.96	1.0060
Oct.	268.88	258.33	1.0011	54.06	50.78	0.9963
Nov.	271.14	257.41	1.0131	54.12	51.02	0.9927
Dec.	265.31	254.26	1.0036	54.16	50.71	0.9996

variations due to the atmosphere. This being so, the month to month variations indicated by the ratios in Table I appear most likely to be due to differences in the primary intensity above the two stations. In the case of the meson component the usual problem of residual atmospheric effects makes a similar conclusion less reliable. On the other hand the fact that the variations in the ratio of the meson components at Resolute and Ottawa are not greater than those for the nucleon component may be regarded as evidence in favor of the procedures used during correction of the meson data.

Two types of decreases, relatively short compared with the 11-year changes, are often distinguished in the literature, viz. the rather abrupt Forbush decreases which are often but not always associated with severe magnetic disturbances, and the slower decreases that sometimes recur through several solar rotations. In this paper no distinction will be drawn between these variations, which will be referred to as transient decreases because their recovery appears to be complete in times of the order of days or weeks.

The question arises as to whether or not the greater prevalence of transient intensity decreases observed during periods of high solar activity can be the cause of the long period variation of intensity during the solar cycle. In an attempt to answer this question for the period 1954-57 the daily mean meson and nucleon intensities observed at Ottawa have been examined.

Two short-term transient decreases are shown in Fig. 5, and data concerning these and other decreases observed during 1957 are given in Table II. The first day of each decrease was chosen by inspection of a plot of the daily mean intensities, and was taken as the G.M.T. day on which the intensity

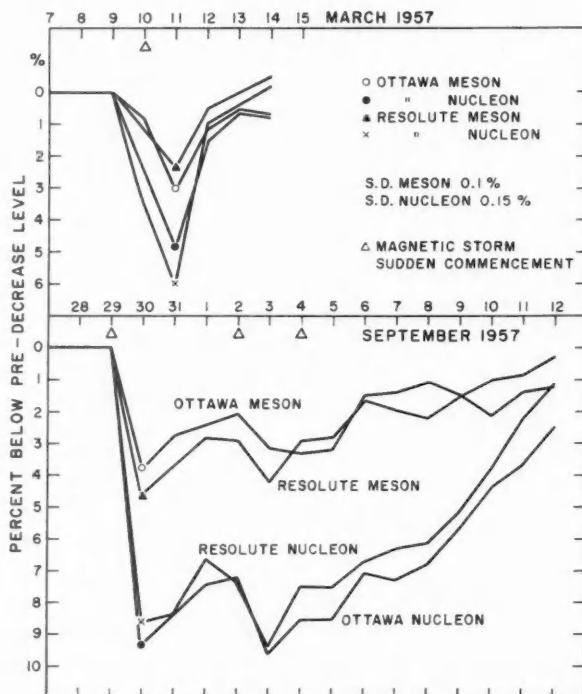


FIG. 5. Daily mean intensities during two transient decreases observed at Ottawa and Resolute, plotted as percentages below the average intensity for 3 days before the decrease.

was significantly lower than the mean for the previous 2 or 3 days. The last day of each interval presented in Table II was selected to represent either (a) the day on which the intensity recovered to roughly the pre-decrease intensity, or (b) the first day on which the intensity settled down for a time to a new level, lower than the pre-decrease value, or (c) the day before a further obvious decrease began, provided that most of the recovery had taken place by this time. The upper section of Fig. 5 illustrates selection according to criterion (a) while the lower section illustrates (c) as another decrease began on September 13. It should be noted that in this section of Fig. 5 a small subsidiary decrease which occurred during the early stages of recovery has been included with the main event.

Table II shows that the ratio of the nucleon to meson departures from the

TABLE II

TRANSIENT DECREASES CHOSEN FROM 1957 DATA, SHOWING THE MAXIMUM AND AVERAGE DEPARTURES FROM THE PRE-DECREASE LEVEL (IN PER CENT) AND THE CORRESPONDING RATIOS FOR THE NUCLEON ( $\Delta N$ ) AND MESON ( $\Delta M$ ) COMPONENTS

First and last day of interval	Station	$\Delta N$ (%) (maximum)	$\Delta M$ (%) (maximum)	Ratio	$\Delta N$ (%) (average)	$\Delta M$ (%) (average)	Ratio
Jan. 21-28	Ottawa	13.25	6.70	1.98	6.75	2.66	2.54
	Resolute	12.44	5.78	2.15	6.55	2.75	2.38
Mar. 10-14	Ottawa	4.85	3.02	1.61	2.36	1.38	1.71
	Resolute	6.00	2.38	2.52	2.15	0.71	3.03
Apr. 15-30	Ottawa	8.16	6.03	1.35	4.52	2.78	1.63
	Resolute	7.26	3.34	2.17	3.80	1.54	2.47
July 20-24	Ottawa	1.54	1.74	0.89	1.32	0.66	2.00
	Resolute	2.57	1.33	1.93	2.07	0.86	2.41
Aug. 4-15	Ottawa	5.76	2.29	2.52	2.76	1.03	2.68
	Resolute	5.73	3.12	1.84	2.69	1.15	2.34
Aug. 30-Sept. 12	Ottawa	9.32	3.82	2.44	6.90	2.21	3.12
	Resolute	9.48	4.23	2.24	6.23	2.41	2.59
Sept. 29-Oct. 5	Ottawa	5.28	3.28	1.61	3.20	1.83	1.75
	Resolute	5.55	2.27	2.44	3.32	1.29	2.57
Oct. 22-28	Ottawa	8.69	4.82	1.80	5.87	3.13	1.88
	Resolute	9.20	4.83	1.90	6.04	3.69	1.64
Mean ratios	Ottawa	—	—	1.78	—	—	2.16
	Resolute	—	—	2.15	—	—	2.43

pre-decrease level lies between about 1 and 2.5 for the intensity minima that are reached, while the ratio of the average departures represented by the area of the decrease (decrease  $\times$  time) is only slightly larger than this. This indicates that the main recovery phase of the short term transient decreases listed in Table II takes about the same time in both the meson and the nucleon components.

If the 11-year variation were due only to the changes in frequency and magnitude of the transient decreases observed in the daily mean intensities one would expect to find either complete recovery between decreases to the level prevailing near solar minimum, or else considerable overlapping of events, a fresh decrease often occurring before the complete recovery from earlier ones. Inspection of the daily mean intensities plotted as a function of time indicates that this is not so, since it is possible to find groups of days between decreases during which the intensity remains fairly steady and at a lower level than prevailed during 1954. Furthermore, since the recovery from transient decreases takes about the same time in both the nucleonic and the meson components we would expect that, even with considerable overlapping, the decreases in the nucleon component would be at least four times as great as those in the meson component, in order to account for the factor of 4 in the long term changes in these components. The final column of Table II clearly indicates that this is not the case. The decreases listed in Table II vary in

peak amplitude from less than 2% to over 13% in the nucleon component, and there is no evidence that the small decreases are consistently associated with higher ratios; therefore, it does not seem likely that the 11-year variation is caused by the superposition of a large number of transient decreases produced by the same mechanism as these but too small to be recognized as separate events.

Thus, it is concluded that the transient decreases that occurred during the period 1954-57 did not themselves produce the over-all intensity decrease, but are superimposed upon it. If this statement is accepted it is possible to estimate the extent to which the intensity data of Figs. 3 and 4 are influenced by the transient effects. This has been done for the period October 1956 to December 1957. Since there were no large intensity decreases during October 1956 this

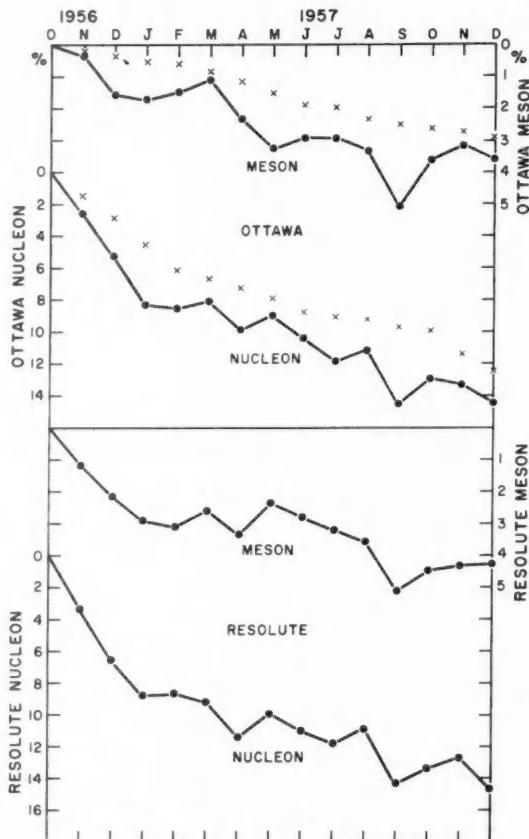


FIG. 6. Monthly mean intensities, October 1956-December 1957. The crosses indicate the corresponding Ottawa meson and nucleon intensities after correction for transient decreases.

was taken as a reference month, and the average intensity for succeeding months, corrected for transient decreases, was obtained as follows. A straight line was drawn through the high points on a time plot of the daily mean intensities (corrected for atmospheric effects), taking 3 months at a time; then the position of the line at the mid-point of the middle month of the three was taken to represent the mean intensity for that month, corrected for transient decreases. This process was then repeated to obtain a value for each month. In Fig. 6 the solid lines represent the appropriate sections of Figs. 3 and 4, while the crosses give the Ottawa results corrected for transients as just described. This process effectively removes most of the month to month fluctuations in the intensity attributable to transient decreases and leads to a re-evaluation of the over-all decrease between 1954 and 1957, due only to the long term modulation effect. Since there were very few transient decreases during 1954 we conclude that the intensity change at Ottawa during this period, after correction for transients, was about 20% in the nucleonic component and about 4% in the meson intensity. The ratio of these corrected changes is 5, compared with 4 for the ratio of the over-all changes.

#### DISCUSSION

The decrease in meson intensity between 1954 and 1957 is in good agreement with the ionization chamber results reported by Forbush (1954) for 1944-47, which was a comparable period of increasing solar activity. Forbush obtained an intensity change of slightly less than 4% for the mean of four stations, namely, Huancayo, Christchurch, Cheltenham, and Godhavn. One feature of his observations is that the intensity variation is practically independent of latitude, as shown by the data for the individual stations. For example, the data given by Forbush show that both the Huancayo and the Godhavn annual mean intensities decreased by 3.5% between 1944 and 1947. The change of about 5% for the Ottawa and Resolute annual mean meson intensities is consistent with these results in view of the greater change that has taken place in the sunspot numbers, from the exceptionally low level in 1954 to the unusually high sunspot numbers near the end of 1957 (Ellison 1957).

The evidence that the slow intensity changes over the solar cycle are not due to the shorter transient decreases is consistent with a similar conclusion arrived at by Forbush (1954). Forbush based his conclusion on the similarity of the variation in groups of data selected according to geomagnetic activity, finding that the annual means of cosmic ray intensity were practically the same for international magnetic quiet days and international disturbed days. The conclusion given in this paper has the advantage that it is independent of arguments based on geomagnetic activity, being derived from cosmic ray data alone.

Although there is an obvious relationship between the cosmic ray intensity and the general level of solar activity as shown by the sunspot numbers and sum of  $K_p$  indices in Fig. 3, there is no evidence for a consistent and detailed month by month agreement. Other phenomena we have examined, such as the horizontal component of the earth's magnetic field and solar radio emission,

do not show any better detailed tracking with changes in the cosmic ray intensity. As may be seen from Figs. 3 and 4 the cosmic ray intensity levelled off in June 1956 and then increased until October of that year, when the intensity was higher than during the previous 5 months. This may be compared with information given in the preliminary reports on solar activity from the High Altitude Laboratory and National Bureau of Standards, Boulder, Colorado. These reports indicate that the general level of solar activity, as judged from a number of phenomena, decreased appreciably after the relatively high activity in January and February 1956 to a low level in June and began to increase again during August. A time constant of 2 to 3 months for the mechanism producing the slow variation of cosmic ray intensity is suggested by these observations if the upward trend during this period was due to a relaxation process.

The much greater change in the Ottawa and Resolute neutron monitor data as compared with the counter telescope records indicates that the mechanism responsible for the decrease between 1954 and 1957 is more effective at the lower energies, to which neutron monitors are more sensitive than counter telescopes. This is consistent with results obtained at balloon altitudes by Neher and Anderson (1958) who have reported recently that the primary particle intensity at Thule decreased by a factor of 4 between August 1954 and August 1957. The energy dependence of the intensity change during this period appears to be steeper than for the more abrupt transient decreases though by no means as steep as that found for sudden increases associated with solar flares (Meyer, Parker, and Simpson 1956).

An investigation of the latitude dependence of this long-term intensity change would be worthwhile, but sufficiently extensive data are not available to us at present for this to be made. The ionization chamber data given by Forbush (1954) for an earlier period suggest that a very small latitude effect exists for the 11-year change in the meson component. Thus the rather large change reported here for the nucleonic component may be predominantly a high-latitude phenomenon, possibly associated with the low energy cutoff that develops at times of high solar activity. More information about this may be available when data from the world-wide network of I.G.Y. stations can be assembled.

As already pointed out the response of the Ottawa and Resolute neutron monitors at the minima of the short-term changes is about twice that of the telescopes on the average; however, as may be seen from Table II, these ratios vary from 0.89 to 2.52 for the 1957 decreases. Furthermore, there are significant variations both between the two components at the one station and between the same component at different stations. This may be seen from Fig. 5 and the difference plots of Fig. 7. These observations indicate that the cause of the transient intensity decreases is variable in its energy dependence in the range from a few Bev to over 30 Bev (the average primary particle energies detected by sea level neutron monitors and meson telescopes are about 7 and 30 Bev respectively). The variation in response to transient decreases observed with similar equipment at different stations suggests that a primary anisotropy is

present at these times, since both Ottawa and Resolute are at latitudes above the knee of the sea level latitude-intensity curve, which precludes effects due to changes in the low cutoff rigidities. (Meyer and Simpson (1957) have presented evidence that in August 1956 the intensity at aircraft altitudes levelled off at about 52° geomagnetic latitude. Since then the sun has become more active and the "knee" may now be nearer the equator.)

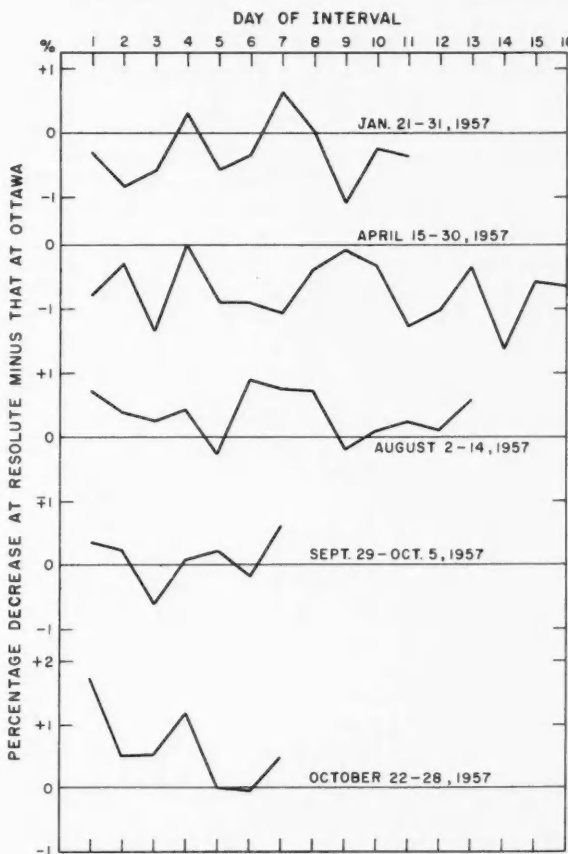


FIG. 7. Difference in response of the neutron monitors at Ottawa and Resolute during five transient decreases, derived from tabulated data in percentages below pre-decrease levels (as used for construction of Fig. 5). Positive differences indicate a larger departure at Resolute than at Ottawa. Standard deviation of points, calculated from counting rate,  $\pm 0.2\%$ .

The relative response of neutron monitors and ionization chambers to intensity variations has been discussed by Fonger (1953) and Simpson (1957) who reported a 5 to 1 ratio for the response of the Climax neutron monitor as

compared with records from the Freiburg ionization chamber for the period July to October 1951. This is to be compared with the ratio of about 2 to 1 reported here for the Ottawa and Resolute data. It is not clear why this difference should exist, but the possibility should not be overlooked that the response is different for different phases of solar activity. Further data will be needed to settle this question.

#### CONCLUSIONS

From a study of the intensity variations observed with counter telescopes and neutron monitors at Ottawa and Resolute during the period 1954-57 we conclude that:

(1) The sea level meson intensity at these latitudes decreased by 5 to 6%, while the nucleonic component decreased during the same period by over 22%. The decrease in meson intensity is comparable to the world-wide decrease observed with the Carnegie ionization chambers during the last period of increasing solar activity, 1944-47.

(2) It has been shown that the short-term transient decreases observed during 1954-57 are not in themselves the cause of this intensity variation during the solar cycle; these events appear to be superimposed upon the longer-term variation, and are less dependent on energy.

(3) Significant variations are found in the energy dependence of transient decreases, and also in the form of these decreases observed at different high latitude stations. The latter effect may be interpreted in terms of primary anisotropy.

#### ACKNOWLEDGMENTS

In the continuous operation of cosmic ray equipment particularly at a remote station like Resolute successful results depend on the assistance of many people. Practically every member of the Cosmic Ray Group has taken some part in obtaining the results presented here. The counter telescope at Resolute from 1954 to 1956 was operated by the staff of the Dominion Observatory's Geomagnetic Division who were stationed there. The cubical telescope and neutron monitor were installed by Dr. J. Katzman and Mr. D. Johnston in 1956 and since then have been operated by Mr. Johnston. The equipment at Resolute is located at the ionosphere station of the Telecommunications Division of the Department of Transport. The I.B.M. machine handling of the data was supervised by Mrs. F. Friedman. We are grateful to Mr. K. G. McCracken of the University of Tasmania for the Hobart neutron monitor data. Meteorological data were supplied by the Meteorological Division of the Department of Transport. We are particularly grateful for the special tabulation of upper atmosphere data which they prepared for us. Dr. P. M. Mathews gave considerable assistance in discussions regarding the correction of the meson data for temperature and the height of the 200 mb layer. A. G. Fenton gratefully acknowledges the award of a travel grant by the Committee of the Royal Society and Nuffield Foundation Bursaries Scheme.

## REFERENCES

- ELLISON, M. A. 1957. Nature (London), **180**, 1173.  
FONGER, W. H. 1953. Phys. Rev. **91**, 351.  
FORBUSH, S. E. 1954. J. Geophys. Research **59**, 525.  
MEYER, P., PARKER, E. N., and SIMPSON, J. A. 1956. Phys. Rev. **104**, 768.  
MEYER, P. and SIMPSON, J. A. 1957. Phys. Rev. **106**, 568.  
MORRISON, P. 1956. Phys. Rev. **101**, 1397.  
NEHER, H. V. and ANDERSON, H. 1958. Phys. Rev. **109**, 608.  
PARKER, E. N. 1956. Phys. Rev. **103**, 1518.  
SIMPSON, J. A., FONGER, W., and TREIMAN, S. B. 1953. Phys. Rev. **90**, 934.  
SIMPSON, J. A. 1957. Proc. Natl. Acad. Sci. U.S. **43**, 42.  
SINGER, S. F. Proc. 1957 IUPAP Cosmic Ray Conference. Nuovo cimento, Suppl. (to be published).

# ANALYSIS OF METEORIC BODY DOPPLER RADAR RECORDS TAKEN DURING A GEMINID SHOWER PERIOD<sup>1</sup>

M. SRIRAMA RAO<sup>2</sup>

## ABSTRACT

The determination of the prevailing wind in the 80–100 km region of the upper atmosphere by a new method, involving the simultaneous use of a CW doppler radar at 30.02 Mc/sec and three-station pulsed radars at about the same frequencies, is presented in this paper. This method involves the determination of the exact location of each observed meteor train and the component of the velocity of its horizontal drift in the direction of the azimuth from Ottawa. A 49-minute period during the Geminid shower on the night of Dec. 10/11, 1948, has been selected for this investigation. Theory for the analysis of the body doppler records is briefly outlined. The prevailing wind speed obtained from the body doppler frequencies ( $f_d$ ) is 54 m/sec. The observed linear variation in the average  $f_d$  with time, in the case of each meteor, has been explained as caused by the effective point of reflection drifting along its train towards the maximum echo duration level. Periodic fluctuations of  $f_d$  of the order of 1–3 c.p.s., on the average, have also been observed. The above two phenomena can be explained from a postulate of atmospheric turbulence on a scale of about 1 km or above.

## 1. INTRODUCTION

Interest in the study of meteors and their associated phenomena has been growing in recent years. Study of the motion of the ionized meteor trains has led, among other things, to the determination of upper atmospheric winds. During 1948–1950, a good number of doppler beat records of meteors were photographed at the South Gloucester station of the National Research Council, using continuous wave (CW) transmissions at 30.02 Mc/sec transmitted from the Metcalfe Road station, 7.5 km distant. The initial doppler whistles, in each record, caused by the motion of the meteoroids through the atmosphere, have already been analyzed by McKinley (1951) for meteor velocities. These doppler whistles are usually followed by a comparatively slow variation of signal strength known as the body doppler which is caused by a drifting motion of the ionized meteor train.<sup>3</sup> Such body dopplers have been analyzed previously by Manning, Villard, and Peterson (1950), of Stanford University, California, for the determination of wind speeds and directions by a method involving the determination of average doppler frequency for each azimuth angle. The atmospheric motion was found to be predominantly horizontal. As quite a number of meteors are required in this method to determine the average doppler frequency independent of range, it is not always practical. The method used in the present paper is different from the Stanford procedure as a single meteor will give a determination of a

<sup>1</sup>Manuscript received February 26, 1958.

Contribution from the Division of Radio and Electrical Engineering, National Research Council, Ottawa.

Issued as N.R.C. No. 4782.

<sup>2</sup>National Research Council Postdoctorate Fellow; on leave from Andhra University, Waltair, India.

<sup>3</sup>The word "train" as used in this paper refers to the column of dust or ionization left in the wake of the meteor.

component of wind velocity in the horizontal plane in the direction of the azimuth. The actual position of each meteor is determined from simultaneous range-time records taken from Ottawa, Arnprior, and Carleton Place stations, using pulsed radar at about the same frequencies. The actual frequencies of radiation used at these stations were 32.7, 36.0, and 34.5 Mc/sec respectively. The method of calculation of the coordinates of the meteor position with respect to Ottawa has been given by McKinley and Millman (1949a). Hence we have, for each meteor, its azimuth angle  $A$  measured in degrees eastward from the north point as seen from Ottawa, its elevation angle  $h$  measured from the horizon, and its height  $H$  above the ground. A complete 100-ft roll of 35 mm photographic film has been used for recording the doppler phenomena of meteors during each 40-minute period. Results of the analysis of all meteoric body dopplers occurring during the period from 0412 to 0452 E.S.T. on Dec. 11, 1948, are presented in this paper. The Geminid shower is known to be active during this period.

## 2. EXPERIMENTAL DETAILS AND OBSERVATIONS

The techniques used in the doppler radar equipment of the National Research Council have already been discussed in detail by McKinley (1951). The CW radiation, on 30.02 Mc/sec from the Metcalfe Road station, reaches South Gloucester by way of reflection from the meteor train as well as by way of ground transmission. Provision was made to control the ground wave to a required level of intensity to prevent overloading of the receiver. As the meteor train drifts bodily in a horizontal direction, the reflected wave suffers doppler shift of frequency, giving rise to a beat frequency  $f_d$ . This body doppler frequency is recorded as variation in echo amplitude with time. Fig. 1 shows a portion of such body doppler record taken on Dec. 11, 1948, at 04<sup>h</sup> 38<sup>m</sup> 28<sup>s</sup> E.S.T., by a technique referred to by McKinley as the fast doppler method. The doppler whistle can easily be identified at the left end of the sixth line from the bottom, followed by the body doppler of a longer period. The bright spots on the various lines are the time markers, the distance between consecutive markers corresponding to 1 second. It can be easily seen that the length of the record reproduced here corresponds to slightly more than a second.

Each body doppler record, obtained during the period of this investigation, is analyzed by measuring the time differences between the peak points of successive beat waves, from the first wave after the doppler whistle to the end of the body doppler duration of the meteor train. Thus we get the periods  $T$  of consecutive beat waves, where

$$(1) \quad T = 1/f_d.$$

These periods could be measured to an accuracy of 0.001 second. A graph is then drawn to show the variation of  $f_d$  with time. Fig. 2 shows a typical curve obtained in this way for the meteor of Fig. 1. The body doppler in this case persists for about 3 seconds. In general, durations between 2 and 9 seconds are observed in this investigation.



FIG. 1. A portion of the body doppler record obtained at 04<sup>h</sup> 38<sup>m</sup> 28<sup>s</sup> E.S.T. on Dec. 11, 1948.

The nearly periodic fluctuation of  $f_d$  apparent in Fig. 2 is interpreted as due to the effect of interference between the echoes from the various centers of reflection scattered along the meteor train, as the train moves bodily in a

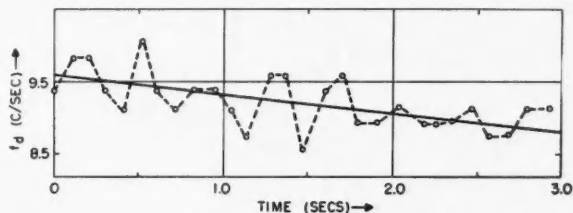


FIG. 2. A typical curve of the variation of  $f_d$  with time, drawn for the body doppler of Fig. 1.

horizontal direction. These various centers of reflection along a meteor train may be produced in various ways. Atmospheric turbulence and flares may both contribute their share in producing various blobs of ionization along the meteor train, reflecting radio waves by back scatter. Previous work in this connection will be reviewed in more detail later in this paper. However, the interference or fading frequency  $f_i$  observed in the  $f_d-t$  curves is thought to be caused by the interference of these various echoes from the train. In each case, the average value of  $f_i$  may be measured by counting the number of waves, such as those in Fig. 2, for the whole duration of the doppler record. This frequency  $f_i$  is generally found to be small compared to the main doppler beat frequency  $f_d$ . For example, in the particular case of Fig. 2, a low frequency of  $f_i = 2.66$  c.p.s. is found to be superposed on the primary doppler frequency, which varies within the limits of 8.5 and 10 c.p.s. Graphs drawn in the case of the other meteors also show a similar effect of the same order of magnitude.

In order to find the average value of  $f_d$  in each case, a mean straight line is drawn through the  $f_d-t$  curve of the variation of  $f_d$  with time. The value read from this straight line at the middle of the duration is taken as the average  $f_d$  for purposes of calculation of the average prevailing wind. These straight lines are not, in general, parallel to the time axis, but show a regular gradient  $df_d/dt$ . Thus the straight line of Fig. 2 shows a linear change of  $f_d$  from 9.6 c.p.s. at 0 second to 8.8 c.p.s. at 3 seconds, with an average value of 9.2 c.p.s. at 1.5 seconds. From this, the value of the slope of this line is found to be  $-0.27$  c/sec<sup>2</sup>. Slopes of either sign are observed in this investigation, and the interpretation of these results will be taken up later in this paper.

Other data for each meteor have been obtained from simultaneous three-station range-time ( $R-t$ ) records. The values of the azimuth  $A$ , elevation  $h$ , and height  $H$  for each meteor have been deduced by triangulation.

The various data derived from the doppler and the range-time records for eight meteors observed in this investigation are presented in Table I, along with the time of occurrence and the Ottawa range.

From this table it can be seen that the doppler durations vary between 2 and 9 seconds, and that the average values of  $f_d$  vary between 4 and 11 c.p.s.

TABLE I  
DATA OBTAINED FROM PULSED RADAR AND BODY DOPPLER OBSERVATIONS

Meteor No.	Time, E.S.T. h-m-s	Ottawa range, km	<i>h</i> , deg	<i>A</i> , °E. of N.	<i>H</i> , km	Doppler duration, sec	Average <i>f<sub>d</sub></i> , c.p.s.	<i>f<sub>t</sub></i> , c.p.s.	$df_d/dt$ , c/sec <sup>2</sup>
1	04-14-51	157	36.4	104	94	2.2	7.30	2.78	-0.42
2	04-21-05	120	43.7	138	88	6.2	3.97	1.17	+0.23
3	04-26-44	187	27.0	42	87	6.0	6.40	1.64	+0.20
4	04-32-10	132	41.4	55	88	2.3	11.30	2.00	-0.90
5	04-34-48	218	23.8	35	91	3.0	7.95	1.96	+0.58
6	04-38-28	173	30.5	261	90	3.0	9.20	2.66	-0.27
7	04-38-40	123	44.3	215	89	8.9	5.20	1.60	+0.05
8	04-52-11	181	29.2	247	90	2.1	9.44	2.00	-0.37

Average *H* = 90 km

The values of *f<sub>t</sub>* are found to vary between 1.2 and 2.8 c.p.s., and these values appear to be larger in the case of meteors of smaller duration. This fact may give a clue to the origin of the fading mechanism in different cases, if verified with more observations. It can be noticed from the values of *A* that the various meteors occur randomly in almost all directions, as we look from Ottawa. Another interesting point is the fact that the heights, obtained by triangulation for the various meteors, vary in a small range between 87 and 94 km, the average of all being 90 km. It can hence be assumed that the midpoint of the ionization train is at a height of roughly 90 km for the group of meteors observed. The measured height is given for each meteor.

In this investigation, the meteors observed thus appear to be situated in the 80–100 km region in the upper atmosphere, which may be called the M-region, following McKinley and Millman (1949b). The M-region has been defined by them as that region in which the great majority of the radar echoes from meteors occur, or as that region which has physical properties which sustain the ionization caused by the passage of a meteor. Though the average height of the M-region varies with time of the day, it may remain reasonably constant for about an hour during any part of the day. The M-region, at a particular time, may differ for meteors of different velocity but will be the same for meteors of a given shower. Thus the M-region, in this particular case, is the one centered at 90 km height above the ground.

### 3. THEORY FOR THE ANALYSIS OF BODY DOPPLER

In view of the previous investigations, we may assume that the meteor train moves chiefly in a horizontal direction in the upper atmosphere, and that the vertical drift can be considered negligible compared to the horizontal drift. With a horizontal velocity *v* given in m/sec, in a direction *ϕ* measured in degrees E. of N., each wave reflected from the train undergoes a doppler shift of  $\pm f_d$ , which is given by

$$(2) \quad \begin{aligned} f_d &= 2v_r/\lambda, \\ &= (2v_p \cos h)/\lambda, \\ &= \{2v \cos(\phi - A) \cos h\}/\lambda, \end{aligned}$$

where  $\lambda$  is the radio wavelength transmitted,  $v_p$  is a horizontal component of  $v$  in the vertical plane passing through the midpoint of the meteor train and the observer (see Fig. 3), and  $v_r$  is the component of  $v_p$  along the line from the midpoint to the observer. Now using the values of  $v_p$  obtained from equation (2) for each meteor, a graph can be drawn with values of  $v_p$  plotted against

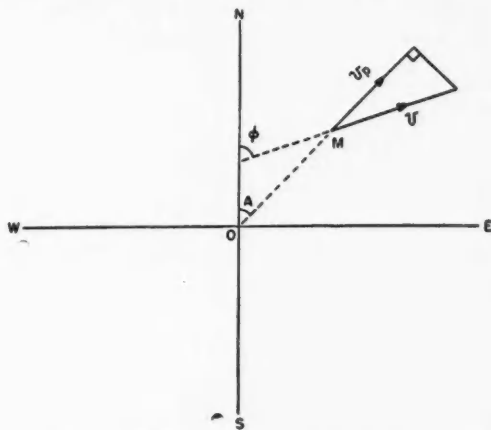


FIG. 3. Diagram showing the motion of point  $M$  on the meteor train, in the horizontal plane through  $O$ , the overhead point at 90 km height.

the values of  $A$ . If the prevailing wind in the upper atmosphere does not appreciably change in speed and direction, this plot should give a smooth cosine curve with a positive maximum when  $A = \phi$ , the corresponding value of  $v_p$  being equal to the true velocity  $v$ . Thus it should be possible to determine the average prevailing wind at the average height of occurrence of the meteors for the 40-minute period of the investigation. In fact, in the present investigation,  $f_d$  is taken as positive, and is assumed to be caused by the horizontal motion of the meteor train in a direction that is either  $\phi$  or  $\phi+180^\circ$ .

If we define  $x$  and  $y$  as the right-angled coordinates in the horizontal plane, and  $z$  the vertical coordinate, then for any point on the meteor train at any given instant, measured from the observing station as origin, we have

$$(3) \quad R^2 = x^2 + y^2 + z^2,$$

where  $R$  is the range of the point on the meteor train as observed from Ottawa. Now differentiating twice with respect to time and cancelling off the accelerations along the three directions of  $x$ ,  $y$ , and  $z$  (assuming a constant velocity for the wind drift of this point), we obtain the relation

$$(4) \quad v_r^2 + R(dv_r/dt) = v^2 + v_z^2, \\ = v^2,$$

where  $v_z$  is the vertical component of the true wind velocity, which is neglected.

The variation in  $v_r$  is dependent on the variation in  $h$  with time, as the train moves. We also have

$$(5) \quad dv_r/dt = (\lambda/2)(df_d/dt).$$

If the accurate value of the gradient  $df_d/dt$ , caused by the motion of the train, and its sign could be determined from experiment, the value of wind velocity,  $v$ , can be easily obtained from equation (4) for each meteor observation. The direction of motion,  $\phi$ , is then given from the relation

$$(6) \quad v_p = v \cos(\phi - A).$$

It should be noted here that the motions of individual sections of the train may be different, and hence the doppler beat frequencies produced by the various sections along the train, reflecting the CW radio waves independently, would all combine at the receiving station. The effect of this is to produce a new interference frequency,  $f_t$ , which is superposed on the average doppler frequency,  $f_d$ , which corresponds practically to the motion of the midpoint of the train, at any particular instant. We can now write an expression for  $f_t$  similar to equation (2), as

$$(7) \quad f_t = 2 v_t/\lambda \simeq v_t/5,$$

as  $\lambda = 9.994$  m in this case;  $v_t$  is the differential velocity of two consecutive reflecting points along the train. The  $f_t$  values given in Table I are in fact those averaged for the total echo durations.

Let us now proceed to see how the theory outlined above can be applied to the observational data presented in Table I, to determine the prevailing wind at the 90 km level in the upper atmosphere from the observed values of  $f_d$ , and to give proper interpretations to the observed values of  $df_d/dt$  and  $f_t$ .

#### 4. RESULTS AND DISCUSSION

##### (a) Prevailing Wind at the 90 km Level

The values of  $v_p$  for each of the eight meteors, observed in this investigation, are determined from the values of  $f_d$  in Table I using equation (2), where  $\lambda = 9.994$  m. These values of  $v_p$  are then plotted on a graph against the corresponding values of azimuth,  $A$ . It has already been noted that these points should fall on a cosine curve, if the prevailing wind is reasonably constant for the 40-minute period of this investigation; and that the peak value of  $v_p$ , occurring at  $A = \phi$  or  $\phi + 180^\circ$ , should give the true horizontal wind velocity,  $v$ , blowing in the direction of  $\phi^\circ$  E. of N. Various cosine curves with different amplitudes were drawn on a transparent sheet, and this was slid over a plot of  $v_p$  against  $A$  to get the best fit. Fig. 4 shows the plotted observations along with the best fitting cosine curve superposed on them. The values of  $v$  and  $\phi$  corresponding to this figure are

$$v = 54 \text{ m/sec}, \quad \phi = 80^\circ \text{ or } 260^\circ \text{ E. of N.}$$

One of the two peaks is in fact negative, and the angle  $\phi$  actually corresponds to the value of  $A$  at the positive peak. A technique for detecting the approaching and receding trains was developed later at Ottawa but was not

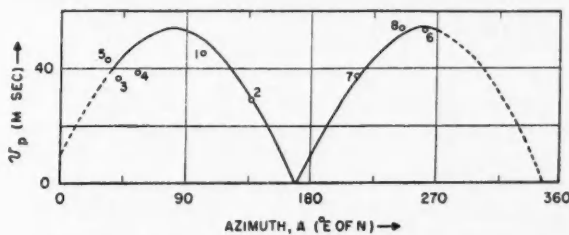


FIG. 4. Graph showing a plot of the various  $v_p$  values against azimuth,  $A$ , with the best fitting cosine curve superposed.

used in 1948. Hence it is not possible to identify the negative peak in this particular case. Nevertheless, by comparing these two values of  $\phi$  with those of previous investigators at Ottawa, one of these two values can be selected. For example, the results of Chapman (1953) for the winter months of 1950 and of McKinley (1956) for August 1948 favor the value of  $\phi = 80^\circ$ . Thus we may conclude that

$$v = 54 \text{ m/sec} \quad \text{and} \quad \phi = 80^\circ \text{ E. of N.}$$

give the average prevailing wind for the period 0412 to 0452 E.S.T. on Dec. 11, 1948, at a height of 90 km above the ground. This order of velocity is in good agreement with that of 50 m/sec for the 85 to 100 km region, obtained by Greenhow and Neufeld (1956). The average value of 35 m/sec obtained by Manning, Villard, and Peterson (1950) is lower and the average value of 80 m/sec obtained by Chapman (1953) for the 100 km height is higher than the value reported in this investigation. The value of 119 m/sec obtained by McKinley (1956) for about 90 km level for a single meteor appears to be high compared to the present value. However, it is known that wind velocities at these levels fluctuate widely from time to time. One point that should be mentioned about the present results is the fact that range measurements are subject to a slight error owing to the finite pulse width (about 20  $\mu$ sec) of the transmission used. This error slightly affects the determinations of  $A$  and  $h$ , but does not seriously affect the velocity. It is interesting to note here that both sporadic and shower meteors may be used together in this method of wind determination.

#### (b) Meteor Positions in Relation to the Shower Radiant

The Geminid radiant was known to be active during the night of Dec. 10/11, 1948, and it is of interest to see if the various meteors observed in this investigation belong to this radiant. The radiant parameters of this shower do not change appreciably during the 40-minute period between 0412 and 0452 hours E.S.T. and hence on the average those at 0430 hours E.S.T. can be taken to be true for this total period. The following values are deduced for the position of the Geminid radiant at this time:

$$\text{elevation of the radiant, } h_r = 60^\circ \quad \text{azimuth of the radiant, } A_r = 258^\circ.$$

Taking the average height of occurrence of meteors to be 90 km in this case, it is of interest to study the theoretical distribution of  $\alpha$  (the angle between the meteor track and the line joining the observing station to the point in the meteor track at 90 km height) over the visible sky. This has been done by McKinley and Millman (1949b) for a hypothetical case of  $h_r = 45^\circ$  and  $H = 100$  km. A similar diagram of conic sections for  $h_r = 60^\circ$  and  $H = 90$  km is reproduced here in Fig. 5(b). This gives curves of constant  $\alpha$  defined by the intersection of the layer at 90 km height with the cone of half-angle  $\alpha$  and apex at the radar station. The maximum range ( $R_{\max}$ ) recorded on the radar display was 300 km. Fig. 5(a) represents the vertical plane containing the radar station and the meteor path, in the ideal case when the radiant lies in the plane of the diagram. In Fig. 5(b)  $A_r$  represents the azimuth of the radiant, knowing which, the N., E., S., and W. directions are also marked on the diagram. Now, from the data given in Table I, the positions of the eight meteors are plotted and identified by number on this diagram.

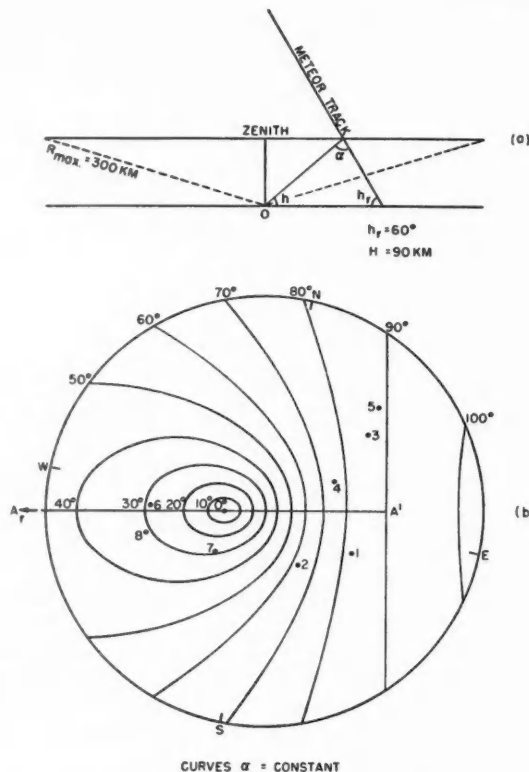


FIG. 5. (a) Diagram showing the vertical plane containing the meteor track and the radar station. (b) Diagram of conic sections in the horizontal plane at 90 km height, showing curves of constant  $\alpha$  and the positions of occurrence of the various meteors.

From examination of the data obtained by visual observations made during this night, it is found that meteor 2 is a non-shower meteor. The variation of  $\alpha$  for meteors 1, 3, 4, and 5 is between 75 and 90 degrees, and hence these are quite likely to be Geminids. In fact, in the ideal condition, all meteors belonging to the Geminid shower should cluster around the straight line representing  $\alpha = 90^\circ$ . Point  $A'$  in Fig. 5(b) represents the position of a hypothetical Geminid meteor whose path lies in the vertical plane containing the observer. Meteors 6, 7, and 8 have a value of  $\alpha =$  nearly  $30^\circ$ , and radar reflections are normally not possible at that low value of  $\alpha$ . Hence they are, quite likely, non-shower meteors. Thus at least four out of eight meteors recorded here may belong to the Geminid shower.

(c) *Rate of Drift of the Effective Point of Reflection along the Meteor Train*

It is now of interest to see if the observed values of  $df_d/dt$  fit into equations (4) and (5) to give the correct order of velocity  $v$ . On the other hand, knowing the velocity  $v = 54$  m/sec, the values of  $df_d/dt$  that would be produced by the wind effect, corresponding to each value of  $v_r$ , in Table I, can be calculated and verified with the observed values of  $df_d/dt$ . Thus the observed and calculated values of  $df_d/dt$  for the eight meteors recorded here are presented in Table II, from which it can be easily seen that the calculated values are much too low in magnitude, compared to the observed values. The calculated

TABLE II  
OBSERVED AND CALCULATED VALUES OF  $df_d/dt$

No. of the meteor	Observed $df_d/dt$	Calculated $df_d/dt$
1	-0.42	0.0020
2	0.23	0.0042
3	0.20	0.0020
4	-0.90	-0.0004
5	0.58	0.0012
6	-0.27	0.0009
7	0.05	0.0036
8	-0.37	0.0008

values, here, are obtained from the assumption that  $f_d$  values are positive. It may be noticed that the small order of values of  $df_d/dt$  that would be caused by the motion of the meteor train due to the wind cannot be detected in this experiment. Further, the values of  $df_d/dt$  actually observed from the doppler records, which are comparatively very high, are definitely not caused by the wind motion of the meteor train. Now modifying equation (4) to accommodate this observed effect, we may write

$$(8) \quad v_r^2 + R(dv_r/dt) + R(dV_r/dt) = v^2 + V^2$$

where  $dv_r/dt$  and  $dV_r/dt$  indicate the values due to the wind effect and the secondary cause respectively, and  $V$  is the new velocity which has to be accounted for by this secondary cause. Now subtracting equation (4) from equation (8), we get

$$(9) \quad R(dV_r/dt) = V^2.$$

Only the magnitude of the observed value of  $df_d/dt$  has to be used in equation (5) to get the new value of  $dV_r/dt$  for substituting in equation (9), or otherwise we get an imaginary quantity for  $V$ , which is not possible. Using this equation in the case of meteor 6, we obtain  $V = 483 \text{ m/sec}$ , which is quite a high value compared to the order of wind velocities in the 80–100 km region.

In fact, owing to the effect of diffusion of the ionization in the meteor train, the total effective length of the train goes on decreasing. From the theoretical ionization curves for meteor trains (Clegg 1952), it will be seen that the ionic density is a maximum somewhere along the length of the train, and decreases outwards on either side of this point. Thus the disappearance of ionization due to diffusion progresses from either end of the train inwards towards the maximum echo duration level. If the result of the combination of the echoes from the various sections of the train be visualized as equivalent to an echo from the effective point of reflection, which may in general coincide with the midpoint of the effective length, then the aforesaid effect may be transformed into that of the drifting of this effective point of reflection towards the level of maximum echo duration along the meteor train. Actually the position of the maximum ionization will be much lower than the midpoint of the train (Clegg 1952), so that the effective point of reflection generally moves down the length of the train with time. The high velocities of  $V$  may now be explained as being the rates of drift of the effective points of reflection in the different cases.

Now, it will be of interest to see if equation (9) can be derived theoretically. Let the effective point of reflection on the meteor train, at any particular instant, be at a distance  $R$  from the observing station and at a distance  $s$  along the train from the  $R_0$  point of normal incidence of the radio waves. From simple Pythagoras theorem, it follows that

$$(10) \quad R^2 = R_0^2 + s^2.$$

If  $s$  is small compared to  $R_0$ , we have

$$(11) \quad R = R_0 + (s^2/2R_0).$$

Now differentiating this with respect to time, and writing  $V_r = dR/dt$ , and  $V = ds/dt$ , we have

$$(12) \quad R_0 \cdot V_r = s \cdot V.$$

Further differentiating this with respect to time, and assuming  $V$  to be constant, we have

$$(13) \quad R_0(dV_r/dt) = V^2,$$

which is the same as equation (9); only the previous  $R$  values referred to in Table I should be approximated to  $R_0$ .

From Equation (12), we see that if  $V$  is constant for any meteor,  $V_r$  is directly proportional to the distance,  $s$ , of the effective point of reflection from the  $R_0$  point along the train. As the effective point of reflection generally moves down, the sign of the gradient  $dV_r/dt$  simply depends upon the position of  $R_0$  point on the train, relative to the other point. The smooth linear variation of the average  $f_d$  with time in Fig. 2 indicates that  $s$  is decreasing as the

effective point moves, or that the  $R_0$  point is at, or lower than, the maximum duration level. More observational evidences for different types of gradients, caused by different relative positions of the aforesaid points on the train, have been obtained by the author from the doppler records taken at the South Gloucester station during 1948–50 in support of this phenomenon of the movement of the effective point of reflection along the meteor train. These will be reproduced in another paper, which deals with the theoretical aspects of this problem in more detail. This regularity of the observed values of the gradients of  $dV_r/dt$ , even in the case of 1-second duration meteors, indicates indirectly that soon after its formation the meteor train offers several reflecting points closely distributed along its length. The origin of this may be the large scale turbulence or wind shears of the order of 1 km or more (Manning and Eshleman 1957) existing in the 80–100 km region of the upper atmosphere.

As the afore-mentioned phenomenon is actually an effect of the meteor train duration, these velocities  $V$  should possibly be some function of the total echo duration in each case. To verify this, the various values of  $V$  thus obtained are plotted in Fig. 6 against the corresponding values of echo duration, as obtained from the doppler records. An average curve drawn through all

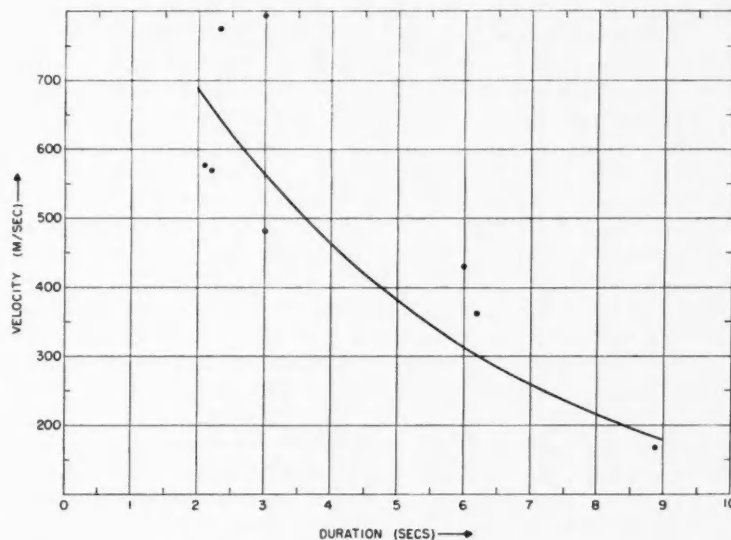


FIG. 6. Graph showing a plot of the various  $V$  values against the total durations, with a smooth curve drawn through the points.

these points in this graph shows that as duration increases, this velocity  $V$  decreases. This fact is found to be true from more observations, which are presented in another paper, to which reference has already been made.

(d) *Probable Cause of the Periodic Fluctuation Observed in the Main Doppler Frequency*

It has already been mentioned that periodic fluctuations ranging between 1.2 and 2.8 c.p.s. are generally observed in the  $f_d-t$  curves. These fluctuations are possibly due to the effect of interference between the CW radio waves reflected from the various centers of reflection distributed (with separations of 1 km or more) along the train. The existence of these various centers of reflection has to be postulated to explain the observed phenomenon of drift of the effective point of reflection along the train towards the maximum echo duration level. This postulate appears to be compatible with the existing knowledge of meteor phenomena. Recently, Manning and Eshleman (1957) have pointed out that the pertinent properties of both long as well as short duration echoes result from scales of atmospheric turbulence of about 1 km and larger, similar to the distortions of meteor trains photographed by Whipple (1953). Greenhow (1952a) has found that the average delay in the start of fading observed in the intensity of meteor echoes is about 0.4 second after the train formation. The average frequency of high speed flutter observed by Greenhow (1950) on 36 Mc/sec is 11 c.p.s. in echo durations up to 32 seconds. Following Herlofson (1948), McKinley and Millman (1949b), and Ellyett (1950), he assumed that this flutter fading is due to the interference between the waves reflected from the various sections of the train. These sections have been supposed to offer right angle reflecting points to the observer, owing to the deformations of the train by turbulent winds. Greenhow's work suggests that these deformations of the train, at a time interval of 0.4 second after its formation, are sufficient to cause radio reflections from different sections of the train.

An attempt has been made to see if the fluctuation frequencies  $f_t$ , observed in the present investigation, are related in any way to the frequencies of fading observed in the echoes of pulsed radar range-time records.  $R-t$  records photographed on a 35 mm film moving at a fast speed of 30 inches per minute show clearly the intensity modulations superposed on the meteor echoes. Analysis of about 80 meteors observed on June 26, 1948, during 1215-1245 hours and 0115-0145 hours E.S.T. shows that the fading frequencies observed initially at about half a second after the beginning of the echo, range between 1 and 15 c.p.s. The upper limit of this range steadily decreases to about 5 c.p.s. at durations over 10 seconds. From about 80 observations of the  $f_t$  values obtained from the body doppler records taken during the Geminid shower periods of 1948-50, it is found that the average value of  $f_t$  decreases with time from about 3 c.p.s. at a time of about 0.5 second after the train formation to about 1 c.p.s. at durations of about 20 seconds. Thus the general tendency of decrease of the frequency with time is observed in both the above cases. In fact, owing to the limitations of period measurements of body doppler beat waves, values of  $f_t$  greater than  $f_d$  values cannot be detected in the present method. This possibly explains the higher limit for the observed values of  $f_t$ , which is only 6 c.p.s., obtained from the 80 doppler observations referred to above. The flutter frequencies of 5 to 10 c.p.s. superposed on random fluctuations have been observed on 32.7 Mc/sec by McKinley and Millman (1949b). The random

fluctuations, referred to here, will have lower frequencies than their flutter values, and are probably the same as the  $f_t$  values observed in doppler records.

The origin of the variation of these two types of frequencies with time within the duration of echo is not completely understood. However, a knowledge of this may give a clue to the origin of each of the above two types of fluctuations. It can be seen from equation (7) that the average  $f_t$  values of 3 c.p.s. and 1 c.p.s. are caused by differential velocities of 15 m/sec and 5 m/sec respectively. Assuming an average vertical wind velocity gradient of  $\pm 5$  m/sec km at any position in the M-region, following Greenhow (1952b), the average height difference between any two reflecting points would then be 3 km and 1 km corresponding to  $f_t$  values of 3 c.p.s. and 1 c.p.s. respectively. Liller and Whipple (1954) pointed out that high gradient values up to 50 m/sec km are also observed. In such cases, vertical scales of turbulence of 0.1 km–0.6 km would be responsible for producing  $f_t$  values of the order of 1 c.p.s.–6 c.p.s. It has already been mentioned that  $f_t$  values up to 6 c.p.s. have also been observed at the beginning of echo durations. But assuming the general picture of Greenhow to be an average case,  $f_t$  values of 1–6 c.p.s. would be caused by scales of turbulence of 1–6 km respectively. Thus it is suggested that at the beginning of the echo duration, large scale wind shears of the order of 6 km may predominate in causing sufficiently large scale deformations in the train to cause radio reflections from different sections. With the advance of time, smaller scale wind shears of the order of 1 km may slowly gain importance, and produce several reflecting centers along the train. Large scale wind shears are known to be present in the upper atmosphere where meteors occur. Several visual observations, on long enduring meteor dust trains, have been reported from different parts of the world (Trowbridge 1907; Fisher 1926; Millman 1938; Størmer 1939; Olivier 1942; Nielsen 1953). These observations show that meteor trains are invariably distorted into wavy or helical shapes in course of time after their initial formation into a straight line. From a collection of about 77 observations on S-shaped long-enduring meteor trains, Millman and Bernstein (unpublished) have found that the most probable spacing between successive bends of opposite sense is about 8 km. Much photographic evidence (Monnig 1939, 1944; meteor train over Puerto Rico 1947; Astropowitsch and Fedynsky 1940) for the presence of these large scale wind shears has also been reported. From results of photographic work on long enduring meteor trains occurring in the 81–113 km region of the upper atmosphere, Liller and Whipple (1954) have suggested that about half the kinetic energy of the high altitude winds is contained in large-scale systematic motions and the other half in shallow (3–10 km) eddies. From the illustrations of the variation of wind velocities with height presented by them, it is clear that wind shears of the scale of 1 km are also present in the 80–100 km region.

There is still one more possible method of the production of more than one reflecting point on a meteor train. Flares (Jacchia 1949) are known to occur frequently in bright meteors. These may produce dense blobs of ionization, at different positions along the train, which may independently reflect radio waves towards the observer. Jacchia has pointed out that flares are found

more frequently in meteors with high and with low velocities than in those with average velocities ( $\log v$  between 6.55 and 6.75). He has also pointed out that low velocity meteors may have any number of flares, while the fastest meteors, as a rule, have only one flare, if any, at the end of the trail. Thus flares may also play an important role in a low velocity meteor in producing different points of reflection along its length. In the case of Geminid meteors having a velocity of 35.3 km/sec, i.e.,  $\log v = 6.55$  (McKinley 1951), flares may or may not occur, and if they do occur, their number in each case may be more than one.

However, from the results of the present investigation, it seems more likely that large-scale turbulence, of the order of 1 km, is mainly responsible for the production of several points of reflection along the length of most meteor trains. These points may be closely and evenly distributed (of the order of 1-km separation). Large-scale wind shears of the order of 6 km will probably play an important role at the beginning of echo durations. In the case of some of the Geminid meteors, there is also the possibility of the occurrence of flares producing the effect of fading, besides the mechanism of turbulent winds producing a similar effect.

#### ACKNOWLEDGMENTS

The author is deeply indebted to the National Research Council for the award of a Postdoctorate Fellowship, which enabled this investigation to be carried out. He is grateful to Dr. P. M. Millman for taking personal interest during the progress of this work. He is also thankful to Drs. D. W. R. McKinley and A. G. McNamara for some helpful discussions and suggestions.

#### REFERENCES

- ASTOPOWITSCH, I. S. and FEDYNISKY, V. V. 1940. *Meteory*, Moscow.
- CHAPMAN, J. H. 1953. *Can. J. Phys.* **31**, 120.
- CLEGG, J. A. 1952. *Monthly Notices Roy. Astron. Soc.* **112**, 399.
- ELLYETT, C. D. 1950. *Phil. Mag.* **41**, 694.
- FISHER, W. J. 1926. *Popular Astronomy*, **34**. No. 7, Aug-Sept.
- GREENHOW, J. S. 1950. *Phil. Mag.* **41**, 682.
- 1952a. *Proc. Phys. Soc.* **B65**, 169.
- 1952b. *J. Atmospheric and Terrest. Phys.* **2**, 282.
- GREENHOW, J. S. and NEUFELD, E. L. 1956. *Phil. Mag. [8]* **1**, 1157.
- HERLOFSON, N. 1948. *Rept. Progr. in Phys.* **11**, 444.
- JACCIA, L. G. 1949. Harvard College Obs. Tech. Rept. No. 3.
- LILLER, W. and WHIPPLE, F. L. 1954. *J. Atmospheric and Terrest. Phys. Suppl.* **1**, 112.
- MANNING, L. A., VILLARD, O. G., and PETERSON, A. M. 1950. *Proc. Inst. Radio Engrs.* **38**, 877.
- MANNING, L. A. and ESHLEMAN, V. R. 1957. *J. Geophys. Research*, **62**, 367.
- MCKINLEY, D. W. R. and MILLMAN, P. M. 1949a. *Can. J. Research, A*, **27**, 53.
- 1949b. *Proc. Inst. Radio Engrs.* **37**, 364.
- MCKINLEY, D. W. R. 1951. *Astrophys. J.* **113**, 225.
- 1956. *J. Atmospheric and Terrest. Phys.* **8**, 76.
- METEOR TRAIN OVER PUERTO RICO. 1947. *Sky and Telescope*. No. 6, April 5.
- MILLMAN, P. M. 1938. *J. Roy. Astron. Soc. Can.* **32**, 91.
- MONNIG, O. E. 1939. *The Sky*. Aug. 7.
- 1944. *Sky and Telescope*. III, No. 11, Sept. 3.
- NIELSEN, A. V. 1953. *Meddelelser fra Ole Romer Observatoriet* Nr. 23. Marts. 305.
- OLIVIER, C. P. 1942. *Proc. Am. Phil. Soc.* **85**, 93.
- STØRMER, C. 1939. *Astrophysica Norvegica*. III, No. 5, 117.
- TROWBRIDGE, C. C. 1907. *Monthly Weather Rev.* Sept. 390.
- WHIPPLE, F. L. 1953. *J. Meteorol.* **10**, 390.

# MEASURED SELF-IMPEDANCE OF A DIPOLE ANTENNA NEAR A CONDUCTING CYLINDER OF ELLIPTICAL CROSS SECTION<sup>1</sup>

J. Y. WONG

## ABSTRACT

This paper presents the results of an experimental investigation of the impedance of an axial dipole antenna located near a conducting cylinder of elliptical cross section. Measurements were carried out for various spacings of the antenna from the cylinder along the major and minor axes, and for four different values of cylinder ellipticity.

For a cylinder having a maximum dimension of 0.76 wave length it is found that the impedance (resistive and reactive components) is an oscillating function of the antenna-to-cylinder spacing, having a period of approximately one-half wave length. For spacings greater than one wave length, the impedance is within 5% of the free-space dipole impedance.

## INTRODUCTION

This paper presents the results of an experimental investigation of the self-impedance of an axial dipole antenna located near a conducting cylinder of elliptical cross section. Practical applications of this problem often arise in the determination of a nearby object on the impedance characteristics of an antenna. As an example, parts of a ship's superstructure, for example a stack, can sometimes be approximated by a cylinder of elliptical shape.

The radiation pattern problem of a dipole near a conducting cylinder has been treated analytically by Carter (1943) for circular cylinders, and by Sinclair (1951) for elliptical cylinders. Because of their methods of analysis, information about only the real part of the impedance, that is, the radiation resistance, can be obtained. Lucke (1951), employing a Green's function method of solution, has derived expressions for the near field of the antenna as well as for the radiation field. Hence, in theory the complete impedance function of the antenna can be found. In practice, however, evaluation of the complex integral expressions presents an extremely formidable problem, and to the author's knowledge, no satisfactory solution has ever been achieved. Some measurements for the circular-cylinder case have been published by DuHamel (1951), and in this paper the measurements have been extended for a conducting cylinder of elliptical cross section.

## IMPEDANCE MEASUREMENTS

The investigation was carried out at a frequency of 1500 Mc/s using the image-plane technique. The experimental arrangement is shown in Fig. 1. Measurements were conducted for various antenna-to-cylinder spacings  $s$  along the major and minor axes of the cylinder and for four different values of ellipticity ( $a/b$  ratio), viz., circular cylinder, 2:1 cylinder, 4:1 ellipse, and a

<sup>1</sup>Manuscript received March 12, 1958.

Contribution from the Radio and Electrical Engineering Division, National Research Council, Ottawa, Canada.

Issued as N.R.C. No. 4788.

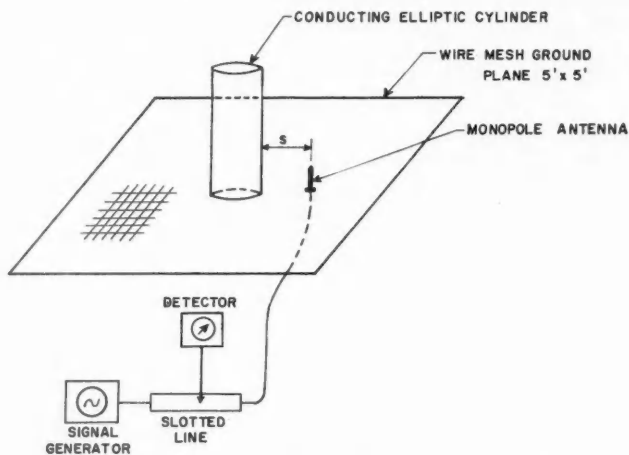


FIG. 1. Experimental arrangement illustrating cylinder and monopole antenna.

flat plate. For all cases the maximum cross-sectional dimension of the cylinder was held constant, having a value of 0.76 wave length, and the height of the cylinder was arbitrarily chosen at 1.5 wave lengths. A one-quarter wave length monopole antenna of length 0.225 wave length was employed.

#### DISCUSSION OF RESULTS

The effect of antenna-to-cylinder spacing on the self-impedance, for an antenna located along the major axis, is illustrated in Fig. 2. The resistive and reactive components of the impedance are plotted as functions of the spacing for the four different shapes of cylinder. It is observed that the impedance is an oscillating function of the distance of the antenna from the

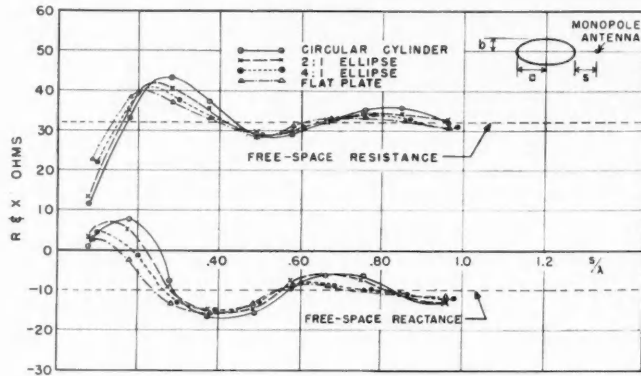


FIG. 2. Effect of antenna-to-cylinder spacing on impedance, for antenna on major axis.

cylinder, having a period of approximately one-half wave length. For spacings greater than about one wave length, the impedance is within 5% of its free-space value.

Fig. 3 applies to an antenna located along the minor axis of the cylinder. Comparison with the previous curve reveals that the impedance is less sensitive to cylinder ellipticity. For a given spacing, therefore, it appears that the effect of the cylinder on the impedance is dependent on the rate of change of curvature of the cylinder surface.

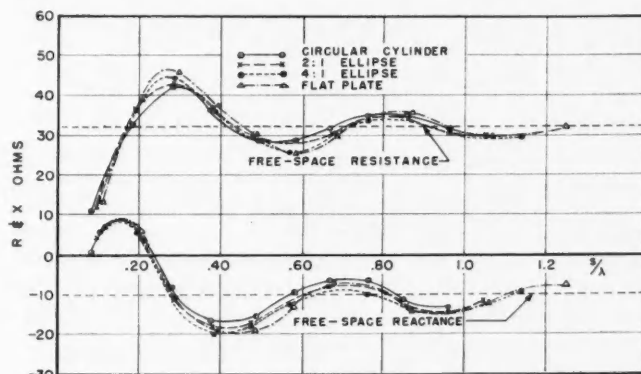


FIG. 3. Effect of antenna-to-cylinder spacing on impedance, for antenna on minor axis.

#### CONCLUSION

Measurements have been carried out to determine the effect of the presence of a conducting cylinder of elliptical shape on the self-impedance of a dipole antenna. It is found that the impedance is an oscillating function of the antenna-to-cylinder spacing, having a period of approximately one-half wave length. For spacings greater than one wave length, the impedance is within 5% of its free-space value.

#### ACKNOWLEDGMENT

The author wishes to express his thanks to Mr. A. Jurkus, who performed the impedance measurements.

#### REFERENCES

- CARTER, P. S. 1943. Proc. I.R.E. **31**, 671.
- DUHAMEL, R. H. 1951. Tech. Report No. 14, Electrical Engineering Research Laboratory, University of Illinois.
- LUCKE, W. S. 1951. J. Appl. Phys. **22**, 14.
- SINCLAIR, G. 1951. Proc. I.R.E. **39**, 660.

# ON THE FLUORESCENCE OF AIR, EXCITED BY FAST ELECTRONS: LIGHT YIELD AS A FUNCTION OF PRESSURE<sup>1</sup>

A. E. GRÜN

## ABSTRACT

The fluorescence of air was excited by electrons of 4.2 to 43.7 kev and the light intensity  $I_f$  was measured by a 1 P 28 photomultiplier tube. The energy  $W$  transferred from the electrons to the gas molecules in a defined space could be accurately measured. The light yield, as defined by  $\Phi = I_f/W$ , was experimentally determined as a function of the gas density  $\rho$ , or pressure  $p$ , respectively. The result is:  $1/\Phi + p/p' = 11.5 \text{ mm Hg}$ .

## INTRODUCTION

The fluorescence of a gas which is excited by a beam of fast electrons has recently been utilized to measure gas densities in a wind tunnel. The local density  $\rho$  in an inhomogeneous stream of gas can be determined by measuring the intensity  $I_f$  of the fluorescence for each spot (Schumacher and Grün 1955; Schumacher and Gadamer 1958).

The idea of the method may be expressed as follows: a definite space with volume  $V$  containing a gas with density  $\rho$  is traversed by fast electrons. Within this space, the electrons lose a fraction  $W$  of their energy to the gas molecules. A certain proportion of this fraction  $W$  appears again as fluorescence, with intensity  $I_f$ . The ratio

(1)

$$I_f/W = \Phi$$

will be called the light yield.  $I_f$  and  $W$  may be determined in watts. Usually  $I_f$  will be measured only for some limited spectral range  $\Delta\lambda$ , and the corresponding light yield refers to the same limited spectral range.

It is assumed that the volume ( $V$ ) of space under observation and the temperature ( $T$ ) of the gas are kept constant, whereas the density  $\rho$  and the pressure  $p$  of the gas are varied. It is also assumed that changes in the directional and energy distribution of the primary electrons are small, in spite of the variation of the density  $\rho$ .\* Then, the energy  $W$  which is transferred to the gas will be proportional to the density  $\rho$  and we get for the fluorescence intensity

(2)

$$I_f(\rho) \propto \Phi(\rho) \times \rho.$$

Here, the function  $\Phi(\rho)$ , representing the light yield as a function of the gas density, is still unknown. It was the purpose of the present investigation to determine the function  $\Phi(\rho)$  experimentally.

The measurement of gas density using the fluorescence intensity becomes

<sup>1</sup>Manuscript received March 25, 1958.

Contribution from the Institut für Kernphysik der Johann Wolfgang Goethe Universität, Frankfurt/M, Germany.

\*In the gas density measurements by Schumacher *et al.*, this requirement is fulfilled because the electrons, forming a confined beam, lose only a fraction of their energy in passing the space element which is determined by the optical devices used for the observation of the fluorescence.

most simple if  $\Phi(\rho)$  becomes a constant, or if the dependence of  $\Phi$  on  $\rho$  can be neglected. It was to be expected and it has been confirmed by the present measurements that for low densities the light yield  $\Phi$  is nearly independent of the gas density  $\rho$ . However, this is no longer true at higher gas densities, when radiation free quenching processes begin to compete with the emission processes. In turn our experimental determination of the functions  $\Phi(\rho)$  and  $\Phi(p)$ , respectively, is of interest not only in connection with gas density measurements but also in studying such quenching processes.

#### REMARKS ON THE FLUORESCENCE MECHANISM

To understand the experiments better, we shall first discuss briefly some details of the fluorescence mechanism using a somewhat simplified model, although our experiments are quite independent of any assumptions on this mechanism.

Let us designate by  $N$  ( $\text{cm}^{-3}$ ) the number of neutral molecules in the gas. Under the influence of a stationary bombardment by the electrons with current density  $j$  a stationary content of  $C$  ( $\text{cm}^{-3}$ ) excited molecules is produced. In the experiments the condition  $C \ll N$  is always met. For simplicity  $C$  is taken to refer to one particular quantum state only. If  $A$  ( $\text{sec}^{-1}$ ) is the frequency factor for the emission of radiation,  $\Lambda$  ( $\text{cm}^{-3} \text{ sec}^{-1}$ ) the number of quenching processes, and  $v$  ( $\text{cm}^{-3} \text{ sec}^{-1}$ ) the rate of production of excited molecules, the following relations exist:

$$(3) \quad I_f(\text{cm}^{-3}) \propto C \times A,$$

expressing the spontaneous emission of radiation with a time constant  $1/A$ . (Note:  $A$  is independent of  $N$ .)

$$(4) \quad \Lambda = \delta CN = kC$$

as the expression for a bimolecular quenching reaction,  $\delta$  being the "quenching speed,"  $k$  being the velocity constant of the reaction (dependent upon  $N$ ). Obviously, this expression implies that reaction rates between two excited molecules, or an excited molecule and secondary products, e.g. ions, are negligibly small.

$$(5) \quad v - C(A + k) = 0 \quad \text{or} \quad C = v/(A + k)$$

expressing the stationary state.

We can assume that  $v \propto W$  holds independent of the current density  $j$  of the electrons, as long as  $C \ll N$  and as long as the primary electrons entering the space under observation possess energies of some 100 ev or more.

It follows:

$$(6) \quad I_f \propto C \times A = v/(A + k) \propto W/(A + k),$$

and from (1) and (6):

$$(7) \quad 1/\Phi \propto 1 + k/A.$$

Since  $k = \delta N = \delta N_0 \times p/p_0$ , and if we introduce a reference pressure  $p' = p_0 A/N_0 \delta$ , we get from (7):

$$(8) \quad 1/\Phi \propto 1 + p/p'.$$

This is a linear function for the pressure or density dependence on the reciprocal light yield  $\Phi$ . (At  $p'$  the light yield has dropped to 50% of its maximum.)

The model is, of course, oversimplified. We must keep in mind that it is valid for one quantum transition only. If several transitions are contributing to the observed fluorescence, then  $p'$ , for instance, will depend upon the spectral response curve of the light detector, etc.

However, as we shall see, equation (8) can represent the experimental results very well.

#### EXPERIMENTAL METHOD

The experimental method employed here was in principle that used by the author (Grün and Schopper 1954) to measure the light yield of gases excited by alpha-particles. The apparatus used in the present experiments is described elsewhere (Grün 1956, Fig. 3).

A parallel, narrow beam of electrons is formed in the vacuum and fired into the gas through dynamic pressure stages. The volume  $V$  of the gas chamber is kept large so that nearly all the electrons are stopped in the gas. This is accompanied by the usual scattering.\* The main advantage of this arrangement is that the energy  $W$ , introduced into the gas, can be determined very easily. It is given by the product of the acceleration voltage  $U_0$  of the electrons and of the electron current  $J$ . Electron source and gas chamber were especially designed to allow a reliable, accurate measurement of the current  $J$  entering the chamber (see Grün 1956).

The temperature of the gas is kept constant and the pressure  $p$  varied in order to change the gas density. At the same time, the acceleration voltage  $U_0$  is varied in order to keep the range  $R_0$  of the electrons in the gas at a constant value for all pressures. It has been demonstrated that the scatter distribution is nearly the same for a wide range of energies  $U_0$ , provided  $R_0$  is the same (Grün 1956). Therefore, if  $R_0$  is kept constant as stated, the small fraction of electrons which are backscattered into the source is constant throughout the experiment, and does not cause errors.

Evidently, neither the current density  $j$  nor the electron energy  $U$  are constant throughout the gaseous space which is under observation. This, however, does not constitute any drawback of the method, as long as the light yield  $\Phi$  is independent of  $j$ . We considered this independence as fulfilled throughout the observation space as long as the value obtained for  $\Phi$  was independent of the current  $J$ . This independence was always checked.

In our experiments the intensity of the fluorescence is measured by a photomultiplier tube of type 1 P 28. It is located at a distance of about  $40 R_0$ . Hence, the light source can be considered to be a point source and the photocurrent  $i_p$  is proportional to the total light emission in the observation space.

\*In the experiments by Schumacher *et al.* (1958) it was more important to get confined electron beams with negligible changes of the beam characteristics across the observation field, hence, e.g. negligible changes in  $dW/ds$ . However, the same function  $\Phi$  applies.

The photomultiplier tube has been checked for linearity and its sensitivity has been regularly watched, using a constant light source.

### RESULTS

The function  $\Phi(p)$  for the light yield of air of  $20^\circ\text{C}$  was obtained within the pressure range from 10 to 600 mm Hg. The energy of the primary electrons was varied between 4.2 and 43.7 kev in order to keep the range of the electrons at  $R_0 = 3.5$  cm. The electron current used was 1.7 to  $5.0/\mu\text{a}$ . The maximum current density encountered under these conditions was  $j_0 \approx 25/\mu\text{a}/\text{mm}^2$ . The power  $W$  assumed values between 7.2 and 218 milliwatts.

An active area of  $8 \times 8$  mm of the cathode of the photomultiplier tube was selected by an aperture. Its distance from the axis of the electron beam was 144 cm. The spectral response of the cathode was of the type S-5. A plate glass, 6 mm thick, was located in the path of the light (window of the observation chamber).

Fig. 1 represents the experimental values of the function  $1/\Phi$  plotted against  $p$ . The scale of the ordinate is chosen to obtain  $1/\Phi = 1$  for  $p = 0$ .

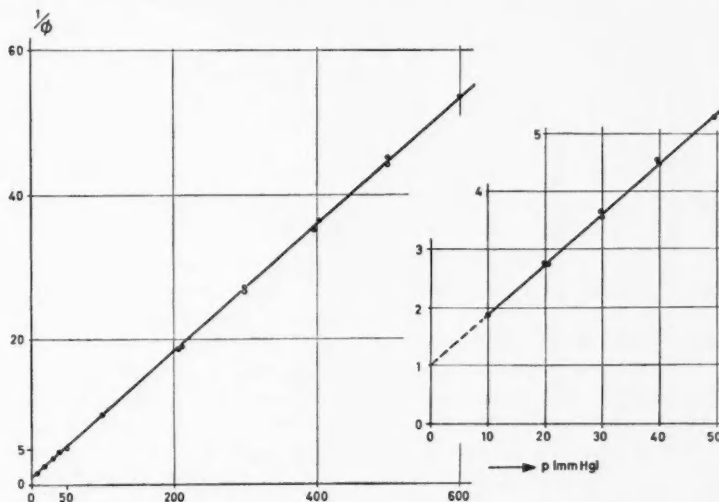


FIG. 1. Reciprocal light yield  $1/\Phi$  as a function of pressure  $p$ , for air of  $20^\circ\text{C}$ . Experimental values.

Within experimental error  $1/\Phi$  is a linear function of  $p$ , as expected according to (8). The line that fits the data has an equation

$$(9) \quad 1/\Phi = 1 + p/11.5$$

giving an experimental value  $p' = 11.5$  mm Hg. This is an average over a large spectral range. Other measurements, where  $\Phi$  will be determined for single spectral lines are under preparation.

Some conclusions can be drawn from (9). For  $p \ll p'$  or  $p \ll 11.5$  mm Hg we can write

$$(10) \quad \Phi = 1 - p/p'.$$

Hence, if we treat  $\Phi$  as a constant the relative error will be in the order of  $p/p'$  (provided (9) holds to very low pressures). For  $p = 0.1$  mm Hg we can expect an error below 1%.

The influence of the temperature  $T$  is not yet considered. In a flowing gas  $T$  may vary considerably. Earlier measurements (Grün and Schopper 1954) have shown that the influence of  $T$  on  $\Phi$  is small. It can most probably be neglected as long as  $p \ll p'$ .

#### REFERENCES

- GRÜN, A. E. 1956. Z. Naturforschung **12a**, 89.  
GRÜN, A. E. and SCHOPPER, E. 1954. Z. Naturforschung **9a**, 134.  
SCHUMACHER, B. W. and GADAMER, E. 1958. Can. J. Physics (in press).  
SCHUMACHER, B. W. and GRÜN, A. E. 1955. German Patent Application Sch 18144 IX 142/I.

# THE CROSS SECTION FOR THE REACTION $\text{Cs}^{135}(n, \gamma)\text{Cs}^{136}$ <sup>1</sup>

A. P. BAERG, F. BROWN, AND M. LOUNSBURY

## ABSTRACT

The effective cross section for the reaction  $\text{Cs}^{135}(n, \gamma)\text{Cs}^{136}$  with reactor neutrons is  $10.4 \pm 0.5$  barns. The measured reaction rate under cadmium yields a value of  $61.7 \pm 2.3$  barns for the resonance integral of  $\text{Cs}^{135}$ . The thermal cross section is  $8.7 \pm 0.5$  barns as obtained by combining the reaction rates for uncovered and cadmium-covered samples.

## INTRODUCTION

The neutron absorption cross sections of long-lived fission products are of importance in predicting the reactivity of nuclear reactors in which prolonged irradiation of fuel is contemplated. One such fission product is  $\text{Cs}^{135}$  which has a half-life of about  $2 \times 10^6$  years and in addition has a high yield of 6.3% in  $\text{U}^{235}$  fission (Steinberg and Glendenin 1956). Neutron capture leads to  $\text{Cs}^{136}$  which is reported to decay to stable  $\text{Ba}^{136}$  by  $\beta^-$  emission with a half-life of 12.9 days (Olsen and O'Kelley 1954). Assuming that there is no isomeric state and no decay by electron capture in  $\text{Cs}^{136}$ , then the activation cross section of  $\text{Cs}^{135}$  to the 12.9 day activity should represent essentially all of the  $\text{Cs}^{135}$  neutron absorption cross section. The activation cross section of  $\text{Cs}^{135}$  has been measured previously and found to be  $15 \pm 8$  barns (Sugarman 1949). A more accurate value for this cross section was desired.

## METHOD

Fission product cesium which has been allowed to decay for several months contains  $\text{Cs}^{133}$  (stable),  $\text{Cs}^{135}$  ( $2 \times 10^6$  yr), and  $\text{Cs}^{137}$  (30 yr) in approximately equal proportions, together with a much smaller proportion of  $\text{Cs}^{134}$  (2.19 yr). The radioactivity of such a sample is due almost entirely to  $\text{Cs}^{137}$ ; the  $\text{Cs}^{134}$  contribution to the activity of the present sample was  $< 1\%$  (based on the mass spectrometric analysis) and the  $\text{Cs}^{135}$  contribution negligible. If such a sample is irradiated in a high neutron flux, the reaction  $\text{Cs}^{135}(n, \gamma)\text{Cs}^{136}$  produces sufficient of the 12.9-day activity for this to be  $\beta$ -counted in the presence of the  $\text{Cs}^{137}$ , and its decay observed. From the resulting decay curves the ratio of  $\text{Cs}^{136} : \text{Cs}^{137}$  in the irradiated sample can be obtained. If the  $\text{Cs}^{137} : \text{Cs}^{135}$  ratio of the original sample is known from mass spectrometric analysis, the  $\text{Cs}^{136} : \text{Cs}^{135}$  ratio of the irradiated sample is thus found and, knowing the neutron flux and the times of irradiation and decay, the cross section for the reaction  $\text{Cs}^{135}(n, \gamma)\text{Cs}^{136}$  can be calculated. The neutron capture cross section of  $\text{Cs}^{137}$  is  $< 2$  barns (Hughes and Harvey 1955) and thus its concentration is not sensibly altered by the neutron irradiation. The amount of  $\text{Cs}^{134}$  produced

<sup>1</sup>Manuscript received April 2, 1958.

Contribution from Research Chemistry Branch, Atomic Energy of Canada Limited, Chalk River, Ontario.

Issued as A.E.C.L. No. 641.

by the reaction  $\text{Cs}^{133}(n, \gamma)\text{Cs}^{134}$  is also negligible within the accuracy of the present experiment.

## EXPERIMENTAL

### *Purification of Starting Material*

The fission product cesium, which was at least one year old, was purified as follows. The solution containing 2 mg cesium in 8 N hydrochloric acid was first passed through a Dowex A-1 anion exchange column. The effluent containing the cesium was evaporated to dryness, the residue dissolved in 0.1 N hydrochloric acid, and the cesium absorbed onto a column of Dowex-50 cation exchange resin (200-400 mesh, 8% cross linkage) 10 cm long by 0.6 cm diameter. This column was washed with hydrochloric acid using successively 10 ml of 0.1 N, 5 ml of 0.5 N, and finally 1.0 N. The cesium appeared after 12 ml of the 1.0 N acid had been passed through the column and was contained in about 8.0 ml of this eluant. These conditions are such as to separate cesium from other cations including sodium, potassium, and rubidium (Cabell and Smales 1957). The cesium solution was evaporated to dryness and dissolved in 2 ml of water containing 20  $\lambda$  of concentrated sulphuric acid. This solution thus contained approximately 1 mg/ml of cesium and was used to prepare samples for irradiation. A 20-fold dilution of this solution was used for mass spectrometer analysis.

### *Mass Spectrometry*

A 60°-deflection, 8-in.-radius mass spectrometer (Lounsbury 1952) with a mass resolution of 0.3% was used for this work. The thermionic emission ion source employed a tantalum ribbon filament (0.001 in.  $\times$  0.030 in.  $\times$  0.250 in.) mounted on pickled Kovar terminals. One-tenth microgram of cesium contained in 2 microliters of sulphate solution was dried on the filament by passing a current of about 1 amp through it in air. The sulphate was chosen rather than the nitrate because of the higher melting point of the former.

The loaded filament was mounted in the ion source, and by differential pumping, the mass spectrometer tube was evacuated to about  $2 \times 10^{-7}$  mm Hg as indicated by the ionization gauge. Ions of  $\text{Cs}^+$  were detected when a current of 0.7 amp d-c. was passed through the filament. The ions were accelerated to 8000 v energy, collimated in a beam, and separated according to mass in a magnetic field of about 7500 gauss. The mass spectrum was scanned magnetically, and the ion current was amplified by a vibrating reed electrometer. The output from the amplifier was fed through a calibrated attenuator system to a fast (0.8 second full-scale response) Speedomax recorder. The mass spectrum was scanned slowly (10 seconds per peak) and continuously in the direction of increasing and decreasing mass alternately.

The results obtained from 70 recorded mass spectrograms are presented in Table I(a) for the three major peaks. An upper limit of 0.03 atom % was put on the abundance of  $\text{Cs}^{134}$ .

### *Irradiations*

Samples for irradiation were prepared by evaporating 2-4  $\lambda$  of solution

TABLE I  
EXPERIMENTAL DATA

## (a) Mass analysis of unirradiated sample

Mass	Abundance (atom %)
133	43.71±0.20
134	<0.03
135	21.79±0.05
137	34.49±0.05

(b)  $\beta$ -Counting and irradiations

	Uncovered irradiation	Cadmium-covered irradiation
$\text{Cs}^{136}/\text{Cs}^{137}$ (ratio of observed activities at end of irradiation, not corrected for $\text{Ba}^{137m}$ )	Source a 0.3475 " b 0.3377 " c 0.3610 Mean: 0.349±0.008	Source a 0.04289 " b 0.04463 Mean: 0.0438±0.0008
$\text{Co}^{60}$ activity (disintegrations/sec)	$(2.06 \pm 0.01) \times 10^8$	$(5.57 \pm 0.03) \times 10^6$
Weight $\text{Co}^{60}$ monitor (milligrams)	1.150±0.005	1.150±0.005
Duration of irradiation (seconds) See Note (1)	$(1.67 \pm 0.03) \times 10^6$	$(1.67 \pm 0.03) \times 10^6$

Note (1). The error in these figures does not arise from the measurement of the total "in pile" time but rather from the occurrence of short reactor "shutdowns" and small periods of varying reactor power which affect the calculation of the saturation factor  $(1 - e^{-\lambda t})/\lambda t$ . The two irradiations were not carried out simultaneously, although the irradiation times were identical.

(2–4  $\mu\text{g}$  cesium) onto about 100 mg of pure ferric oxide in a small, thin walled silica tube and then sealing the tube. The use of the iron oxide matrix, which is soluble in hydrochloric acid, prevents loss of neutron capture products by recoil into the insoluble silica. Irradiations of up to 3 weeks' duration were carried out in a high neutron flux position of the NRX reactor ( $6 \times 10^{13}$  neutrons/cm $^2$ /sec) and the samples were accompanied by standard cobalt wire flux monitors. The activities of the monitors were measured in an ion chamber which had been standardized against a  $4\pi$   $\beta$ -counter. Details of this system of neutron flux monitoring are given by Jervis (1957). A sample was also irradiated under cadmium, and for this irradiation the sample and monitor were placed inside a cadmium box of 0.040 in. wall thickness and irradiated in a position similar to that used for the uncovered sample.

*Purification of Irradiated Material*

The irradiated cesium was purified as follows. The iron was removed by passing a solution of the sample in 8 *N* hydrochloric acid through a Dowex A-1 column (3 cm long by 0.6 cm diam. using resin of 200–400 mesh size and 4% cross linkage). The effluent was evaporated to dryness and the cesium purification described above was carried out. The cesium solution thus obtained was designated "first purification." A portion was set aside for source preparation and the remainder was further purified as follows. Cesium carrier (1 mg) was added and a silicotungstate precipitation carried out (Bartholomew and Baerg 1956). The cesium was recovered from the

precipitate by dissolving in 2 M lithium hydroxide and passing the solution through a column of Dowex-50 in the lithium form. The column was washed well with 0.1 N hydrochloric acid to remove lithium and the cesium was then stripped off with 6 N acid. This solution, designated "second purification," was evaporated to dryness, re-evaporated several times with a little concentrated nitric acid, and taken up in dilute nitric acid for source preparation. Cesium chloride is deliquescent and makes unsatisfactory sources; the first purification solution contained such a small weight of cesium chloride that no trouble was encountered, but the second purification solution, containing carrier, had to be converted to cesium nitrate.

#### Counting

Sources for  $4\pi$   $\beta$ -counting were prepared by evaporating aliquots onto VYNS films ( $10 \mu\text{g}/\text{cm}^2$ ) coated with gold ( $10 \mu\text{g}/\text{cm}^2$ ) (Pate and Yaffe 1955). The dried sources were covered with a similar film. Two  $4\pi$  counters of the methane-flow proportional-type were used. Such counters should have the same efficiency for  $\text{Cs}^{136}$  and  $\text{Cs}^{137}$  to within 1% and this accuracy is more than sufficient for the present experiment. The corrections required to the counting data were (a) for counter dead time ( $5 \mu\text{sec}$ ) and (b) for the conversion electrons of  $\text{Ba}^{137m}$ ; this involves multiplying the observed  $\text{Cs}^{137}$  activity by a factor 0.909 when calculating numbers of  $\text{Cs}^{137}$  atoms (Brown, Hall, and Walter 1955). The counting rates were in the order of  $1-3 \times 10^3$  counts/sec and by taking long counts (10-30 minutes) the statistical accuracy of the counting data was made very high. The sources from each experiment were counted over a period of about 5 weeks. The treatment of data is discussed in the next section.

Sources for  $\gamma$ -ray spectroscopy were prepared on aluminum trays and examined with a  $1\frac{1}{2}$  in. NaI crystal, photomultiplier, and multichannel kicksorter.

#### RESULTS AND DISCUSSION

It was necessary to obtain, from the  $\beta$ -counting data, the ratio of the  $\text{Cs}^{136}$  activity at zero time (end of irradiation) to the  $\text{Cs}^{137}$  activity (constant over the times involved). The  $\text{Cs}^{136}$  contribution was not large—about 30% of the  $\text{Cs}^{137}$  activity for the uncovered irradiation and about 4% for the cadmium-covered irradiation. The treatment used was to plot the measured activity on a linear scale against  $e^{-\lambda_6 t}$  where  $\lambda_6$  is the decay constant of  $\text{Cs}^{136}$  and  $t$  the time elapsed since the end of irradiation. Provided that  $\text{Cs}^{136}$  is the only decaying species and that the chosen value of  $\lambda_6$  is correct a straight line should result. The intercept of this line at  $e^{-\lambda_6 t} = 0$  is the constant  $\text{Cs}^{137}$  activity and the slope is equal to the  $\text{Cs}^{136}$  activity at  $t = 0$ . Fig. 1 shows such a plot for a source from the uncovered irradiation. The value of  $\lambda_6$  used was  $6.219 \times 10^{-7} \text{ second}^{-1}$  corresponding to a half-life of 12.9 days. However, the values of the  $\text{Cs}^{137}$  and  $\text{Cs}^{136}$  activities obtained from such a plot are not very sensitive to the half-life value used for  $\text{Cs}^{136}$ . For example, a 5% error in this half-life causes an insignificant error in the relative activities. The points lie on a straight line to within their statistical accuracy which, in Fig. 1, is better

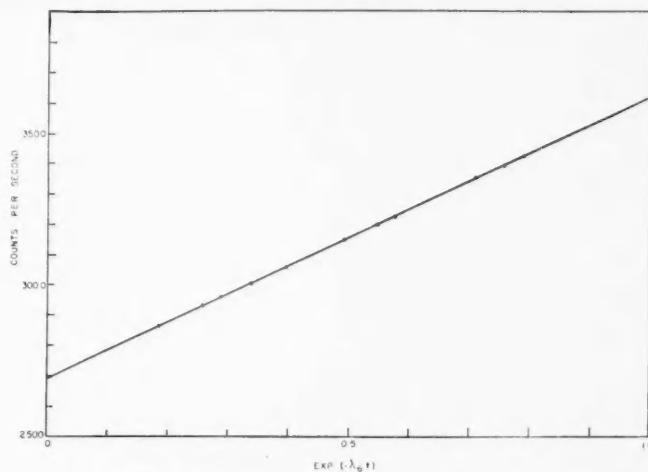


FIG. 1. Decay of neutron irradiated cesium.

than represented by the size of the circles. Fig. 2 is a similar plot for a source from the cadmium-covered irradiation. The total decay is much smaller than

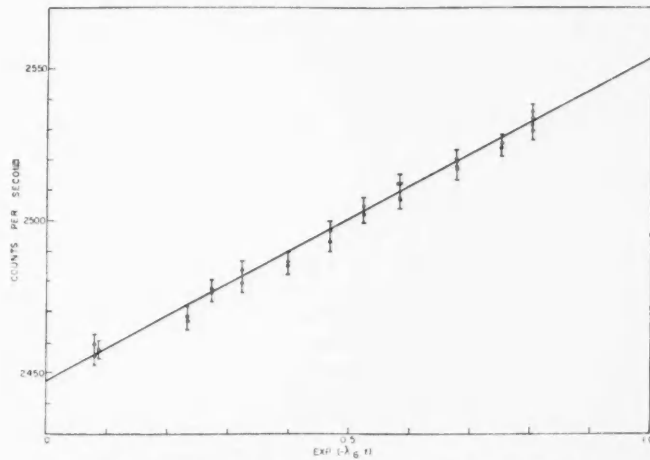


FIG. 2. Decay of cesium irradiated under cadmium.

that shown in Fig. 1 and the statistical errors, represented by the vertical lines, are thus larger in proportion to the amount of decay. Having thus obtained the value of the  $\text{Cs}^{137}$  contribution in a given source it was possible, as a check on the treatment, to subtract this contribution from the observed

counts and plot a conventional decay curve showing the logarithm of the Cs<sup>136</sup> activity versus time. Fig. 3 shows such a plot for one of the "uncovered" sources. The results of this plot are sensitive to the value used for the Cs<sup>137</sup> contribution to the activity. The fact that a straight line results indicates that this contribution has been correctly estimated.

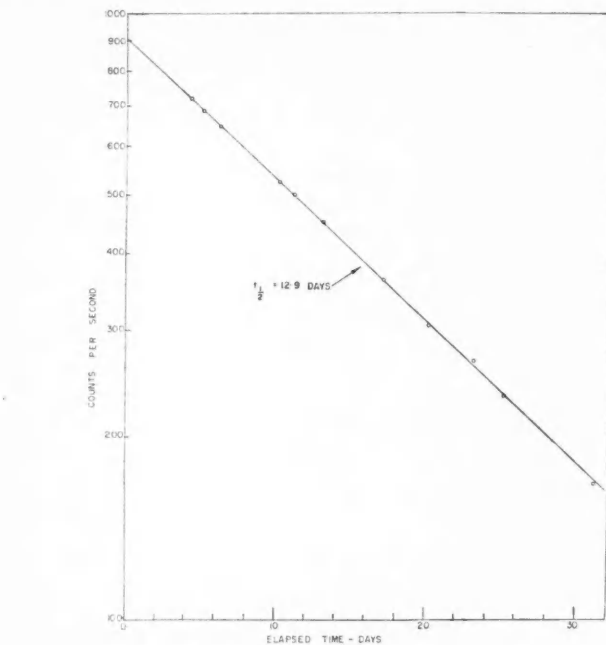


FIG. 3. Decay of Cs<sup>136</sup> component.

The chemical purifications used were such that the cesium should have been radiochemically pure. Several considerations indicate that this was the case. Firstly sources were prepared from both first and second purifications. In both types of source the decay corresponded to a half-life of 12.9 days with no contamination; furthermore the ratio of the decaying activity (Cs<sup>136</sup>) to the non-decaying activity (Cs<sup>137</sup>) was the same in both types of source. Secondly the  $\gamma$ -ray spectra of sources from the first and second purifications were compared. The spectra, normalized to have equal intensities in the Cs<sup>137</sup>  $\gamma$ -ray peak at 660 kev, were found to be identical.

The Cs<sup>136</sup>/Cs<sup>137</sup> activity ratios obtained are given in Table I (b) together with other data pertinent to the irradiations, viz. the activities and weights of the cobalt wire monitors and the times of irradiation.

Table II lists the values used for the other parameters which were required but not measured in this experiment, viz. the effective and thermal cross

sections and the resonance integral for Co<sup>59</sup>, the half-lives of Cs<sup>136</sup>, Cs<sup>137</sup>, and Co<sup>60</sup>, the ratio of the neutron flux in the covered irradiation to that in the uncovered irradiation, and the factor relating the true Cs<sup>137</sup> disintegration rate to the observed Cs<sup>137</sup> activity (i.e., the correction for Ba<sup>137m</sup>).

TABLE II  
VALUES OF PARAMETERS USED TO CALCULATE THE Cs<sup>135</sup> CROSS SECTIONS

Effective cross section of Co <sup>59</sup>	37.7 barns (Note (1))
Thermal cross section of Co <sup>59</sup>	36.5 barns (Hughes and Harvey 1955)
Resonance integral for Co <sup>59</sup>	48.6 barns (Macklin and Pomerance 1956)
Half-life of Co <sup>60</sup>	5.28 years (Hughes and Harvey 1955)
Half-life of Cs <sup>136</sup>	12.9 days (Olsen and O'Kelley 1954)
Half-life of Cs <sup>137</sup>	30.0 years (Brown, Hall, and Walter 1955)
Correction to Cs <sup>137</sup> activity	0.909 (Brown, Hall, and Walter 1955)
Ratio of neutron flux for covered irradiation to that for uncovered irradiation	0.794 (Note (2))

Note (1). This cross section applies to the moderator in the NRG reactor and is such that it gives the reaction rate, Co<sup>59</sup>(n,  $\gamma$ )Co<sup>60</sup>, when multiplied by the "2200 m/sec flux." This latter flux is the total neutron density multiplied by 2200 m/sec. The effective cross section of 37.7 barns was derived from the "2200 m/sec" value of 36.5 barns, which is the mean of the two values given by Hughes and Harvey (1955), and used with data for the NRG reactor given by Westcott (1957).

Note (2). The positions in the reactor were not identical for the two irradiations but had similar neutron spectra. The ratio of fluxes in the two positions at the same reactor power was known to be 0.885 (Butler and Merritt 1958). The ratio of the average power during the covered irradiation to that during the uncovered irradiation was 0.896. The product of these numbers is the ratio of fluxes for the two irradiations, where flux for the cadmium-covered irradiation means the flux to which the sample would have been subjected in the absence of the cadmium box. These figures are subject to significant errors due to changes in pile loading and other factors. The over-all error is difficult to estimate but experience points to its being not more than 10%.

The data for the uncovered sample yields a value of  $10.4 \pm 0.5$  barns for the effective cross section for the reaction Cs<sup>135</sup>(n,  $\gamma$ )Cs<sup>136</sup>. The term "effective cross section" is defined as in Note (1), Table II. The data for the covered sample yields a value of  $61.7 \pm 2.3$  barns for the resonance integral of Cs<sup>135</sup> relative to a resonance integral of 48.6 barns for Co<sup>59</sup> (Macklin and Pomerance 1956). Combining the data for both samples yields a value of  $8.7 \pm 0.5$  barns for  $\sigma_0$ , the thermal component of the cross section. This cross section, when multiplied by the thermal flux, gives the thermal component of the reaction rate. The thermal flux is defined as the density of neutrons, with energy less than the cadmium cutoff energy, multiplied by 2200 meters per second.

Errors have been assigned on the basis of those given in Table I. The values given in Table II are also subject to error but these are not included. A possible 10% uncertainty in the relative fluxes for the covered and uncovered samples would introduce an additional error of about 2% to the value for the thermal cross section ( $\sigma_0$ ). However, the errors associated with the effective cross section and the resonance integral would remain unchanged. The data for cobalt provide evidence that the relative flux values are not greatly in error: thus the measured cadmium ratio for cobalt is 29.3, while a previous measurement (Butler and Merritt 1958) for a similar reactor position gave 28 and the calculated value is 35 (Westcott 1957) with perhaps 20% error.

## REFERENCES

- BARTHOLOMEW, R. M. and BAERG, A. P. 1956. Can. J. Chem. **34**, 201.  
BROWN, F., HALL, G. R., and WALTER, A. J. 1955. J. Inorg. & Nuclear Chem. **1**, 241.  
BUTLER, J. P. and MERRITT, J. S. 1958. Atomic Energy of Canada Limited Publication CRC-735.  
CABELL, M. J. and SMALES, A. A. 1957. Analyst, **82**, 390.  
HUGHES, D. J. and HARVEY, J. A. 1955. U.S. Atomic Energy Commission Report BNL 325.  
JERVIS, R. E. 1957. Atomic Energy of Canada Limited Publication CRDC-730.  
LOUNSBURY, M. 1952. Proc. Roy. Soc. Can. **46**, 128.  
MACKLIN, R. L. and POMERANCE, H. S. 1956. Proceedings of the International Conference on the Peaceful Uses of Atomic Energy, Geneva, Vol. 5 (United Nations, New York).  
OLSEN, J. L. and O'KELLEY, G. D. 1954. Phys. Rev. **95**, 1539.  
PATE, B. D. and YAFFE, L. 1955. Can. J. Chem. **33**, 15.  
STEINBERG, E. P. and GLENDEEN, L. E. 1956. Proceedings of the International Conference on the Peaceful Uses of Atomic Energy, Geneva, Vol. 7 (United Nations, New York).  
SUGARMAN, N. 1949. Phys. Rev. **75**, 1473.  
WESTCOTT, C. H. 1957. Atomic Energy of Canada Limited Publication CRRP-680.

## PHOTON CORRELATION IN COHERENT LIGHT BEAMS<sup>1</sup>

E. BRANNEN, H. I. S. FERGUSON, AND W. WEHLAU<sup>2</sup>

### ABSTRACT

Experiments have been carried out in an attempt to detect any correlation between photons in coherent light rays using a coincidence circuit of resolving time  $2\tau = 8 \times 10^{-9}$  second. A Hg 198 electrodeless discharge tube under rf excitation was used to provide an intense monochromatic source of narrow line width (0.006 Å and 0.009 Å) at 5461 Å. A positive correlation was detected and compared with theoretical predictions.

### PHOTON CORRELATION IN COHERENT LIGHT BEAMS

Recently several papers, listed below, have appeared which discuss correlation between photons in coherent light beams. In the experiments performed a light source illuminates a small pinhole, producing a pencil of light which strikes a distant half-silvered mirror. The reflected light is detected in one photomultiplier and the transmitted light in another photomultiplier. Nearly monochromatic light is selected by the isolation of a particular emission line of the source. The degree of coherence over the illuminated surface of the photocathode is determined by the dimensions of the pinhole and the distance from the photocathode to the pinhole. The outputs of the photomultipliers are fed into a coincidence circuit and the coincidence rate obtained is compared with that expected for purely random coincidences.

The existence of an excess of coincidences over the random rate has been predicted by several authors (Purcell 1956; Hanbury Brown and Twiss 1956b). Jánossy (1957) has investigated the problem theoretically using a particular physical model for the source and has calculated the "classical fluctuations" expected. Purcell gives the following expression for the coincidence rate expected

$$C_t = C_r \left( 1 + \frac{\tau_0}{2T} \right)$$

where  $C_r$  is the random coincidence rate,  $\tau_0$  is the reciprocal of the width of the spectral line in c.p.s.,  $T$  is the resolving time of the apparatus ( $T = 2\tau$ ). In practice the enhancement of coincidence rate would be decreased by a factor determined by the degree of coherence (Hanbury Brown and Twiss 1958) and polarization introduced by reflection at the surface of the mirror. Short resolving times and narrow line widths are desirable in order to obtain conditions such that the predicted enhancement would be appreciably larger than the statistical errors in the counting rates.

At this laboratory (Ferguson 1957), as well as at others (Twiss *et al.* 1957; Rebka and Pound 1957), experiments have been carried out in an attempt to detect this predicted enhancement. For good statistics in reasonable counting

<sup>1</sup>Manuscript received March 10, 1958.

<sup>2</sup>Postdoctoral Fellow, National Research Council of Canada, 1955-57.

times, a high intensity source is necessary. This requirement and that of narrow line width were achieved by the radio frequency excitation of an electrodeless Hg 198 lamp. A tunable coaxial line chamber (Fig. 1) was constructed similar to that of Forrester *et al.* (1956), the Hg 198 tube forming part of the inner conductor. Radio frequency power at 2450 megacycles was

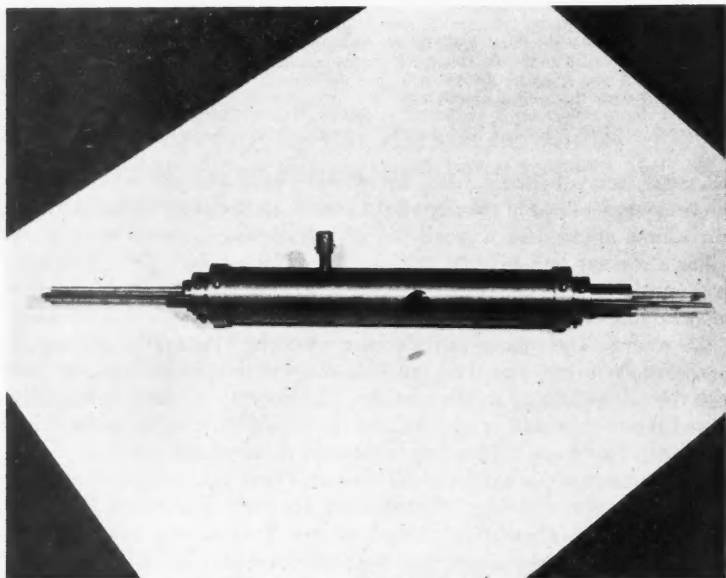


FIG. 1. A photograph of the co-axial line chamber. The small glass tube below the viewing port is one of the Hg 198 lamps. In operation the lamp is placed in the glass tube seen on the axis of the chamber and coolant is passed down the tube.

provided by a Raytheon Microtherm unit and with proper tuning about 90 watts of power was absorbed by the lamp. Both forced air and water cooling of the lamp are possible with this design by placing a small Hg 198 lamp, about two inches long, inside glass tubing running down the center of the inner conductor. Of necessity, as little water as possible should be in the region of the lamp, where the rf field is high, in order to avoid wasting rf power. In our arrangement about 20% of the rf power was absorbed by the water. The intensity was measured using a 929 phototube calibrated against a standard lamp. Intensities in the 5461 Å line ranged from 0.0001 to greater than 0.010 watts/cm<sup>2</sup>/steradian. At high intensities the line widths were greater than 0.03 Å, as measured with a Fabry Perot interferometer with a 5 cm spacer, while at lower intensities a width of 0.006 Å was obtained. It was found that with water cooling a higher intensity could be obtained by heating the water to 45° C without greatly increasing the line width. The experimental results given in this note were obtained using air cooling and a line width

of  $0.009 \text{ \AA}$  for the first set and with water cooling and a line width of  $0.006 \text{ \AA}$  for the second set. The light was focussed on an aperture  $0.13 \text{ mm}$  square in the first case, and  $0.4 \text{ mm}$  diameter in the second. Glass filters, Schott BG 20 (5 mm) and GG 11A (2 mm), isolated the 5461 line giving about 90% transmission. At a distance of 4 meters a half-silvered mirror (dielectric type) was placed and was viewed by two 1P21 photomultipliers, each 25 cm from the mirror. The aperture of each photomultiplier was restricted to a square of dimensions 1 cm by 1 cm. The outputs of the photomultipliers were fed to a standard fast coincidence circuit,  $2\tau = 8 \times 10^{-9} \text{ second}$ , of the Bell, Graham, and Petch (1952) type. Coincidences at zero and long delay,  $12 \mu\text{sec}$ , were recorded. To minimize the effect of any drift in resolving time, 5-minute runs at zero and long delay were alternated.

The experimental results obtained under these conditions and previously reported at the November, 1957, Tri-College Conference at the University of Buffalo, are

$$C_0/C_\tau = 1.014 \pm 0.005$$

for a line width of  $0.009 \text{ \AA}$  and

$$C_0/C_\tau = 1.025 \pm 0.002$$

for a line width of  $0.006 \text{ \AA}$  where  $C_0$  is the counting rate at zero delay and  $C_\tau$  is the counting rate at long delay. The probable errors were computed from the variations in the experimental readings. These results have been corrected for noise in the photomultipliers. For comparison, the theoretical predictions have to be corrected for polarization introduced by the mirror (30%) and for the degree of coherence of the light beam. After these corrections were made the predicted results are 1.028 and 1.027 respectively. At this time, this is felt to be reasonable agreement when one considers the uncertainty in the resolving time ( $\sim 20\%$ ) using single photons (compared to that using stilbene and cobalt 60), in the efficiency of the coincidence circuit, and in the determination of the line profile. It is interesting to note that we are close to the limit required by the theoretical calculation, namely  $T \gg \tau_0$ .

In conclusion, we have detected an enhancement of coincidence rate but comparison with the theory with certainty is difficult because of the uncertainty in the values of the parameters required. The variation of enhancement with spectral line width is not in disagreement with the theoretical predictions.

It is desirable to obtain higher accuracy in the measurements and to test the variation of enhancement with line width, resolving time, coherence factor, and polarization of the beam. We are attempting to do this using identical coincidence circuits capable of recording long delay and zero delay coincidences simultaneously and where one of the photomultipliers can be displaced from the superimposed position. Further, if sufficient accuracy is obtained, a more direct measurement of the resolving time of the apparatus for single photon pulses should be possible using this effect as a source of prompt coincidences and then inserting small delays in one channel in the usual way.

We are indebted to K. M. Baird of the National Research Council for furnishing us with several Hg 198 lamps and for information concerning their characteristics, and to Professor M. F. Crawford and D. Fraser of the University of Toronto for use of their equipment and assistance in determining the spectral line width. We are grateful to J. A. Fulford for advice in some of the electronic difficulties encountered in our laboratory. We gratefully acknowledge financial assistance in this and associated work from the National Research Council.

## REFERENCES

- ADÁM, A., JÁNOSSY, L., and VARGA, P. 1955. *Acta Physiol. Acad. Sci. Hung.* **4**, 301.  
BELL, R. E., GRAHAM, R. L., and PETCH, R. E. 1952. *Can. J. Phys.* **30**, 35.  
BRANNEN, E. and FERGUSON, H. I. S. 1956. *Nature*, **178**, 301.  
FERGUSON, H. I. S. 1957. Tri-College Conference, University of Buffalo.  
FORRESTER, A. T. 1956. *J. Opt. Soc. Am.* **46**, 339.  
HANBURY BROWN, R. and TWISS, R. Q. 1956a. *Nature*, **177**, 27.  
——— 1956b. *Nature*, **178**, 1447.  
——— 1958. *Proc. Roy. Soc.* **243**, 291.  
JÁNOSSY, L. 1957. *Nuovo cimento*, **6**, 111.  
PURCELL, E. M. 1956. *Nature*, **178**, 1449.  
REBKA, G. A., Jr. and POUND, R. V. 1957. *Nature*, **178**, 301.  
TWISS, R. Q., LITTLE, A. G., and HANBURY BROWN, R. 1957. *Nature*, **180**, 324.

## LOW TEMPERATURE RESISTIVITY OF THE TRANSITION ELEMENTS : RUTHENIUM AND OSMIUM<sup>1</sup>

G. K. WHITE AND S. B. WOODS

### ABSTRACT

Experimental values are reported for the electrical resistivity of ruthenium and osmium from 2 to 300° K and for the thermal resistivity from 2 to 140° K. The samples were produced by arc-melting pressed pellets of metallic powder in an inert gas atmosphere. Two osmium samples and one ruthenium sample showed a satisfactorily low residual electrical resistance. By grinding these rods to a regular shape, absolute values of resistivity were obtained and the impurity and thermal components of resistivity derived; at room temperature (295° K) we deduce that for ideally pure Os,  $\rho \approx 9.1\mu\Omega\text{cm}$  and for ideally pure ruthenium  $\rho \approx 7.3\mu\Omega\text{cm}$ . The temperature dependence of the resistivity was markedly different for another ruthenium sample but it seems likely that this was not representative of pure h.c.p. ruthenium.

### INTRODUCTION

In previous papers dealing with experimental investigations of the electrical and thermal resistivity of the transition elements at low temperatures (White and Woods 1957a, b, c, d; Kemp *et al.* 1955, 1956; Harper *et al.* 1957; White 1956), the possible influence of interband electron transitions and electron-electron interactions was discussed. Experimental data on these electron transport properties have been collected over a wide range of low temperatures for various transition elements. Samples of the highest available purity were used so that values for the ideal resistivities might be deduced, i.e., the resistivities due to scattering of electrons by other than static imperfections. We hoped in this way to see whether any definite conclusions could be drawn regarding the theoretical proposals of Mott and of Wilson concerning the behavior of the conduction electrons in the transition elements.

In order to complete the survey and also to obtain information which might be of general technical interest, we have extended these experimental studies to cover osmium and ruthenium, two transition elements for which little data existed. As far as we are aware there are no published heat conductivity measurements for these metals. For the electrical resistivity of ruthenium, values between 7 and  $8 \times 10^{-6}$  ohm cm have been obtained at room temperature by Justi (1949) and by Meissner and Voigt (1930) as well as values at about 80° K and 20° K. However, many physical tables, textbooks, and reviews quote room temperature values ranging up to  $15 \times 10^{-6}$  ohm cm, some of which appear to stem from a value of  $14.4 \times 10^{-6}$  ohm cm reported by Benedicks (1915).

For osmium, most physical tables quote an electrical resistivity at room temperature of approximately  $9.5 \times 10^{-6}$  ohm cm, the original measurements

<sup>1</sup>Manuscript received February 21, 1958.

Contribution from the Division of Pure Physics, National Research Council, Ottawa, Canada.

Issued as N.R.C. No. 4786.

having been made by Blau (1905) on an osmium filament. However, some tables give values as high as 60 and even  $90 \times 10^{-6}$  ohm cm.

#### EXPERIMENTAL METHOD

Measurements of thermal conductivity from 2° K to 150° K and of electrical resistivity from 1° K to room temperature were made on each specimen in the cryostat described previously (White and Woods 1955).

The principal difficulty has been in the preparation of suitable specimens in terms of purity (physical and chemical) and geometrical shape. We were unable to buy ruthenium and osmium except in powdered form, which was obtained both from Messrs. Johnson Matthey and Mallory Ltd. and from the Baker Platinum Company. The powder was pressed into small pellets and arc-melted in an inert gas atmosphere in our laboratories to form solid rods. We were led to use arc-melting by the success of Hulm and Goodman (1957), who used this method to prepare rods of rhenium, another high melting point transition element. The arc-melting equipment used by us was originally built by Dr. I. M. Templeton for making solid beads of some superconducting alloys. The pellets of pressed powder, which form the anode of the arc, are placed in a shallow groove in a water-cooled copper block. The cathode is a small rod of tungsten (or other high melting point material as discussed below) held in the end of a movable water-cooled rod. The pellets were arc-melted to form a rod and, in some cases, ground or cut to remove thick spots and then remelted. The inert gas used as an atmosphere was generally helium purified by being passed over charcoal cooled with liquid nitrogen although on occasion argon was used in an effort to prevent the arc striking to the copper part of the anode beyond the tip.

TABLE I  
PHYSICAL DATA FOR SPECIMENS

	Diameter (mm)	$10^3 \rho_0 / \rho_{295}$	$10^6 \rho_0$ (ohm cm)	$W_0 T$ (cm deg <sup>2</sup> /watt <sup>-1</sup> )	$10^3 L_0$ (watt ohm deg <sup>-2</sup> )	$10^6 \rho_{295}$ (ohm cm)
*Ru 2	~6	27.7	0.23 <sub>5</sub>	9.8	2.40	8.49
*Ru 3	~5	2.14	0.015 <sub>8</sub>	0.643	2.46	7.39
*Os 2	~6	10.8	0.10	3.8 <sub>5</sub>	2.60	9.23
Os 3	1.88	9.46	0.087 <sub>2</sub>	3.33	2.61	9.23

\*Absolute values of  $\rho$  and  $W$  were obtained by a normalization procedure discussed below.

The history of the specimens is as follows:

#### (1) Osmium

Os 1 was prepared from Johnson Matthey powder (purity quoted as better than 99.995%) using a tungsten tip in the arc furnace. The specimen, which was a short irregular rod, had a residual electrical resistance ratio,  $R_{4.2}/R_{295}$  of  $49 \times 10^{-3}$ ; the resistivity at room temperature,  $\rho_{295}$ , was  $10 \pm 1$  micro-ohm cm, the uncertainty being due to its irregular shape. This rod was used afterwards as the cathode for melting further osmium specimens; this procedure was adopted in order to obtain specimens without serious tungsten contamination.

Os 2 was also prepared from Johnson Matthey powder but with an osmium cathode (Os 1) in the arc furnace. The specimen was about 6 cm long, had an approximate room temperature resistivity,  $\rho_{295}$ , of  $9 \pm 1$  micro-ohm cm and, as shown in Table I, gave  $\rho_0/\rho_{295}^*$  ( $= R_{4.2}/R_{295}$ ) of  $10.8 \times 10^{-3}$ . It was mounted in the cryostat using a non-superconducting Zn-Cd eutectic solder for attaching current and potential leads; measurements of both electrical and thermal resistance were then made. These were later reduced to absolute values by normalizing  $\rho_{295} - \rho_0 \equiv \rho_{t(295)}$  to a value of  $9.13 \times 10^{-6}$  ohm cm (see Os 3 below).

Several attempts were made to reduce Os 2 to a regular geometrical shape. It was first ground with tungsten carbide wheels and later cut with a diamond saw and ground on a milling bench with a diamond wheel, but the rod repeatedly broke and eventually became too small for any accurate absolute measurements. Approximate measurements of  $R_{295}$  and the ratio,  $R_{4.2}/R_{295}$ , merely confirmed that  $\rho_{295}$  (and  $\rho_{t(295)} = \rho_{295} - \rho_0$ ) had a value of  $10 \pm 1$  micro-ohm cm.

Os 3 was arc-melted from Baker Platinum Company osmium powder† using an osmium cathode and gave  $\rho_0/\rho_{295} = 6.3 \times 10^{-3}$ . After some preliminary grinding to remove very thick spots on the rod, it was re-melted and then ground to a regular cylinder of about 5 cm length using a diamond grinding wheel attached to a lathe. Current and potential leads were attached with a non-superconducting Bi-Cd eutectic solder and it was mounted in the cryostat. As the results followed a pattern quite similar to that for Os 2, the "ideal" value of the electrical resistivity of Os 3, namely,  $\rho_{t(295)} = 9.13 \times 10^{-6}$  ohm cm, was used to convert the results for Os 2 to absolute values.

### (2) Ruthenium

Ru 1 was melted from Johnson Matthey powder of quoted purity better than 99.995%. During the arc-melting a small tungsten bead fell into the specimen and presumably this tungsten contamination was largely responsible for the high residual resistance ratio:  $R_{4.2}/R_{295} \simeq 0.5$ .

Ru 2 was arc-melted using powder from the Baker Platinum Company to produce a rod 7 cm long and with an average diameter of 6 mm (see Table I). Many attempts were made to use Ru 1 as a cathode during this melting but we were unsuccessful in striking a stable arc to the ruthenium tip in either helium or argon. Finally a tungsten cathode was used with a small ruthenium bead on its end. Ru 2 was mounted in the cryostat with the aid of Zn-Cd solder and measurements of electrical and thermal resistance were made. As seen in Table I,  $R_{4.2}/R_{295} = \rho_0/\rho_{295} \simeq 27.7 \times 10^{-3}$  but absolute values of the resistivity were in doubt owing to the irregular shape; measurements of weight, length, and average diameter combined to give an approximate value for  $\rho_{295}$  of  $8.5 \pm 0.5$  micro-ohm cm so that  $\rho_{t(295)} = \rho_{295} - \rho_0 = 8.3 \pm 0.5$  micro-ohm cm.

\*Below 10° K, the resistance or resistivity is independent of temperature and is assumed to be due to impurity scattering; this impurity resistance may conveniently be determined at 4.2° K and is frequently denoted by  $R_0$  (resistance) or  $\rho_0$  (resistivity). The total electrical resistivity at 295° K,  $\rho_{295}$ , is assumed to be the sum of the impurity resistivity,  $\rho_0$ , and a temperature sensitive resistivity due to scattering by thermal vibrations,  $\rho_{t(295)}$ .

†No analysis was supplied but our measurements suggest it to be of comparable purity to that from Johnson Matthey and Mallory.

Ru 2 was then ground to a right cylinder using a tungsten carbide grinding wheel attached to a lathe. This specimen, called Ru 2a, gave  $\rho_{295} = 8.42 \times 10^{-6}$  ohm cm and  $\rho_{4.2} = \rho_0 = 0.152 \times 10^{-6}$  ohm cm so that  $\rho_{t(295)} \approx 8.27 \times 10^{-6}$  ohm cm. This latter value was used to normalize the "resistivity" values obtained on Ru 2. Ru 2a was later remelted in the arc and further measurements of  $R_{295}$ ,  $R_{78}$ ,  $R_{4.2}$  were taken.

Ru 3 was also melted from Baker Platinum Company powder using a tungsten tip with a ruthenium bead on the end. The rod which was 6 cm long and  $5 \pm 1$  mm in diameter had a low residual resistance ratio (see Table I) and so further measurements were made with it mounted in the cryostat with Zn-Cd solder. After Ru 3 had been ground to a right cylinder it was found that  $\rho_{295} = 7.39 \times 10^{-6}$  ohm cm and  $\rho_0/\rho_{295} \approx 2.68 \times 10^{-3}$ . Thus a value of  $\rho_{t(295)} = 7.37 \times 10^{-6}$  ohm cm was obtained which was used for the conversion of the previous measurements on Ru 3 to resistivity values. Ru 4 was also melted from Baker Platinum Company powder to try to resolve the discrepancy in behavior between Ru 2 and Ru 3. Unfortunately, a little tungsten bead from the electrode tip dropped into the specimen during melting so that its residual resistance ratio was rather high. After melting it also was ground to a right cylinder but cracked during the later stages of grinding, was rejoined in the arc furnace and gave an approximate value for  $\rho_{t(295)}$  of  $10.5 - 2.5 = 8.0$  micro-ohm cm. After it was ground again to regain a true cylindrical shape, it gave  $\rho_{295} = 10.53 \times 10^{-6}$ ,  $\rho_0 = 2.43 \times 10^{-6}$  so that  $\rho_{t(295)} = 8.10 \times 10^{-6}$  ohm cm.

## RESULTS

Values obtained for thermal conductivity,  $\lambda$ , are shown in Fig. 1. Below  $10^{\circ}$  K, it can be seen that  $\lambda/T$  is sensibly constant for each specimen. This

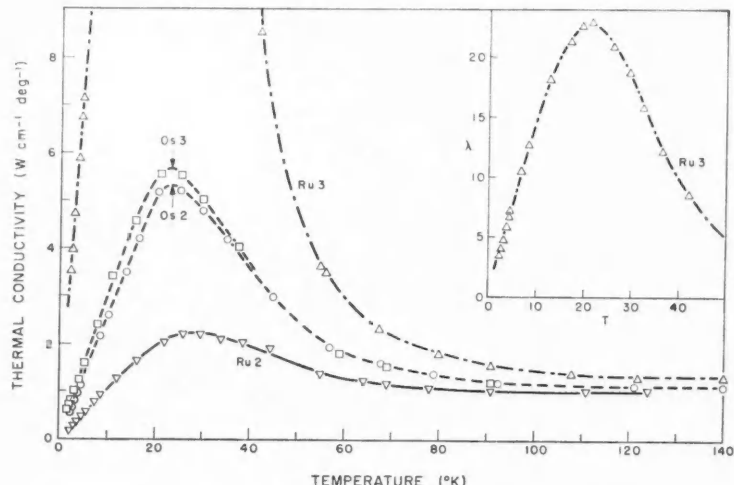


FIG. 1. Thermal conductivity of osmium and ruthenium.

indicates that the thermal resistivity in this region is determined almost entirely by static imperfections and this resistivity is denoted by  $W_0 \equiv 1/\lambda_0$ . Values for  $W_0 T$  for each specimen are given in Table I together with values of the (constant) residual electrical resistivity,  $\rho_0$ . In each case the Lorenz ratio,  $L_0 = \rho_0 \lambda_0 / T = \rho_0 / W_0 T$ , has a value close to the theoretical figure of  $2.45 \times 10^{-8} \text{ w } \Omega \text{ deg}^{-2}$ .

If we assume that the impurity thermal resistivity,  $W_0$ , and the "ideal" thermal resistivity,  $W_t$ , due to scattering of the electrons by thermal vibrations, are strictly additive, that is

$$1/\lambda \equiv W = W_0 + W_t,$$

then values for  $W_t$  may be calculated from the experimental data. These are shown in Fig. 2 together with some high temperature values ( $W_\infty$ ) for  $W_t$

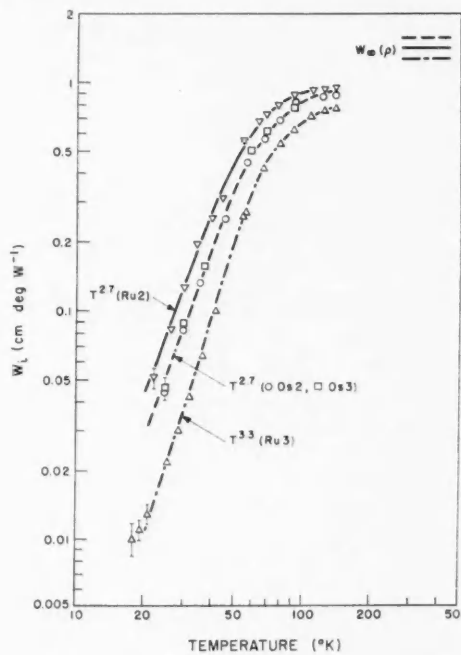


FIG. 2. Ideal thermal resistivity,  $W_t$ , for osmium and ruthenium.

calculated from the ideal electrical resistivity at room temperature,  $\rho_{(295)}$ , assuming the validity of the Wiedemann-Franz-Lorenz law in this region, i.e.

$$\rho_t/W_t T \simeq 2.45 \times 10^{-8} \text{ w } \Omega \text{ deg}^{-2}.$$

Results of the electrical resistivity measurements at room temperature and at very low temperatures where  $\rho \simeq \text{constant}$  are listed in Table I under

the headings  $\rho_{295}$  and  $\rho_0$  respectively. Values for the ideal electrical resistivity  $\rho_i = \rho - \rho_0$ , are shown in Fig. 3 and in Table II.

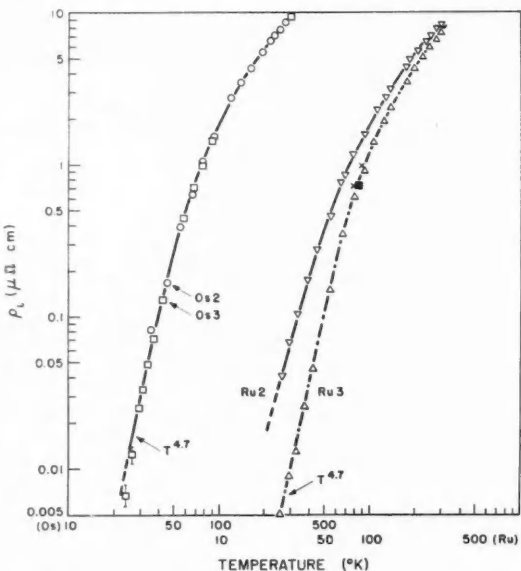


FIG. 3. Ideal electrical resistivity,  $\rho_i$ , of osmium and ruthenium.

TABLE II  
IDEAL ELECTRICAL RESISTIVITY IN MICRO-OHM CM

T, °K	Os	Ru 2	Ru 3	T, °K	Os	Ru 2	Ru 3
295	9.13	8.27	7.37	75	0.9 <sub>5</sub>	1.0 <sub>7</sub>	0.5 <sub>4</sub>
273.1 <sub>5</sub>	8.35	7.60	6.69	50	0.2 <sub>6</sub>	0.3 <sub>8</sub>	0.1 <sub>1</sub>
250	7.50	6.85	5.96	40	0.1 <sub>1</sub>	0.1 <sub>0</sub>	0.03 <sub>7</sub>
200	5.70	5.26	4.38	30	0.02 <sub>8</sub>	0.06 <sub>7</sub>	0.01 <sub>0</sub>
150	3.85	3.61	2.80	25	0.01 <sub>2</sub>	0.03 <sub>4</sub>	0.00 <sub>5</sub>
100	1.90	1.90	1.25				

## DISCUSSION

### Osmium

As discussed in earlier papers and also in recent reviews (Olsen and Rosenberg 1953; Klemens 1956), theoretical treatment of electron transport in elements which have one free electron per atom in the *s*-band suggests that  $\rho_i \propto T^3$  and  $W_i \propto T^2$  for  $T \ll \theta_D$ . Experiments on monovalent metals have seemed to confirm this although discrepancies have arisen in the magnitudes of  $\rho_i$  or  $W_i$  as compared with their high temperature values (cf. MacDonald, White, and Woods 1956).

The ideal electrical resistivity and also the ideal thermal resistivity results

are similar in the two osmium specimens. Below 40° K  $\rho_i$  approaches a  $T^5$  dependence but  $W_i$  appears to fall rather more rapidly in this region than the  $T^2$  law would predict. Because of this, it is difficult to compare its magnitude directly with that predicted by the semiempirical expression

$$\frac{W_i}{W_\infty} = 2 \left( \frac{T}{\theta_D} \right)^2 \int_0^{\theta/T} \left[ \frac{x^3 dx}{(e^x - 1)(1 - e^{-x})} \right]$$

which reduces to

$$\frac{W_i}{W_\infty} \simeq 14.4 \left( \frac{T}{\theta_D} \right)^2 \quad \text{for } T < \frac{\theta_D}{10}.$$

(See MacDonald, White, and Woods 1956, and previous papers on transition elements.) A crude comparison may be made by evaluating  $(W_i/W_\infty)(\theta/T)^2$  at a temperature of say  $T \simeq \theta_D/10$ : for this purpose we will use  $\theta_D \simeq 400^\circ$  K (Wolcott 1956) and the value for the high temperature thermal resistivity given by  $W_\infty \simeq \rho/LT = 1.26$  cm deg w<sup>-1</sup>, evaluated at 295° K. At 40° K ( $\theta_D/10$ ) our results give  $W_i \simeq 0.19$  from which

$$\frac{W_i}{W_\infty} \left( \frac{\theta}{T} \right)^2 = 15.1.$$

This is fortuitously close to the value of about 14.4 given by the expression above.

It may be noted that the high temperature value of the ideal thermal resistivity deduced from the Wiedemann-Franz-Lorenz law, namely  $W_\infty = 1.26$  cm deg w<sup>-1</sup>, appears from Fig. 2 to be some 20 to 30% higher than the values that would be obtained by extrapolation of the ideal resistivity values obtained at lower temperatures. This discrepancy seems rather large in osmium and ruthenium and also has been noticeable in niobium, vanadium, cobalt, and rhenium. It is tempting to ascribe this to the presence in these metals of an appreciable component of lattice conductivity,  $\lambda_g$ ; this would be expected to diminish with  $1/T$  in the region of  $T > \theta/5$ , but may not yet be negligible (as is usually assumed) in the neighborhood of 100° K. If this component is appreciable, it should be subtracted from the measured total conductivity,  $\lambda$ . There appears to be no obvious method of separating the components of thermal conductivity at these higher temperatures; however, accurate measurements of the thermal conductivity at 300° K or 400° K, where the lattice conduction should be much less than at 100° K, would allow a much better test of the Wiedemann-Franz-Lorenz law than this extrapolation of our low temperature measurements.

#### Ruthenium

The most startling feature of the results on ruthenium is the general difference in behavior between the two specimens, Ru 2 and Ru 3. The difference of about 10% in the room temperature electrical resistivities is no more remarkable than the very different temperature dependence of the thermal as well as the electrical resistivities exhibited by the two specimens, which makes it appear as though Ru 2 had an effective Debye temperature which is 30 or

40% less than that of Ru 3. Values for the ratio  $\rho_0/\rho_{295}$  listed in Table I show that there is a considerable difference in the residual electron scattering by impurities. Spectrographic analysis of the rods showed little difference; there were no obvious lines of tungsten, copper, or other major impurities present in either Ru 2 or Ru 3. Specific gravity measurement at 22° C gave 12.0 for Ru 2 and 12.2<sub>5</sub> for Ru 3 which might suggest some incompletely melted regions or holes in the Ru 2 although the arc-melting procedure and examination during grinding did not confirm this. A simple measure of the difference in resistivity behavior is the ratio  $\rho_{t(295)}/\rho_{t(78)} \equiv \{\rho_{295} - \rho_t\}/\{\rho_{78} - \rho_t\}$ . For Ru 3 this ratio was about 12.4 and it remained within about 1% of this value after cutting and remelting and again after grinding. However, for Ru 2 this ratio was about 7.2 and after grinding rose to about 8.1 and later when the specimen was remelted rose to about 9.0.

Although small departures from Matthiessen's rule, i.e., the additivity hypothesis  $\rho = \rho_0 + \rho_t$ , may be expected, the results on ruthenium seem far too varied to be explained in this manner. There is in addition the small difference in density of specimens Ru 2 and Ru 3 to be explained and the greater hardness of Ru 3 which was quite obvious when the rods were being ground. Since the spectrographic analysis revealed no distinguishable impurities it seems that different crystallographic phases must be present although the recent X-ray investigations by Hall and Crangle (1957) revealed only the normal close-packed hexagonal phase in ruthenium powder between 0 and 1400° C. We therefore examined our specimens with a metallographic microscope after polishing and electrolytically etching their surfaces with an alternating current. The etching was done in a saturated sodium chloride solution containing 20% hydrochloric acid. In contrast to Ru 3, the specimens Ru 2 and Ru 4 showed some slight evidence for the presence of a decomposed phase and it was hoped that an X-ray diffraction study might reveal whether phases other than the normal close-packed hexagonal were present. However oscillation X-ray pictures in a Debye-Scherrer camera showed no obvious differences among the specimens; this investigation was complicated by the large grain size which the metallographic examination showed was about 1 mm in the ruthenium (and also the osmium) specimens.

Some values for the electrical resistivity of ruthenium obtained by Justi (1949) and Meissner and Voigt (1930) on sintered rods are also shown in Fig. 3. Justi found  $\rho_{t(273)} = 6.67 \times 10^{-6} \Omega \text{ cm}$ , which agrees closely with our values for Ru 3; his value at 81.7° K also lies very close to our curve for Ru 3. Meissner and Voigt give a value of about  $8.3 \times 10^{-6}$  for  $\rho_{t(295)}$  and their values at 87.2° K and 77.6° K are a little higher than those for Ru 3. However, their reduced resistivity values  $\rho_{t(T)}/\rho_{t(295)}$  for  $T = 87.2$  and 77.6° K agree quite well with the values for Ru 3.

Thus it seems probable that values of resistivity for Ru 3 represent those for pure close-packed hexagonal ruthenium. Again if we adopt  $\theta_D \simeq 500^\circ \text{ K}$  (from specific heat measurements near 20° K by Wolcott 1956) and  $W_\infty \simeq 1.02 \text{ cm deg w}^{-1}$  (from  $W = \rho L/T$  at 295° K), we find  $(W_t/W_\infty)(\theta_D/T)^2 \simeq 19$  for Ru 3 at  $T \simeq \theta_D/10 \simeq 50^\circ \text{ K}$  which contrasts with a value of about 40 for this parameter for Ru 2.

## CONCLUSIONS

Measurements of heat conductivity and electrical conductivity of arc-melted osmium rods have provided data on the ideal thermal resistivity below 150° K and ideal electrical resistivity below 300° K. At room temperature it appears that  $\rho_i = 9.2 \times 10^{-6} \Omega \text{ cm}$  and extrapolation of the thermal data suggests  $\lambda \approx 0.9 \pm 0.1 \text{ w cm}^{-1} \text{ deg}^{-1}$  at room temperature.

For ruthenium a puzzling discrepancy emerges between different specimens but we believe the data for Ru 3 represent the true values of resistivity for close-packed hexagonal ruthenium. At room temperature,  $\rho_i = 7.4 \times 10^{-6} \Omega \text{ cm}$  and extrapolation of the thermal data (obtained only below 150° K) to room temperature suggests  $\lambda \approx 1.1 \pm 0.1 \text{ w cm}^{-1} \text{ deg}^{-1}$ .

## ACKNOWLEDGMENTS

We are very grateful to Dr. Z. S. Basinski and Dr. W. B. Pearson for metallurgical assistance and advice and to Dr. D. K. C. MacDonald for helpful criticism of the manuscript. As before, the hard work of Messrs. F. Richardson and J. Broome has provided us with supplies of liquid helium.

## REFERENCES

- BENEDICKS, C. 1915. *Z. Metallk.* **7**, 225.  
 BLAU, F. 1905. *Elektrotech. Z.* **25**, 198.  
 HULM, J. K. and GOODMAN, B. B. 1957. *Phys. Rev.* **106**, 659.  
 JUSTI, E. 1949. *Z. Naturforsch.* **4a**, 472.  
 HALL, E. D. and CRANGLE, J. 1957. *Acta Cryst.* **10**, 240.  
 HARPER, A. F. A., KEMP, W. R. G., KLEMENS, P. G., TAINSH, R. J., and WHITE, G. K. 1957. *Phil. Mag.* **2**, 577.  
 KEMP, W. R. G., KLEMENS, P. G., SREEDHAR, A. K., and WHITE, G. K. 1955. *Phil. Mag.* **46**, 811.  
 KEMP, W. R. G., KLEMENS, P. G., and WHITE, G. K. 1956. *Australian J. Phys.* **9**, 180.  
 KLEMENS, P. G. 1956. *Handbuch der Physik*, **14**, 198.  
 MACDONALD, D. K. C., WHITE, G. K., and Woods, S. B. 1956. *Proc. Roy. Soc. London, A*, **235**, 358.  
 MEISSNER, W. and VOIGT, B. 1930. *Ann. Physik*, **7**, 892.  
 OLSEN, J. L. and ROSENBERG, H. M. 1953. *Phil. Mag. Suppl.* **2**, 28.  
 WHITE, G. K. 1956. *Can. J. Phys.* **34**, 1328.  
 WHITE, G. K. and Woods, S. B. 1955. *Can. J. Phys.* **33**, 58.  
 ——— 1957a. *Can. J. Phys.* **35**, 248.  
 ——— 1957b. *Can. J. Phys.* **35**, 346.  
 ——— 1957c. *Can. J. Phys.* **35**, 656.  
 ——— 1957d. *Can. J. Phys.* **35**, 892.  
 WOLCOTT, N. M. 1956. *Conférence de physique des basses températures*, Paris, 1955, p. 286. Annexe 1955-3, Supplément au *Bulletin de l'Institut International du Froid*. Paris.

# REFRACTIVE INDEX OF He<sup>4</sup>: LIQUID<sup>1</sup>

M. H. EDWARDS

## ABSTRACT

Changes in the phase refractive index  $n$  with temperature have been measured between 1.6 and 4.2° K at  $\lambda = 5462.27 \text{ \AA}$ , for liquid He<sup>4</sup> at its saturated vapor pressure, using a metal optical cryostat and a Jamin interferometer. A novel adaptation of the Jamin interferometer has been made so that, in addition, an absolute determination of the group refractive index,  $n_g$ , could be made using white light of "effective wavelength"  $5595 \pm 40 \text{ \AA}$ . When the dispersion correction is made, the phase index for the Hg green line at  $T_{\text{sat}} = 3.700^\circ \text{ K}$  is  $n = 1.026124 \pm 0.000035$ . The relative measurements have been adjusted to this value. The more than 200 experimental points show a random scatter of less than  $5 \times 10^{-6}$  in index. Using Kerr's density data the polarizability is thus  $(N_{\alpha\alpha}) = (0.12454 \pm 0.00021) \text{ cm}^3 \text{ mole}^{-1}$  at  $\lambda = 5462.27 \text{ \AA}$ , for liquid He<sup>4</sup> at  $3.7^\circ \text{ K}$ . Within experimental error ( $N_{\alpha\alpha}$ ) is found to be independent of temperature. Thus the refractive index data may be considered as a measurement of the liquid density and coefficient of expansion.

The region near the  $\lambda$ -point is of special interest. The expansion coefficient determined from the refractive index,  $\beta_n$ , may be represented within experimental error by  $10^3 \beta_{nI} = +41.5 + 14.5 \log |T - T_\lambda|$  for  $T > T_\lambda$ , from about  $0.1^\circ$  above  $T_\lambda$  to within  $0.01^\circ$  of  $T_\lambda$ ; and by  $10^3 \beta_{nII} = -1.5 + 14.5 \log |T - T_\lambda|$  for  $T < T_\lambda$ , from about  $0.1^\circ$  below  $T_\lambda$  to within  $0.002^\circ$  of  $T_\lambda$ . This implies that the density-temperature curve has both a vertical tangent and a point of inflection at the  $\lambda$ -point; and that the maximum in density occurs about  $0.001^\circ$  above the  $\lambda$ -point.

## 1. INTRODUCTION

The refractive index of liquid helium has been measured by Wilhelm and Cove (Satterly 1936), who obtained  $1.028 \pm 0.006$  as the index of liquid helium II (against gaseous helium) at a temperature just below  $2.1^\circ \text{ K}$ ; and by Johns and Wilhelm (1938), who obtained  $1.0206 \pm 0.0012$  at  $4.22^\circ \text{ K}$  and  $1.0269 \pm 0.0004$  at  $2.25^\circ$  and  $2.142^\circ \text{ K}$  for  $\lambda = 5462.27 \text{ \AA}$ . In both cases a Wollaston cell was used to determine critical angles, which were nearly  $80^\circ$ . The uncertainties stated did not include the effects of possible distortion of the plates of the cells near the edges.

A re-investigation of the refractive index seemed worthwhile to check the change of 13% in the polarizability per mole implied by the above results.

This paper reports measurements of changes with temperature from 1.6 to  $4.2^\circ \text{ K}$  in the phase refractive index  $n$  of liquid He<sup>4</sup> at its saturated vapor pressure using a metal optical cryostat and a Jamin interferometer for  $\lambda = 5462.27 \text{ \AA}$ ; and an absolute measurement of the group refractive index  $n_g$  using a novel adaptation of the Jamin interferometer.

## 2. APPARATUS AND METHOD

### 2.1 Relative Measurements

A preliminary report of these relative measurements has been made

<sup>1</sup>Manuscript received March 11, 1958.

Contribution from Department of Physics, Royal Military College, Kingston, Ontario. Supported in part by the Defence Research Board of Canada under Grant No. 9510-10, Project D44-95-10-10.

(Edwards 1956). The optical system used here was the same as that used to measure the refractive index of  $\text{He}^4$  saturated vapor (Edwards 1957). A full description of the apparatus is given in the two references cited.

For these liquid measurements the optical cell was filled about 90% with liquid, 10% with vapor. Thus the liquid remained at its saturated vapor pressure during all of these measurements. Stops were placed outside the apparatus so that only the light passing through the liquid in the cell suffered interference. This is in contrast to the vapor measurements, where only the part of the light which had passed through the vapor was allowed to suffer interference.

As the temperature of the liquid helium in the bath was slowly lowered, the index of refraction changed, and fringes were counted visually as they moved past the cross-hairs of the interferometer telescope. As in the vapor case, each fringe corresponded to a change in index of  $(5.701 \pm 0.003) \times 10^{-6}$ . For these relative measurements, temperatures were measured using the carbon resistance thermometer.

## 2.2 Absolute Measurement

Candler (1950, page 457) states that "The absolute refractive index of a liquid is always measured by a deviation method; interferometers are used only to measure small changes of refractive index, or to compare the refractive indices of two liquids." Nevertheless, the absolute value of the group refractive index,  $n_g$ , of liquid  $\text{He}^4$  has now been measured using a novel adaptation of the Jamin interferometer, involving the use\* of a special air-filled etalon  $E$ . A report of part of this method and preliminary results has been made elsewhere (Edwards and Hanes 1957).

See Fig. 1 for a horizontal section of the optical system, as modified for this

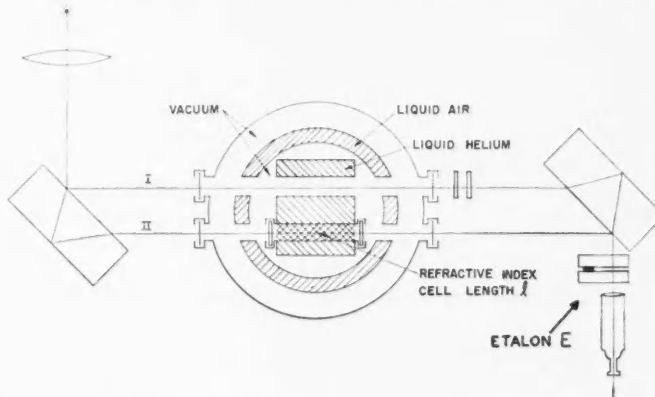


FIG. 1. The optical system, as modified for absolute measurement of refractive index of liquid  $\text{He}^4$ .

\*This method was suggested, and the etalon made and measured, by Dr. G. R. Hanes, Interferometry Section, Applied Physics Branch, National Research Council, Ottawa.

absolute measurement. The etalon,  $E$ , was placed between the second Jamin block and the telescope. The etalon (Fig. 2) was made by wringing two 2-in. diameter,  $\frac{1}{2}$ -in. thick quartz flats on a 0.050-in. gauge block. The inner faces

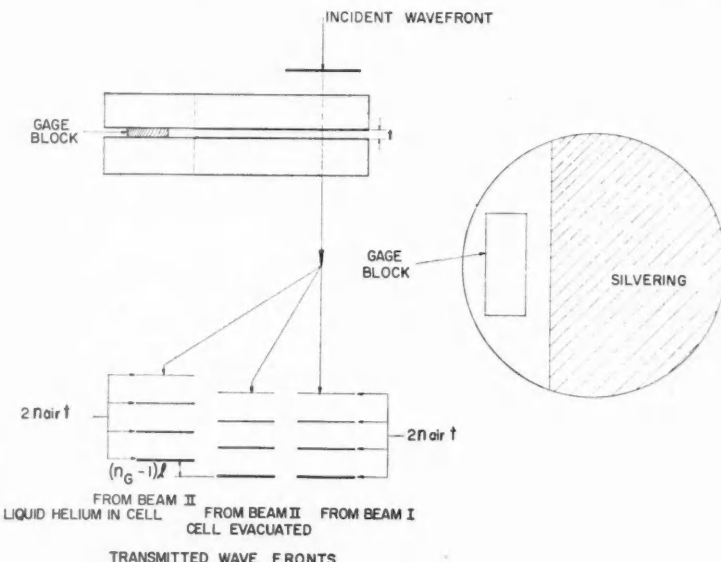


FIG. 2. The etalon, illustrating its effect upon plane wavefronts.

of the flats were each silvered to have a transmittance of 9% and a reflectance of 87%. The etalon gap was  $t = 0.050000$  in. at 25°C. The etalon was aligned accurately perpendicular to the emerging beam of the Jamin by auto-collimation. Any incident plane wavefront, after passing through the etalon, appears as a sequence of successively dimmer wavefronts (see Fig. 2) each retarded by a multiple of  $2n_{\text{air}} t$  where  $n_{\text{air}}$  is the refractive index of air.

In the condition, refractive index cell evacuated, Jamin compensator (not shown) adjusted so that there is zero path difference between beam I and beam II, the  $i$ th retarded wavefronts from the two beams (shown separated in Fig. 2) will be coincident and white light fringes may be seen. (In this condition white light fringes may also be seen without the etalon in place.)

When the cell of length  $l$  is filled with liquid helium, the corresponding wavefronts from beam II are retarded with respect to those from beam I. The temperature of the liquid helium may be changed to adjust this retardation slightly so that the  $i$ th retarded wavefront from beam II and the  $(i+1)$ th retarded wavefront from beam I interfere, and white light fringes may again be seen. Since the first wavefront from beam I does not suffer interference, these fringes are of rather poorer contrast.

The general condition for white light fringes is that the phase difference shall not change with the wavelength at the achromatic fringe. (See, e.g., Candler 1950, page 477). This requires that

$$O = \frac{d}{d\lambda} (\text{phase difference}) = \frac{d}{d\lambda} \left( \frac{2\pi \text{ optical path difference}}{\lambda} \right)$$

$$O = \frac{d}{d\lambda} \left[ \frac{(n-1)l}{\lambda} - \frac{2n_{\text{air}}t}{\lambda} \right],$$

where

$n$  = phase refractive index,  
 $l$  = length of cell,  
 $t$  = etalon spacing.

That is:

$$(2.1) \quad (n-1) - \lambda \frac{dn}{d\lambda} = \frac{2n_{\text{air}}t}{l}$$

or

$$(2.2) \quad (n_g - 1)l = 2n_{\text{air}}t$$

where  $n_g = n - \lambda(dn/d\lambda)$  is the group refractive index.

Thus what is measured here is the group refractive index  $n_g$ , at the "effective wavelength",  $\lambda_w$  of the white light. From (2.1) and (2.2) we see the phase index at this wavelength may be obtained from

$$(2.3) \quad (n-1) = \frac{n_g - 1}{1 - \delta}$$

where

$$(2.4) \quad \delta = \frac{\lambda}{(n-1)} \frac{dn}{d\lambda}.$$

This correction term  $\delta$  depends on the dispersion of liquid helium and thus on the effective wavelength of the white light. Cuthbertson and Cuthbertson (1932) measured the dispersion of He<sup>4</sup> gas at N.T.P. They obtained

$$(2.5) \quad n-1 = \frac{1.32614 \times 10^{27}}{38313.7 \times 10^{27} - c^2/\lambda^2}.$$

Thus

$$(2.6) \quad \delta = \frac{2}{1 - 4.26298 \times 10^{10} \lambda^2}$$

where  $\lambda$  is the effective wavelength of the white light.

The effective wavelength,  $\lambda_w$ , of the white light may be determined by comparing the number of white light fringes,  $\Delta N_w$ , which move by the cross-hairs in the telescope with the number of Hg fringes,  $\Delta N_{\text{Hg}}$ , which move by, for the same change in optical path. Thus if the temperature of the helium is changed through the same interval twice, the change in optical path

$$(2.7) \quad \Delta(n-1)l = \Delta N_{\text{Hg}} \lambda_{\text{Hg}} = \Delta N_w \lambda_w.$$

Thus one measures the group index for  $\lambda = \lambda_w$ , as given by equation (2.2);  $\lambda_w$  is determined from equation (2.7);  $\delta$  is calculated from equation (2.6); and thus one gets the absolute value of the phase index  $(n-1)$  at  $\lambda = \lambda_w$  by equation (2.3). The absolute value of  $(n-1)$  at  $\lambda = 5462.27 \text{ \AA}$  is then obtained by assuming the proportional change in  $(n-1)$  with wavelength for liquid helium is the same as for helium gas at N.T.P., as given by equation (2.5). This gives a single absolute value of the phase index,  $n$ , for liquid  $\text{He}^4$ , at the temperature of the midpoint of the white light fringe pattern. There are, of course, only a limited number of white light fringes (about 45), and the middle fringe is taken to be the achromatic fringe.

### 3. EXPERIMENTAL RESULTS

#### 3.1 Relative Measurements

As the temperature was lowered from  $4.2^\circ \text{ K}$  to the  $\lambda$ -point some 729 fringes were counted; between the  $\lambda$ -point and  $1.6^\circ \text{ K}$  about 32 fringes were counted, moving in the opposite sense. More than 200 experimental points were taken. They show a random scatter of less than  $5 \times 10^{-6}$  in index over most of this range. Smoothed values of  $(n-1)$  as read from a large graph of all the measurements are given in Table I, after adjusting the absolute value at  $3.700^\circ \text{ K}$  to agree with the one absolute measurement (see 3.2 below). Temperatures are given on the scale  $T_{55E}$  (Clement *et al.* 1955).

TABLE I

MEASURED VALUES OF REFRACTIVE INDEX,  $n$ , OF  $\text{He}^4$  LIQUID AT SATURATED VAPOR PRESSURE FOR  $\lambda = 5462.27 \text{ \AA}$ ; CORRESPONDING DENSITIES  $\rho_l$  CALCULATED FROM LORENZ-Lorentz LAW ASSUMING ( $N_{\text{gas}}$ ) =  $0.12454 \text{ cm}^3 \text{ MOLE}^{-1}$  AND CONSTANT; AND COEFFICIENTS OF EXPANSION,  $\beta$ , CALCULATED FROM LORENZ-Lorentz LAW

$T_{55E}$ $^\circ \text{K}$	$10^6$ $(n-1)$	$\rho_l$ $\text{g cm}^{-3}$	$10^3 \beta$ $\text{deg}^{-1}$	$T_{55E}$ $^\circ \text{K}$	$10^6$ $(n-1)$	$\rho_l$ $\text{g cm}^{-3}$	$10^3 \beta$ $\text{deg}^{-1}$
1.6	28488	.14505	-3.7	2.9	27819	.14166	+57.8
1.7	28500	.14511	-4.7	3.0	27652	.14081	62.2
1.8	28516	.14519	-6.6	3.1	27473	.13990	67.3
1.9	28539	.14530	-9.6	3.2	27281	.13893	72.4
2.0	28572	.14547	-13.4	3.3	27076	.13789	77.4
2.1	28617	.14570	-18.4	3.4	26859	.13679	82.1
2.15	28648	.14586	-27	3.5	26631	.13564	88.7
2.1735	28668	.14596	(-∞)	3.6	26385	.13439	95.6
2.2	28654	.14589	+19	3.7	26124	.13307	102.
2.3	28585	.14554	+27.9	3.8	25845	.13165	111.
2.4	28494	.14508	+35.8	3.9	25545	.13013	121.
2.5	28382	.14451	+41.9	4.0	25223	.12873	132.
2.6	28256	.14387	+45.8	4.1	24878	.12675	142.
2.7	28121	.14319	+49.7	4.2	24511	.12489	154.
2.8	27975	.14245	+53.5				

#### 3.2 Absolute Measurement

The etalon was aligned perpendicular to the emerging beam of the Jamin interferometer by autocollimation. With the refractive index cell evacuated the Jamin compensator was set to give white light fringes at  $3.7^\circ \text{ K}$ . In this condition about five or six white light fringes could be seen. Thereafter the compensator was not moved.

The cell was filled with liquid helium at 3.9° K and then cooled slowly until white light fringes could again be seen. The bath was cooled slowly and white light fringe numbers,  $N_w$ , and corresponding bath vapor pressures recorded at every white fringe for all that could be seen (about 45). There are more white fringes in this case because of the dispersion of liquid helium. The apparatus was warmed to 3.9° K and the procedure repeated, reading fringe numbers,  $N_{He}$ , for  $\lambda = 5462.27 \text{ \AA}$ , and vapor pressures over the same range of pressures.

Since the saturated vapor pressure,  $P$ , is linear in fringe number,  $N$ , over small pressure ranges, these two runs were fitted to straight lines to get  $P = (481.077 \pm 0.013) - (1.01578 \pm 0.00459)N_w$  and  $P = (483.951 \pm 0.012) - (0.99175 \pm 0.00485)N_{He}$ , where the constants, and the probable errors in the constants were calculated by least squares using formulas given by Birge (1932). Thus by equation (2.7) the "effective wavelength" of the white light,

$$\lambda_w = \frac{1.01578}{0.99175} \times 5462.27 \text{ \AA} = 5595 \pm 40 \text{ \AA}. \quad \text{The temperature of the cell at the}$$

midpoint of the white fringe pattern was  $3.700 \pm 0.010^\circ \text{ K}$ . Assuming that the achromatic fringe is at the center of the pattern this means that by equation (2.2),  $(n-1)_{5595} \text{ \AA} = 26,508 \times 10^{-6}$  and so by (2.3) and (2.6),  $(n-1)_{5595} \text{ \AA} = 26,114 \times 10^{-6}$ , and  $(n-1)_{5462.27} \text{ \AA} = 26,124 \times 10^{-6}$  at  $3.700 \pm 0.010^\circ \text{ K}$ . This result is uncertain by  $\pm 14 \times 10^{-6}$  due to the probable errors in the length of the cell and the length of the etalon;  $\pm 8 \times 10^{-6}$  due to the probable error in the effective wavelength of the white light; and  $\pm 30 \times 10^{-6}$  due to the probable error in the temperature of the cell, this error being lumped in with the refractive index error. Finally then, at  $T_{He} = 3.700^\circ \text{ K}$ , the phase index for liquid helium at  $\lambda = 5462.27 \text{ \AA}$  is given by  $n = 1.026,124 \pm 0.000035$ .

#### 4. DISCUSSION

##### 4.1 Polarizability

The polarizability per mole,  $N_0\alpha$ , may be calculated from these results by using the Lorenz-Lorentz equation

$$(4.1) \quad \frac{n^2 - 1}{n^2 + 2} = \frac{4\pi}{3M} N_0\alpha\rho_1,$$

where  $n$  = refractive index,  $M$  = molecular weight = 4.003864 g (Duckworth *et al.* 1954),  $\alpha$  = polarizability per molecule,  $N_0\alpha$  = polarizability per mole, and  $\rho_1$  = liquid density. (The use of a more complicated expression than equation (4.1), say for example equation 27 of Kirkwood (1936), only alters  $(n-1)$  by about  $2 \times 10^{-6}$ .)

Kerr (1957a) has recently determined the density of liquid He<sup>4</sup> from 1.2° K to 4.4° K with an estimated absolute accuracy (Kerr 1957b) at 3.7° K of 0.1%. Using Kerr's value  $\rho_1 = 0.13307 \text{ g cm}^{-3}$  at 3.7° K this research shows that  $(N_0\alpha) = (0.12454 \pm 0.00021) \text{ cm}^3 \text{ mole}^{-1}$  for liquid He<sup>4</sup> at 3.700° K at  $\lambda = 5462.27 \text{ \AA}$ . About half of the stated error is due to  $\rho_1$ .

Fig. 3 shows the apparent variation of  $(N_0\alpha)$  with temperature using  $(n-1)$  values from Table I and densities by Kerr (1957a). Also shown are the values of  $(N_0\alpha)$  obtained from this research using densities by Edeskuty and Sherman

(1957). Fig. 3 also includes values of  $(N_0\alpha)$  calculated using liquid densities as measured by Onnes and Boks (1924). The numerical values of Onnes and Boks densities were obtained from  $\rho_1 = 4.003864/(27.66 - 0.0047168 p)$  for

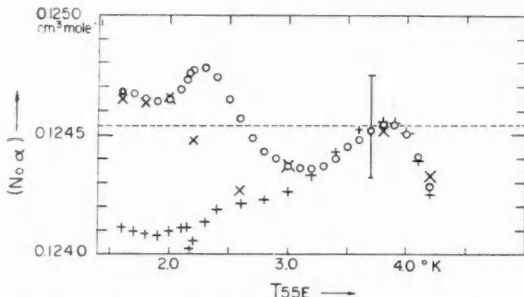


FIG. 3. Molar polarizability,  $N_0\alpha$ , of liquid  $\text{He}^4$  as a function of temperature, at  $\lambda = 5462.27 \text{ \AA}$ ; calculated from present refractive index measurements using liquid densities by Kerr (+), Edeskuyt and Sherman (X), and Onnes and Boks (O). The uncertainty in absolute value at  $3.700^\circ \text{ K}$  is indicated by the vertical line.

$p \leq 38 \text{ mm Hg}$  and  $\rho_1 = 4.003864/(27.24 + 0.0063145 p)$  for  $p > 38 \text{ mm Hg}$  where  $p$  is the saturated vapor pressure, given in mm Hg at  $20^\circ \text{ C}$ , as read from the  $T_{55E}$  temperature scale. These formulas are essentially those stated by Van Dijk and Durieux (1955) to "fit very nicely" the data of Onnes and Boks. All the density measurements are nearly identical at  $3.7^\circ \text{ K}$ , the only temperature at which  $(n-1)$  was measured absolutely.

Fig. 4 shows the apparent temperature variation of molar polarizability,  $\Delta(N_0\alpha) = (N_0\alpha)_T - (N_0\alpha)_{3.7^\circ \text{ K}}$  indicated by other workers' investigations of dielectric constant. These have all been recalculated to the  $T_{55E}$  temperature scale, using densities by Kerr (1957a). The procedure used in plotting these data normalizes the results at  $3.7^\circ \text{ K}$ . The data shown were obtained by Wolfke and Keesom (1928a, 1928b) at 0.5 Mc/s, using the absolute value of Wolfke and Onnes (1924); by Lathrop (1949), at 1.5 Mc/s; by Grebenkemper and Hagen (1950), at 9100 Mc/s; and by Maxwell *et al.* (1957), at 0.1 Mc/s. The refractive index results of Johns and Wilhelm (1938) cannot be shown on Fig. 4, as they give  $\Delta(N_0\alpha)$  of  $-32 \times 10^{-4} \text{ cm}^3 \text{ mole}^{-1}$  at  $4.22^\circ \text{ K}$ ,  $+98 \times 10^{-4} \text{ cm}^3 \text{ mole}^{-1}$  at  $2.255^\circ \text{ K}$ , and  $+86 \times 10^{-4} \text{ cm}^3 \text{ mole}^{-1}$  at  $2.142^\circ \text{ K}$ .

The question as to whether there is any temperature variation of  $(N_0\alpha)$  is a difficult one to resolve. The definitive experiment would involve filling the cell to more than saturation density and then changing the temperature, so that the liquid in the cell follows an isopycnal, meanwhile measuring the refractive index. If the refractive index did not change, the polarizability would then be strictly constant. Such an experiment was attempted, but the "dead space" in the 1.37 mm i.d. Inconel filling tube connected to the optical cell obscured the results. Only small temperature changes could be made before the dead space effects became pronounced. Nevertheless, the author believes that the present results suggest that the polarizability does remain

strictly constant from room temperature, where it is  $(0.1246 \pm 0.0002)$   $\text{cm}^3 \text{mole}^{-1}$  (calculation in Edwards 1957), down to and throughout the liquid helium temperature region, where it is  $(0.12454 \pm 0.00021)$   $\text{cm}^3 \text{mole}^{-1}$ .

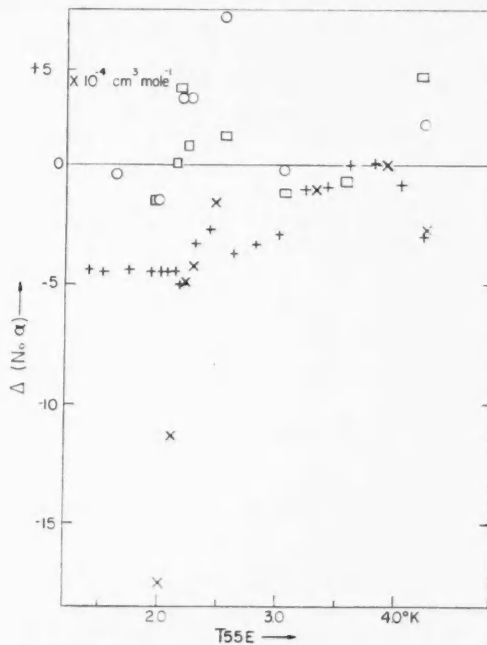


FIG. 4. Temperature variation of molar polarizability,  $\Delta(N_0\alpha) = (N_0\alpha)_T - (N_0\alpha)_{1.7^\circ\text{K}}$ , of liquid  $\text{He}^4$  from investigations of dielectric constant. ( $\square$ ) by Wolfke and Keesom; ( $\times$ ) by Lathrop; ( $\circ$ ) by Grebenkemper and Hagen; ( $+$ ) by Maxwell *et al.* Where necessary the data have been changed to the  $T_{\text{abs}}$  temperature scale; and densities by Kerr have been used throughout.

Table II shows the absolute values of molar polarizability which have been reported. All the dielectric constant results have been changed to  $\lambda = 5462.27 \text{ \AA}$  by increasing the reported values of  $(N_0\alpha)$  by  $0.0010 \text{ cm}^3 \text{mole}^{-1}$ .

TABLE II  
ABSOLUTE VALUES OF POLARIZABILITY AT  $\lambda = 5462.27 \text{ \AA}$  FOR  
LIQUID  $\text{He}^4$  AT  $3.7^\circ\text{K}$

Reference	$(N_0\alpha)$ $\text{cm}^3 \text{mole}^{-1}$
Wolfke <i>et al.</i> (1924, 1928)	$0.1211 \pm 0.0025$
Johns and Wilhelm (1938)	$0.1080 \pm 0.0061$
Lathrop (1949)	$0.1163 \pm 0.0076$
Grebenkemper and Hagen (1950)	$0.1244 \pm 0.0012$
Maxwell <i>et al.</i> (1957)	$0.1235 \pm 0.0002$
Present results	$0.12454 \pm 0.00021$

#### 4.2 Density and Coefficient of Expansion

If the polarizability remains constant, the refractive index measurements may be considered as a measurement of liquid density,  $\rho_1$ . Assuming that  $(N_0\alpha) = (0.12454 \pm 0.00021) \text{ cm}^3 \text{ mole}^{-1}$ , and constant, the Lorenz-Lorentz law, equation (4.1), has been used to calculate the liquid densities. The results of this calculation are shown in Table I. For the He II region they are nearer to Onnes and Boks' (1924) and Edeskuty and Sherman's (1957) measurements than to Kerr's (1957a). Between  $2.8^\circ$  and  $3.4^\circ$  and above  $4.0^\circ \text{ K}$  they are lower than any of the direct measurements. Whether this is due to errors in the density or the refractive index measurements, or both, is not now clear.

An expression for the coefficient of thermal expansion for liquid helium under its saturated vapor pressure,  $\beta_s = -\rho^{-1}d\rho/dT$ , may be obtained by differentiating equation (4.1) (Edwards 1956).

Thus

$$(4.2) \quad \beta_s = \beta_\alpha + \beta_n$$

where

$$(4.3) \quad \beta_\alpha = (N_0\alpha)^{-1} d(N_0\alpha)/dT$$

and

$$(4.4) \quad \beta_n = -6n(n^2-1)^{-1}(n^2+2)^{-1} dn/dT.$$

If  $(N_0\alpha)$  is independent of temperature,  $\beta_s = \beta_n$ . Using measured values of  $n$  and  $dn/dT$  from this research, the values of  $\beta_n$  given in Table I were calculated. The previously reported rapid fall of  $\beta_n$  above the  $\lambda$ -point (Edwards 1956) is again evident.

#### 4.3 The $\lambda$ -Transition

Special attention was paid to measurements of  $dn/dT$  near the  $\lambda$ -point. Temperature changes were measured using the resistance thermometer which is attached to the outside of the cell. Fringe numbers,  $N$ , and resistance readings,  $R$ , were read as the cell was slowly cooled over the  $\lambda$ -point. The  $\lambda$ -temperature,  $T_\lambda$ , was taken to be at the maximum point on the  $N-R$  curves obtained.  $dn/dT$  values were taken from these  $N-R$  curves and hence  $\beta_n$  obtained as a function of  $|T-T_\lambda|$ . It will be seen later that this procedure places  $T_\lambda$  too low by about 1 mdeg, since the density maximum actually occurs above  $T_\lambda$  (see Table III, column 4). This means that the  $\beta_n$  results of Fig. 5 should be shifted about 1 mdeg to the right for liquid He I, and to the left for liquid He II. The effect of this shift is negligible in Fig. 5 for  $|T-T_\lambda| > 10$  mdeg. It has long been known that  $\beta_s$  for liquid He II is linear in  $\log |T-T_\lambda|$  (Edwards 1953; Atkins and Edwards 1955). This research now shows (see Fig. 5) that  $\beta_n$  is linear in  $\log |T-T_\lambda|$  from about 100 mdeg to within 10 mdeg of the  $\lambda$ -point from above; and parallel to  $\beta_n$  for liquid He II on this logarithmic plot.\* Fig. 5 also shows the earlier data of  $\beta_s$  of Atkins and Edwards (1955).

\*Both J. R. Clement and J. K. Logan suggested such a plot of the He I data to the author.

TABLE III

CALCULATED EXPANSION COEFFICIENT  $\beta$ ; AND DENSITY CHANGES  $\delta\rho = \rho - \rho_0$ , USING  $\rho_0 = 0.14596 \text{ g cm}^{-3}$ , FOR LIQUID He I AND LIQUID He II NEAR THE  $\lambda$ -POINT

$T - T_\lambda$ mdeg	$10^3 \beta_I$ $\text{deg}^{-1}$	$10^3 \beta_{II}$ $\text{deg}^{-1}$	$10^5 \delta\rho_I$ $\text{g cm}^{-3}$	$10^5 \delta\rho_{II}$ $\text{g cm}^{-3}$
0	( $-\infty$ )	( $-\infty$ )	0	0
0.0001	-60.0	-103	0.00010	-0.00015
0.001	-45.5	-88.5	0.00075	-0.00134
0.01	-31.0	-74.0	0.00543	-0.0113
0.02	-26.6	-69.6	0.00959	-0.0213
0.04	-22.3	-65.3	0.0167	-0.0400
0.06	-19.7	-62.7	0.0228	-0.0578
0.08	-17.9	-60.9	0.0283	-0.0750
0.1	-16.5	-59.5	0.0333	-0.0916
0.2	-12.1	-55.1	0.0538	-0.170
0.4	-7.77	-50.8	0.0821	-0.316
0.6	-5.22	-48.2	0.101	-0.451
0.8	-3.40	-46.4	0.113	-0.580
1	-2.00	-45.0	0.121	-0.705
2	+2.36	-40.6	0.115	-1.28
4	+6.73	-36.3	-0.0253	-2.31
6	+9.28	-33.7	-0.274	-3.23
8	+11.1	-31.9	-0.560	-4.11
10	+12.5	-30.5	-0.905	-4.93
20	+16.9	-26.1	-3.08	-8.59
40	+21.2	-21.8	-8.72	-14.6
60	+23.8	-19.2	-15.3	-19.7
80	+25.6	-17.4	-22.5	-24.2
100	+27.0	-16.0	-30.2	-28.2

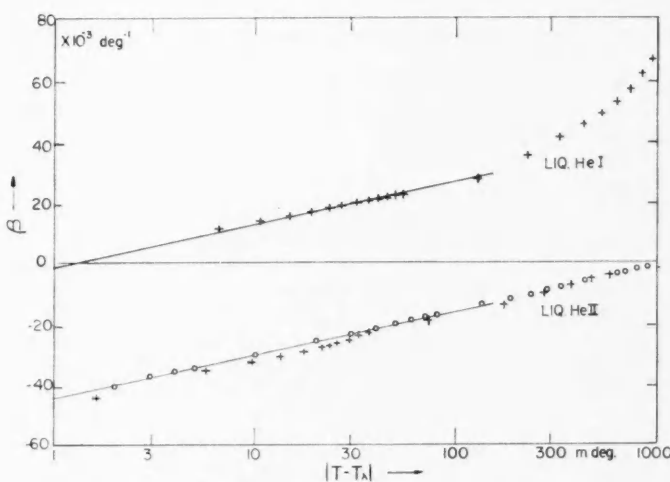


FIG. 5. Coefficient of expansion of liquid He<sup>4</sup> as a function of  $\log |T - T_\lambda|$ . (O) Atkins and Edwards (1955) values of  $\beta_e$  for liquid He II. (+) Present results for  $\beta_n$  for liquid He II and liquid He I.

For liquid He II,  $\beta_s - \beta_n$  is about  $1.5 \times 10^{-3}$  from about  $2.07^\circ$  K to the  $\lambda$ -point,  $2.1735^\circ$  K. Thus either errors in  $d\rho/dT$  of as much as 7% have been made, or  $\beta_\alpha$  is not zero. If no errors in  $d\rho/dT$  have been made, this implies an increase in  $(N_0\alpha)$  of  $2 \times 10^{-5} \text{ cm}^3 \text{ mole}^{-1}$  between  $2.07^\circ$  and  $2.1735^\circ$  K. Neither possibility can be ruled out entirely at present.

The expansion coefficient data of Fig. 5 may be represented within the experimental error by the two equations

$$(4.5) \quad 10^3 \beta_I = +41.5 + 14.5 \log |T - T_\lambda|$$

for  $T > T_\lambda$  from about  $0.1^\circ$  above  $T_\lambda$  to within  $0.010^\circ$  of  $T_\lambda$ ; and by

$$(4.6) \quad 10^3 \beta_{II} = -1.5 + 14.5 \log |T - T_\lambda|$$

for  $T < T_\lambda$  from about  $0.1^\circ$  below  $T_\lambda$  to within  $0.002^\circ$  of  $T_\lambda$ . Table III gives values of  $\beta_I$  and  $\beta_{II}$  as calculated by equations (4.5) and (4.6) near the  $\lambda$ -point, assuming that equations (4.5) and (4.6) are valid right up to the  $\lambda$ -point. It will be seen that equations (4.5) and (4.6) suggest that  $\beta_I$  becomes negative about 1 mdeg above  $T_\lambda$ , and that both  $\beta_I$  and  $\beta_{II}$  decrease logarithmically to minus infinity at  $T_\lambda$ . This implies that the density-temperature curve has both a vertical tangent and a point of inflection at the  $\lambda$ -point; and that there is a maximum in density about 1 mdeg above the  $\lambda$ -point. Equations (4.5) and (4.6) may be integrated to give density changes within about  $0.1^\circ$  of  $T_\lambda$ . The results are:

$$(4.7) \quad 10^3 \delta\rho_I/\rho_\lambda = -41.5|T - T_\lambda| - 14.5|T - T_\lambda|(\log |T - T_\lambda| - 0.434294)$$

for  $T > T_\lambda$ , and

$$(4.8) \quad 10^3 \delta\rho_{II}/\rho_\lambda = +1.5|T - T_\lambda| + 14.5|T - T_\lambda|(\log |T - T_\lambda| - 0.434294)$$

for  $T < T_\lambda$ . In equations (4.7) and (4.8),  $\delta\rho$  means  $\rho - \rho_\lambda$ , and  $\rho_\lambda$  may be taken to be  $0.14596 \text{ g cm}^{-3}$  (see Table I). Values of  $\delta\rho$  calculated from these equations, for various values of  $|T - T_\lambda|$ , are shown in Table III. Fig. 6 shows the predicted variation of density in the immediate vicinity of the  $\lambda$ -point. The previously unreported density maximum above  $T_\lambda$  should be noted. On this picture, the  $\lambda$ -point is a point of inflection in the density-temperature curve, at which coefficient of expansion makes a discontinuous change.

Ehrenfest's treatment of the  $\lambda$ -transition as a second order phase transition (Ehrenfest 1933; Keesom 1942, p. 255) relates the slope of the  $\lambda$ -line, at the saturated vapor pressure curve, to the "discontinuities"  $\Delta C$ ,  $\Delta\beta$ , and  $\Delta k$  in specific heat, coefficient of expansion, and isothermal compressibility over the  $\lambda$ -point. Ehrenfest's two relations give, as the slope of the  $\lambda$ -line,

$$(4.9) \quad (dP/dT)_\lambda = \rho \Delta C / T \Delta \beta$$

and

$$(4.10) \quad (dP/dT)_\lambda = \Delta\beta / \Delta k$$

where, as Keesom (1933) has shown, the quantities  $C$ ,  $\beta$ , and  $k$  may be measured for the liquid under its saturated vapor pressure. The quantity  $\Delta\beta$  was taken to mean the (assumed finite) value  $\beta_{II} - \beta_I$ , where the suffixes II and I refer

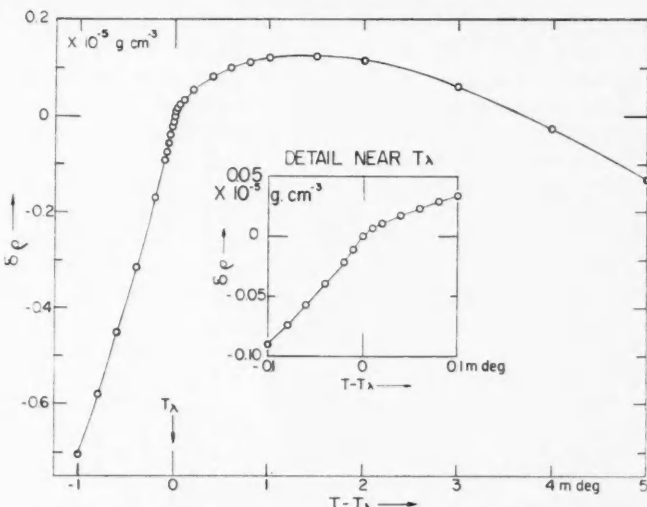


FIG. 6. Variation of density of liquid  $\text{He}^4$  with temperature in the vicinity of the  $\lambda$ -point. The inset shows the last  $10^{-4}$  K in greater detail.

to the helium II and helium I conditions, in the immediate vicinity of the  $\lambda$ -point. The difficulty of assigning actual numerical values to any of these rapidly varying quantities "at" the  $\lambda$ -point has long been known. However, Keesom (1936) has shown that equations (4.8) and (4.9) are still valid provided that  $\Delta C$ ,  $\Delta\beta$ , and  $\Delta k$  are taken relative to the same interval of temperature about the  $\lambda$ -point.

Fig. 5, and equations (4.5) and (4.6) show that if by  $\Delta\beta$  we understand  $(\beta_{II} - \beta_I)$  taken at  $|T - T_\lambda| = \text{const.}$ , for  $|T - T_\lambda| < 0.1^\circ\text{K}$ ; then  $\Delta\beta = -43 \text{ deg}^{-1}$ . In view of the errors in  $\beta_1$  and  $\beta_{II}$  this difference is probably uncertain by  $\pm 3 \text{ deg}^{-1}$ .

Fairbank, Buckingham, and Kellers (1956, 1957) have shown that when the specific heat of liquid  $\text{He}^4$  is plotted against  $\log |T - T_\lambda|$ , that from about  $0.1^\circ$  from  $T_\lambda$  to within  $10^{-4}$  deg of  $T_\lambda$ , two similar lines result, separated by  $5.6 \text{ joule g}^{-1} \text{ deg}^{-1}$ .

Using  $\Delta C = 5.6 \text{ joule g}^{-1} \text{ deg}^{-1}$ ,  $\Delta\beta = -(43 \pm 3) \times 10^{-3} \text{ deg}^{-1}$ ,  $\rho_\lambda = 0.14596 \text{ g cm}^{-3}$ , and  $T_\lambda = 2.1735^\circ\text{K}$ , equation (4.9) suggests that  $(dP/dT)_\lambda = -(86 \pm 6) \text{ atm deg}^{-1}$ . The stated uncertainty is due to the uncertainty in  $\Delta\beta$ .

The early data on the slope of the  $\lambda$ -line gave  $(dP/dT)_\lambda = -80.8 \text{ atm deg}^{-1}$ . Keesom (1942, p. 256) calculated this value by drawing a line on the  $P-T$  diagram of  $\text{He}^4$  connecting the temperatures of specific heat maxima, measured above 6 atmospheres by Keesom and Clusius (1931), to the vapor pressure curve at  $2.19^\circ\text{K}$ , which Keesom took to be the  $\lambda$ -point.

Peshkov and Zinov'yeva (1948) determined points on the  $\lambda$ -line by locating "resistance jumps" in a phosphor bronze thermometer inside their second-sound copper pressure cell. They published only a small graph of their results,

which suggests that  $(dP/dT)_\lambda$  is nearer  $-90 \text{ atm deg}^{-1}$ . They show no points between 3 atm and the saturated vapor pressure however.

At the moment it appears that the Ehrenfest relation (4.9) correctly relates  $(dP/dT)_\lambda$ ,  $\Delta C$ , and  $\Delta\beta$  provided we evaluate  $\Delta C$  and  $\Delta\beta$  at equal intervals on either side of the  $\lambda$ -point. However, a redetermination of the slope of the  $\lambda$ -line should be made, to check this point.

If equation (4.10) also holds, then the present results suggest that the isothermal compressibility,  $k$ , is also logarithmic in  $\log |T - T_\lambda|$  near the  $\lambda$ -point. It is nearly so for He II (see values in Table II of Atkins and Edwards 1955). Equation (4.9) also shows that  $\Delta k = 5.0 \times 10^{-4} \text{ atm}^{-1}$ . This means that at 10 mdeg above the  $\lambda$ -point,  $k$  is about 3.4% lower than at 10 mdeg below the  $\lambda$ -point. It may be difficult to check this by direct measurement.

Near the  $\lambda$ -point,  $\gamma$ , the ratio of specific heats at constant pressure and constant volume, may be obtained from

$$(4.11) \quad \gamma - 1 = Tu_1^2 \beta^2 / C$$

where  $u_1$  is the velocity of ordinary sound, and each of the quantities is evaluated at the saturated vapor pressure. Fig. 7 and Table IV show the results

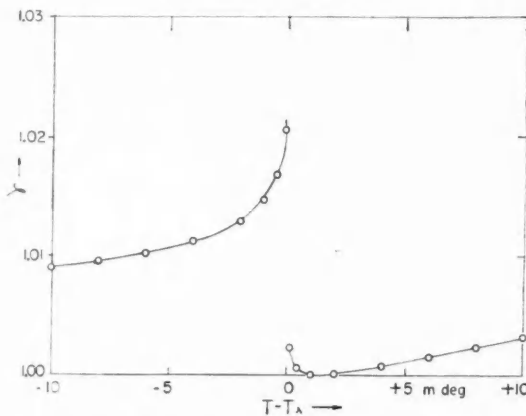


FIG. 7. Ratio of specific heats,  $\gamma$ , of liquid  $\text{He}^4$  near the  $\lambda$ -point.

TABLE IV  
RATIO OF SPECIFIC HEATS,  $\gamma$ , NEAR THE  $\lambda$ -POINT

$ T - T_\lambda $ mdeg	$10^3 (\gamma - 1)$ for He I	$10^3 (\gamma - 1)$ for He II
0.1	2.31	20.6
0.4	0.620	17.0
1	0.048	14.7
2	0.076	12.9
4	0.711	11.2
6	1.49	10.3
8	2.28	9.60
10	3.07	9.07

for 10 mdeg on each side of the  $\lambda$ -point. Values of  $u_1$  were taken from Chase (1957); of  $\beta$  from this research; and of  $C$  from Fairbank *et al.* (1957). Below the  $\lambda$ -point the results are about 10% higher than calculated by Atkins and Edwards (1955, Table II), owing to their use of erroneous  $C$  values from Hercus and Wilks (1954). It is interesting to note that  $\gamma - 1$  is very nearly zero about 1 mdeg above  $T_\lambda$ , but increases again as  $T_\lambda$  is approached from above. The interesting approximate linearity of  $\gamma$  with  $T - T_\lambda$  noted by Atkins and Stasior (1953) for liquid He I at 19 atm pressure is also found here, for  $|T - T_\lambda| > 2$  mdeg.

It should be emphasized that the coefficient of expansion data from this research, on which many of these calculations have been based, only extends down to within about 10 mdeg of  $T_\lambda$  from above, and to within 2 mdeg of  $T_\lambda$  from below. Thus the results closer to  $T_\lambda$  depend upon the validity of the extrapolation of equations (4.5) and (4.6). The further assumption that the molar polarizability ( $N_{0\alpha}$ ) remains constant and equal to  $0.12454 \text{ cm}^3 \text{ mole}^{-1}$  has also been made.

#### ACKNOWLEDGMENTS

The author is grateful to Mr. A. J. Filmer, Dr. R. A. Aziz, and Mr. R. Khan, who have assisted with temperature measurements during some of the runs. He is also grateful to Dr. G. R. Hanes for many helpful discussions concerning the optical problems.

#### REFERENCES

- ATKINS, K. R. and EDWARDS, M. H. 1955. Phys. Rev. **97**, 1429.
- BIRGE, R. T. 1932. Phys. Rev. **40**, 207.
- CANDLER, C. 1950. Modern interferometers (Hilger and Watts Ltd., London).
- CHASE, C. E. 1957. Proc. Fifth International Conference on Low Temp. Phys., Madison, Wis., Paper 33-3.
- CLEMENT, J. R., LOGAN, J. K., and GAFFNEY, J. 1955. Phys. Rev. **100**, 743, "Note added in proof."
- CUTHBERTSON, C. and CUTHBERTSON, M. 1932. Proc. Roy. Soc. London, A, **135**, 40.
- DUCKWORTH, H. E., HOGG, B. G., and PENNINGTON, E. M. 1954. Revs. Mod. Phys. **26**, 463.
- EDESKUTY, F. E. and SHERMAN, R. H. 1957. Proc. Fifth International Conference on Low Temp. Phys., Madison, Wis., Paper 15-3; and private communication.
- EDWARDS, M. H. 1953. Ph.D. Thesis, University of Toronto, Toronto, Ontario.
- 1956. Can. J. Phys. **34**, 898.
- 1957. Phys. Rev. **108**, 1243.
- EDWARDS, M. H. and HANES, G. R. 1957. Proc. Fifth International Conference on Low Temp. Phys., Madison, Wis., Paper 10-3.
- EHRENFEST, P. 1933. Leiden Comm. Suppl. No. 75b; Proc. Roy. Acad. Amsterdam, **36**, 153.
- FAIRBANK, W. M., BUCKINGHAM, M. J., and KELLERS, C. F. 1957. Bull. Am. Phys. Soc. Ser. II, **2**, 183; Proc. Fifth International Conference on Low Temp. Phys., Madison, Wis., Paper 6-1.
- GREBENKEMPER, C. J. and HAGEN, J. P. 1950. Phys. Rev. **80**, 89.
- HERCUS, G. R. and WILKS, J. 1954. Phil. Mag. **45**, 1163.
- JOHNS, H. E. and WILHELM, J. O. 1938. Can. J. Research, A, **16**, 131.
- KESOM, W. H. 1933. Leiden Comm. Suppl. No. 75a; Proc. Roy. Acad. Amsterdam, **36**, 147.
- 1936. Leiden Comm. Suppl. No. 80b.
- 1942. Helium (Elsevier, Amsterdam).
- KESOM, W. H. and CLUSIUS, K. 1931. Leiden Comm. No. 216b; Proc. Roy. Acad. Amsterdam, **34**, 605.
- KERR, E. C. 1957a. J. Chem. Phys. **26**, 511.
- 1957b. Private communication.
- KIRKWOOD, J. G. 1936. J. Chem. Phys. **4**, 492.
- LATHROP, A. 1949. O.N.R. Annual Progress Report of the Rice Institute (unpublished).

- MAXWELL, E., CHASE, C. E., and MILLETT, W. E. 1957. Proc. Fifth International Conference on Low Temp. Phys., Madison, Wis., Paper 10-2.
- ONNES, H. K. and BOKS, J. D. A. 1924. Leiden Comm. No. 170b.
- PESHKOV, V. P. and ZINOV'YEVA, K. N. 1948. Zhurnal Eksper. i Teoret. Fiziki U.S.S.R. **18**, 438.
- SATTERLY, J. 1936. Revs. Mod. Phys. **8**, 347.
- VAN DIJK, H. and DURIEUX, M. 1955. Helium vapour pressure scale  $T_{LBB}$  (Leiden), p. 17.
- WOLFKE, M. and KEESOM, W. H. 1928a. Leiden Comm. No. 190a; Proc. Roy. Acad. Amsterdam, **31**, 81.
- 1928b. Leiden Comm. No. 192a; Proc. Roy. Acad. Amsterdam, **31**, 800.
- WOLFKE, M. and ONNES, H. K. 1924. Leiden Comm. No. 171b; Proc. Roy. Acad. Amsterdam, **27**, 621.

# DIFFUSION IN MULTICOMPONENT METALLIC SYSTEMS

## I. PHENOMENOLOGICAL THEORY FOR SUBSTITUTIONAL SOLID SOLUTION ALLOYS<sup>1</sup>

J. S. KIRKALDY<sup>2</sup>

### ABSTRACT

Onsager's generalization of Fick's law for diffusion in multicomponent systems is examined with a view to determining the conditions imposed on the diffusion coefficients by the second law of thermodynamics and by "microscopic reversibility." The generalized differential equations with constant coefficients, obtained by combining Fick's law and the continuity equations, are solved for the boundary conditions corresponding to the semi-infinite diffusion couple.

### INTRODUCTION

Onsager (1945-46) proposed as a logical extension of Fick's law (Fick 1855) that the diffusion currents in a multicomponent system can be represented as linear functions of all the concentration gradients, viz.,

$$(1) \quad J_i = - \sum_{k=1}^n D'_{ik} \nabla C_k, \quad (i = 1, 2, \dots, n)$$

where the  $D'_{ik}$  are functions of all the  $C_k$ . A number of authors, including Onsager and Fuoss (1932) and Darken (1951), have suggested that the alternative phenomenological description

$$(2) \quad J_i = - \sum_{k=1}^n M_{ik} \nabla \mu_k,$$

where the  $\mu_k$  are the chemical potentials, is more fundamental since the forces for diffusion are represented as free energy gradients. Onsager (1945-46) has also used the inverse form of this,

$$(3) \quad \nabla \mu_i = - \sum_{k=1}^n R_{ik} J_k,$$

where the matrix  $[R_{ik}]$  is assumed to be the "reciprocal" of  $[M_{ik}]$ . Since, however, for diffusion in substitutional alloys we usually ignore volume changes of mixing and assume the conservation of lattice sites, the  $J_i$ , as referred to a stationary lattice outside the diffusion zone, are linearly related by

$$(4) \quad \sum_{i=1}^n J_i = 0$$

so that  $[M_{ik}]$  is singular.\* Accordingly, the matrix inversion is not, in general, valid.

<sup>1</sup>Manuscript received April 9, 1958.

Contribution from the Department of Metallurgical Engineering, McGill University, Montreal, Quebec; and from the Department of Metallurgy and Metallurgical Engineering, Hamilton College, McMaster University, Hamilton, Ontario.

<sup>2</sup>Present address: McMaster University, Hamilton, Ontario.

\*The existence of marker movement in the diffusion zone (Kirkendall effect) does not invalidate this analysis. It is, however, incomplete as indicated in paper III (Kirkaldy 1958).

De Groot (1952) has noted the consequences of the second law of thermodynamics and equation (4) as applied to (2), viz.,

$$(5) \quad \sum_{k=1}^n M_{ik} = 0$$

and

$$(6) \quad \sum_{i=1}^n M_{ik} = 0.$$

The statistical mechanics of irreversible processes based on the early work of Onsager (1931) and reviewed by de Groot (1952) leads to the principle of "microscopic reversibility," a consequence of which is that  $[M_{ik}]$  is symmetric, i.e.,

$$(7) \quad M_{ik} = M_{ki}.$$

Further restrictions are imposed on the coefficients by the second law of thermodynamics which states that the rate of entropy production is positive definite. In the following sections we shall discuss Onsager's derivation of the reciprocal relations applicable to the  $D'_{ik}$  and the restrictions imposed on the  $M_{ik}$  and the corresponding diffusion coefficients by the second law.

While relation (2) is fundamental, equation (1) is most convenient for mathematical manipulation and for application to specific boundary conditions. It is for these reasons that an effort is made to relate (1) to the other.

If the concentrations are in such units that

$$(8) \quad \sum_{i=1}^n C_i = \text{constant}$$

then equation (1) can be written as

$$(1a) \quad J_i = - \sum_{k=1}^{n-1} D_{ik} \nabla C_k,$$

where  $D_{ik} = D'_{ik} - D'_{ki}$ . As a consequence of (4) the  $D_{ik}$  satisfy relations of the form

$$(9) \quad \sum_{i=1}^n D_{ik} = 0.$$

If, finally, we combine (1a) with the continuity equations,

$$(10) \quad \text{div } J_i + \frac{\partial C_i}{\partial t} = 0,$$

we obtain the generalized differential equation

$$(11) \quad \frac{\partial C_i}{\partial t} = \sum_{k=1}^{n-1} \nabla \cdot (D_{ik} \nabla C_k).$$

In a later section, solutions of (11) for the boundary conditions corresponding to the semi-infinite diffusion couple will be given.

#### THE CONSEQUENCES OF MICROSCOPIC REVERSIBILITY

Following a procedure suggested originally by Onsager (1945-46) and later

clarified by Hooyman (1956), it is possible to obtain certain relationships between the  $D_{ik}$  corresponding to the reciprocal relations (7). Writing

$$(12) \quad J_k = - \sum_{j=1}^n M_{kj} \sum_{i=1}^{n-1} \mu_{ji} \nabla C_i = - \sum_{i=1}^{n-1} D_{ki} \nabla C_i$$

where

$$(13) \quad \mu_{ik} = \frac{\partial \mu_i}{\partial C_k}$$

gives

$$(14) \quad D_{ki} = \sum_{j=1}^n M_{kj} \mu_{ji}, \quad (i, k = 1, 2, \dots, n-1).$$

Now as a consequence of the reciprocal relations (7), the equality

$$(15) \quad \sum_{j, l=1}^n \mu_{ji} M_{jl} \mu_{lk} = \sum_{j, l=1}^n \mu_{jk} M_{jl} \mu_{li}$$

exists, so that

$$(16) \quad \sum_{j=1}^n D_{jk} \mu_{ji} = \sum_{j=1}^n \mu_{jk} D_{ji}, \quad (i, k = 1, 2, \dots, n-1).$$

Onsager originally presented the same expression relating the  $D'_{ik}$ .\* His result is only valid for a system in which the  $n$  diffusion currents are independent, so it has little practical value. In Hooyman's approach, both phenomenological equations (1) and (2) contain  $n-1$  terms in the linear expansion. He has shown that if the frame of reference is chosen such that  $J_n = 0$ , then the relations (16) take the shorter form

$$(17) \quad \sum_{j=1}^{n-1} D_{jk} \mu_{ji} = \sum_{j=1}^{n-1} \mu_{jk} D_{ji}, \quad (i, k = 1, 2, \dots, n-1).$$

In the more usual reference system in which the mean flow is zero, the corresponding relations contain a transformation matrix. We prefer to refer all diffusion currents to a frame at rest with respect to a fixed lattice network and to obtain an equivalent elimination of coefficients by application to equation (16) of

$$(9a) \quad D_{nk} = - \sum_{j=1}^{n-1} D_{jk}, \quad (k = 1, 2, \dots, n-1)$$

and the modified Gibbs-Duhem relations

$$(18) \quad \mu_{ni} = - \sum_{l=1}^{n-1} \frac{C_l}{C_n} \mu_{li}, \quad (i = 1, 2, \dots, n-1).$$

This gives

$$(19) \quad \sum_{j, l=1}^{n-1} D_{jk} \left( \delta_{lj} + \frac{C_l}{C_n} \mu_{li} \right) \mu_{ji} = \sum_{j, l=1}^{n-1} D_{ji} \left( \delta_{lj} + \frac{C_l}{C_n} \mu_{lk} \right) \mu_{jk}, \quad (i, k = 1, 2, \dots, n-1),$$

where  $\delta_{lj}$  is the Krönecker  $\delta$ .

\*Onsager's result, which has been previously quoted by the author (1957) and Darken (1951), has the subscripts to the  $\mu$ 's erroneously reversed.

## CONSEQUENCES OF THE SECOND LAW OF THERMODYNAMICS

We note with de Groot (1952) that the second law of thermodynamics imposes the condition that the rate of entropy production in a diffusive process be positive definite, i.e.,

$$(20) \quad \Delta S = - \sum_{i=1}^n J_i \cdot \nabla \mu_i \geq 0.$$

Substituting from (2) this becomes

$$(21) \quad \sum_{i,k=1}^n M_{ik} \nabla \mu_i \cdot \nabla \mu_k \geq 0.$$

According to de Groot (1952) the necessary conditions that the inequality be satisfied are that

$$(22) \quad M_{ii} \geq 0$$

and

$$(23) \quad M_{ii} M_{kk} \geq M_{ik} M_{ki} \quad (i, k = 1, 2, \dots, n).$$

To find corresponding relations involving the  $D$ 's, we consider the case  $n = 3$  and calculate the quantity

$$(24) \quad \mathcal{D} = D_{11} D_{22} - D_{12} D_{21}.$$

Substituting from (14) and using relations (5) and the modified Gibbs-Duhem relations (18), we can show that

$$(25) \quad \mathcal{D} = \frac{C_1 + C_2 + C_3}{C_3} (\mu_{11}\mu_{22} - \mu_{12}\mu_{21}) (M_{11}M_{22} - M_{12}M_{21}).$$

Prigogine and Defay (1954) have stated that for systems in states which are "stable with respect to diffusion," i.e., which show no tendency towards spontaneous concentration discontinuities such as in the precipitation of new phases,

$$(26) \quad \frac{\partial \mu_1}{\partial N_1} \frac{\partial \mu_2}{\partial N_2} \geq \frac{\partial \mu_1}{\partial N_2} \frac{\partial \mu_2}{\partial N_1}$$

where the  $N$ 's are the number of moles of each component in the system. If we note as well that

$$(27) \quad \mu_i = \mu_i(C_1, C_2) = \mu_i \left( \frac{N_1}{N_1 + N_2 + N_3}, \frac{N_2}{N_1 + N_2 + N_3} \right),$$

where the concentrations are in mole fractions, we can then show that

$$(28) \quad \mu_{11} \mu_{22} - \mu_{12} \mu_{21} \geq 0.$$

It follows therefore as a consequence of (23) and (28) that a necessary condition for consistency between the 3-component phenomenological theory and the second law is that

$$(29) \quad D_{11} D_{22} - D_{12} D_{21} \geq 0.$$

An attempt has been made to show that there exists a necessary condition corresponding to (22) such that

$$(30) \quad D_{ii} \geq 0.$$

The application of the Gibbs-Duhem relations and the conditions (Prigogine and Defay 1954)

$$(31) \quad \frac{\partial \mu_i}{\partial N_i} \geq 0 \quad \text{and} \quad \frac{\partial \mu_i}{\partial N_k} = \frac{\partial \mu_k}{\partial N_i}$$

to equation (14) does not, however, lead to a definitive result and it appears that we require further theoretical information about the thermodynamic functions if (30) is to be proved. For the moment, we can state only that  $D_{ii} \geq 0$  provided the off-diagonal elements in  $[M_{ik}]$  and  $[\mu_{ik}]$  are sufficiently small in absolute value. These conditions can be relaxed somewhat in proportion to the increasing diluteness of the first  $n-1$  components.

#### SOLUTION OF THE ONE-DIMENSIONAL DIFFUSION EQUATION FOR THE SEMI-INFINITE DIFFUSION COUPLE

If the initial condition for each component consists of a linear step-function at the origin, i.e.,

$$(32) \quad C_i(x, 0) = C_{i0}, \quad x > 0$$

and

$$(33) \quad C_i(x, 0) = C_{in}, \quad x < 0,$$

then there exist solutions of the parametric form (Gosting and Fujita 1956; Kirkaldy 1957),

$$(34) \quad C_i = C_i(\lambda)$$

where

$$(35) \quad \lambda = x/\sqrt{t}.$$

This substitution in the one-dimensional form of (11) leads to the ordinary equations

$$(36) \quad -\frac{\lambda}{2} \frac{dC_i}{d\lambda} = \sum_{k=1}^{n-1} \frac{d}{d\lambda} \left[ D_{ik} \frac{dC_k}{d\lambda} \right],$$

which have, for constant coefficients, the solutions

$$(37) \quad C_i = a_{i0} + \sum_{k=1}^{n-1} a_{ik} \operatorname{erf} \frac{\lambda}{2\sqrt{u_k}}.$$

By direct substitution we obtain the indicial equations

$$(38) \quad u_k = \sum_{j=1}^{n-1} \frac{a_{jk}}{a_{ik}} D_{ij}.$$

This set uniquely determines the  $u_k$  in terms of the diffusion coefficients and provides a further  $(n-1)^2 - (n-1)$  independent relation between the  $a_{ik}$ . When these are combined with the  $2(n-1)$  boundary values, the  $(n-1)^2 + (n-1)$   $a$ -coefficients are uniquely determined.

The special case  $n = 3$ , which has been treated previously by Gosting and Fujita (1956), has the solutions

$$(39) \quad C_1 = a \operatorname{erf} \frac{\lambda}{2\sqrt{u}} + b \operatorname{erf} \frac{\lambda}{2\sqrt{v}} + c$$

and

$$(40) \quad C_2 = d \operatorname{erf} \frac{\lambda}{2\sqrt{u}} + e \operatorname{erf} \frac{\lambda}{2\sqrt{v}} + f$$

where

$$a = \frac{1}{2D} \left\{ D_{12}(C_{20} - C_{21}) - [(D_{22} - D_{11}) - D] \frac{(C_{10} - C_{11})}{2} \right\},$$

$$b = \frac{1}{2} \{ C_{10} - C_{11} - 2a \},$$

$$c = \frac{1}{2} \{ C_{10} + C_{11} \},$$

$$d = \frac{1}{2D} \left\{ D_{21}(C_{10} - C_{11}) - [(D_{11} - D_{22}) - D] \frac{(C_{20} - C_{21})}{2} \right\},$$

$$e = \frac{1}{2} \{ C_{20} - C_{21} - 2d \},$$

$$f = \frac{1}{2} \{ C_{20} + C_{21} \},$$

$$u = D_{11} + \frac{1}{2} \{ (D_{22} - D_{11}) + D \},$$

$$v = D_{22} + \frac{1}{2} \{ (D_{11} - D_{22}) - D \},$$

$$D = \sqrt{(D_{11} - D_{22})^2 + 4D_{12}D_{21}}.$$

Provided  $D_{11}$  and  $D_{22}$  are positive, physically significant solutions exist only for

$$(41) \quad -\frac{1}{4}(D_{11} - D_{22})^2 < D_{12}D_{21} < D_{11}D_{22}$$

since at the lower bound the radical  $D$  becomes imaginary while at the upper bound  $\sqrt{v}$  becomes imaginary. This mathematical limitation has the significance that any set of data, which cannot be fitted by solutions of (11), must be analyzed with a higher order phenomenological scheme. It is interesting to note that the upper bound of (41) corresponds exactly to that required for consistency with the second law of thermodynamics, inequality (29).

Solutions (39) and (40) suggest several cases of special interest:

*Case 1:* For  $D_{11} = D_{22}$  and  $D_{21} = 0$ , the coefficients  $a, b, e$ , and  $f$  are indeterminate, but by a limiting procedure we can show that

$$(42) \quad C_1 = \frac{C_{10} - C_{11}}{2} \operatorname{erf} \frac{\lambda}{2\sqrt{D_{11}}} - \frac{C_{20} - C_{21}}{2} \frac{D_{12}}{2\sqrt{\pi D_{11}}^{3/2}} \lambda \exp \left[ -\frac{\lambda^2}{4D_{11}} \right] + \frac{C_{10} + C_{11}}{2}$$

and

$$(43) \quad C_2 = \frac{C_{20} - C_{21}}{2} \operatorname{erf} \frac{\lambda}{2\sqrt{D_{11}}} + \frac{C_{20} + C_{21}}{2}.$$

*Case 2:* There appear to be many physically acceptable choices for the  $D$ 's and the boundary  $C$ 's for which the equations give negative concentrations in the distribution. While these must clearly be excluded from the present calculations, they may correspond to real physical situations, in which case new principles will have to be developed for them. The special case when one of the initial concentrations goes to zero while the off-diagonal coefficients remain non-zero must always be excluded. This case should, of course, be treated with the theory for one less component. For a similar reason, radioactive tracer measurements with a low concentration tracer species may have to be excluded from this description.

*Case 3:* For coefficients which cause the upper bound of inequality (41) to be approached, the quantity  $\sqrt{v}$  tends to zero which leads to a discontinuity in both concentration distributions. The results of Darken (1949) may be interpreted as just such a case (see later section).

#### SOLUTIONS FOR OTHER BOUNDARY CONDITIONS

The parametric solution (34) exists only for conditions (32) and (33). If, however, all the  $D_{ik}$  are constant then (36) is a linear set, so we can obtain solutions for any initial condition which can be represented as a sum (finite or infinite) of step functions of type (32) and (33). Jost (1952) and Barrer (1951) have compiled important solutions of this type for binary systems.

#### RE-EXAMINATION OF DARKEN'S EXPERIMENTAL RESULTS FOR IRON, CARBON, SILICON

In a previous communication (Kirkaldy 1957), an approximate solution of (11) was fitted to the results of Darken (1949) for the diffusion of carbon (component 1) in iron in the presence of a silicon (component 2) gradient. The initial conditions for the diffusion couple tested were

$$\begin{aligned} C_1(x > 0, 0) &= 0.441\% \\ C_1(x < 0, 0) &= 0.478\% \\ C_2(x > 0, 0) &= 0.05\% \\ C_2(x < 0, 0) &= 3.89\% \end{aligned}$$

and the penetration curve after annealing for 13 days at  $1050^\circ\text{C}$  was as shown by the points of Fig. 1. If, contrary to the previous communication, we interpret these results as showing a sharp discontinuity at the origin, then it must be that

$$(44) \quad D_{11} D_{22} \cong D_{12} D_{21}.$$

If we take  $D_{22} = 0.1 \times 10^{-7}$  (as given by Smithells 1955 for diffusion of Si in Fe) and fit (39) to the experimental results in such a way that (44) is adhered to, we obtain the discontinuous solid curve of Fig. 1. This curve specifies the coefficients  $D_{11} = 4.8 \times 10^{-7}\text{ cm}^2/\text{sec}$ ,  $D_{12} = 0.34 \times 10^{-7}\text{ cm}^2/\text{sec}$ , and from (44),  $D_{21} = 1.4 \times 10^{-7}\text{ cm}^2/\text{sec}$ . In agreement with our earlier statement we see that the values of  $D_{11}$  and  $D_{12}$  have not been affected noticeably by the change in the values of the other coefficients from  $D_{22} = 0.023 \times 10^{-7}$  and  $D_{21} = 0$ . While

this new fit appears to be appreciably better than the old one, the accuracy of the data in the critical region near the origin does not justify a choice one way or the other. It would therefore appear to be very worthwhile to examine the system more thoroughly experimentally, with emphasis on both the carbon and the silicon distributions near the origin.

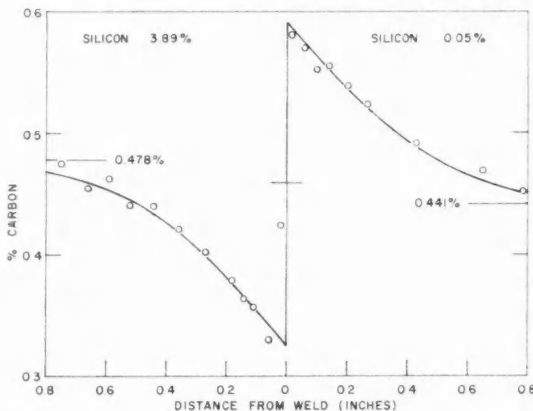


FIG. 1. Penetration curve for carbon in an iron, carbon, silicon diffusion couple. Experimental points after Darken (1949).

#### ACKNOWLEDGMENTS

The author is greatly indebted to Dr. J. W. Lorimer of the Atlantic Regional Laboratory of the National Research Council for his careful criticism of the original manuscript and to Professor P. R. Wallace of McGill University for several helpful discussions.

#### REFERENCES

- BARRER, R. M. 1951. Diffusion in and through solids (Cambridge University Press, Cambridge).
- DARKEN, L. S. 1949. AIME Trans. **180**, 430.
- 1951. Atom movements (American Society for Metals, Cleveland).
- DE GROOT, S. R. 1952. Thermodynamics of irreversible processes (Interscience, New York).
- FICK, A. 1855. Pogg. Ann. **94**, 59.
- GOSTING, L. J. and FUJITA, H. 1956. J. Am. Chem. Soc. **78**, 1099.
- HOODYMAN, G. J. 1956. Physica, **22**, 751.
- JOST, W. 1952. Diffusion in solids, liquids, gases (Academic Press Inc., New York).
- KIRKALDY, J. S. 1957. Can. J. Phys. **35**, 435.
- 1958. Can. J. Phys. **36**, 917.
- ONSAGER, L. 1931. Phys. Rev. **37**, 405.
- 1931. Phys. Rev. **38**, 2265.
- 1945-6. Ann. N.Y. Acad. Sci. **46**, 241.
- ONSAGER, L. and FUOSS, R. M. 1932. J. Phys. Chem. **36**, 2689.
- PRIGOGINE, I. and DEFAY, R. 1954. Chemical thermodynamics (Longmans Green and Co., London).
- SMITHILLS, C. J. 1955. Metals reference book (Butterworth Scientific Publications, London).

## DIFFUSION IN MULTICOMPONENT METALLIC SYSTEMS

### II. SOLUTIONS FOR TWO-PHASE SYSTEMS WITH APPLICATIONS TO TRANSFORMATIONS IN STEEL<sup>1</sup>

J. S. KIRKALDY<sup>2</sup>

#### ABSTRACT

The generalized differential diffusion equation for multicomponent systems with constant coefficients is solved for an advancing linear, cylindrical, or spherical two-phase interface. Representative numerical calculations for ternary alloys based on the iron, carbon system demonstrate how inhibition of the transformation austenite to ferrite + carbide can occur through the requirement of maintaining (extrapolated) equilibrium at the interface and through the interaction of carbon atoms with the off-diagonal gradients in the diffusion matrix. It is proposed that these interactions are the primary cause of hardenability effects in steel.

#### INTRODUCTION

In a recent review, Mehl and Hagel (1956) have examined the position of our theoretical understanding of the effect of alloying elements on the austenite to pearlite transformation rate in steel. They currently support the view that the observed inhibitions are connected with the relatively slow diffusion rates of the alloying elements as compared to that of carbon. The early work of Wells and Mehl (1941) demonstrated that the inhibiting effect was not, as might be thought, due to a reduction in the carbon diffusion coefficients. Other experiments by Bowman and Parke (1944), showing a partition of alloying elements between the ferrite and the carbide in pearlite, indicated that parallel and accordingly inhibited diffusion of carbon and alloying elements does occur. Zener (1946), in apparent contradiction to the facts, has opposed the view that the carbon can be forced to keep pace with the more slowly diffusing alloying elements.

The present work proposes to demonstrate, with the help of solutions of the multicomponent diffusion equations and Hultgren extrapolations (Hultgren 1938) of the ternary phase diagram, that the carbon can in fact be forced to keep pace with more slowly diffusing elements through adjustment of the extrapolated equilibrium interface concentrations and through counter diffusion gradients. Specifically, the iron, carbon, silicon and iron, carbon, manganese systems are examined using available data and it is demonstrated that a simple diffusion mechanism can explain the inhibition of both the austenite to carbide and austenite to ferrite transformations which occur in sidewise growth of pearlite.

#### SOLUTIONS OF THE MULTICOMPONENT DIFFUSION EQUATIONS FOR AN ADVANCING TWO-PHASE INTERFACE

Zener (1949) has given solutions of the two-component diffusion equation

<sup>1</sup>Manuscript received April 9, 1958.

Contribution from the Department of Metallurgy and Metallurgical Engineering, Hamilton College, McMaster University, Hamilton, Ontario.

<sup>2</sup>Present address: McMaster University, Hamilton, Ontario.

for the growth of linear, cylindrical, and spherical precipitates in an infinite medium. For the  $n$ -component system as described in paper I (Kirkaldy 1958), we follow Zener and seek solutions of the differential equations with constant diffusion coefficients,

$$(1) \quad \frac{\partial C_i}{\partial t} = \sum_{k=1}^{n-1} D_{ik} \nabla^2 C_k,$$

of the parametric form

$$(2) \quad C_t = C_t(\lambda)$$

where

$$(3) \quad \lambda = x/\sqrt{t}.$$

With these substitutions and symmetric diffusion fields (1) becomes

$$(4) \quad -\frac{\lambda}{2} \frac{dC_i}{d\lambda} = \sum_{k=1}^{n-1} \frac{D_{ik}}{\lambda^{p-1}} \frac{d}{d\lambda} \left[ \lambda^{p-1} \frac{dC_k}{d\lambda} \right],$$

where  $p = 1, 2$ , or  $3$  for linear, cylindrical, or spherical interfaces respectively. Subject to the boundary conditions

$$(5) \quad C_i(\lambda = \infty) = C_{i0},$$

$$(6) \quad C_i(\lambda = \alpha_+) = C_{i1},$$

and the corollary

$$(7) \quad C_i(\lambda = \alpha_-) = C_{i2},$$

where  $\alpha$  is the position of the interface in  $\lambda$ -space, the required solutions are

$$(8) \quad C_i = a_{i0} + \sum_{k=1}^{n-1} a_{ik} \int_{\lambda}^{\infty} \lambda^{-(p-1)} \exp[-\lambda^2/4u_k] d\lambda.$$

Substitution in (4) leads to the indicial equations

$$(9) \quad u_k = \sum_{j=1}^{n-1} D_{ij} a_{jk} / a_{ik}.$$

When combined with the  $2(n-1)$  boundary values, these determine the  $a_{ik}$  uniquely in terms of the boundary values and the diffusion coefficients and the  $u_k$  in terms of the diffusion coefficients. For the growth of a planar precipitate into a ternary alloy, the solutions for the two solute elements can be written as

$$(10) \quad C_1 = a_{10} + \frac{d_{11}}{I_1} \int_{\lambda}^{\infty} \exp[-\lambda^2/4u_1] d\lambda + \frac{d_{12}}{I_2} \int_{\lambda}^{\infty} \exp[-\lambda^2/4u_2] d\lambda$$

and

$$(11) \quad C_2 = a_{20} + \frac{d_{21}}{I_1} \int_{\lambda}^{\infty} \exp[-\lambda^2/4u_1] d\lambda + \frac{d_{22}}{I_2} \int_{\lambda}^{\infty} \exp[-\lambda^2/4u_2] d\lambda,$$

where the normalization integrals

$$(12) \quad I_k = \int_{\alpha}^{\infty} \exp[-\lambda^2/4u_k] d\lambda.$$

The formal solution is completed by fitting the boundary values and applying (9) to obtain

$$\begin{aligned} a_{10} &= C_{10}, \quad a_{20} = C_{20}, \\ d_{11} &= \{D_{12}(C_{21}-C_{20}) + [(D_{11}-D_{22})+D](C_{11}-C_{10})/2\}/D, \\ d_{21} &= \{D_{21}(C_{11}-C_{10}) - [(D_{11}-D_{22})-D](C_{21}-C_{20})/2\}/D, \\ d_{12} &= C_{11}-C_{10}-d_{11}, \quad d_{22} = C_{21}-C_{20}-d_{21}, \\ D &= \sqrt{(D_{11}-D_{22})^2 + 4D_{12}D_{21}}, \\ u_1 &= (D_{11}+D_{22}+D)/2, \quad u_2 = (D_{11}+D_{22}-D)/2. \end{aligned}$$

Physically significant solutions exist for the range of diffusion coefficient values,

$$(13) \quad D_{11} > 0 \text{ and } -(D_{11}-D_{22})^2/4 < D_{12}D_{21} < D_{11}D_{22}.$$

The value of the parameter  $\alpha$  must be determined through the mass balance at the interface,

$$(14) \quad (C_{i2}-C_{i1})\alpha/2\sqrt{t} = -J_i(\alpha),$$

where the velocity of precipitate growth is

$$(15) \quad v = \alpha/2\sqrt{t}.$$

For the ternary, linear case this gives two simultaneous equations involving the unknown  $\alpha$  and one independent interface concentration, say  $C_{11}$  (the other three interface concentrations,  $C_{12}$ ,  $C_{21}$ , and  $C_{22}$  are dependent and are given by the tie-line on the extrapolated phase diagram that passes through  $C_{11}$ ). By cross-substitution we can convert these simultaneous equations to the form

$$(16) \quad G_1(C_{11}) = F_1(\alpha)$$

and

$$(17) \quad G_2(C_{11}) = F_2(\alpha),$$

which can easily be solved graphically. The quantity  $\alpha$  can be conveniently used as a measure of the transformation rate since it is proportional to the velocity of interface motion.

#### APPLICATION OF THE SOLUTIONS TO THE PEARLITE TRANSFORMATION IN STEEL

Consider a ternary eutectoid alloy with an iron-carbon basis initially homogenized in the austenitic state and quenched to below the eutectoid temperature so that the pearlite (austenite to carbide+ferrite) reaction will occur isothermally. While it is not possible at present to consider the whole transformation problem involving nucleation with edge and sidewise growth of pearlite, it appears reasonable to consider that the rate variation of sidewise growth of single carbide and ferrite plates into supercooled austenite, as obtained via solutions (10) and (11), will qualitatively represent the rate variation of the whole process.

The present calculations are restricted to the iron, carbon, silicon and

iron, carbon, manganese systems since their ternary constitutions are simple and reasonably well known (ASM Metals Handbook 1948; Owen 1951) and some information is available on diffusion in these systems (Darken 1949; Smithells 1955). Figs. 1, 2, 3, and 4 give the austenite to austenite + carbide

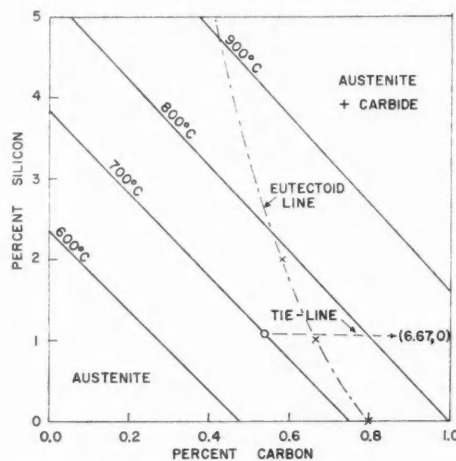


FIG. 1. Extrapolated austenite to austenite + carbide surface of the iron, carbon, silicon constitution diagram.

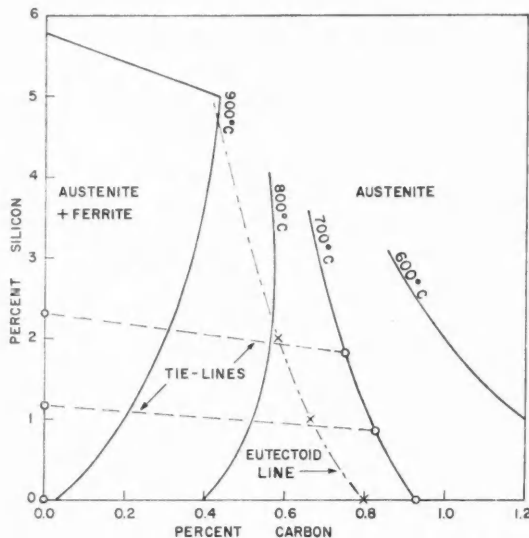


FIG. 2. Extrapolated austenite to austenite + ferrite surface of the iron, carbon, silicon constitution diagram.

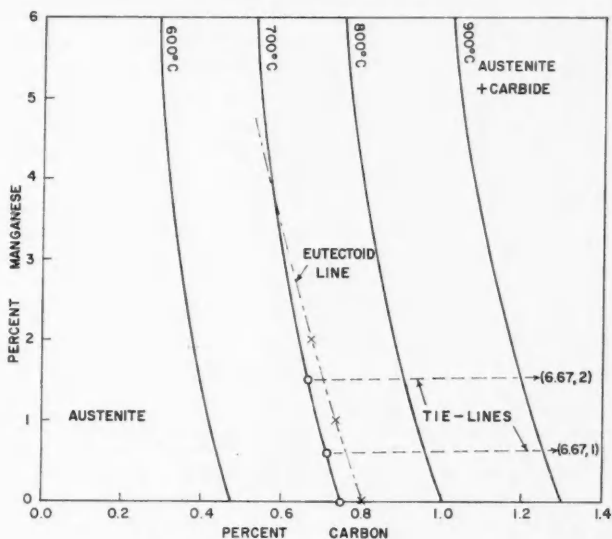


FIG. 3. Extrapolated austenite to austenite + carbide surface of the iron, carbon, manganese constitution diagram.

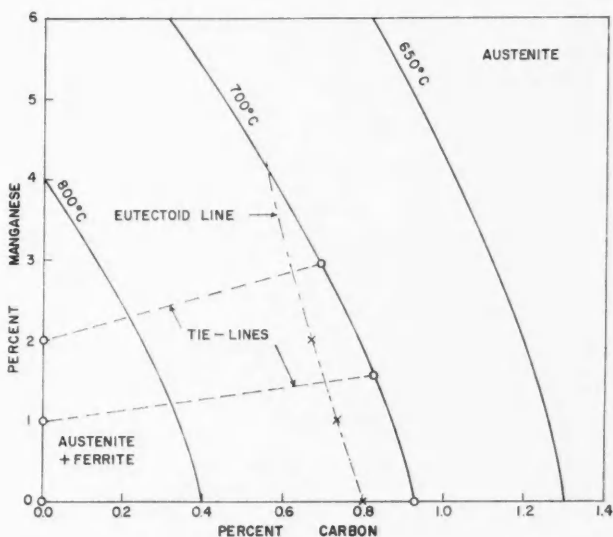


FIG. 4. Extrapolated austenite to austenite + ferrite surface of the iron, carbon, manganese constitution diagram.

and austenite to austenite+ferrite surfaces of the silicon and manganese steel phase diagrams as compiled from the Metals Handbook, together with a Hultgren extrapolation of the surfaces to below the eutectoid temperature. As the precision of these extrapolations is in question, calculations are restricted to a temperature of 700° C, just below the eutectoid value. The directions of the tie-lines in the two-phase regions are very tentative, the sign of the slope being chosen to agree with that at higher temperatures.

On the basis of data given in Smithells (1955) we have estimated for a system in which carbon is component 1 and silicon component 2 that at 700° C,  $D_{11} = 4 \times 10^{-9}$  cm<sup>2</sup>/sec,  $D_{22} = 0.2 \times 10^{-9}$  cm<sup>2</sup>/sec and from Darken's measurements (1949) and Kirkaldy's analysis of them (1957, 1958),  $D_{12} \sim 10^{-9}$  cm<sup>2</sup>/sec. The value of  $D_{21}$  is not critical to the calculation so we set it equal to zero and in the first calculation test the effect of the silicon gradient on the carbon diffusion rate by varying  $D_{12}$ . Table I summarizes the conditions and results

TABLE I

THE VARIATION OF THE CARBIDE GROWTH PARAMETER  $\alpha$  AS A FUNCTION OF THE OFF-DIAGONAL DIFFUSION COEFFICIENT  $D_{12}$  FOR A EUTECTOID IRON, CARBON, SILICON ALLOY AT 700° C.  
THE BASE ALLOY AND INTERFACE CONCENTRATIONS ARE ALSO GIVEN

$D_{12}$ (cm/sec <sup>2</sup> )	$C_{20}$ %	$C_{10}$ %	$\alpha \times 10^4$ (cm sec <sup>-1</sup> )	$C_{11}$ %	$C_{12}$ %	$C_{21}$ %	$C_{22}$ %
0	1.00	0.665	0.0153	0.532	6.67	1.100	0
$0.4 \times 10^{-9}$	1.00	0.665	0.0137	0.535	6.67	1.095	0
$2.0 \times 10^{-9}$	1.00	0.665	0.0098	0.540	6.67	1.070	0

of this calculation for the austenite to carbide transformation of a 1% silicon, eutectoid alloy as constituted in Fig. 1. As expected, with an increase in the (positive) value of  $D_{12}$ , the counter gradient of the silicon inhibits the austenite to carbide interface motion as measured by the parameter  $\alpha$ . The corresponding solute distributions have been calculated and are given in Fig. 5.

A similar calculation for the corresponding austenite to austenite+ferrite transformation is summarized in Table II and Fig. 6. In this case  $D_{12}$  was

TABLE II

THE VARIATION OF THE FERRITE GROWTH PARAMETER  $\alpha$  AS A FUNCTION OF THE SILICON CONTENT OF EUTECTOID STEELS AT 700° C. THE BASE ALLOY AND INTERFACE CONCENTRATIONS ARE ALSO GIVEN

$D_{12}$ (cm/sec <sup>2</sup> )	$C_{20}$ %	$C_{10}$ %	$\alpha \times 10^4$ (cm sec <sup>-1</sup> )	$C_{11}$ %	$C_{12}$ %	$C_{21}$ %	$C_{22}$ %
—	0.00	0.800	0.108	0.930	0	0	0
$2 \times 10^{-9}$	1.00	0.665	0.100	0.826	0	0.862	1.162
$2 \times 10^{-9}$	2.00	0.580	0.083	0.750	0	1.810	2.310

held constant at  $2 \times 10^{-9}$  cm<sup>2</sup>/sec and the silicon content  $C_{20}$  was varied. There is a small decrease in  $\alpha$  and therefore in the transformation rate as the silicon content is increased. The inhibition in both cases would be intensified if  $D_{22}$  were in fact smaller (very likely) or  $D_{12}$  larger (unlikely) and the effect would persist well below 600° C, but even so, silicon, as a result of the particular ternary constitution, would not appear to be a very effective hardenability agent.

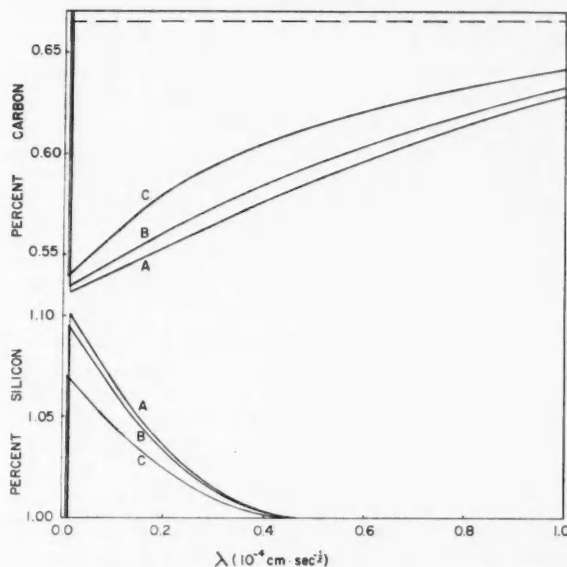


FIG. 5. Solute distributions for carbon and silicon near a planar carbide-austenite interface. A.  $D_{12} = 0$ ,  $\alpha = 0.0153 \times 10^{-4} \text{ cm sec}^{-\frac{1}{2}}$ . B.  $D_{12} = 4.0 \times 10^{-9} \text{ cm}^2/\text{sec}$ ,  $\alpha = 0.0137 \times 10^{-4} \text{ cm sec}^{-\frac{1}{2}}$ . C.  $D_{12} = 2.0 \times 10^{-9} \text{ cm}^2/\text{sec}$ ,  $\alpha = 0.0098 \times 10^{-4} \text{ cm sec}^{-\frac{1}{2}}$ .

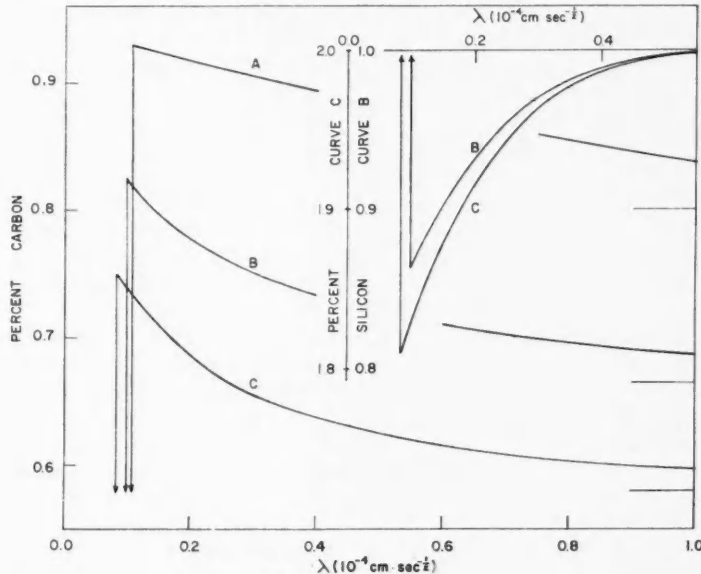


FIG. 6. Solute distributions for carbon and silicon near a planar ferrite-austenite interface with  $D_{12} = 2.0 \times 10^{-9} \text{ cm}^2/\text{sec}$ . A.  $C_{20} = 0$ ,  $\alpha = 0.108 \text{ cm sec}^{-\frac{1}{2}}$ . B.  $C_{20} = 1.00\%$ ,  $\alpha = 0.100 \text{ cm sec}^{-\frac{1}{2}}$ . C.  $C_{20} = 2.00\%$ ,  $\alpha = 0.083 \text{ cm sec}^{-\frac{1}{2}}$ .

The available diffusion data for the iron, carbon, manganese system is even more limited than for the silicon alloys. The data of Darken (1949) suggests that  $D_{12}$  for this system at 1050°C takes a small negative value and this is in agreement with observations on the carburization and decarburization rates of manganese steels (Rollason 1949; Metals Handbook 1948). We prefer, initially, to ignore this possible interaction term since these steels appear to exhibit at the higher temperatures a strong constitutional inhibition and we wish to demonstrate this effect unambiguously. At 700°C we take  $D_{11} = 4 \times 10^{-9} \text{ cm}^2/\text{sec}$  as in the silicon alloys and from an extrapolation of data from Smithells (1955),  $D_{22} \sim 10^{-15} \text{ cm}^2/\text{sec}$ . This is so much smaller than  $D_{11}$  that we set  $D_{22} = 0$  and in this calculation neglect the off-diagonal terms by setting  $D_{12} = D_{21} = 0$ . The consequence of these specifications is to deny any partition of manganese between the carbide and ferrite as indicated in the constitution diagrams of Figs. 3 and 4. Table III summarizes the variation of the carbide growth parameter  $\alpha$  with manganese content and Table IV does the same thing for the ferrite growth into austenite.

TABLE III

THE VARIATION OF THE CARBIDE GROWTH PARAMETER  $\alpha$  AS A FUNCTION OF THE MANGANESE CONTENT OF EUTECTOID STEELS AT 700°C. THE BASE ALLOY AND INTERFACE CONCENTRATIONS ARE ALSO GIVEN

$C_{20}$ %	$C_{10}$ %	$\alpha \times 10^4$ ( $\text{cm sec}^{-\frac{1}{2}}$ )	$C_{11}$ %	$C_{12}$ %	$C_{21}$ %	$C_{22}$ %
0.00	0.800	0.0060	0.750	6.67	0.00	0.00
1.00	0.736	0.0026	0.713	6.67	0.60	1.00
2.00	0.670	0.0007	0.664	6.67	1.50	2.00

TABLE IV

THE VARIATION OF THE FERRITE GROWTH PARAMETER  $\alpha$  AS A FUNCTION OF THE MANGANESE CONTENT OF EUTECTOID STEELS AT 700°C. THE BASE ALLOYS AND INTERFACE CONCENTRATIONS ARE ALSO GIVEN

$C_{20}$ %	$C_{10}$ %	$\alpha \times 10^4$ ( $\text{cm sec}^{-\frac{1}{2}}$ )	$C_{11}$ %	$C_{12}$ %	$C_{21}$ %	$C_{22}$ %
0.00	0.800	0.110	0.930	0	0.00	0.00
1.00	0.736	0.080	0.826	0	1.56	1.00
2.00	0.670	0.024	0.692	0	2.95	2.00

The constitutional inhibition is in both cases quite effective. However, we do not attach too much significance to this result since it depends rather critically on the precise constitution and, furthermore, the effect decreases in intensity as the transformation temperature is lowered. It appears much more likely that  $D_{12}$  is in fact some negative magnitude and even if very small, because of the steep manganese gradients, would lead to a powerful inhibition to carbon diffusion and at the same time, a partition of the manganese. This effect would exist at all transformation temperatures. Taking the very limited data at face value, we might anticipate that manganese is a powerful hardenability agent.

## DISCUSSION

While it is impossible at present to make any quantitative predictions using the above formalism, familiarity with these two sample calculations has suggested some principles of general interest.

1. Inhibition of pearlite growth can occur for purely constitutional reasons in the sense that a slowly diffusing element can force a reduction of the difference between the austenite and interface carbon concentrations to such a value that the carbon flow keeps pace with the alloying element flow. The sample calculation for the iron, carbon, manganese system indicates that this effect is only important near the eutectoid temperature.

2. In a system in which  $D_{22} \ll D_{11}$  and in which the off-diagonal terms are negligible, a diffusion solution exists only if the partition of the alloying element in the pearlite is constitutionally allowed to go to zero.

3. The interaction with the off-diagonal elements of the diffusion matrix, when combined with a suitable extrapolated alloy constitution, can lead to a powerful inhibition of interface motion. It is our belief that this is the main cause of hardenability effects. These effects, when evident, are the more intense the smaller the relative alloy diffusion rate and the larger the off-diagonal coefficients (of suitable sign).

4. It is quite feasible that the sign of the off-diagonal interaction will be such as to produce an acceleration of growth, e.g., as observed in the iron, carbon, cobalt system. Assuming that cobalt diffuses much more slowly than carbon, a necessary corollary would be that the alloy exhibits nearly zero partition of the cobalt in the pearlite.

5. It appears possible that for a given extrapolated stable constitution no diffusion solution exists. One might speculate in such a case that the transformation occurs according to the laws of diffusion in an associated metastable system.

6. If the basic conception presented here is correct, it appears that the empirical hardenability correlations due to Grossman (1952) can represent at best a very crude approach to the truth since the growth and nucleation rates, and therefore the hardenability, depend in a complicated and by no means monotonic way on the concentration, constitution, and the diffusion behavior. This, of course, is not the first time that reservations have been expressed about the validity of the simple additive and multiplicative correlation of hardenabilities (see, for example, Bucknall and Steven 1949).

The applications of this formalism are not restricted to the pearlite transformation. All precipitation and solution processes are amenable to this description—tempering and stability of high-speed steels, solution treatment and aging in aluminum alloys, and the solution of carbides in the soaking of steel. The method can be very simply applied in the form presented in paper I to the processes of carburizing and decarburizing. It is worth noting in this respect that the off-diagonal coefficients  $D_{12}$  as specified by Darken's experiments (1949) are of the correct sign to explain the acceleration of carburization by manganese in steels and the deceleration by silicon. Furthermore, banding in steels, which has been previously attributed solely to the con-

stitutional effects of manganese segregation, is probably accentuated by the existence of the negative off-diagonal coefficient  $D_{12}$  which is indicated for this system.

#### ACKNOWLEDGMENTS

The author is indebted to Dr. H. E. Petch and Dr. R. G. Summers-Gill of the Physics Department, McMaster University, for their critical reviews of the manuscript.

#### REFERENCES

- BOWMAN, F. E. and PARKE, R. M. 1944. Trans. Am. Soc. Metals, **33**, 481.  
BUCKNALL, E. H. and STEVEN, W. 1949. Progress in metal physics, Vol. 1, *edited by* B. Chalmers (Butterworth Scientific Publications, London), p. 269.  
DARKEN, L. S. 1949. Trans. Am. Inst. Mining Met. Engrs. **180**, 430.  
GROSSMAN, M. A. 1952. Elements of hardenability (American Society for Metals, Cleveland).  
HULTGREN, A. 1938. Discussion to Mehl, R. F. (1938), "Hardenability of Alloy Steels" (American Society for Metals, Cleveland).  
KIRKALDY, J. S. 1957. Can. J. Phys. **35**, 435.  
——— 1958. Can. J. Phys. **36**, 899.  
MEHL, R. F. and HAGEL, W. C. 1956. Progress in metal physics, Vol. 6, *edited by* B. Chalmers and R. King (The Pergamon Press, Ltd., London), p. 74.  
METALS HANDBOOK 1948. (American Society for Metals, Cleveland).  
OWEN, W. S. 1951. J. Iron and Steel Inst. **167**, 117.  
ROLLASON, E. C. 1949. Metallurgy for engineers (Edward Arnold, London), p. 155.  
SMITHHELLS, C. J. 1955. Metals reference book, Vol. 2 (Butterworth Scientific Publications, London).  
WELLS, C. and MEHL, R. F. 1941. Trans. Am. Inst. Mining Met. Engrs. **145**, 315, 329.  
ZENER, C. 1946. Trans. Am. Inst. Mining Met. Engrs. **167**, 550.  
——— 1949. J. App. Phys. **20**, 950.

# DIFFUSION IN MULTICOMPONENT METALLIC SYSTEMS

## III. THE MOTION OF PLANAR PHASE INTERFACES<sup>1</sup>

J. S. KIRKALDY<sup>2</sup>

### ABSTRACT

Onsager's phenomenological scheme is adapted to unidimensional diffusion in a multiphase, multicomponent system with constant diffusion coefficients. Subject to initial conditions corresponding to the semi-infinite diffusion couple, an exact solution of the multicomponent equations is obtained from which the planar interface motions can be calculated. The similar but unrelated motion of markers that occurs in the diffusion zone of some single-phase couples is discussed and Darken's phenomenological description for binary alloys is extended to multicomponent systems.

### INTRODUCTION

Jost (1952) and Wagner (1946) have given expressions for the diffusion penetration for several interesting unidimensional boundary conditions in multicomponent and multiphase systems. In particular, Jost has given a solution for the diffusion penetration of a completely soluble component diffusing in a semi-infinite diffusion couple consisting of two mutually insoluble phases. While this system must necessarily have three components, in view of the mutual insolubility of the two phases, it is possible to obtain solutions of the binary diffusion equations on either side of the weld and match them according to the requirement that the diffusion current of the soluble component be continuous at the couple interface. This is what Jost has done for the case of constant diffusion coefficients. In the present discussion we treat a similar, but more general problem without any restriction on the mutual solubility of the two phases and with explicit account being taken of the off-diagonal diffusion coefficients. Wagner (1946) has treated the related problem of linear interdiffusion of two phases in a binary alloy system. Both of these results are special cases of the general calculation.

In paper II (Kirkaldy 1958) the ternary diffusion equations were solved for the diffusion field about a precipitating phase of uniform concentration. In the present work we consider the problem of linear interdiffusion of two different multicomponent phases in the form of a diffusion couple, with or without the appearance of intermediate phases in the diffusion zone. This particular physical arrangement has great potential value for the determination of alloy constitution since the theory to follow and the available experimental data indicate that very close to equilibrium concentrations exist at all phase interfaces. As suitable microanalytic techniques become available, the analysis of diffused couples should become an economical method of determining phase boundaries.

<sup>1</sup>Manuscript received April 9, 1958.

Contribution from Aluminium Laboratories Limited, Kingston, Ontario; the Department of Metallurgical Engineering, McGill University, Montreal, Quebec; and the Department of Metallurgy and Metallurgical Engineering, McMaster University, Hamilton, Ontario.

<sup>2</sup>Present address: McMaster University, Hamilton, Ontario.

The observation of marker movement in the diffusion zone of diffusion couples (Smigelskas and Kirkendall 1947; Correa da Silva and Mehl 1951) has evinced much interest in recent years. While consideration of this phenomenon is not necessary to the phenomenological description of most alloy processes, the effect is sufficiently fundamental as to demand a place in any discussion of diffusion. Accordingly, in a later section, we extend in a somewhat trivial way, the phenomenological description for binary alloys due to Darken (1948).

#### THE DIFFUSION EQUATIONS AND SOLUTIONS

The general system of one-dimensional diffusion equations for multicomponent diffusion in a substitutional solid solution alloy are from paper I (Kirkaldy 1958),

$$(1) \quad J_i = - \sum_{k=1}^{n-1} D_{ik} \frac{\partial C_k}{\partial x},$$

and

$$(2) \quad \frac{\partial C_i}{\partial t} = \sum_{k=1}^{n-1} \frac{\partial}{\partial x} \left[ D_{ik} \frac{\partial C_k}{\partial x} \right].$$

These have the parametric solutions

$$(3) \quad C_i = C_i(\lambda), \quad \lambda = x/\sqrt{t},$$

provided the initial conditions can be expressed as

$$(4) \quad C_i(+\infty) = C_{i0}$$

and

$$(5) \quad C_i(-\infty) = C_{iW},$$

i.e., the conditions for the semi-infinite diffusion couple.

As the following analysis will demonstrate, these same parametric solutions exist in linear multiphase systems provided very close to constant concentrations obtain at all interfaces, irrespective of the number of phases which appear in the diffusion zone of the couple. That these constant concentrations must be equilibrium values follows from the fact that as  $t \rightarrow \infty$  and the diffusion gradients approach zero, each increment in the zone, including the interface increment, must approach local equilibrium. Accordingly, any diffusion measurement that confirms relation (3) demonstrates uniquely that very close to interfacial equilibrium is maintained throughout the diffusion period. The only preconditions to be imposed on the terminal alloys in this description are that they be homogeneous solid solutions, that diffusion be structure independent, and that the constitution allows diffusion to proceed from them without any compositions appearing in the zone which require more than two phases in equilibrium. For example, the two alloys *A* and *B* marked on the 775°C section of the copper-nickel-zinc phase diagram of Fig. 1 would probably meet the conditions. In this case, a third phase  $\beta$  would appear in the diffusion zone between the terminal  $\alpha$  and  $\gamma$  phases.

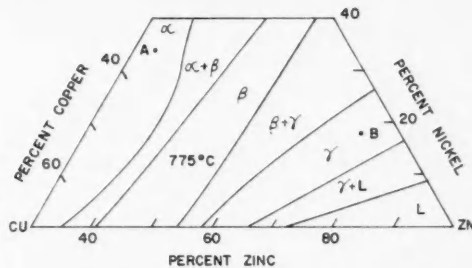


FIG. 1.  $775^{\circ}\text{C}$  section of the copper-nickel-zinc constitution diagram.

Fig. 2 is a diagrammatic penetration curve for an  $n$ -component alloy involving a total of  $N$  phases. Each continuous region of the curve is described by the solution of the ordinary equations

$$(6) \quad -\frac{\lambda}{2} \frac{dC_i}{d\lambda} = \sum_{k=1}^{n-1} \frac{d}{d\lambda} \left[ D_{ik} \frac{dC_k}{d\lambda} \right],$$

which fits the appropriate phase boundary compositions. In general, the  $D_{ik}$  are functions of all the concentrations but in the present calculation we assume them to be an appropriate average value for each phase so that an analytic solution can be obtained.

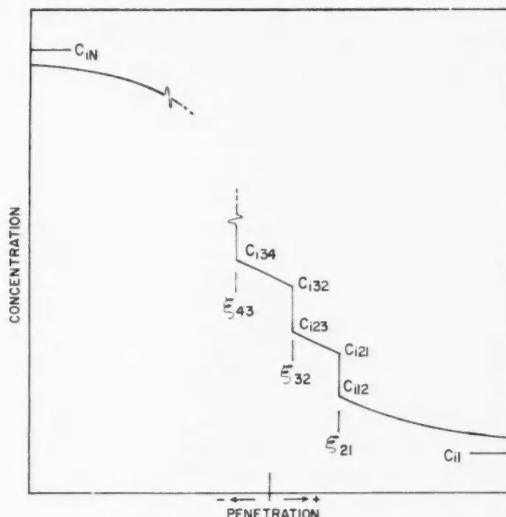


FIG. 2. Schematic penetration curve for the  $i$ th component of a multicomponent diffusion couple with intermediate phases.

The co-ordinates of the interfaces,  $\xi$ , are determined simultaneously with the interface concentrations by application of interface continuity relations of the form

$$(7) \quad (C_{i21} - C_{i12}) \xi_{21}/2\sqrt{t} = J_{i12} - J_{i21}^*$$

and the equilibrium conditions. In this evaluation we have  $2(N-1)n$  interface concentrations plus  $N-1$  phase boundary co-ordinates as unknowns and these are uniquely determined by the  $(n-1)(N-1)$  independent relations of type (7), the  $n(N-1)$  equilibrium free energy relations of the form

$$(8) \quad \mu_{i1}(C_{112}, C_{212}, \dots, C_{n-1,12}) = \mu_{i2}(C_{121}, C_{221}, \dots, C_{n-1,21}),$$

and the  $2(N-1)$  concentration balances of the form

$$(9) \quad \sum_{i=1}^n C_{i12} = 1.$$

The isothermal constitution diagram is equivalent to the latter two sets of equations.

The required solutions take the same form as those presented in papers I and II, viz.,

$$(10) \quad C_i = a_{i0} + \sum_{k=1}^{n-1} a_{ik} \int_{\lambda}^{\xi_{ij}} \exp[-\lambda^2/4u_k] d\lambda$$

subject to the indicial equations

$$(11) \quad u_k = \sum_{j=1}^{n-1} \frac{a_{jk}}{a_{ik}} D_{ij}$$

and the appropriate phase boundary values. In the evaluation of the coefficients it is convenient to normalize the integrals by letting

$$(12) \quad a_{ik} = d_{ik} / \int_{\xi_{i+1,j+1}}^{\xi_{ij}} \exp[-\lambda^2/4u_k] d\lambda$$

where the  $d_{ik}$  are functions of the boundary  $C$ 's and the  $D$ 's as determined by equation (11). The complete numerical calculation involves as well the solution of the simultaneous non-linear set of equations (7) with the phase diagram equivalent of sets (8) and (9). Such a calculation might require the services of an electronic computer for  $N > 2$  and  $n > 3$ .

#### COMPARISON WITH EXPERIMENT

In testing the validity of this phenomenological description it is sufficient to demonstrate experimentally that equation (3) is valid, or what is equivalent, that approximate equilibrium is maintained throughout the diffusion. It is relatively easy to test the  $\lambda$ -dependence of the concentrations since this implies that all points of constant concentration ( $x/\sqrt{t} = \text{constant}$ ) must move a distance in the  $x$ -direction proportional to  $\sqrt{t}$ . Such points are easy to recognize metallographically. They may be the original phase boundaries

---

\*To assure the validity of these with changing lattice parameter and crystal structure, it is necessary to measure the  $x$  co-ordinate in units which contain an equal number of atoms.

existing at the diffusion temperature or boundaries dividing the transformation products after cooling from the diffusion temperature. Fig. 3 is a micrograph of the zone of an aluminum to zinc couple annealed at 370° C for

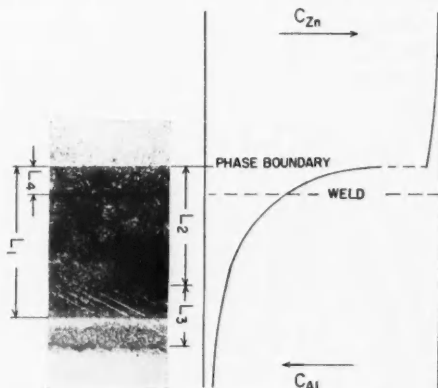


FIG. 3. Etched diffusion zone of an aluminum-zinc diffusion couple with a corresponding schematic penetration curve. Annealed for 114.2 hours at 370° C.  $L_1 = 210$  microns.

114.2 hours and quenched, along with a qualitative penetration curve deduced from it and the binary constitution diagram. When the various characteristic lengths  $L$  are plotted as a function of  $\sqrt{t}$ , the required linear curves are obtained as indicated in Fig. 4.  $L_4$  is the approximate distance of the phase boundary from the original weld while all other interfaces appear as a result of transformations on quenching ( $L_1$ ) or slow cooling ( $L_2$  and  $L_3$ ).

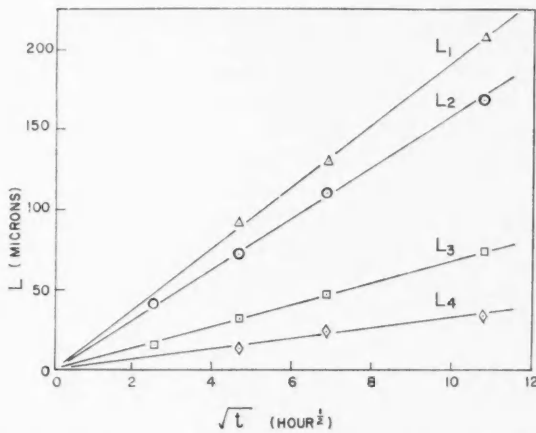


FIG. 4. Time-dependence of the penetration in the aluminum-zinc diffusion couple of Fig. 3.

Bücke (1946) has examined a number of binary alloy couples in the same manner and has observed a  $\sqrt{t}$  dependence in all cases—even when as many as three intermediate phases are involved in the system. It is probable that this will be the usual result even though we know from fundamental growth theory that the specification of equilibrium interface conditions is at best a good approximation. For a phase boundary to migrate there must be a free energy difference which implies some deviation from equilibrium, however small.

In the growth theory for a crystal-vapor interface, the growth rate depends in a monotonically increasing manner on the excess of the vapor concentration over its equilibrium value (Burton *et al.* 1951) so we might expect a similar though more complicated behavior for a two-solid interface. In general, the initial deviation from equilibrium will be quite high to correspond to the high initial velocities (though not infinite velocities as implied in the phenomenological description). However, the limitation of the mass supply by diffusion must rapidly cause a reduction in the velocity and the free energy difference between the phases.

To make an estimate of the deviation of the interface concentrations from their equilibrium values, consider a two-phase interface for which the average adjacent concentration gradients in atom fractions are about 400 per cm. This number is chosen since it is above the limit of measurement by ordinary mechanical-chemical means and is such as would be obtained in the first few seconds of a typical diffusion anneal. Converting this to atom fraction per lattice plane for a lattice with  $a = 2.5 \times 10^{-8}$  cm we obtain a change of  $10^{-5}$  atom fraction per atom plane. This demonstrates that on the atomic scale, very close to equilibrium has already been attained. As a matter of fact, it is this rapid approach to local equilibrium which validates a linear phenomenological description of extended diffusion processes (de Groot 1952). If, finally, we assume that the jump frequency and activation energy for atom transfer across the phase boundary are of the same magnitude as for diffusion in the surroundings then we expect the equilibrium concentrations to be attained to within a few atoms in  $10^6$  in the same first few seconds.

It still appears conceivable that measurably non-equilibrium interface conditions could exist in a diffusing system for experimentally significant times. This would appear as deviations from the  $\sqrt{t}$  dependence of the diffusion penetration near the time origin.

#### MARKER MOVEMENT IN MULTICOMPONENT DIFFUSION COUPLES

One of the most general phenomenological relations that can be written for linear mass transfer of component  $i$  relative to an arbitrary origin is

$$(13) \quad J_i = - \sum_{k=1}^n D''_{ik} \frac{\partial C_k}{\partial x} + C_i v,$$

where  $v$  is a convection velocity in the  $x$ -direction. It is usual to imbed the co-ordinate system in the lattice at points far removed from the diffusion zone, to neglect the volume changes of mixing, and to assume the conservation of

lattice sites (Darken 1948). In the oft-considered case of diffusion by a simple exchange mechanism, the diffusion flow terms must exactly balance so that  $v = 0$ . It is, however, possible to conceive of atomic mechanisms whereby the diffusion flows do not balance so that  $v$  is not equal to zero.

Here we follow common practice and represent the vacancies in the metal as the  $n$ th component, choose concentration units of atom fractions so that

$$(14) \quad \sum_{i=1}^m C_i = 1, \quad m = n-1,$$

and assume that in compatible units

$$(15) \quad \sum_{i=1}^m J_i = 0.$$

Provided no lateral dimensional changes occur and the vacancy concentration is relatively uniform and/or relatively small, equation (15) will be accurate.

If the vacancy gradient terms in (13) are non-zero we assume after Seitz (1950) that the vacancy concentration at any point is a unique function of the solute concentration. (The assumption of local thermal equilibrium is somewhat more restrictive.) Accordingly,

$$(16) \quad \frac{\partial C_n}{\partial x} = \frac{\partial C_n}{\partial C_1} \frac{\partial C_1}{\partial x} + \dots + \frac{\partial C_n}{\partial C_{n-1}} \frac{\partial C_{n-1}}{\partial x},$$

and by application of this and (14), equation (13) is transformed to the shorter form,

$$(17) \quad J_i = - \sum_{k=1}^{m-1} D'_{ik} \frac{\partial C_k}{\partial x} + C_i v.$$

Then, by application of (14) and (15) we obtain

$$(18) \quad v = \sum_{i=1}^m \sum_{k=1}^{m-1} D'_{ik} \frac{\partial C_k}{\partial x},$$

which, on substitution into (17), gives the simplified phenomenological equation,

$$(19) \quad J_i = - \sum_{k=1}^{m-1} D_{ik} \frac{\partial C_k}{\partial x}.$$

In this, the  $D_{ik}$  are related linearly to the  $D'_{ik}$  and the  $C_i$ . The identity of relation (19) and the corresponding one for a simple exchange mechanism implies that insofar as the assumption (15) is valid, the existence of convection in the diffusion zone does not in any way alter the usual phenomenological correlation of concentration distributions. However, if the marker movement, which is presumed to proceed at a rate equal to the convection velocity, is also to be described, further diffusion coefficients are required for the evaluation of (18).\* It is our opinion that in most applications of diffusion this movement

---

\*For the semi-infinite diffusion couple the solutions will have their usual parametric form  $C_i = C_i(\lambda)$  and the co-ordinate of weld markers will advance, as a result of (18), proportionately to  $\sqrt{t}$ , i.e., markers originally at the origin must migrate in step with some point of constant composition.

is of no consequence so the usual assumption of a simple exchange mechanism will not lead to inconsistencies.

While the phenomenon of marker movement seems to be of little practical importance, it is of very great theoretical importance since it sheds considerable light on the mechanism of diffusion. Since experiments for binary alloys indicate the approximate validity of the above description and the assumptions leading to it, the mechanism of diffusion must be such as to support the assumptions, and the number of possible mechanisms that can do this are very limited. Thus far, only two have been proposed—a vacancy exchange and an interstitialcy mechanism (Seitz 1950)—and the former is presently favored on energetic grounds. Seitz's statistical theory for a vacancy exchange mechanism in binary alloys leads in a very direct way to the above phenomenological equations provided sufficient sources and sinks for vacancies, presumably in the form of dislocations, are available to assure the validity of (15).

#### SUMMARY

In the absence of experimental data it is not possible to apply this discussion of the multicomponent, multiphase diffusion process to specific alloy systems. However, there are certain results of a general nature which are worth summarizing:

1. For a semi-infinite diffusion couple consisting of an arbitrary number of components and an arbitrary number of parallel intermediate phases, the diffusion penetration depth will tend to follow a parabolic ( $x = a\sqrt{t}$ ) law. This statement holds for both constant and variable diffusion coefficients and is a result of the fact that approximate local equilibrium is attained in a very short time. Exceptions, if such appear, could be due to an unusually high activation energy for atom transfer across one or more of the phase interfaces and would be exemplified by deviations from the parabolic law near the time origin.
  2. Intermediate phases with a "zero" solubility range will have "zero" width in the diffusion zone.
  3. Intermediate phases with a small solubility range and/or relatively small diffusion coefficients will have correspondingly small widths in the diffusion zone.
  4. Intermediate phases with a large solubility range and/or relatively large diffusion coefficients will have a correspondingly large width in the diffusion zone.
  5. The existence of a Kirkendall effect is unlikely to vitiate a phenomenological description which ignores it.
  6. The accuracy of the phenomenological description will be prejudiced to a greater or lesser extent by interface inhibitions (films or high transfer activation energies), grain boundary diffusion, high defect densities, anisotropic diffusion, and porosity and lateral dimensional changes due to the Kirkendall effect.
- The theoretical and experimental description of multicomponent diffusion with the appearance of intermediate phases should have applications in the understanding of metal to metal bonding and in the determination of alloy

constitution (Castleman and Seigle 1957). The full potential in the latter application can only be realized with the development of high resolution microanalytic techniques.

## REFERENCES

- BÜCKLE, H. 1946. Metallforschung, **1**, 175.  
BURTON, W. K., CABRERA, N., and FRANK, F. C. 1951. Trans. Roy. Soc. (London), A, **243**, 299.  
CASTLEMAN, L. S. and SEIGLE, L. L. 1957. Trans. Am. Inst. Mining Met. Engrs. **209**, 1173.  
CORREA DA SILVA, L. C. and MEHL, R. F. 1951. Trans. Am. Inst. Mining Met. Engrs. **191**, 155.  
DARKEN, L. S. 1948. Trans. Am. Inst. Mining Met. Engrs. **175**, 184.  
DE GROOT, S. R. 1952. Thermodynamics of irreversible processes (North-Holland Publishing Company, Amsterdam), pp. 5-7.  
JOST, W. 1952. Diffusion in solids, liquids, gases (Academic Press Inc., New York), p. 68.  
KIRKALDY, J. S. 1958a. Can. J. Phys. **36**, 899.  
——— 1958b. Can. J. Phys. **36**, 907.  
SEITZ, F. 1950. Acta Cryst. **3**, 355.  
SMIGELSKAS, A. D. and KIRKENDALL, E. O. 1947. Trans. Am. Inst. Mining Met. Engrs. **171**, 130.  
WAGNER, C. 1946. Quoted in Bückle, H. 1946.

## SOME OBSERVATIONS OF AURORA USING A LOW-POWER FREQUENCY-MODULATED RADAR<sup>1</sup>

C. COLLINS

### ABSTRACT

A frequency-modulated, continuous-wave radar seems to be particularly well suited to the observation of auroral ionization, since it provides both range information and a Doppler indication of radial motion. An experimental equipment of this type has been operated for a few months near Ottawa. The system parameters are briefly considered and the radar observations are compared with similar measurements made with higher-powered pulse systems.

### INTRODUCTION

Since World War II radio-echo techniques have been used extensively in the study of auroral phenomena, and on both sides of the Atlantic research teams have recorded both forward-scattered and back-scattered signals in the investigation of particular aspects of the ionized regions in auroral displays. Kaiser (1955) has summarized the work of most of these groups and the extreme usefulness of these radio-echo techniques is now well established. Most of this work has been done with radars, and while there has been a variety of operating parameters in the different systems, nearly all have been of the high-power pulse-type. This almost exclusive dependence on pulse radar continued until quite recently when McNamara (1955) extended the pulse-radar techniques by employing a double-Doppler system for investigation of the movements of auroral ionization. Since then there have been further developments in pulse radars for use during the I.G.Y. (McNamara 1958) but these have been more in the nature of refinements rather than basic changes in the technique.

Another approach to the problem of applying radio-echo techniques in auroral studies involves the use of continuous-wave transmissions. This method was used by Moore (1951) and Bowles (1952) in their studies of the fading characteristics of aurorally propagated signals, and more recently by Forsyth and Vogan (1957) in their investigation of the frequency dependence of auroral radio reflections. These workers did not, however, employ a radar technique since they used very widely separated transmitters and receivers. Bowles (1955) was perhaps the first to use a simplified form of continuous-wave radar for auroral work at College, Alaska.

It is the purpose of this paper to describe some preliminary experimental results obtained with a continuous-wave system in which frequency modulation of the transmitted energy is used in order to obtain range and Doppler information. This type of radar system does not appear to have been used previously in auroral studies.

<sup>1</sup>Manuscript received March 28, 1958.

Contribution from the Radio Physics Laboratory of the Defence Research Board, Ottawa, Canada. Work carried out under Project No. D-48-95-11-15.

## CW FM RADAR

Continuous-wave radar is probably one of the oldest forms of radar and as such has been extensively treated in the literature. (See, for example, Wolf and Luck 1948.) The system has many variants. Gnanalingam (1954) has discussed the usefulness of one form for the detection of weak low-level ionospheric echoes. Most accounts, however, describe systems operating in the UHF band that were designed for use as navigational aids. The basic problem in auroral radio studies is equivalent to the long range detection of a multiplicity of moving targets. With properly chosen operating parameters the CW FM system offers many advantages for such service, and with certain forms of frequency modulation the range and Doppler information can easily be obtained from the reflected signal. The factors that affect the choice of parameters are illustrated in Fig. 1. This shows frequency-time graphs of the transmitted and reflected signals for the particular case when the modulating

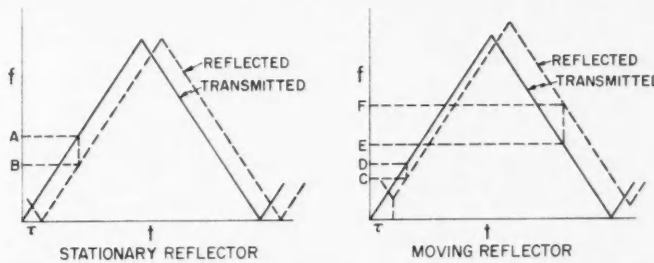


FIG. 1. Curves showing the difference frequencies between the transmitted and reflected signals.

waveform is in the form of a symmetrical triangle. On these curves the origins of the ordinates denote not zero frequency but some operating frequency. For both the moving and stationary reflectors the echo signal is delayed in time by an interval,  $\tau$ , which results in a frequency difference between the transmitted and returned signals. This difference frequency (AB for a stationary reflector) can be detected as beats between the transmitted and received signals and used as a direct measure of the range of the aurora. If the target is moving, then the curve for the reflected signal will be displaced in frequency, and there will now be two range frequencies, one for each half of the modulation cycle. The range will then be given by the mean of these two frequencies (CD and EF) and their relative shifts from the mean will give the direction of motion of the auroral reflecting area. Range errors will be negligible if the displacement of the curves for the reflected signal is small during the period of the modulation waveform. This will be the case with auroral echoes where ranges are of the order of 500 to 1000 km and apparent radial velocities are expected to be of the order of a few hundred meters per second. The resultant Doppler shifts may not correspond, however, to any gross movement of aurora, but rather to individual motions of short-lived elements in the display. It is obvious that there will be conflicting frequency requirements for such

a system, but for operation in the VHF band of 30 to 300 Mc/s a convenient selection of operating and modulating frequencies can be made which will provide range beat frequencies in the lower part of the audio spectrum. The other main advantages of continuous-wave radar are associated with the transmitter power and the receiver sensitivity. An estimate of the power of the reflected signal can be obtained by putting into the radar equation reasonable figures for the system parameters. The reflected power  $P_R$  is given by the expression

$$P_R = \frac{P_T G_T G_R \lambda^2 \sigma}{64\pi^3 R^4} \quad (\text{Ridenour 1947})$$

where

$P_T$  = transmitted power = 30 w,

$G_T$  = gain of transmitting antenna = 20,

$G_R$  = gain of receiving antenna = 20,

$\sigma$  = reflecting area =  $10^6$  m<sup>2</sup>,

$\lambda$  = wavelength = 8 m,

$R$  = range = 600 km.

Then

$$P_R = 3 \times 10^{-16}$$

where the value for the size of the auroral reflecting area is based on the work of Currie *et al.* (1953). Although a wide-band receiver is required to accommodate the frequency deviation of the signal at the receiver i-f, the over-all system bandwidth is set by the characteristic of the audio filter which selects the range beat note. At a frequency of 50 Mc/s cosmic noise is about  $4 \times 10^{-20}$  watts/cycle/sec so that with a filter bandwidth of 40 c.p.s. the above signal can be detected easily.

#### INSTRUMENTATION

The complete CW FM radar system tested at the Radio Physics Laboratory is shown in the block diagram in Fig. 2. The small amount of energy required at the receiver for heterodyning with the reflected signal was provided by direct propagation from the transmitter to the receiver. Control of this direct signal to prevent overloading of the receiver is one of the more serious problems inherent in all CW radars, and at frequencies in the VHF band it is one of the major obstacles to a simple system. A satisfactory working arrangement was obtained in this case by the use of interferometer-type antennas set one behind the other, and phased so that the horizontal radiation patterns gave the necessary isolation between the transmitter pair and the receiver pair. In this way the direct signal from the transmitter was reduced to  $1.3 \times 10^{-10}$  watts at the receiver input.

The spectrum analyzer needed for the resolution of the range frequencies consisted of 10 narrow-band (40 c.p.s.) twin-T filters having center frequencies ranging from 210 c.p.s. to 1190 c.p.s. in increments of 110 cycles. The outputs of the filters were then applied to the 20 pens of an operational recorder. This is a paper-chart instrument designed to indicate the times of occurrence and

the sequence of events. The pens are essentially on-off devices and they are actuated when the rectified outputs of the filters rise above a predetermined level. An integration time of 2 seconds was used in the detectors to improve the sensitivity of the system. Doppler shifts in the range frequencies were resolved

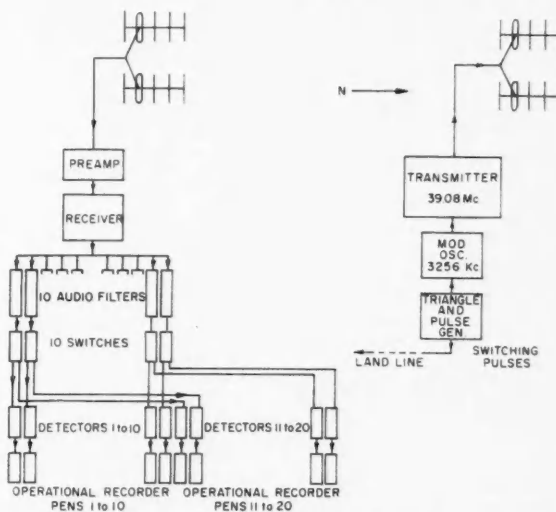


FIG. 2. Block diagram of CW FM radar system.

by switching the outputs of the range filters in synchronism with the vertices of the triangular modulation waveform, so that the beat note during the upsweep of the modulation wave was recorded on one set of pens, and the beat note detected during the downsweep was recorded on the other set of pens. With such an arrangement echo ranges from 210 to 1190 km could be recorded in intervals of 110 km. At the center ranges of 650 km and 760 km this permitted the detection of radial velocities of  $\pm 2100$  meters per second. For the ranges of 320 km and 1080 km this is reduced to  $\pm 420$  meters per second. The operating parameters for the experimental radar are given in Table I.

TABLE I

1. Transmitter frequency	39.08 Mc/s
2. Transmitter power	10 w
3. Modulation waveform	Symmetrical triangle
4. Modulation frequency	7.5 c.p.s.
5. Maximum frequency deviation	10 kc/s
6. Antenna gain	10 db
7. Elevation angle of first lobe max.	9.5°
8. Polarization	Horizontal
9. Beam width	50°
10. Receiver sensitivity	$2 \times 10^{-18}$ w
11. Audio filter pass band	40 c.p.s.

A reduction in transmitter power to 10 watts from the originally estimated 30 watts was found necessary when very strong echoes caused overloading of the receiver.

#### OBSERVATIONS AND DISCUSSION

The equipment operated continuously from the beginning of September, 1956, until the end of December of that year. During the early part of the test confirmation of only two points was sought: (*a*) that the low transmitter power of 10 watts was adequate for the detection of auroral ionization and (*b*) that movements of the reflecting regions within the auroral display could be detected as Doppler shifts on the returned signal. During the 4 months of operations, echoes were received on 20 nights. Evidence of auroral activity on these nights was obtained from visual observations, 3-component magnetometer records, and the occurrence of the auroral type signal enhancements on the VHF recordings made at this laboratory (Forsyth and Vogan 1957). These other data also suggested that on only two other nights was there a high probability of auroral activity which had not been detected by the CW FM radar.

A sample of the record made during the auroral display on the night of October 26-27 is shown in Fig. 3. The off or no-signal position of the pens is indicated by the lower position of the lines. The occurrence of an echo is recorded when a pen is deflected by a small fixed amount towards the top of the chart. It can be seen that at times there is considerable spread in the range of the returned signal. This could have been due to overloading of the filters by a strong echo from a discrete range, or it might have been indicative of a true geographic distribution of the reflecting regions within the auroral display. In either case this spreading made the analysis of the records somewhat difficult, and for this preliminary investigation, only the mean ranges were tabulated. These range measurements were taken from the record at arbitrary intervals, and then only when the echo seemed to be clearly defined. No attempt was made to divide the record into regular time intervals and only one occurrence was counted for an echo without regard to its duration.

A histogram of the range distribution is shown in Fig. 4. In order to attach some physical significance to this distribution of range measurements it may be of interest to compare them with similar distributions obtained from other radar data, and to consider them in the light of echo distribution analyses performed by other workers. Forsyth (1954), in examining the 106 Mc/s data from the Saskatoon radar for the purpose of determining the height of the auroral reflecting centers, has shown that the echo-range distribution may be due primarily to the variation of the sensitivity of the radar equipment as measured in the vertical plane. The latitude effect has been considered by Bachynski and Kornelson (1953), who produced a weighting factor which they applied to their 56 Mc/s results to enable them to fit the range distribution to a sensitivity curve. While such a correction does change slightly the shape of the range curve, it causes only a relatively small displacement of the maximum, and it would seem to be of importance only where the range

## PLATE I

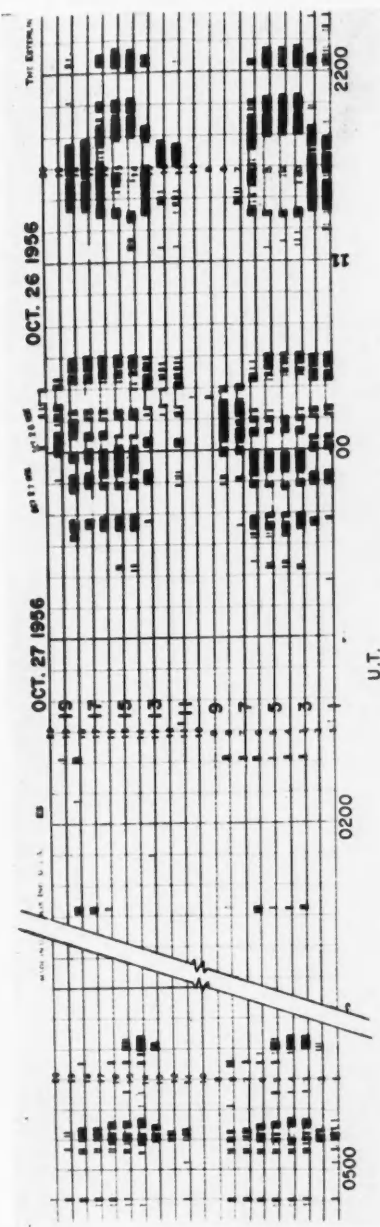


FIG. 3. Sample record from the CW radar made on Oct. 26-27.



resolution is high. Following these studies an extensive theoretical analysis of echo distributions was carried out by McNamara (1954). In this he showed that the echo distribution could be the result of a number of complex factors

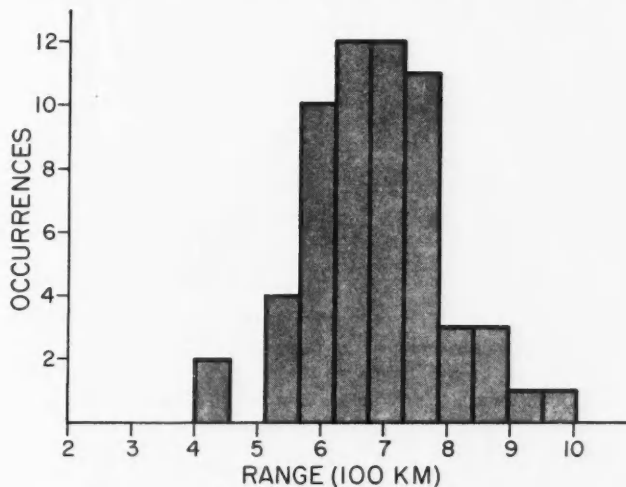


FIG. 4. Distribution of echo ranges.

such as target shape and cross section, pulse length, magnetic field orientation, altitude attenuation, and plasma resonance. It is of interest to note that, in discussing target cross section, McNamara points out that the extreme sensitivity of the echo distribution to the radar parameters does not always exist in practice. While it is not reasonable to expect close similarity between the results obtained at widely differing times and places, the limited data available from the present experiment appear to be adequate for very rough comparisons. The maximum of the range distribution shown in Fig. 4 is between 650 and 750 km. For the generally assumed reflection height of 110 km and the present angle of elevation of the first lobe maximum ( $9.5^\circ$ ) the maximum of the range distribution might be expected at about 550 km. The application to the 2-way antenna pattern of a range correction factor for the inverse square law of echo amplitude would shift this maximum to slightly higher ranges but the shift would be relatively small. It must be concluded that in this instance the range distribution curve is not sensitive to the antenna sensitivity pattern. The increase in echo occurrence with range may indicate a real increase in the latitudinal distribution of the auroral reflecting areas north of Ottawa. This seems reasonable since Ottawa is 1500 km south of the auroral zone maximum. The range distribution may also be influenced by the aspect sensitivity of auroral echoes, but in the interval, 550 to 750 km, the geomagnetic inclination or aspect angle changes only by about  $2^\circ$ . It is unlikely, therefore, that the approach to the specular reflection

condition accounts for all of the increase in echo occurrence. Bullough and Kaiser (1955) have published a range distribution for the Manchester radar data which also shows a maximum at 750 km. The geomagnetic latitude of Manchester is almost the same as that of Ottawa and the angle of the first lobe maximum for Kaiser's measurements was  $8.5^\circ$ . The frequency of 75 Mc/s is almost twice the operating frequency of the Ottawa radar and this may account in part for the slight difference in the positions of maxima. However, as in the case of the Ottawa measurements, the maximum appears at a greater range than would be expected if the distribution was very sensitive to the antenna sensitivity pattern. The range measurements made by Dyce (1955) at Pt. Barrow on 51.7 Mc/s have a similar distribution to those made at Ottawa, and show a peak at 750 km. This curve, however, correlates well with that to be expected from consideration of aspect sensitivity alone and it may be that aspect sensitivity is the dominant factor at that location. The fact that the Ottawa histogram in the range interval of 800 to 1000 km departs from the distributions plotted at other sites probably indicates only that at these ranges the system sensitivity is the controlling parameter. For so high an angle of radiation ( $9.5^\circ$ ) the sensitivity at the maximum ranges is greatly reduced. The minimum range of 430 km is in good agreement with almost all other results if some frequency dependence is accepted at these minimum ranges. Forsyth (1954) with the Saskatoon radar on 106 Mc/s records no reflections from ranges less than 600 km. Kaiser (1954) operating on 75 Mc/s has plotted nothing below 600 km, and Dyce (1955) on 51.7 Mc/s shows a minimum range at 400 km. Both Harang and Landmark (1954) and Hellgren and Meos (1952) with radars on 35 Mc/s and 30 Mc/s respectively report echo occurrences in the 200–300 km range interval. The problem of the aspect sensitivity of auroral reflections and the effect of this on the echo-range distribution has been treated extensively by several workers. Booker (1955), in the development of his theory of scattering, has published a set of auroral-response versus range curves which incorporate an aspect-sensitivity factor. As these are calculated for a location where the magnetic inclination is  $75^\circ$  and for an antenna system very similar to the present one, the Ottawa echo distribution has been compared with the 50 Mc/s curve (A) on the left-hand side of Booker's Fig. 4. While the long- and short-range cutoffs are in reasonably good agreement, there is a large difference in the positions of the maxima and the two figures may be incompatible.

Some of the echoes recorded at Ottawa showed Doppler shifts, and a distribution of these is drawn in Fig. 5. Once again there are too few data to permit any great significance to be attached to the measurements, but it may be noted that they are in good agreement with the results of Bowles (1955), and those obtained later by McNamara (1954). The agreement with Bullough and Kaiser's results (1955) is not as good, as they seem to indicate much lower velocities than many of the range speeds measured by the Manchester group. Their results do, however, refer to range drift measurements and not to Doppler results. The two kinds of measurement might reasonably be expected to give different orders of magnitude.

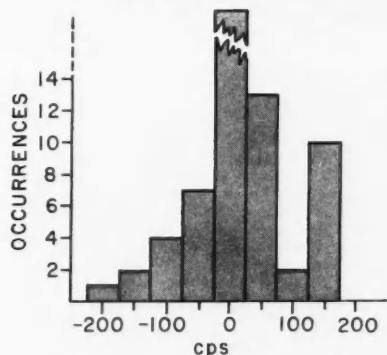


FIG. 5. Distribution of Doppler-shifted echoes.

### CONCLUSION

In conclusion, while the small amount of data available from this preliminary test could hardly contribute significantly to the general knowledge of auroral phenomena, the fact that the measurements are in good agreement with those of other groups can be taken as an indication of the validity of the measurements and a demonstration of the usefulness of the CW FM radar for auroral research. Both range and Doppler measurements can be made and the adequacy of a very low transmitter power is clearly demonstrated. This feature of the system is most important since it provides a number of attractive operational features. For example, the equipment may be left in unattended operation for appreciable periods. Since the completion of the test period, modifications have been made to the data recording sections of the system to allow the use of a simple photographic recorder. With these refinements the radar seems particularly well suited to multifrequency operation with scaled systems and it is towards this that future work will probably be directed. At the time of writing a three-frequency installation is nearing completion at the University of Saskatchewan. Transmitter powers will be the same and antenna heights will be scaled to produce similar radiation patterns. The other parameters of the systems such as frequency deviations and filter bandwidths will also be scaled so that a direct comparison of the range and Doppler measurements on the three frequencies will be possible.

### ACKNOWLEDGMENT

The author wishes to express his appreciation for the advice and encouragement given by Dr. P. A. Forsyth of the Radio Physics Laboratory.

### REFERENCES

- BACHYNSKI, M. P. 1953. M.A. Thesis, University of Saskatchewan, Saskatoon, Sask.
- BOOKER, H. G. 1955. Cornell University, Ithaca, N.Y., School of Electrical Engineering Tech. Report No. 28.
- BOWLES, K. L. 1952. J. Geophys. Research, **57**, 157.
- 1955. Cornell University, Ithaca, N.Y., School of Electrical Engineering Tech. Report No. 22.

- BULLOUGH, K. and KAISER, T. R. 1955. *J. Atmospheric and Terrest. Phys.* **6**, 198.  
CURRIE, B. W., FORSYTH, P. A., and VAWTER, F. E. 1953. *J. Geophys. Res.* **58**, 179.  
DYCE, R. B. 1955. Cornell University, Ithaca, N.Y., School of Electrical Engineering  
Tech. Report No. 23.  
FORSYTH, P. A. 1951. Conference of Auroral Physics, University of Western Ontario, London,  
Ontario.  
FORSYTH, P. A. and VOGAN, E. L. 1957. *J. Atmospheric and Terrest. Phys.* **10**, 215.  
GNANALINGAM, M. A. 1954. *Proc. Inst. Elec. Engrs. Part III*, **101**, 243.  
HARANG, L. and LANDMARK, B. 1954. *J. Atmospheric and Terrest. Phys.* **4**, 322.  
HELLGREN, G. and MEOS, J. 1952. *Tellus*, **4**, 249.  
KAISER, T. R. 1955. The airglow and the aurorae (The Pergamon Press, Ltd., London).  
MCNAMARA, A. G. 1954. Ph.D. Thesis, University of Saskatchewan, Saskatoon, Sask.  
— 1958. *Can. J. Physics*, **36**, 1.  
MOORE, R. K. 1951. *J. Geophys. Research*, **56**, 97.  
RIDENOUR, L. N. 1947. Radar system engineering (McGraw-Hill, New York), p. 18 et seq.

# MEASURED PHASE DISTRIBUTION IN THE IMAGE SPACE OF A MICROWAVE LENS<sup>1</sup>

G. W. FARNELL

## ABSTRACT

Detailed measurements at a wavelength of 3.2 cm have been made of the phase distribution in the diffraction image produced by an aberration-free lens illuminated from a point source. The behavior of the phase of the electric field is shown by contours of constant phase (wavefronts) in the plane of the image space containing the axis and the *H*-vector of the radiating source. The region of the image space considered extends from the solid dielectric lens to a surface somewhat beyond the focus. Results are also shown of the phase distribution measured within about one wavelength of certain phase singularities which occur at the minima of intensity on the focal arc and on the axis. In general, there is very good agreement between plots of measured phase contours and plots of phase contours previously calculated from scalar diffraction theory.

## I. INTRODUCTION

While phenomena near the focus of a lens system have been of continuing interest in optical studies for some hundreds of years, it is only in more recent years that the detailed structure of the diffraction image has been calculated (Zernike and Nijboer 1949; Linfoot and Wolf 1956). With the measurements possible at optical wavelengths, it is extremely difficult to make accurate point-by-point determinations of the field near a focus in order to confirm the calculated values. However, more recently, "microwave optics" has been able to contribute certain measuring techniques to the investigation of the imaging process (Bekefi 1957). It has been shown previously that the intensity distribution produced by microwave lenses can be calculated from the scalar diffraction theory of aberrations as used in light optics (Bachynski and Bekefi 1957), and in this paper some results are shown of an experimental investigation of corresponding phase distributions which also agree with such scalar calculations. Thus, the accurate measurements of intensity and phase which can be made at microwave frequencies provide convenient means for investigating the diffraction structure of the image of a point source.

The phase measurements reported here were made at a wavelength of 3.2 cm in the image of a point source produced by a solid-dielectric, rotationally symmetric lens. This lens had a radius of 25 cm and was essentially free of all the Seidel aberrations at the image distances used. In Section II the arrangement of the experimental equipment is outlined, while Sections III and IV discuss respectively the general phase distribution in the image space, and the detailed phase behavior near the positions of minimum intensity.

<sup>1</sup>Manuscript received April 3, 1958.

Contribution from Eaton Electronics Research Laboratory, McGill University, Montreal, Quebec.

This research forms part of a project on microwave optics that is supported at McGill University by the U.S. Air Force, Cambridge Research Center, under Contract AF.19(604)-2228.

## II. MEASURING EQUIPMENT

A plan view of the basic measuring arrangement is illustrated in Fig. 1. Part of the signal from a klystron oscillator is modulated by an audio voltage in a balanced modulator, and the resulting suppressed carrier signal is radiated

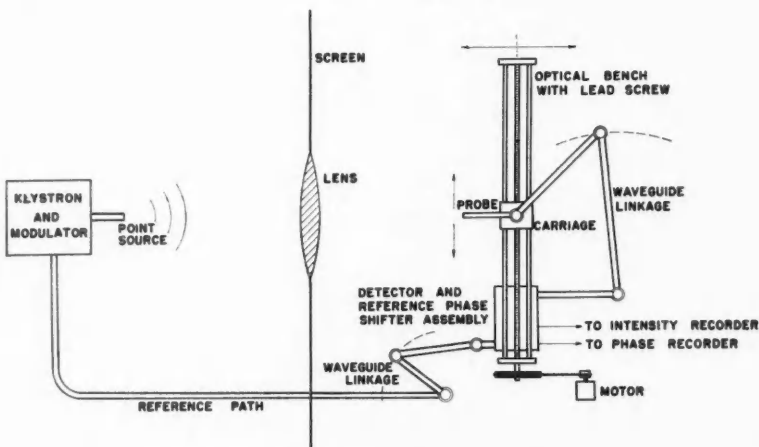


FIG. 1. Plan view of the measuring arrangement showing the scanning mechanism and the two open waveguides used as point source and probe respectively.

from an open waveguide simulating a point source. This special form of modulation is required for the automatic phase plotter designed by Pavlasek (1958; also Bekefi 1957) in order to measure and record the phase distribution in the image space independent of the intensity variations from point to point. The radiated microwave energy in the form of the two sidebands is focussed towards a "geometrical image point" by the lens under investigation. A conducting screen supports the lens and ensures that only energy which has traversed the lens reaches the open waveguide used as a probe in the image space. The position of this probe along the optical bench on which it is mounted is transmitted by selsyn generators to the chart drives of the intensity recorder and of the phase recorder.

The signal received by the probe passes through a waveguide linkage arrangement to the detector assembly where it is divided into two parts. One part is detected by a crystal diode, and the resulting audio signal is recorded on a logarithmic recorder to indicate the intensity of the measured field. The other part is recombined with the unmodulated carrier which is brought from the klystron along a waveguide path of fixed mechanical length. From the recombined signal an audio voltage is obtained which actuates the servo-drive on a phase shifter in the reference path. Thus the phase shifter is automatically adjusted until this audio voltage is zero, and the corresponding position of the reference phase shifter, which is proportional to the relative

phase of the measured signal, is registered on the second strip-chart recorder. Hence, simultaneous measurements of intensity and phase are provided as a function of the position of the probe along the optical bench.

### III. GENERAL PHASE DISTRIBUTION

Using the equipment described in the previous section, extensive measurements of the phase distributions of different microwave lenses have been carried out. To determine the general phase distribution over large areas of the image space for a given lens, the relative phase was recorded along several hundred scans perpendicular to the axis, and from these measurements the lines of constant phase in a given plane were plotted. Fig. 2 shows the co-phasal contours in half-wavelength increments for a lens system with image distance  $R = 110$  cm, lens radius  $a = 25$  cm, and wavelength  $\lambda = 3.22$  cm. The drawing represents the central  $H$ -plane, that is, the plane containing the axis and the  $H$ -vector of the radiating source. Experimental results obtained in the  $E$ -plane give a similar phase distribution. These phase contours agree very well with the contours calculated from the scalar theory of physical optics for a microwave lens system with about the same parameters (Farnell 1957, Fig. 2(a)). The component of measured electric field with the same polarization as that of the source is identified with the scalar quantity of such calculations.

The  $H$ -plane contours of constant intensity and of constant phase are shown in Figs. 3(a) and 3(b) respectively for the same lens system considered in Fig. 2, but with the image distance reduced to 63 cm by displacement of the source. In the isophote diagram the intensity is measured in decibels with respect to the intensity at the geometrical focus. The dark rings of the Airy pattern which lie on an arc centered at the middle of the exit pupil are shown by small crosses, and at these points the intensity is below the noise level of the measuring equipment (-40 db). Outside of the contour marked -30 db, which forms an upper boundary on the diagram, the intensity remains more than 30 db (0.1%) below that at the focus. The point of maximum intensity occurs on the axis at about  $-2\lambda$ , and the axial variations of intensity become more rapid as the lens is approached, until in Region A the fluctuations are too violent to be shown on a diagram of this scale.

In Figs. 2 and 3(b) the reference circles indicate the approximate curvature of the wavefronts at different places in the image space. The center of circle 1 on each of the diagrams is the geometrical image point, that of circle 2 is the center of the lens, and that of circle 3 is the point of maximum intensity. Circle 3 is omitted from Fig. 2 because the experimental results do not extend sufficiently far beyond the focus for this circle to be significant. As detected by the open waveguide probe oriented parallel to the source waveguide, the wavefront leaving the lens is nearly that of a spherical wave converging towards the geometrical image. Except near the axis this wave deforms gradually until in crossing the focal arc it is a spherical wave diverging from the center of the exit pupil. At the points of zero intensity on the focal arc the phase has singular points which are discussed in more detail below. Somewhat beyond the focus the center of curvature of the wavefront is the point

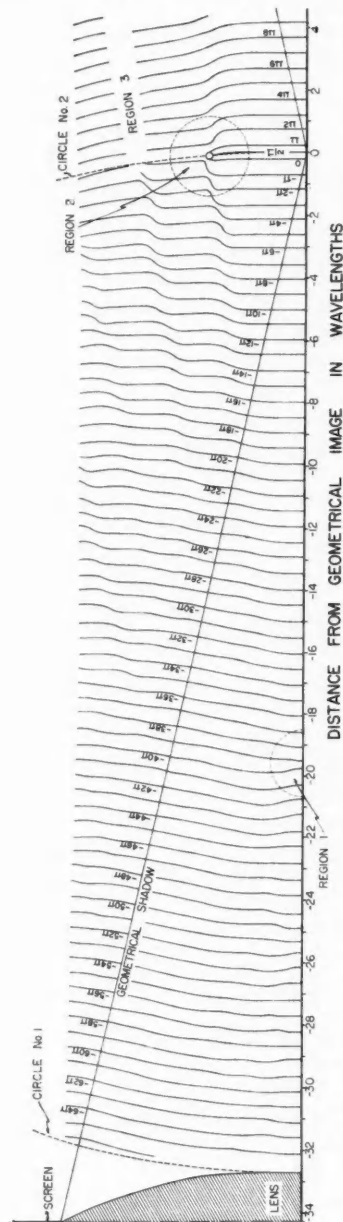


FIG. 2. Measured  $H$ -plane contours of constant phase in the image space of a microwave lens with image distance  $R = 110$  cm, lens radius  $a = 25$  cm, and wavelength  $\lambda = 3.22$  cm. The phase at the geometrical focus is taken as  $\pi/2$  radians and an  $e^{-i\omega t}$  time dependence is implied.

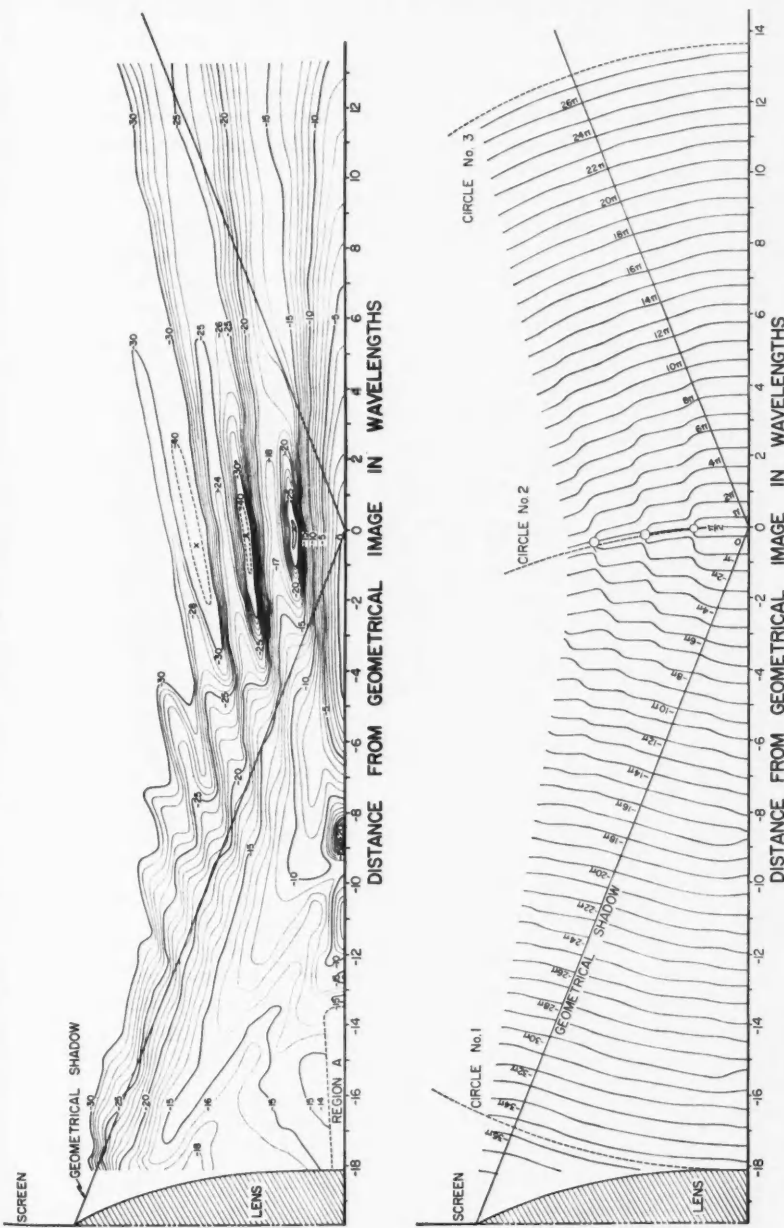


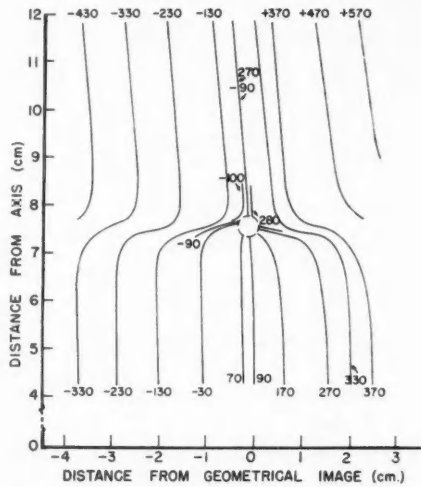
FIG. 3. (a) Measured contours of constant intensity, and (b) measured contours of constant phase for a lens with  $R = 63$  cm,  $a = 25$  cm, and  $\lambda = 3.22$  cm. The intensity is shown in decibels with respect to the intensity at the geometrical image point, and the phase at the geometrical image is taken as  $\pi/2$  radians.

of maximum intensity. Along the axis itself the phase shift is almost a linear function of distance, but very detailed investigation of this region shows the "phase anomaly" long known in light optics (Reiche 1909). A separate paper discussing the axial phase behavior in microwave lens systems is being prepared.

The measured phase distribution in Region 3 of Fig. 2 was very erratic for this lens at this image distance. It is believed that the cause of the irregularity was energy reaching the probe by reflection from some surface within the laboratory. A very small amount of spurious signal could cause the erratic phase behavior because the intensity in this region is very low, more than 30 db below the corresponding axial values. This effect does not occur on the other side of the axis, nor for other image distances.

#### IV. THE SINGULAR REGIONS

In the vicinity of the focal arc and of the axial intensity minima, rapid phase transitions of the order of  $180^\circ$  occur in distances corresponding to a small fraction of a wavelength. To eliminate any errors due to the finite response time of the phase plotter, automatic recording was replaced by manual point-by-point measurements in these singular regions. The contours of Fig. 4 give the phase behavior for the lens with 110 cm image distance within about



the axis along a short path on the lens side of the singularity the phase progresses to more negative values, while along a parallel path on the other side the phase goes to more positive values. Thus, in the region above the singularity in Fig. 4 there is a discontinuity in the numbering of the contours, but because the phase is arbitrary to any multiple of  $360^\circ$ , the phase itself changes continuously along a path across the focal arc in this region. As a result of the contours which emanate from the singularity, if the phase changes are measured along a closed path enclosing this singularity, then on return to the starting point the phase will have advanced or retarded by  $360^\circ$ , depending on the direction of travel. The discontinuity in the numbering of the contours across the focal arc above the singularity then arises from the imposition of the arbitrary condition that the numbering of the contours on the axial side of the singularity be continuous.

The contours of Fig. 5 correspond to a region extending about one wavelength on either side of the geometrical image in Fig. 3(b) (image distance 63 cm). The singular nature of the phase at the zeros of intensity is shown here for the first

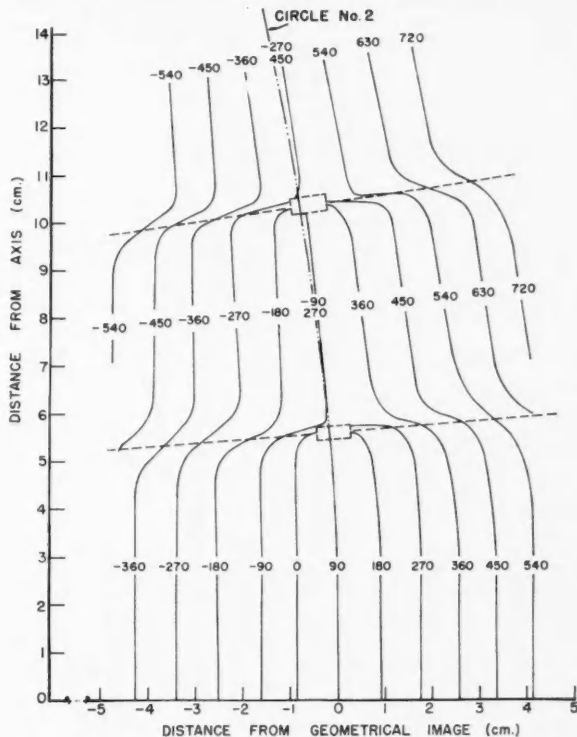


FIG. 5. Measured contours of constant phase within about one wavelength of the focal arc for the lens system considered in Fig. 3.

two dark rings. Also it can be seen that the  $90^\circ$ ,  $-90^\circ$ ,  $-270^\circ$  set of contours which characterizes the focal arc deviates but little from the theoretical shape calculated from scalar theory, that is from circle 2 which is centered at the exit pupil. The two broken lines in this illustration are normals to the circle.

Because of the shape of the respective contours, the curvature of the focal arc is more readily observed in plots of phase contours than in plots of intensity contours. (Compare Figs. 3(a) and 3(b).) The elongated nature of the intensity contours near the dark rings and the finite noise level of the measuring equipment prohibit the direct determination of the exact longitudinal positions of the minima of intensity. However, the corresponding phase singularities can be located quite accurately; in fact the small crosses indicating the points of minimum intensity in Fig. 3(a) were obtained from the phase information of Fig. 5.

Fig. 6 shows the contours which resulted from a detailed investigation of the phase within about one wavelength of the first axial intensity minimum before the focus for the lens system with an image distance of 110 cm. This region

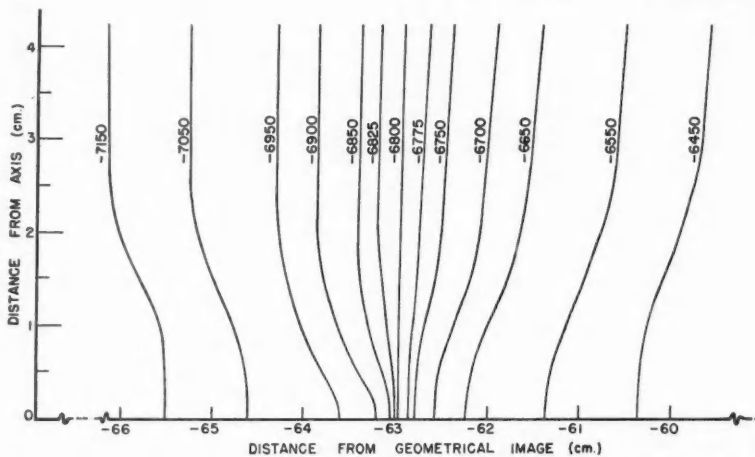


FIG. 6. Measured contours of constant phase within about one wavelength of the first axial intensity minimum for the lens system of Fig. 2. This illustration corresponds to Region 1 of the latter drawing.

corresponds to Region 1 of Fig. 2. Along the axis through this minimum the rapid but continuous variation corresponds to one of the transitions in the axial phase anomaly calculated for optical lenses by Reiche (1909). From the shape of the contours it is seen that the normals to the wavefronts, which can be taken to represent lines of energy flow, bypass the axial intensity minimum (Farnell 1957, Fig. 4).

The phase distributions measured in the image space of typical microwave lenses have shown remarkable agreement in detail with those calculated from scalar optical theory for most regions except within about one lens radius of

the lens surface. The singular behavior of the phase at the dark rings on the focal arc and the rapid phase transitions near these singularities require that any phase measurements in such regions be made with precision and interpreted with care.

Much of the equipment used in these experiments was designed by Dr. M. P. Bachynski and Professor T. J. F. Pavlasek, and was constructed by Mr. V. Avarlaid and his technical staff. The comments and suggestions of Dr. G. Bekefi and Professor G. A. Woonton were of great assistance to the author.

#### REFERENCES

- BACHYNSKI, M. P. and BEKEFI, G. 1957. *J. Opt. Soc. Am.* **47**, 428.  
BEKEFI, G. 1957. Final Report to Air Force Cambridge Research Center on Contract AF19(122)-81, Eaton Laboratory, McGill University, ASTIA Doc. No. AD110152.  
FARNELL, G. W. 1957. *Can. J. Phys.* **35**, 777.  
LINFOOT, E. H. and WOLF, E. 1956. *Proc. Phys. Soc. B*, **69**, 823.  
PAVLASEK, T. J. F. 1958. Ph.D. Thesis, McGill University, Montreal, Que.  
REICHE, F. 1909a. *Ann. Physik*, **29**, 65.  
— 1909b. *Ann. Physik*, **29**, 401.  
ZERNIKE, F. and NIJBOER, B. R. N. 1949. *Contribution to Théorie des images optiques* (Editions de la Revue d'Optique, Paris).

# ALPHA DECAY OF SPHEROIDAL NUCLEI<sup>1</sup>

E. M. PENNINGTON<sup>2</sup> AND M. A. PRESTON

## ABSTRACT

A system of coupled differential equations relates the amplitudes of alpha particle waves emitted from a spheroidal nucleus described by the Bohr-Mottelson model. These equations in spheroidal coordinates have been solved for five even-even nuclides with the aid of the electronic computer FERUT. There are four possible cases for each nuclide which are consistent with the boundary conditions. The solutions of the equations are used to calculate the probability density of alpha particles on the nuclear surface for each case. For Case I the peak in the distribution function shifts from the nuclear symmetry axis to the equator with increasing mass number. The probability density for Case II is always peaked between the symmetry axis and the equator, while for Cases III and IV it is always peaked strongly at the equator. The change in the distribution function with increasing distance from the nucleus is considered for a typical case. Barrier penetration factors are calculated and found to differ from those for spherical nuclei by factors of the order of 2 or 3. Comparison with the calculations of an approximation method of Fröman is made for one nuclide.

## INTRODUCTION

In this paper we examine the emission of alpha particles from nuclei with large intrinsic quadrupole moments. Many properties of the nuclides with  $A \gtrsim 220$  indicate that they have spheroidal shape and rotational energy level schemes in accordance with the predictions of the strong coupling collective model (Perlman and Rasmussen 1957; Alder *et al.* 1956).

For even-even nuclides the  $0^+$  ground state of the parent alpha particle emitter decays to the various energetically available levels of the daughter. The intensities are normally appreciable only to the first three levels, which have spins  $0^+, 2^+,$  and  $4^+$  and belong to the ground state rotational band.

As a result of the intrinsic nuclear quadrupole moment, the emitted alpha particle is in a non-central field. Consequently its angular momentum is not a constant of the motion until it has reached distances sufficiently great that the energy of the quadrupole interaction is negligible. The wave function is therefore a superposition with distance-dependent coefficients of the wave functions describing the various individual final states, i.e.

$$(1) \quad \Psi = \sum_i \sum_{I_f} \sum_m \frac{W_{II_f}(r)}{r} (I_f M_f - m | I_f I_i M_i) \left( \frac{2I_f + 1}{8\pi^2} \right)^{\frac{1}{2}} \times D_{M_i - m, K_f}^{I_f}(\Theta_i) Y_{lm}(\theta, \phi) X.$$

The function

$$\left( \frac{2I_f + 1}{8\pi^2} \right)^{\frac{1}{2}} D_{M_i - m, K_f}^{I_f}(\Theta_i)$$

is the normalized rotational wave function of the daughter nucleus having as

<sup>1</sup>Manuscript received March 26, 1958.

Contribution from the Physics Department, McMaster University, Hamilton, Ontario. Partially assisted by grants from the National Research Council. Based on a thesis submitted by E.M.P. for a Ph.D. degree.

<sup>2</sup>Present address: Argonne National Laboratory, Lemont, Illinois.

argument the Euler angles  $\Theta_i$  specifying the orientation of the nuclear spheroid.  $I_f$  is the total angular momentum of the daughter having components  $M_i - m$  and  $K_f$  on the  $z$  axis and the symmetry axis of the nucleus respectively. The coordinates of the alpha particle are  $(r, \theta, \phi)$  and  $Y_{lm}(\theta, \phi)$  is the angular momentum function of the alpha particle. In equation (1) the summation over  $m$  ensures that the system has the same total angular momentum,  $I_i$ , and  $z$  component,  $M_i$ , as the initial nucleus. The function  $X$  represents the intrinsic particle and vibrational state and is the same for all final states considered.

The non-central potential implies that the Schrödinger equation does not separate into individual equations for each  $W_{H_f}(r)$  but that the radial equations are coupled. As  $r \rightarrow \infty$ , the coupling terms become small. In less exact language, we may say that the alpha particle after emission is still in interaction with the nucleus, not only through the central potential  $2Ze^2/r$  which influences only its velocity, but also through the quadrupole moment which can cause the particle and the nucleus to interchange energy and angular momentum. It is only when the separation  $r$  has become large that one can finally decide to which final state the transition has occurred.

The process under discussion is extranuclear and determines the changes in the energy distribution and angular distribution of the alpha particles as they move from the nuclear surface to infinity. In this paper we attempt to use the intensities observed in the laboratory to deduce the distributions on the nucleus. We have studied five representative even-even parent nuclides,  $U^{234}$ ,  $Pu^{238}$ ,  $Cm^{242}$ ,  $Cl^{246}$ , and  $Fm^{254}$ . The equations have been integrated numerically using the electronic digital computer, FERUT, at the University of Toronto. We have compared the results for  $Cm^{242}$  with those of Rasmussen and Segall (1956) and those of an approximation method recently presented by Fröman (1957).

Besides the angular distributions, we have also examined the effect of the spheroidal shape on the absolute barrier penetration and have compared the results with the approximate calculations of Hill and Wheeler (1953).

#### MATHEMATICAL FORMULATION AND METHODS OF CALCULATION

The general problem of a non-central interaction in alpha decay was first formulated and methods of solution indicated in a paper by Preston (1949). The theory for spheroidal nuclei both of even and odd  $A$  was derived by Rasmussen (1953) and Rasmussen and Segall (1956) and was applied by them to the decay of  $Th^{228}$  and  $Cm^{242}$ . The equations derived by Rasmussen and Segall in spheroidal coordinates are the basis of the present calculations.

Taking the symmetry axis of the spheroid as the polar axis and the center of the spheroid as origin, we denote the spheroidal coordinates of a point by  $(\xi, \eta, \phi)$  where  $\phi$  is the usual azimuthal angle and  $\xi$  and  $\eta$  are defined in terms of the distances  $r_1$  and  $r_2$  from the two foci to the point:

$$(2) \quad \begin{aligned} \xi &= (r_1 + r_2)/a & 1 \leq \xi \leq \infty, \\ \eta &= (r_1 - r_2)/a & -1 \leq \eta \leq 1. \end{aligned}$$

The constant  $a$  is the interfocal distance and is defined by the condition that one of the spheroids  $\xi = \xi_0$  must represent the nuclear surface. Spheroidal coordinates are connected with spherical polar coordinates by the relations

$$(3) \quad \begin{aligned} r &= \frac{1}{2}a(\xi^2 + \eta^2 - 1)^{1/2}, \\ \cos \theta &= \xi \eta (\xi^2 + \eta^2 - 1)^{-1/2}, \\ \phi &= \phi. \end{aligned}$$

It will be noted that for large values of  $r$ ,  $\xi \rightarrow 2r/a$  and  $\eta \rightarrow \cos \theta$ .

Rasmussen and Segall (1956) have shown that it is convenient to work in a coordinate system with the  $z$  axis fixed along the nuclear symmetry axis. For even-even nuclides the wave function is given by

$$(4) \quad \Psi = \frac{2}{a} \sum_{l \text{ even}} (\xi^2 - 1)^{-\frac{1}{2}} W_l(\xi) Y_{l0}(\cos^{-1}\eta, \phi) X.$$

This equation can be seen to agree asymptotically with (1) on making use of the facts that for even-even nuclides  $I_f = l$ ,  $I_i = M_i = K_f = 0$ , and

$$(5) \quad Y_{l0}(\theta', \phi') = \sum_m D_{lm}^{l*}(\Omega_i) Y_{lm}(\theta, \phi),$$

where  $(\theta', \phi')$  are polar angles with respect to the coordinate system fixed in the nucleus. We note that (4) shows that the alpha particle has no angular momentum component along the symmetry axis; since it must balance the rotational angular momentum component, this is to be expected.

The Hamiltonian in spheroidal coordinates for even-even nuclei is

$$(6) \quad \left\{ \frac{-\hbar^2}{2\mu} \frac{4}{a^2(\xi^2 - \eta^2)} \left[ \frac{\partial}{\partial \xi} (\xi^2 - 1) \frac{\partial}{\partial \xi} + \frac{\partial}{\partial \eta} (1 - \eta^2) \frac{\partial}{\partial \eta} \right] \right. \\ \left. - \frac{\hbar^2}{2I} \frac{(\xi^2 - 1)}{(\xi^2 - \eta^2)} \frac{\partial}{\partial \eta} (1 - \eta^2) \frac{\partial}{\partial \eta} + H_{\text{intr.}} + V(\xi, \eta) \right\}$$

and the coupled equations for the  $W_l(\xi)$  are

$$(7) \quad \frac{d^2 W_l}{d\xi^2} + \left[ \frac{1}{(\xi^2 - 1)^2} - \frac{l(l+1)}{\xi^2 - 1} - \frac{\mu a^2}{4I} l(l+1) \right] W_l + \frac{\mu a^2}{2\hbar^2(\xi^2 - 1)} \sum_\nu W_\nu \\ \times \int Y_{l0}^* \left[ E - V(\xi, \eta) \right] (\xi^2 - \eta^2) Y_{l0} d\eta d\phi = 0.$$

In the above  $\mu$  is the reduced mass of the alpha particle - residual nucleus system,  $I$  is the effective nuclear moment of inertia, and  $E$  is the total disintegration energy of the ground state transition corrected for electron screening. The terms in the Hamiltonian are the relative kinetic energy, the nuclear rotational energy, the energy of the intrinsic nuclear motion, and the electrostatic potential containing both Coulomb and higher order terms. If it is assumed that the charge is uniformly distributed throughout the spheroidal nucleus, the intrinsic quadrupole moment  $Q_0 = Za^2/10$  and

$$(8) \quad V(\xi, \eta) = \frac{4Ze^2}{a} \left[ Q_0(\xi) - P_2(\eta) Q_2(\xi) \right].$$

where

$$(9a) \quad Q_0(\xi) = \frac{1}{2} \ln \left( \frac{\xi+1}{\xi-1} \right),$$

$$(9b) \quad Q_2(\xi) = \frac{1}{2} P_2(\xi) \ln \left( \frac{\xi+1}{\xi-1} \right) - \frac{3}{2} \xi.$$

With these explicit forms, the equations (7) become

$$(10) \quad \frac{d^2 W_l}{d\xi^2} - [V_0(\xi) + V_l(\xi)] W_l - \sum_{l'} W_{l'} [V^{(2)}_{ll'}(\xi) + V^{(4)}_{ll'}(\xi)] = 0,$$

where

$$(11a) \quad V_0(\xi) = \frac{2\mu Ze^2 a}{\hbar^2 (\xi^2 - 1)} \left[ \left( \xi^2 - \frac{1}{3} \right) \left( Q_0(\xi) - \frac{Ea}{4Ze^2} \right) + \frac{2}{15} Q_2(\xi) \right] - \frac{1}{(\xi^2 - 1)^2},$$

$$(11b) \quad V_l(\xi) = l(l+1) \left( \frac{1}{\xi^2 - 1} + \frac{\mu a^2}{4I} \right) \quad l \neq 0,$$

$$(11c) \quad V^{(2)}_{ll'}(\xi) = - \frac{2\mu Ze^2 a}{\hbar^2 (\xi^2 - 1)} C^{(2)}(l0|l'0) \left[ \frac{2}{3} \left( Q_0(\xi) - \frac{Ea}{4Ze^2} \right) + \left( \xi^2 - \frac{11}{21} \right) Q_2(\xi) \right],$$

$$(11d) \quad V^{(4)}_{ll'}(\xi) = \frac{2\mu Ze^2 a}{\hbar^2 (\xi^2 - 1)} \cdot \frac{12}{35} \cdot C^{(4)}(l0|l'0) Q_2(\xi).$$

The coefficients  $C^{(k)}(l0|l'0)$  are given in terms of Clebsch-Gordan coefficients by

$$(11e) \quad C^{(k)}(l0|l'0) = \left( \frac{2l+1}{2l'+1} \right)^{\frac{1}{2}} (kl00|kll'0)^2.$$

Formulae for  $C^{(2)}$  and  $(l0|l'0)$  and  $C^{(4)}$   $(l0|l'0)$  are given in the Appendix.

On inspecting the expressions for  $V^{(2)}_{ll'}(\xi)$  and  $V^{(4)}_{ll'}(\xi)$  we see that part of the coupling of the various  $W_l$  is caused by the non-central character of the potential and part by the nature of the spheroidal coordinate system. The term  $V^{(4)}_{ll'}(\xi)$  is much smaller than  $V^{(2)}_{ll'}(\xi)$  for all  $\xi$ .

Since the  $W_l(\xi)$  become very large near the nucleus making numerical work inaccurate, we replace the  $W_l$  in this region by  $Y_l \exp f(\xi)$  where  $\exp f(\xi)$  has roughly the behavior of the  $W_l$ . The equations in the  $Y_l(\xi)$  are then suitable for numerical solution. The function  $f(\xi)$  is suggested by the WKB method and is given by

$$(12) \quad f(\xi) = \int_{\xi}^{\xi_T} \left[ A \left( \frac{\xi^2 - \frac{1}{3}}{\xi^2 - 1} \right) (Q_0(\xi) - B) \right]^{\frac{1}{2}} d\xi = \int_{\xi}^{\xi_T} K(\xi) d\xi,$$

where  $A = 2\mu Ze^2 a / \hbar^2$ ,  $B = Ea / 4Ze^2$ , and  $\xi_T$  is the value of  $\xi$  for which  $Q_0(\xi) = B$ . The equations for the  $Y_l(\xi)$  are

$$(13) \quad \frac{d^2 Y_l}{d\xi^2} - 2K(\xi) \frac{dY_l}{d\xi} + [M(\xi) - V_l(\xi)] Y_l(\xi) - \sum_{l'} Y_{l'}(\xi) \times [V^{(2)}_{ll'}(\xi) + V^{(4)}_{ll'}(\xi)] = 0$$

where

$$(14) \quad M(\xi) = \frac{A}{(\xi^2 - 1)^2 K(\xi)} \left[ \frac{2}{3} \xi (Q_0(\xi) - B) + \frac{1}{2} \left( \xi^2 - \frac{1}{3} \right) \right] - \frac{A}{(\xi^2 - 1)} \frac{2}{15} Q_2(\xi) + \frac{1}{(\xi^2 - 1)^2}.$$

Equations (10) in the far region and (13) in the region near the nucleus must be solved subject to the boundary conditions. At infinity the  $W_l$  must behave as outgoing waves. Thus

$$(15) \quad W_l \rightarrow A_l e^{i\delta_l} [G_l(k_l a \xi / 2) + i F_l(k_l a \xi / 2)].$$

The functions  $G_l$  and  $F_l$  are the irregular and regular Coulomb functions respectively while the  $k_l$  are determined by  $E - \hbar^2 l(l+1)/2I = \hbar^2 k_l^2 / 2\mu = \frac{1}{2} \mu V_r^2$ . A summary of Coulomb functions is given in Fröberg (1955). The experimental intensities of the transitions to the states of different energy are proportional to  $V_l |A_l e^{i\delta_l}|^2$  which means that the  $A_l$ , but not the phase factors  $\delta_l$ , can be found from experiment. The  $\delta_l$  are found from the condition that the imaginary parts of the  $W_l(\xi)$  vanish at the nuclear surface.\* This ensures that there will be no large currents of alpha particles near the nuclear surface, which would be in contradiction with the idea of a slowly decaying virtual state. Application of this condition yields not one but  $2^{n-1}$  sets of relative phases for the alpha particle waves where  $n$  is the number of waves considered. This may be seen from the case of a spherical nucleus with no coupling where any  $\delta_l$  may be replaced by  $\delta_l + \pi$ . We have taken into account only the first three alpha particle waves corresponding to  $l = 0, 2, 4$ . The consequences of this limitation will be considered in the Discussion.

The problem is solved by finding six independent solutions of the three equations and choosing the linear combination of these solutions satisfying the boundary conditions. If  $(S_0^i, S_2^i, S_4^i)$  denotes the  $i^{\text{th}}$  independent solution, the general solution may be written as

$$(16) \quad W_l(\xi) = \sum_i \alpha_i S_l^i(\xi) \quad l = 0, 2, 4,$$

where the  $\alpha_i$  are complex constants.

Suppose we write the equations (10) as

$$(17) \quad d^2 W_l / d\xi^2 - (V_0^C + V_l^C) W_l = f_l$$

where  $V_0^C$  and  $V_l^C$  are terms chosen from the expansion of  $V_0$  and  $V_l$  in powers of  $1/\xi$  such that (17) would be the equations for Coulomb functions if  $f_l$  were zero. It then follows that  $f_l$  is the sum of the coupling terms and the remaining terms from the expansion of  $(V_0 + V_l) W_l$ . The solution of (17) satisfying the boundary condition at infinity is

$$(18) \quad W_l = A_l e^{i\delta_l} G_l(\xi) [1 - I_l(\xi)] + i A_l e^{i\delta_l} F_l(\xi) [1 + J_l(\xi)],$$

\*More precisely, the ratios of the imaginary to the real parts of the  $W_l$  must be the same for all  $l$  since the wave function may be multiplied by any complex number of unit magnitude.

where

$$(19a) \quad I_l(\xi) = \frac{2}{A_l e^{i\delta_l} k_l a} \int_{-\infty}^{\xi} F_l(\xi) f_l(\xi) d\xi$$

$$(19b) \quad J_l(\xi) = \frac{2}{i A_l e^{i\delta_l} k_l a} \int_{-\infty}^{\xi} G_l(\xi) f_l(\xi) d\xi,$$

as may be seen by differentiating (18) twice. In (18) and (19) we have written  $G_l(\xi)$  and  $F_l(\xi)$  for what, strictly speaking, should be  $G_l(k_l a \xi / 2)$  and  $F_l(k_l a \xi / 2)$ . Let us choose the independent solutions and their first derivatives at  $\xi_{\max}$ , that is at the value of  $\xi$  where the computer calculations are begun, according to the scheme of Table I.

TABLE I  
INDEPENDENT SOLUTIONS AT  $\xi = \xi_{\max}$

$i$	1	2	3	4	5	6
$l$						
0	$F_0$	$G_0$	0	0	0	0
2	0	0	$F_2$	$G_2$	0	0
4	0	0	0	0	$F_4$	$G_4$

We now summarize the nature of the computer calculations. The differential equations in spheroidal coordinates were programmed for FERUT by Mr. W. K. Hastings of H. S. Gellman and Company of Toronto. For the six cases in Table I and for each nuclide studied the computer integrates the equations in the  $W_l$  from  $\xi_{\max}$  to  $\xi_{T'} \approx \xi_T - 1$ . It then calculates  $f(\xi_{T'})$  and integrates the equations in the  $Y_l$  from  $\xi_{T'}$  to  $\xi_0$ . Also the differential equation  $df/d\xi = -K(\xi)$  is solved in the range from  $\xi_{T'}$  to  $\xi_0$ . The numerical method used for the solution of the equations is the Runge-Kutta method (Gill 1951).

The constants  $\alpha_i$  of the linear combination of the six independent solutions are determined in terms of the amplitudes at infinity by (16), (18), and Table I as

$$(20) \quad \begin{aligned} \alpha_1 &= i A_0 e^{i\delta_0} (1 + J_0) & \alpha_2 &= A_0 e^{i\delta_0} (1 - I_0) \\ \alpha_3 &= i A_2 e^{i\delta_2} (1 + J_2) & \alpha_4 &= A_2 e^{i\delta_2} (1 - I_2) \\ \alpha_5 &= i A_4 e^{i\delta_4} (1 + J_4) & \alpha_6 &= A_4 e^{i\delta_4} (1 - I_4) \end{aligned}$$

with the  $I_l$  and  $J_l$  being evaluated at  $\xi = \xi_{\max}$ , which was taken as 20. In evaluating the  $I_l$  and  $J_l$ , the  $W_l$  are replaced by their unperturbed forms  $A_l e^{i\delta_l} (G_l + iF_l)$ . The calculation of  $I_l$  and  $J_l$  involves products of two Coulomb functions, either with the same or different values of  $l$ , divided by  $\xi^2$  or  $\xi^3$  since we ignore higher inverse powers of  $\xi$ . The approximate expressions for Coulomb functions given in the Appendix can be used in the calculation. Trigonometric functions which are rapidly varying with respect to the rest of the integrand may be replaced by their average values. The evaluation of integrals with Coulomb functions of different  $l$  involves numerical integration.

After calculating the  $I_l$  and  $J_l$  and obtaining the results of the computer calculations, we must solve the equations  $\text{Im}\{W_l(\xi_0)\} = 0$  in order to determine the phase factors. The phase factors are small or differ from  $\pi$  by small amounts.  $\delta_4$  is generally larger than the others (or differs from  $\pi$  by a larger amount) essentially because  $A_4$  is considerably smaller than  $A_2$  or  $A_0$ . This small value of  $A_4$  makes  $J_4 = -I_4$  larger than  $J_0$  or  $J_2$ . In solving the three equations  $\text{Im}\{W_l(\xi_0)\} = 0$ , it is assumed that the  $\delta_l$  appearing in  $J_l$  and  $I_l$  are equal to zero or  $\pi$  and that the factors  $\cos \delta_l$  and  $\sin \delta_l$  appearing in the  $\alpha_l$  are  $\pm 1$  and  $\delta_l$  or  $\delta_l' + \pi$  respectively. This results in three linear algebraic equations for the  $\delta_l$  and  $\delta_l'$  which are solved by the usual method. Then a new value of  $J_4$  is calculated using the values of  $\delta_l$  obtained. This yields three new algebraic equations which are solved to give better values of  $\delta_l$  and  $\delta_l'$ . Then these values are used in calculating the  $W_l(\xi_0)$ . Equation (4) can then be used to find  $\Psi(\xi_0, \eta)$ , the wave function describing the alpha particle on the nuclear surface.

The four cases involving the various choices of phase factors will be referred to as follows. Case I has all three phase factors near zero while Case II has  $\delta_0$  and  $\delta_2$  near zero with  $\delta_4$  near  $\pi$ . For Cases III and IV  $\delta_0$  is near zero,  $\delta_2$  near  $\pi$ , and  $\delta_4$  near zero and  $\pi$  respectively.

#### DATA ON THE NUCLIDES STUDIED

Numerical results have been obtained for the nuclides  $\text{U}^{234}$ ,  $\text{Pu}^{238}$ ,  $\text{Cm}^{242}$ ,  $\text{Cf}^{246}$ ,  $\text{Fm}^{254}$ . These nuclides form a representative selection of the even-even alpha emitters for which energies and intensities of the decay to the first three states of the daughter nucleus have been measured. There are about a dozen of these nuclides which are far enough removed from the  $\text{Pb}^{208}$  closed shell so that the strong coupling Bohr-Mottelson model applies well. Table II gives

TABLE II  
EXPERIMENTAL DATA ON THE NUCLIDES STUDIED

Nuclide	$Q_{\text{eff}} = E$ (mev)	$E_2$ (kev)	$E_4$ (kev)	Intensity (%)		
				$l = 0$	$l = 2$	$l = 4$
$\text{U}^{234}$	4.887	52.4	170	72	28	0.3
$\text{Pu}^{238}$	5.626	43.50	143.31	72	28	0.095
$\text{Cm}^{242}$	6.251	44.11	146	73.7	26.3	0.035
$\text{Cf}^{246}$	6.905	42.12	140	78	22	0.16
$\text{Fm}^{254}$	7.361	42	139	83	17	0.4

experimental data on the nuclides which is of importance for the calculations. All of this data was taken from Perlman and Rasmussen (1957). In Table II,  $Q_{\text{eff}}$  is the effective total decay energy, which is the kinetic energy of the alpha particle-residual nucleus system, when the residual nucleus is in its ground state, plus the electron screening correction. The quantities  $E_2$  and  $E_4$  are the energies of the first and second excited states of the daughter nucleus.

Table III contains values of constants which are of importance for the

TABLE III  
IMPORTANT CONSTANTS USED IN THE NUMERICAL WORK

Nuclide	First $Q_0$ values			Second $Q_0$ values		
	$Q_0$ (barns)	$(10^{-15}\text{cm})$	$\xi_0$	$Q_0$ (barns)	$(10^{-15}\text{cm})$	$\xi_0$
U <sup>234</sup>	7.46	9.10	2.00	9.94	10.51	1.78
Pu <sup>298</sup>	8.37	9.54	1.93	11.16	11.01	1.73
Cm <sup>242</sup>	8.49	9.50	1.95	11.32	10.97	1.74
Cf <sup>256</sup>	8.87	9.61	1.94	11.83	11.10	1.73
Fm <sup>254</sup>	9.07	9.62	1.96	12.10	11.11	1.75

calculations. Two intrinsic quadrupole moments,  $Q_0$ , were used for each nuclide. These were calculated from the semiempirical formula,

$$(21) \quad Q_0 = CZE_2^{-1/2}A^{-1/6} \approx CZE_2^{-1/2} \text{ barns},$$

with  $C$  being taken as 0.6 and 0.8 and  $E_2$  being measured in kilovolts. This type of relationship is suggested by the Bohr-Mottelson model (Bohr and Mottelson 1953), but the constant  $C$  is adjusted to give values in line with the experimental values which have been found for nuclides in this region of  $A$  values (Alder *et al.* 1956). This adjustment is necessary since the deformation parameter  $\beta$  calculated from rotational energy levels does not agree with that calculated from  $Q_0$  (Sunyar 1955).

The value of  $\xi$  at the nuclear surface, i.e.,  $\xi_0$ , is calculated on the assumption that the nuclear spheroid has the same volume as a sphere of radius  $R_0$  where  $R_0$  is found from  $R_0 = 1.35 \times 10^{-13} A^{1/3} \text{ cm}$ . The significance of this value is discussed later.

#### RESULTS OF THE COMPUTATIONS

Table IV gives the values of  $W_2/W_0$  and  $W_4/W_0$  at the nuclear surface for all the nuclides studied. Figs. 1 to 10 are graphs of  $|\Psi|^2$  vs.  $\cos^{-1}\eta$  on the nuclear surface where the wave function  $\Psi(\xi, \eta)$  is given by (4). For these graphs the normalization of the wave function was chosen arbitrarily, but is the same for all four cases of a given nuclide with given  $Q_0$ . Fig. 11 is a graph of  $|\Psi|^2$  vs.  $\cos^{-1}\eta$  for three values of  $\xi$  for Case I of Cm<sup>242</sup>, 2nd  $Q_0$  value. The normalization is chosen to give approximately the same peak height for each value of  $\xi$ .

The penetration factor,  $P$ , of the electrostatic potential barrier is defined as

$$(22) \quad P = \int_{S_\infty} |\Psi|^2 dS / \int_{S_n} |\Psi|^2 dS,$$

where  $S_\infty$  is the surface of a large sphere centered at the nucleus and  $S_n$  is the nuclear surface. In Table V are listed the natural logarithms of the penetration factors or their ratios for all cases studied for the first and second  $Q_0$  values of the nuclides respectively. In this table  $P_e$  refers to the penetration factor for a spherical nucleus with  $l = 0$ , i.e.  $1/[G_0(k_0 R_0)]^2$ , while the symbols

FIGS. 1-10. The density of alpha particles on the nuclear surface as a function of  $\cos^{-1}\eta$ , which is approximately the polar angle. Each figure is for one nuclide with a given quadrupole moment  $Q_0$ . The four cases for each nuclide are discussed in the text.

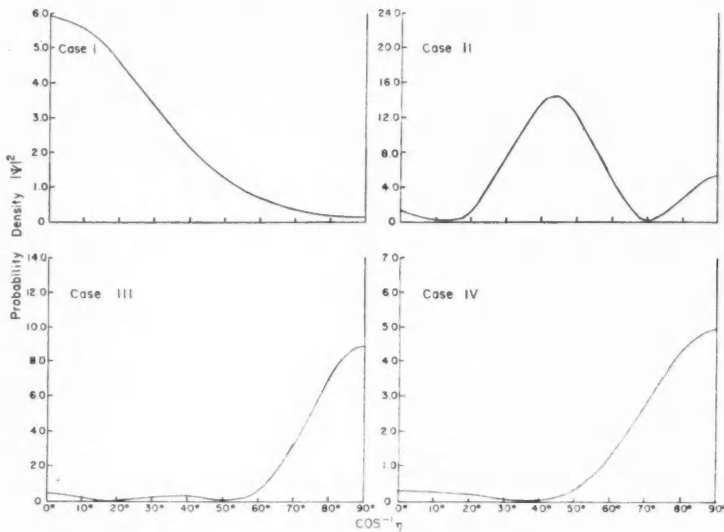


FIG. 1.  $U^{234}$   $Q_0 = 7.46$  barns.

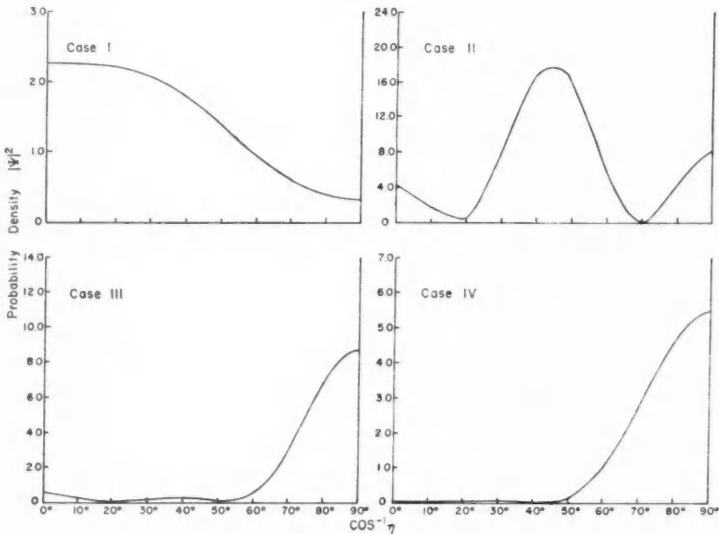
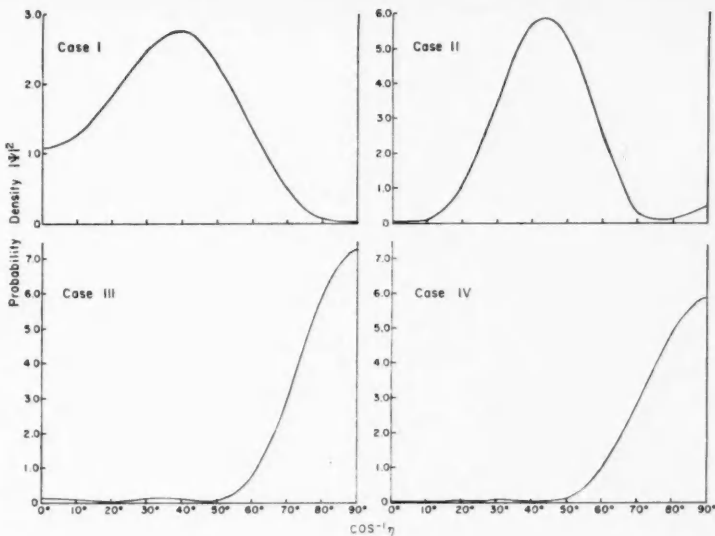
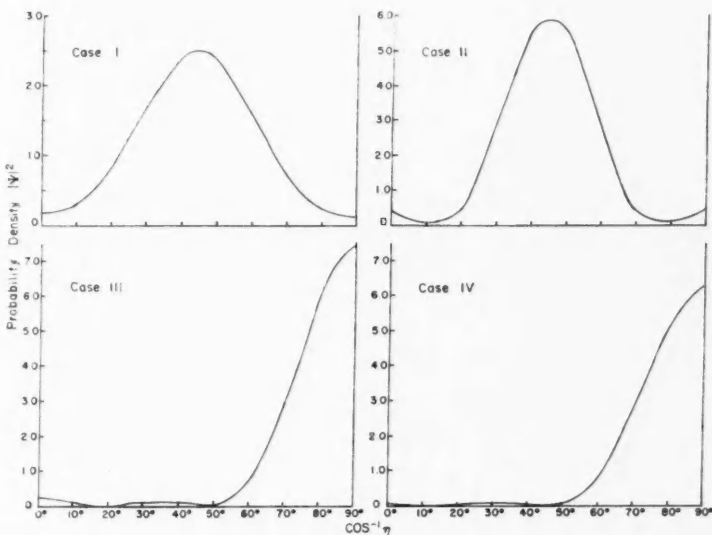
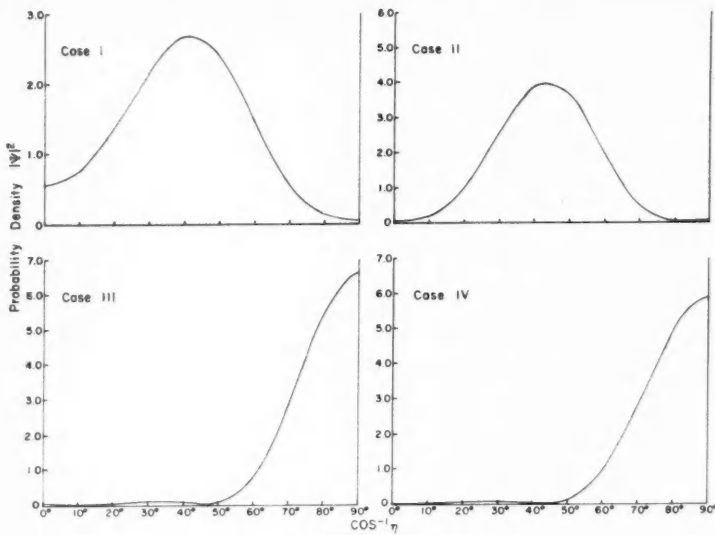
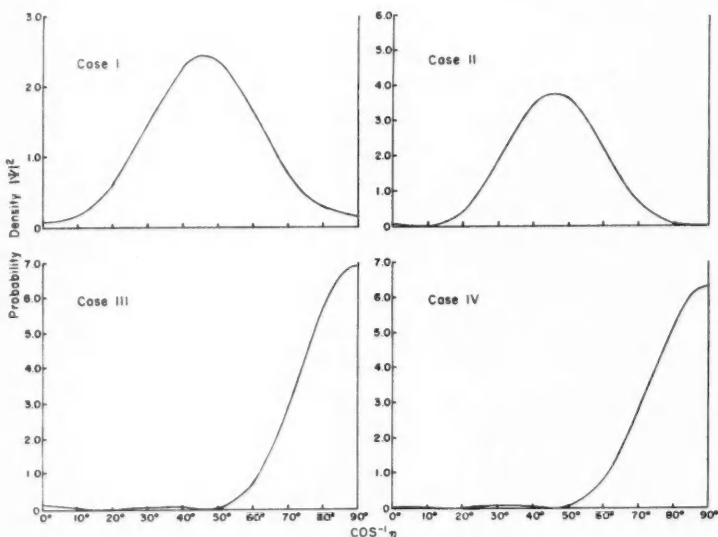
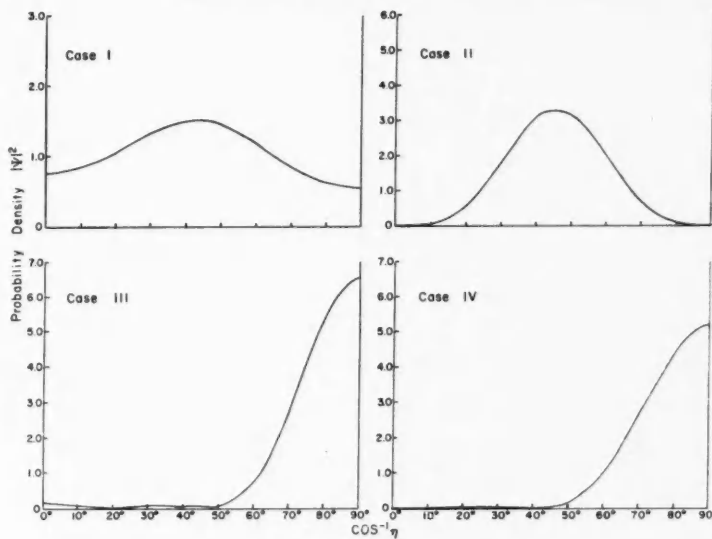
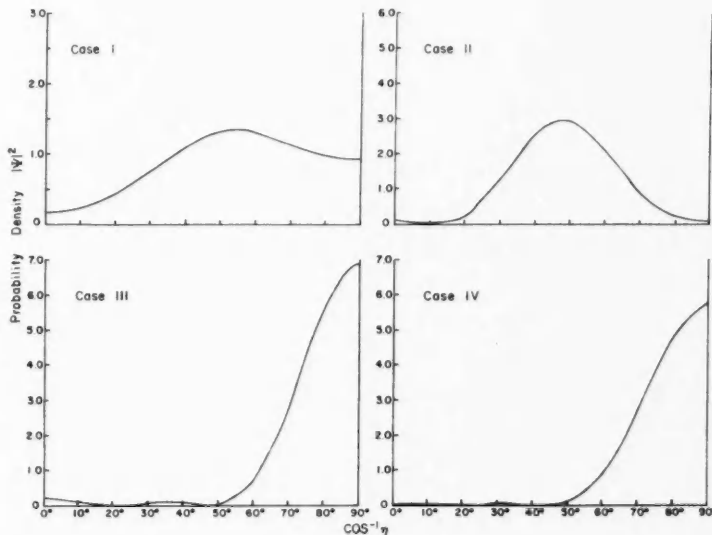


FIG. 2.  $U^{234}$   $Q_0 = 9.94$  barns.

FIG. 3.  $\text{Pu}^{238}$   $Q_0 = 8.37$  barns.FIG. 4.  $\text{Pu}^{238}$   $Q_0 = 11.16$  barns.

FIG. 5.  $\text{Cm}^{242}$   $Q_0 = 8.49$  barns.FIG. 6.  $\text{Cm}^{242}$   $Q_0 = 11.32$  barns.

FIG. 7. Cf<sup>246</sup>  $Q_0 = 8.87$  barns.FIG. 8. Cf<sup>246</sup>  $Q_0 = 11.83$  barns.

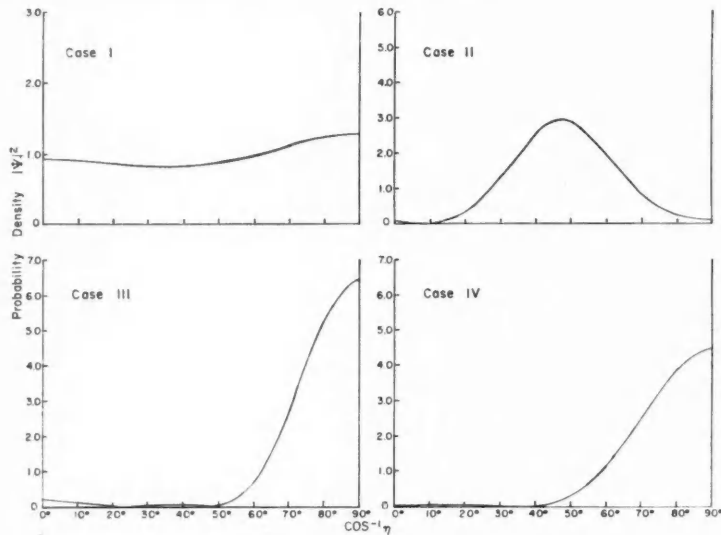
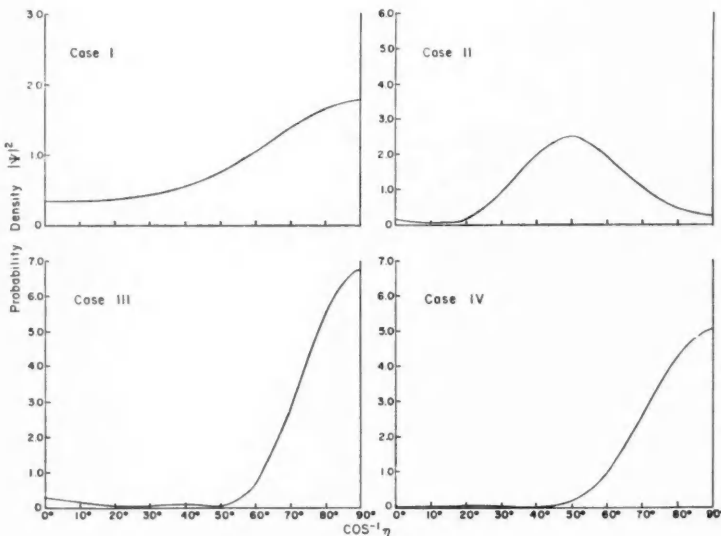
FIG. 9.  $Fm^{264}$   $Q_0 = 9.07$  barns.FIG. 10.  $Fm^{264}$   $Q_0 = 12.10$  barns.

TABLE IV  
VALUES OF  $W_2/W_0$  AND  $W_4/W_0$  AT  $\xi = \xi_0$  FOR THE NUCLIDES STUDIED

Nuclide		Case I	Case II	Case III	Case IV
U <sup>234</sup>		$Q_0 = 7.46$ barns			
	$W_2/W_0$	0.59	1.29	-1.07	-0.92
	$W_4/W_0$	0.04	-1.67	0.70	0.17
		$Q_0 = 9.94$ barns			
	$W_2/W_0$	0.32	1.38	-1.05	-0.91
	$W_4/W_0$	-0.07	-2.04	0.70	0.29
Pu <sup>238</sup>		$Q_0 = 8.37$ barns			
	$W_2/W_0$	0.43	0.67	-0.98	-0.92
	$W_4/W_0$	-0.31	-0.86	0.53	0.34
		$Q_0 = 11.16$ barns			
	$W_2/W_0$	0.23	0.53	-0.98	-0.92
	$W_4/W_0$	-0.37	-0.94	0.56	0.42
Cm <sup>242</sup>		$Q_0 = 8.49$ barns			
	$W_2/W_0$	0.36	0.46	-0.94	-0.91
	$W_4/W_0$	-0.35	-0.61	0.46	0.36
		$Q_0 = 11.32$ barns			
	$W_2/W_0$	0.17	0.30	-0.95	-0.92
	$W_4/W_0$	-0.38	-0.64	0.51	0.43
Cf <sup>256</sup>		$Q_0 = 8.87$ barns			
	$W_2/W_0$	0.11	0.27	-0.91	-0.85
	$W_4/W_0$	-0.13	-0.55	0.48	0.29
		$Q_0 = 11.83$ barns			
	$W_2/W_0$	-0.09	0.11	-0.93	-0.87
	$W_4/W_0$	-0.13	-0.53	0.52	0.37
Fm <sup>254</sup>		$Q_0 = 9.07$ barns			
	$W_2/W_0$	-0.07	0.14	-0.88	-0.79
	$W_4/W_0$	0.04	-0.51	0.49	0.20
		$Q_0 = 12.10$ barns			
	$W_2/W_0$	-0.25	-0.02	-0.91	-0.82
	$W_4/W_0$	0.05	-0.45	0.52	0.29

TABLE V  
BARRIER PENETRATION FACTORS

Nuclide	$\ln P_e$	$\ln(P_{HW}/P_e)$	$\ln(P_I/P_e)$	$\ln(P_{II}/P_e)$	$\ln(P_{III}/P_e)$	$\ln(P_{IV}/P_e)$
First $Q_0$ values						
U <sup>234</sup>	-80.76	2.75	0.99	-0.16	-1.80	-1.35
Pu <sup>238</sup>	-72.48	2.96	0.80	0.37	-1.69	-1.51
Cm <sup>242</sup>	-67.01	2.90	0.77	0.58	-1.49	-1.40
Cf <sup>256</sup>	-62.10	2.90	0.70	0.70	-1.43	-1.25
Fm <sup>254</sup>	-59.40	2.85	0.55	0.44	-1.29	-1.03
Second $Q_0$ values						
U <sup>234</sup>	-80.76	3.67	1.19	-0.13	-2.21	-1.75
Pu <sup>238</sup>	-72.48	3.93	1.06	0.66	-1.91	-1.74
Cm <sup>242</sup>	-67.01	3.84	0.83	0.68	-1.87	-1.79
Cf <sup>256</sup>	-62.10	3.86	0.58	0.50	-1.86	-1.68
Fm <sup>254</sup>	-59.40	3.79	0.39	0.47	-1.63	-1.37

$P_1$  to  $P_{IV}$  refer to Cases I to IV above, and  $P_{HW}$  refers to the penetration factor as calculated by Hill and Wheeler (1953) assuming emission of alphas to occur only radially at the poles ( $\theta = 0, \pi$ ).

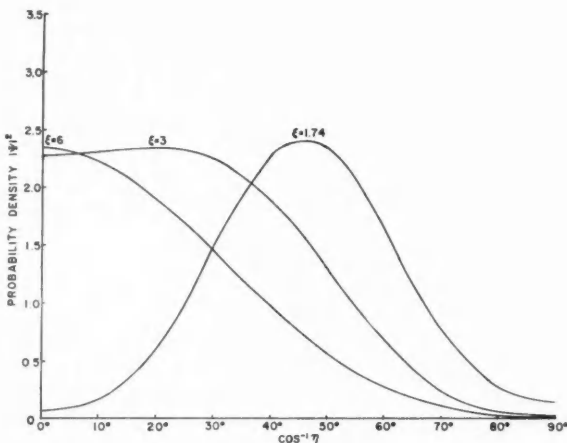


FIG. 11.  $|\Psi|^2$  is plotted against  $\cos^{-1}\eta$  for  $\xi = 1.74, 3, 6$  for Case I of  $\text{Cm}^{232}$ ,  $Q_0 = 11.32$  barns. This figure illustrates how the angular distribution alters as the distance from the nucleus is increased.

#### DISCUSSION

For Case I the probability density on the nuclear surface is peaked about the nuclear symmetry axis for  $\text{U}^{234}$ . The peak shifts to midway between the symmetry axis and the equator for  $\text{Pu}^{238}$ ,  $\text{Cm}^{242}$ , and  $\text{Cf}^{246}$ , while for  $\text{Fm}^{254}$  the distribution is mildly peaked about the equator. The distribution functions are not very different for the two  $Q_0$  values of the nuclides, although there is a tendency for a shift in probability towards the equator for the larger of the two quadrupole moments. However, we cannot say definitely that the shift would be greater if the quadrupole moments were increased still more. The probability density for Case II is always peaked midway between the equator and the poles, while for Cases III and IV the peaking is always very strong at the equator with little chance of an alpha particle being found near the poles.

Rasmussen and Segall (1956) have also integrated the coupled equations inward by a numerical method for  $\text{Cm}^{232}$ . Although they used a quadrupole moment considerably larger than those employed in this paper, their plots of  $|\Psi|^2$  vs.  $\cos^{-1}\eta$  on the nuclear surface are in qualitative agreement with ours.

We note from the data in Table II that the intensities of alphas with  $l = 2$  decrease with increasing mass number from  $\text{U}^{234}$  to  $\text{Fm}^{254}$  while the intensities of particles with  $l = 4$  decrease to a minimum at  $\text{Cm}^{242}$  and then increase. This variation in the experimental intensities of the states is quite important for the different types of behavior of the probability density at the nuclear surface as can be seen by noting that

$$(23) \quad W_l(\xi_0) \approx A_0 S_l^2 + A_2 \cos \delta_2 S_l^4 + A_4 \cos \delta_4 S_l^6,$$

where  $\cos \delta_2$  and  $\cos \delta_4$  are roughly  $\pm 1$  depending on the case. This relation would hold true if the  $J_i$  and  $J_i$  were all zero and if the phase factors were zero or  $\pi$ . Since  $S_l^2$  and  $S_l^6$  always have opposite signs from  $S_l^4$  at the surface because  $V^{(2)}(\xi)$  is negative in the region near the nucleus, the relative values of the  $A_i$  have a large effect on the  $W_l(\xi_0)$ .

The most serious limitation on the accuracy of the present work is the neglect of alpha particle waves with angular momenta greater than  $l = 4$ . This causes an uncertainty in the values of the  $W_l(\xi_0)$  which increases from  $l = 0$  to  $l = 4$ . Besides the computational difficulty involved, the chief justification for the neglect of the waves of higher angular momenta is the fact that the hindrance factors of these waves are high. This means that  $A_6 G_6$  would be considerably less than  $A_0 G_0$  at the nuclear surface if we consider a spherical nucleus without non-central interaction. However, Rasmussen and Hansen (to be published) have made computer calculations for  $Cm^{242}$  including the  $l = 6$  wave and have found that the distributions on the nuclear surface are altered somewhat. The values of  $W_2/W_0$  and  $W_4/W_0$  on the nuclear surface are such that the effect of considering higher  $l$  values on the plot of  $|\Psi|^2$  vs.  $\cos^{-1}\eta$  would likely be greatest for Case I of  $U^{234}$  and  $Fm^{254}$ .

Only one of the four cases represents the actual physical situation. It is therefore important to know which set of phase factors is correct. There appears to be no simple way of finding phase factors for even-even nuclei experimentally. A study of the alpha-gamma angular correlation in  $Am^{241}$  shows that the  $l = 0$  and  $l = 2$  waves have approximately the same phase factors (Perlman and Rasmussen 1957). This is an odd  $A$  nuclide and the two angular momentum waves lead to the same final nuclear state. If we nevertheless assume that the same phase relation holds true for even-even nuclides, we restrict ourselves to Cases I and II. If we go still farther and assume that all phase factors are approximately equal, we restrict ourselves to Case I. Cases III and IV appear improbable a priori because the distribution on the surface is restricted so greatly to the equatorial region.

The graph of  $|\Psi|^2$  vs.  $\cos^{-1}\eta$  for three values of  $\xi$  (Fig. 11) shows a shift in probability density towards the symmetry axis with increasing  $\xi$ . A physical explanation can be given for this behavior. The Coulomb potential on the surface is higher at the equator than at the poles because the nuclear radius is smaller at the equator. This effect outweighs that of the quadrupole potential which is positive at the poles and negative at the equator. Also the spheroids defined by  $\xi$  become more nearly spherical as  $\xi$  increases so that the distance between the surfaces  $\xi_0$  and  $\xi$  is less at the poles than at the equator. For these reasons, alpha particles can penetrate more easily through the polar barrier and consequently the density maximum shifts towards the poles as  $\xi$  increases.

With one exception, the barrier penetration factors for Cases I and II are greater than those for spherical nuclei with  $l = 0$ , but only by a factor which is about two on the average. The penetration factors for Cases III and IV are less than those for spherical nuclei. This is not surprising since the distribution of alphas on the surface in these cases is always highly peaked about the equator. The potential barrier is, of course, higher and thicker at the equator.

Hill and Wheeler (1953) have considered the effect of the spheroidal nucleus on barrier penetration by recalculating the WKB integral for  $1/[G_0(kR_0)]^2$ . This results in an enhancement of the one-dimensional penetration at an angle  $\theta$  to the symmetry axis by the factor  $\exp[2BP_2(\cos\theta)]$  where  $B$  is a parameter proportional to the nuclear deformation. They estimate roughly the magnitude of the effect by setting  $\theta = 0$  in the exponential factor. This gives an enhancement of barrier penetration by a factor of about 15 to 20 for the first  $Q_0$  values and about 40 to 50 for the second  $Q_0$  values. If we average the enhancement factor over solid angle, we get

$$(24) \quad \frac{1}{4\pi} \int \exp[BP_2(\cos\theta)] d\Omega = \sqrt{\left(\frac{1}{3B}\right)} \exp(-B) \int_0^{\sqrt{(3B)}} \exp x^2 dx,$$

which yields values of the order of 2 or 3.

Fröman (1957) has recently given a treatment of the alpha decay of spheroidal nuclei in which he derives approximate analytical expressions relating the distribution on the nuclear surface to the intensities of the various angular momentum waves at infinity. We now compare our results for the larger  $Q_0$  value of  $Cm^{22}$  with those obtained using Fröman's formulae. From Fröman's equation (VI-12) we get

$$(25) \quad \frac{\sum_r k_{rr}(B)a_r}{\sum_r k_{0r}(B)a_r} = \pm \frac{A_t G_t(k_0 R_0)}{A_0 G_0(k_0 R_0)},$$

where the  $k_{rr}(B)$  form a matrix describing the coupling effects and are defined on page 19 of Fröman's paper. The  $a_r$  are the coefficients of the  $Y_w(\theta, \phi)$  in the expansion of the alpha wave function on the nuclear surface in terms of spherical harmonics. Equations (25) are two equations from which we can find the ratios  $a_2/a_0$  and  $a_4/a_0$  from the experimental  $A_t$  and the matrix elements  $k_{rr}(B)$  calculated for  $B = 1.92$ . In equations (25) a plus sign in front of the ratio  $(A_t G_t)/(A_0 G_0)$  corresponds to the case where  $\delta_t$  is near 0 while a minus sign corresponds to the case where  $\delta_t$  is near  $\pi$ . Thus a comparison can be made with the results for the four possible sets of phase factors. Since the  $a_r$  are coefficients of the expansion of the wave function on the nuclear surface in terms of the  $Y_w(\theta, \phi)$ , it is necessary to expand the  $Y_w(\theta, \phi)$  in terms of the  $Y_w(\cos^{-1}\eta, \phi)$  in order to make comparisons with our computer calculations. Table VI contains the results of the calculations based on Fröman's work along with our values for comparison. It is seen that Fröman's results are in reasonable agreement with the numerical calculations.

TABLE VI  
Values of  $W_2/W_0$  and  $W_4/W_0$  at  $\xi = \xi_0$  for  $Cm^{22}$  using Fröman's formulae

	Case I	Case II	Case III	Case IV
$Q_0 = 11.32$ barns				
$W_2/W_0$ Fröman	0.19	0.33	-0.94	-0.92
This work	0.17	0.30	-0.95	-0.92
$W_4/W_0$ Fröman	-0.30	-0.59	0.52	0.44
This work	-0.38	-0.64	0.51	0.43

Fröman has also shown that deformations in the nuclear surface of higher order than the  $Y_{20}$  deformation may be of importance for alpha decay. However, it is difficult to treat this consideration systematically as there is no experimental data on higher order deformations.

Nosov (1957) has derived formulae for the alpha decay of even-even spheroidal nuclei which are similar to those of Fröman except that Fröman's  $B$  is replaced by a quantity which is equal to  $B$  plus a small imaginary part.

We have assumed that the nucleus has a sharply defined surface with a uniform charge distribution inside. Actually the charge density tapers off gradually near the nuclear surface. This effect changes the electrostatic potential somewhat but is probably not too important for our calculations. Also, the short range nuclear forces may be of some importance near the nucleus. However, it is difficult to treat this effect quantitatively since the specific form of the interaction is not known.

A nuclear radius of  $1.35 \times 10^{-13} A^{1/3}$  cm was used in all calculations. Perhaps we should have used a larger radius in determining the value of  $\xi_0$  at which to stop the inward integration of the equations in order to allow for the radius of the alpha particle. Rasmussen and Segall (1956) made their calculations for radii of  $1.2 \times 10^{-13} A^{1/3}$  cm and  $1.35 \times 10^{-13} A^{1/3}$  cm and found that the change in radius did not affect the distribution on the surface greatly.

#### ACKNOWLEDGMENTS

One of the authors (E.M.P.) is grateful to the National Research Council of Canada for financial aid in the form of studentships. We are indebted to Dr. H. S. Gellman for discussions concerning the suitability of the problem for the computer and to Mr. W. K. Hastings for writing the program and for instruction in the operation of the computer. The staff of the Computation Centre of the University of Toronto was helpful in scheduling machine time and in providing assistance in operating the computer.

#### APPENDIX

Explicit formulae for  $C^{(2)}(l0|l'0)$  and  $C^{(4)}(l0|l'0)$  are given below

$$(26a) \quad C^{(2)}(l0|l'0) = \frac{l(l+1)}{(2l-1)(2l+3)},$$

$$(26b) \quad C^{(2)}(l0|l+2, 0) = \frac{3}{2} \frac{(l+1)(l+2)}{(2l+3)[(2l+1)(2l+5)]^{\frac{1}{4}}},$$

$$(26c) \quad C^{(4)}(l0|l'0) = \frac{9}{4} \frac{(l-1)l(l+1)(l+2)}{(2l-3)(2l-1)(2l+3)(2l+5)},$$

$$(26d) \quad C^{(4)}(l0|l+2, 0) = \frac{5}{2} \frac{l(l+1)(l+2)(l+3)}{(2l-1)(2l+3)(2l+7)[(2l+1)(2l+5)]^{\frac{1}{4}}},$$

$$(26e) \quad C^{(4)}(l0|l+4, 0) = \frac{35}{8} \frac{(l+1)(l+2)(l+3)(l+4)}{(2l+3)(2l+5)(2l+7)[(2l+1)(2l+9)]^{\frac{1}{4}}}.$$

Approximate formulae for Coulomb functions in the region well beyond

the classical turning point can be derived from equations in Fröberg (1955). These formulae, valid for small values of  $l$ , are

$$(27a) \quad G_l(kr) = (\coth u)^{1/2} \cos(\phi - g_l)$$

$$(27b) \quad F_l(kr) = (\coth u)^{1/2} \sin(\phi - g_l)$$

with  $\coth u = (kr/2\eta)^{1/2}$ ,  $\phi = 2\eta(\sinh u \cosh u - u) + \pi/4$ ,  $g_l = [l(l+1)/2\eta]\tanh u$ , and  $\eta = 2\mu Ze^2/\hbar^2 k$ .

#### REFERENCES

- ALDER, K., BOHR, A., HUUS, I., MOTTELSON, B., and WINTHER, A. 1956. Rev. Mod. Phys. **28**, 432.
- BOHR, A. and MOTTELSON, B. R. 1953. Kgl. Danske Videnskab. Selskab., Mat.-fys. Medd. **27**, No. 16.
- FRÖBERG, C. 1955. Rev. Mod. Phys. **27**, 399.
- FRÖMAN, P. O. 1957. Kgl. Danske Videnskab. Selskab., Mat.-fys. Skr. **1**, No. 3.
- GILL, S. 1951. Proc. Cambridge Phil. Soc. **47** (Part I), 96.
- HILL, D. L. and WHEELER, J. A. 1953. Phys. Rev. **89**, 1102.
- NOSOV, V. G. 1957. Dokl. Akad. Nauk. SSSR, **112**, 414.
- PERLMAN, I. and RASMUSSEN, J. O. 1957. Alpha radioactivity. Handbuch der Physik, Vol. 42 (Springer-Verlag, Berlin).
- PRESTON, M. A. 1949. Phys. Rev. **75**, 90.
- RASMUSSEN, J. O. 1953. UCRL Report 2431.
- RASMUSSEN, J. O. and HANSEN, E. R. (to be published).
- RASMUSSEN, J. O. and SEGALL, B. 1956. Phys. Rev. **103**, 1298.
- SUNYAR, A. W. 1955. Phys. Rev. **98**, 653.

# THE NUCLEAR ABSORPTION OF X-RAYS BY OXYGEN<sup>1</sup>

A. K. M. SIDDIQ<sup>2</sup> AND R. N. H. HASLAM

## ABSTRACT

The total X-ray attenuation ratio in water was measured as a function of energy in the region 15–25 Mev, with a view to studying the nuclear absorption process in oxygen. The known energy response characteristics of several "activity detectors" ( $Zn^{64}(\gamma, n)Zn^{63}$ ,  $C^{12}(\gamma, n)C^{11}$ ,  $S^{32}(\gamma, d)P^{30}$ ,  $O^{16}(\gamma, n)O^{15}$ ) to bremsstrahlung were employed in these measurements.

The experimental values of the attenuation ratios were compared to the predicted values calculated on the basis of various assumptions concerning the nuclear absorption process.

The best description of the nuclear absorption process in oxygen appears to be continuous absorption on which relatively small absorption peaks are superimposed.

## INTRODUCTION

In the process of absorption of X-rays, electronic effects (Compton effect, photoelectric effect, pair and triplet production) play the major role, but in the energy range 10 to 30 Mev nuclear processes may be appreciable, particularly in the case of low  $Z$  elements. Several investigations of this phenomenon have previously been carried out, notably by Adams (1948), Walker (1949), and Haslam (1953). Electronic effects have been investigated thoroughly both theoretically (White 1952) and experimentally. The object of this paper is to discuss the part played by nuclear absorption leading to photonuclear reactions in the absorption of X-rays by oxygen, in order to estimate the magnitude of the effect, and also to investigate the mechanism of the nuclear absorption process.

Various nuclear reactions result from the absorption of X-rays by nuclei. Investigation of the activation curves for several low  $Z$  elements demonstrates the existence of sharp "breaks" (Haslam 1952), rather than the reaction yield being a smooth function of energy. These breaks have been attributed to the existence of discrete photon "levels" in the nucleus. This raises the question of the relative importance of discrete levels compared to continuous absorption in the "giant resonance" region. A further possibility is a continuous absorption on which is superimposed absorption in discrete levels.

Suppose an X-ray beam is passed through an absorber and the attenuation of the beam is measured by means of the activity induced in a suitable detector placed behind the absorber. If the detector and absorber are of the same material, and if absorption takes place in discrete levels, one would expect the measured nuclear contribution to the absorption process to be enhanced, since just those photons to which the detector is sensitive are preferentially absorbed. If the absorber and detector are of different materials and if the detecting reaction is produced by photons in well-defined energy regions

<sup>1</sup>Manuscript received March 3, 1958.

Contribution from the Department of Physics, University of Saskatchewan.

<sup>2</sup>Now at the University of Dacca, Dacca, East Pakistan.

which differ from the absorbing levels, little or no nuclear absorption would be detected.

The nuclear reactions which are important for absorption of X-rays in the oxygen nucleus in the region up to 25 Mev are  $O^{16}(\gamma, n)O^{15}$  and  $O^{16}(\gamma, p)N^{15}$ . The contributions of other reactions in oxygen are negligible in the 25 Mev energy range. In calculating values of the total absorption ratios, the electronic absorption coefficients as given by White (1952) were used. In the course of the experiment these theoretical electronic coefficients were checked using a zinc detector whose response peaks in the energy region where nuclear absorption is not very important. These results were used to adjust electronic absorption coefficients.

#### EXPERIMENTAL METHOD

##### General

The experimental arrangement adopted is shown in Fig. 1. The well-collimated X-ray beam from a 25 Mev betatron passes through the front

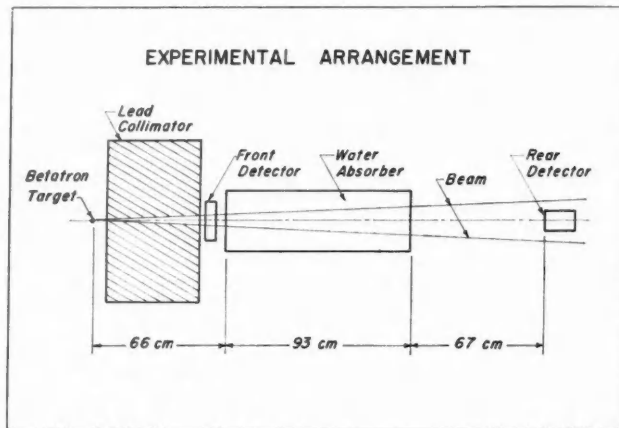


FIG. 1. Experimental arrangement.

detector, water absorber, and a rear detector placed in "good geometry." The front detector serves as a beam monitor and makes it unnecessary to measure the X-ray dose since the activity built up in it is directly proportional to that in the rear detector. The detectors are irradiated in fixed positions, first without the absorber, and a ratio of activity of the front detector,  $A_F$ , to that of the rear one,  $A_B$ , is measured. In the same way the ratio of the activities  $A'_F$  and  $A'_B$  with absorber in place is determined. Thus an absorption ratio  $R$ , which is independent of geometry, dose, etc. is found:

$$R = \frac{A'_F/A'_B}{A_F/A_B} = \frac{A_B/A_F}{A'_B/A'_F}.$$

If  $A_F = A'_F$ , which is the case if the same X-ray dose is given to the front detector with and without the absorber in place, the spectrum of X-rays striking the front detector being, of course, the same in both cases, then,

$$R = \frac{A_B}{A'_B}.$$

In future we shall assume that the appropriate normalization has been carried out.

$$A_B = C \int_{E_t}^{E_0} \sigma(E) P(E, E_0) dE,$$

$$A'_B = C \int_{E_t}^{E_0} \sigma(E) P(E, E_0) e^{-\mu_T(E)X} dE,$$

where  $\sigma(E)$  is the cross section of the detecting reaction at energy  $E$ , and  $E_t$  the threshold of this reaction.  $P(E, E_0)$  is proportional to the number of photons per 1/2 Mev energy interval centered on the energy  $E$  when the betatron is operating at energy  $E_0$ .  $X$  is the thickness of the absorber, and  $\mu_T(E)$  the total absorption coefficient of the absorber at energy  $E$ . Further, since  $C$  is the same in both expressions, and since a ratio of the two is taken, we shall drop the subscript and the proportionality constant and write:

$$R = \frac{A}{A'},$$

with

$$(1) \quad A = \int_{E_t}^{E_0} \sigma(E) P(E, E_0) dE,$$

$$A' = \int_{E_t}^{E_0} \sigma(E) P(E, E_0) e^{-\mu_T(E)X} dE.$$

The ratio  $R$  is determined experimentally (as a function of peak energy  $E_0$ ) and compared with theoretical values obtained by making various assumptions concerning  $\mu_T(E)$ , that is to say, concerning the nature of the absorption process.

#### *Absorber*

The absorber employed in these experiments consisted of a water column 93 cm long and 7.5 cm in diameter. The ends of the water column were closed with lucite windows of 0.3 cm total thickness. The absorption contribution of these windows was taken into account separately in calculation of the total absorption. The apparatus was aligned in the beam using X-ray photographs. The betatron beam was so collimated that it did not strike the absorber walls.

#### *Irradiation*

An irradiation procedure was adopted such that optimum counting statistics were obtained, the length of the irradiation varying with energy. In order to avoid systematic errors arising from energy drift or counter sensitivity change, samples were irradiated alternately with and without an absorber.

### Counting

The detecting samples were counted in cylindrical geometry by Victoreen 1B85 Geiger tubes feeding into Berkeley model 2000 scalers which were started and stopped by a relay timer system. Counter sensitivity was regularly checked against a uranium oxide standard. Loss of counts due to high counting rates was negligibly small.

### Detecting Reactions

Some characteristics of the detecting reactions employed appear in Table I.

TABLE I  
DETECTING REACTION DATA

Detecting reaction	Sample material	Threshold (Mev)	Cross-section peak (Mev)	Half-life (min)	Reference
O <sup>16</sup> ( $\gamma$ , n)O <sup>15</sup>	Boric acid	15.6	24	2.0	Horsley 1952
Zn <sup>64</sup> ( $\gamma$ , n)Zn <sup>63</sup>	Zinc sheet	11.4	19	38.0	Katz 1951a
C <sup>12</sup> ( $\gamma$ , n)C <sup>11</sup>	Polystyrene	18.7	23	20.6	Haslam 1953
S <sup>32</sup> ( $\gamma$ , d)P <sup>30</sup>	Flowers of sulphur	19.4	26	2.55	Katz 1951b

### Errors

The detecting reactions employed exhibited virtually no spurious activities. The maximum energy drift of the betatron was estimated to be of the order of 60 kev during the course of the experiments, while the absolute energy scale calibration was known within  $\pm 50$  kev. The positions and sizes of the samples and the size of the beam being well defined, the secondary scattering into the back detector was calculated and corrections were applied to the measured  $R$  values. The magnitude of these corrections in no case exceeded 0.4% of the apparent value.

The factor limiting the accuracy of these experiments was the achievable counting rate, particularly in the low energy region.

## THEORY

### General

Nuclear absorption in oxygen is due principally to the reactions O<sup>16</sup>( $\gamma$ , n)O<sup>15</sup> and O<sup>16</sup>( $\gamma$ , p)N<sup>15</sup>. The level structure of the ( $\gamma$ , n) reaction has been investigated by Penfold (1955), whose results are followed in this discussion. The integrated cross section of each level was determined, and the peak height was computed, assuming a Breit-Wigner resonance shape, and a width of 25 kev for all levels.

The results of the investigations of Stephens (1955) and of Johansson (1955) and Cohen (1956) seem to indicate that the location and magnitude of the levels in the reaction O<sup>16</sup>( $\gamma$ , p)N<sup>15</sup> are consistent with the observed "breaks" in the oxygen ( $\gamma$ , n) reaction. The cross-section curve of Stephens (1955) was reconstructed taking into account transitions to the 5.3 Mev and 6.3 Mev levels of N<sup>15</sup>, as well as to the ground state.

This reconstructed curve has an integrated cross section almost twice that of the corresponding ( $\gamma$ , n) reaction. A value of the integrated cross section of

the  $(\gamma, p)$  reaction twice that of the  $(\gamma, n)$  reaction seems to be of the order expected from the branching ratio  $G_n = 0.36$  (Penfold 1955).

#### *Smooth Absorber and Smooth Detector*

Consider that nuclear absorption of photons in oxygen takes place continuously over the energy region in question and that the response characteristics of the detectors are smooth, continuous functions of energy.

Then

$$A = \int_{E_t}^{E_0} \sigma(E) P(E, E_0) dE,$$

and

$$A' = \int_{E_t}^{E_0} \sigma(E) P(E, E_0) e^{-(\mu_e + \mu_p + \mu_n)X} dE,$$

where  $\mu_e$ ,  $\mu_p$ , and  $\mu_n$  are the absorption coefficients representing interactions with electrons, protons, and neutrons respectively. Thus the absorption ratio is given by:

$$(2) \quad R \equiv \frac{A}{A'} = \left( \int_{E_t}^{E_0} \sigma(E) P(E, E_0) dE \right) \Bigg/ \left( \int_{E_t}^{E_0} \sigma(E) P(E, E_0) e^{-(\mu_e + \mu_p + \mu_n)X} dE \right).$$

#### *Level Absorber and Level Detector*

Assume that the nuclear absorption of photons takes place in discrete levels and that the detector responds to available photons in discrete levels. For an oxygen detector the contributions to absorption and detection processes that are due to  $(\gamma, n)$  reactions may be calculated from Penfold's data (1955).

Now:

$$A = \sum_i \int_{-\infty}^{+\infty} \sigma_i(E) P(E, E_0) dE,$$

where  $\int_{-\infty}^{+\infty} \sigma_i(E) dE$  is the integrated cross section of the  $i$ th resonance level.

If the levels are narrow and the photon spectrum is nearly constant over one level,

$$A = \sum_i P(E_i, E_0) \int_{-\infty}^{+\infty} \sigma_i(E) dE,$$

where  $E_i$  is the energy corresponding to peak level cross section. With a "smooth absorber"  $e^{-\mu_T(E)X}$  is constant over the level and  $R$  could be expressed as,

$$(3) \quad R = \sum_i P(E_i, E_0) \int_{-\infty}^{+\infty} \sigma_i(E) dE \Bigg/ \sum_i P(E_i, E_0) e^{-\mu_T(E_i)X} \int_{-\infty}^{+\infty} \sigma_i(E) dE.$$

If the  $(\gamma, p)$  process is described by a smooth cross section curve but the  $(\gamma, n)$  reaction takes place in levels, the activity with the absorber in place is,

$$A' = \sum_i P(E_i, E_0) e^{-(\mu_e + \mu_p)X} \int_{-\infty}^{+\infty} \sigma_i(E) e^{-\mu_n(E)X} dE,$$

where  $\mu_e + \mu_p$  is constant over any one level, but  $\mu_n$  is a function of energy, following the Breit-Wigner formula.

Then

$$(4) \quad R = \sum_i P(E_i, E_0) \int_{-\infty}^{+\infty} \sigma_i(E) dE / \sum_i P(E_i, E_0) e^{-(\mu_e + \mu_p)X} \\ \times \int_{-\infty}^{+\infty} \sigma_i(E) e^{-\mu_n(E)X} dE.$$

Note that, if the detector and absorber are the same material,

$$(5) \quad \int_{-\infty}^{+\infty} \sigma_i(E) e^{-\mu_n(E)X} dE = e^{-\mu_m X/2} J_0\left(\frac{i\mu_m X}{2}\right) \int_{-\infty}^{+\infty} \sigma_i(E) dE,$$

where  $\mu_m$  is the maximum cross section of the level at  $E_i$  and  $J_0(i\mu_m X/2)$  is a Bessel function of order zero and imaginary argument.

To obtain the relation (5) write

$$\sigma_i(E) \equiv \mu_n(E) = \frac{a^2}{(E - E_i)^2 + b^2}.$$

The integral

$$I = \int_{-\infty}^{+\infty} \frac{a^2}{(E - E_i)^2 + b^2} \exp\left[\frac{-a^2 X}{(E - E_i)^2 + b^2}\right] dE$$

is reduced by successive transformations

$$E = E_i + b \tan \theta, \quad 2\theta = \pi - \alpha,$$

to the form

$$\frac{a^2}{b} \exp\left[\frac{-a^2 X}{2b^2}\right] \int_0^\pi \exp\left[\frac{a^2 X}{2b^2} \cos \alpha\right] d\alpha.$$

The integral is evaluated through use of the relation:

$$\pi J_0(z) = \int_0^\pi \exp[-iz \cos t] dt, \quad 0 < \arg z < \pi,$$

for  $z = iy$ ,  $y$  real and positive. (See, for instance, page 21 of Vol. II, *Higher Transcendental Functions*, compiled by the staff of the Bateman Manuscript Project, McGraw-Hill Book Co. Inc., New York, 1953.) The final result is

$$I = \frac{\pi a^2}{b} \exp\left[\frac{-a^2 X}{2b^2}\right] J_0\left(\frac{ia^2 X}{2b^2}\right).$$

With

$$\frac{a^2}{b^2} = \mu_{\max},$$

and

$$\frac{\pi a^2}{b} = \int_{-\infty}^{+\infty} \sigma_i(E) dE,$$

this becomes

$$I = \exp\left[-\frac{\mu_m X}{2}\right] J_0\left(\frac{i\mu_m X}{2}\right) \int_{-\infty}^{+\infty} \sigma_i(E) dE,$$

which is the relation (5).

Now from (4) and (5)  $R$  may be written:

$$(6) \quad R = \sum_i P(E_i, E_0) \int_{-\infty}^{+\infty} \sigma_i(E) dE / \sum_i P(E_i, E_0) e^{-(\mu_s + \mu_p)X} e^{-\mu_m X/2} J_0\left(\frac{i\mu_m X}{2}\right) \int_{-\infty}^{+\infty} \sigma_i(E) dE.$$

As a second possibility assume that the  $(\gamma, p)$  reaction as well as the  $(\gamma, n)$  takes place in levels. Since experimental data on the level structure of the  $(\gamma, p)$  reaction are inadequate for our purposes, the  $(\gamma, p)$  levels were considered to coincide with the  $(\gamma, n)$  levels and to have just twice their magnitude. The validity of these assumptions has been discussed in the preceding section. The expression replacing (4) now assumes the form,

$$(7) \quad R = \sum_i P(E_i, E_0) \int_{-\infty}^{+\infty} \sigma_i(E) dE / \sum_i P(E_i, E_0) e^{-\mu_s X} \int_{-\infty}^{+\infty} \sigma_i(E) e^{-3\mu_n(E)X} dE,$$

which reduces to

$$(8) \quad R = \sum_i P(E_i, E_0) \int_{-\infty}^{+\infty} \sigma_i(E) dE / \sum_i P(E_i, E_0) e^{-\mu_s X} e^{-3\mu_m X/2} J_0\left(\frac{i3\mu_m X}{2}\right) \int_{-\infty}^{+\infty} \sigma_i(E) dE,$$

again under the assumption that detector and absorber are the same material.

#### *Level Absorber and Smooth Detector*

These considerations apply in the case of those detectors whose response characteristics are believed to be smooth functions of energy. First consider absorption due to  $(\gamma, p)$  to be smooth and  $(\gamma, n)$  to be in levels.

$$(9) \quad A = \int_{E_l}^{E_0} \sigma(E) P(E, E_0) dE \text{ and}$$

$$A' = \int_{E_l}^{E_0} \sigma(E) P(E, E_0) e^{-(\mu_s + \mu_p)_{\text{smooth}} + (\mu_n)_{\text{level}} X} dE.$$

Splitting this integral into "smooth" and "level" parts, and assuming narrow levels, it follows that,

$$(10) \quad A' = \int_{E_l}^{E_0} \sigma(E) P(E, E_0) e^{-(\mu_s + \mu_p)X} dE$$

$$- 2 \sum_i P(E_i, E_0) \sigma(E_i) e^{-(\mu_s + \mu_p)X} \int_{-\infty}^{+\infty} (1 - e^{-\mu_n X}) dE.$$

The factor 2 in the second term arises from the fact that the bin width in the photon spectrum tables used was  $\frac{1}{2}$  Mev.

Now for  $\mu_n X$  sufficiently small the integral

$$\int_{-\infty}^{+\infty} (1 - e^{-\mu_n X}) dE$$

may be approximated by

$$I = \int_{-\infty}^{+\infty} \left( \mu_n X - \frac{\mu_n^2 X^2}{2} \right) dE.$$

Writing

$$\mu_n = \frac{a^2}{(E - E_i)^2 + b^2},$$

straightforward integration yields

$$I = X \left[ 1 - \frac{a^2 X}{4b^2} \right] \left[ \frac{\pi a^2}{b} \right] = X' \left[ 1 - \frac{\mu_m X}{4} \right] \int_{-\infty}^{+\infty} \sigma_i(E) dE$$

where  $X'$  is the absorber thickness expressed in units that make  $X' \sigma_i(E)$  dimensionless, in this case atoms/millibarn.

Thus:

$$(11) \quad R = \left. \int_{E_i}^{E_0} \sigma(E) P(E, E_0) dE \right/ \\ \int_{E_i}^{E_0} \sigma(E) P(E, E_0) e^{-(\mu_e + \mu_p)X} dE - 2 \sum_i P(E_i, E_0) \sigma(E_i) e^{-(\mu_e + \mu_p)X} \\ \times \left( 1 - \frac{\mu_m X}{4} \right) X' \int_{-\infty}^{+\infty} \sigma_i(E) dE.$$

If now we consider absorption due to  $(\gamma, p)$  to be in levels, under the assumption  $\mu_p = 2\mu_n$  we obtain,

$$(12) \quad R = \left. \int_{E_i}^{E_0} \sigma(E) P(E, E_0) dE \right/ \\ \int_{E_i}^{E_0} \sigma(E) P(E, E_0) e^{-\mu_e X} dE - 6 \sum_i P(E_i, E_0) \sigma(E_i) e^{-\mu_e X} \\ \times \left( 1 - \frac{3\mu_m X}{4} \right) X' \int_{-\infty}^{+\infty} \sigma_i(E) dE.$$

## EXPERIMENTAL RESULTS

Experimental results are presented in graphical form in Figs. 2-5. The indicated errors are probable errors. Each data point represents the average of ten or more determinations. The theoretical curves are the result of straightforward but laborious calculation on the basis of the appropriate equation (2, 6, 8, 11, or 12).

### Zinc Detector

The maximum cross section for the detecting reaction  $Zn^{64}(\gamma, n)Zn^{63}$  is at an energy low compared to the energy region in which strong nuclear absorption in oxygen would be expected. Thus the zinc detector has been used to

provide a check on the theoretical electronic coefficients which have been used in the calculations of  $R$ . In Fig. 2 the center-line curve,  $A$ , shows the value of  $R$  computed from equation (1) assuming electronic absorption only. The upper solid curve,  $B$ , shows the value of  $R$  computed on the assumption

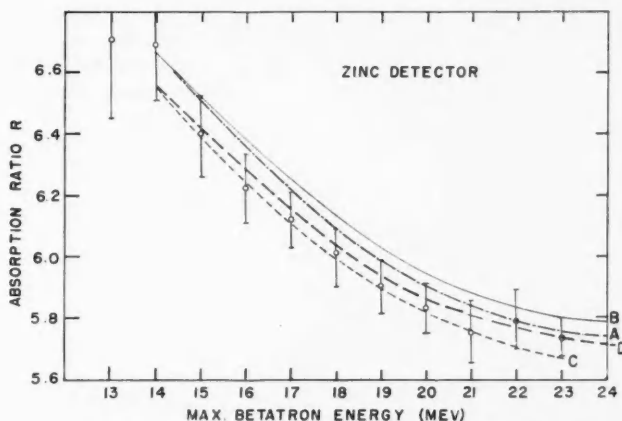


FIG. 2. Absorption ratio  $R$  as a function of maximum betatron energy for a zinc detector, with unrevised and revised electronic absorption coefficients. Curve  $A$  assumes electronic absorption only, curve  $B$  electronic and nuclear absorption, both with unrevised electronic absorption coefficients. Curves  $C$  and  $D$  are the corresponding curves calculated with revised electronic absorption coefficients.

of smooth nuclear absorption, from equation (2). Clearly the experimental points fall below the theoretical curve—even below the curve for electronic absorption only. This indicates that the electronic absorption coefficients used in the calculation (White 1952) are too high. They have been lowered by an arbitrary amount (1.0%) throughout the energy region 15–25 Mev to secure agreement between the experimental and theoretical curves for the zinc detector. The dotted curve,  $C$ , of Fig. 2 shows  $R$  as a function of maximum betatron energy calculated on the basis of revised electronic coefficients, but for electronic absorption only. The broken-line curve,  $D$ , shows the effect of including the contribution of nuclear absorption. The revised electronic coefficients have been used in all cases. The validity of this correction in view of the values of electronic absorption coefficients recently presented by Grodstein (1957) has been discussed in a previous publication (Bergsteinsson 1958).

#### *Carbon and Sulphur Detectors*

Figs. 3 and 4 present the results for carbon and sulphur detectors respectively, assuming that the detectors have smooth response characteristics. The dotted curves,  $A$ , represent the theoretical values of  $R$  assuming electronic absorption only (Eq. (1) with  $\mu_T = \mu_e$ ). The solid curves,  $B$ , represent the calculated values of  $R$  including nuclear absorption on the basis of smooth

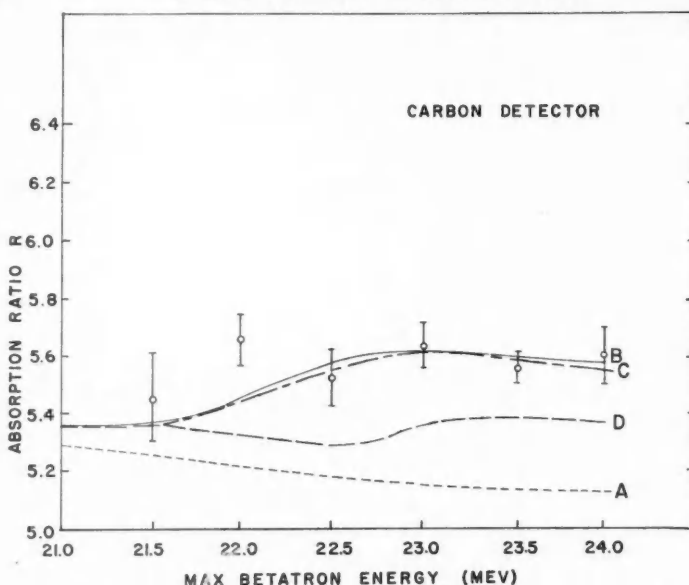


FIG. 3. Absorption ratio  $R$  as a function of maximum betatron energy for a carbon detector, assuming "smooth" detection, but with various assumptions concerning the absorption process. In the calculation of curve  $A$  electronic absorption only is assumed.  $B$  assumes smooth  $(\gamma, n)$  and smooth  $(\gamma, p)$  absorption.  $C$  assumes level  $(\gamma, n)$  and smooth  $(\gamma, p)$  absorption, and curve  $D$  assumes level  $(\gamma, n)$  and  $(\gamma, p)$  absorption.

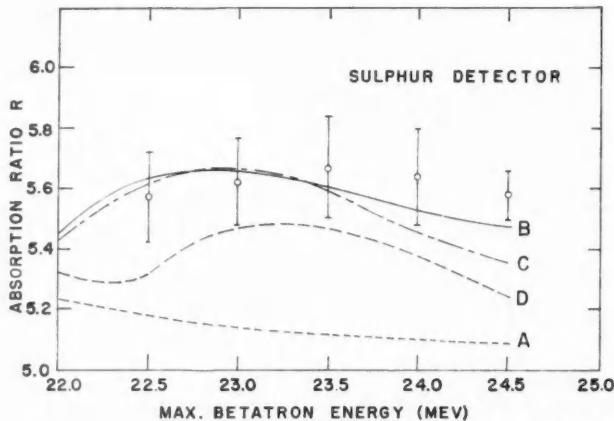


FIG. 4. Absorption ratio  $R$  as a function of maximum betatron energy for a sulphur detector, assuming "smooth" detection, but with various assumptions concerning the absorption process. In the calculation of curve  $A$  electronic absorption only is assumed.  $B$  assumes smooth  $(\gamma, n)$  and smooth  $(\gamma, p)$  absorption.  $C$  assumes level  $(\gamma, n)$  and smooth  $(\gamma, p)$  absorption, and curve  $D$  assumes level  $(\gamma, n)$  and  $(\gamma, p)$  absorption.

$(\gamma, n)$  and  $(\gamma, p)$  cross-sectional values for oxygen (Eq. (2)). The center-line curves,  $C$ , assume smooth absorption due to the  $(\gamma, p)$  reaction and absorption in discrete levels due to the  $(\gamma, n)$  reaction in oxygen (Eq.(11)). The broken line curves,  $D$ , assume level  $(\gamma, p)$  as well as  $(\gamma, n)$  absorption (Eq.(12)).

#### Oxygen Detector

Fig. 5 shows the results for oxygen. The dotted curve,  $A$ , represents the theoretical  $R$  values calculated from equation (1) with  $\mu_T$  set equal to  $\mu_e$ . The solid curve,  $B$ , shows  $R$  calculated on the basis of smooth nuclear absorption

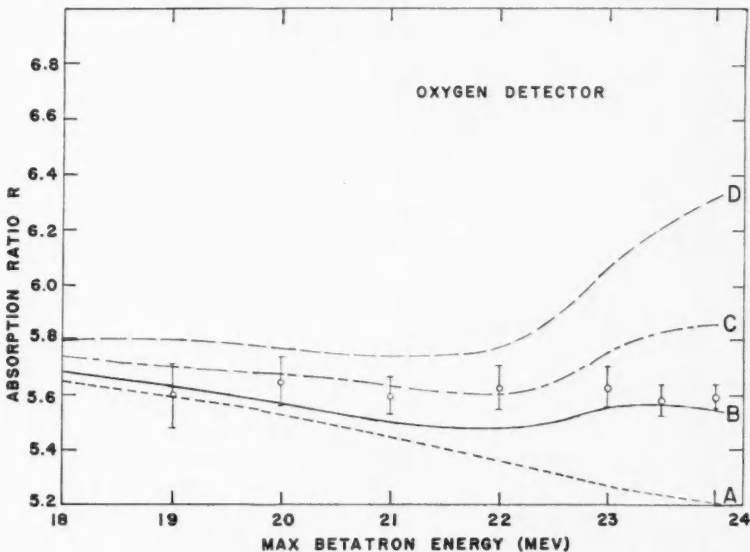


FIG. 5. Absorption ratio  $R$  as a function of maximum betatron energy for an oxygen detector, with various assumptions concerning the absorption process. In the calculation of curve  $A$  electronic absorption only is assumed.  $B$  assumes smooth  $(\gamma, n)$  and smooth  $(\gamma, p)$  absorption.  $C$  assumes level  $(\gamma, n)$  and smooth  $(\gamma, p)$  absorption, and curve  $D$  assumes level  $(\gamma, n)$  and  $(\gamma, p)$  absorption.

(Eq.(2)). In both these cases smooth response characteristics of the detector have been assumed. The  $R$  values represented by the center-line curve,  $C$ , and the dashed curve,  $D$ , have been calculated on the basis of assumed level structure of the detecting reaction  $O^{16}(\gamma, n)O^{15}$  (expressions (6) and (8)). The center-line curve shows the values of  $R$  calculated on the basis of a smooth cross section for the  $(\gamma, p)$  reaction and a level structure for the  $(\gamma, n)$  reaction. The dashed curve represents the values of  $R$  which would be expected when we assume that both the reactions  $(\gamma, n)$  and  $(\gamma, p)$  occur only in discrete levels, and that  $(\gamma, p)$  levels are in the same position but have twice the integrated cross sections of the  $(\gamma, n)$  levels.

## DISCUSSION OF RESULTS

*Carbon and Sulphur Detectors*

An examination of Figs. 3 and 4 shows that, as expected, nuclear absorption makes an appreciable contribution to the total absorption. The theoretical curves obtained on the assumption of smooth nuclear absorption (solid, *B*) and smooth ( $\gamma, p$ ) but level ( $\gamma, n$ ) absorption (center-line, *C*) agree reasonably well with the experimental points, but the precision of the results is not nearly good enough to distinguish between these two hypotheses. The broken-line curves, *D*, based on the assumption of level absorption in ( $\gamma, p$ ) as well as ( $\gamma, n$ ) reactions, fall far below the experimental points, particularly in the region of 22.5 Mev. This appreciable difference may be predicted from inspection of the ( $\gamma, n$ ) and ( $\gamma, p$ ) cross-sectional curves. Whereas in calculating the broken line curves we assumed ( $\gamma, p$ ) levels having twice the magnitude of the ( $\gamma, n$ ) levels, the average value of the smooth ( $\gamma, p$ ) cross section in the region 21.5 Mev to 23 Mev is about four times the value of the smooth ( $\gamma, n$ ) cross section.

An important point may be made from the observation that appreciable nuclear absorption does take place. Experimental evidence indicates that there are discontinuities in the activation curve of the ( $\gamma, n$ ) reaction in carbon (Haslam 1952b). If the assumption is made that nuclear absorption in oxygen occurs only into discrete levels, we might reasonably expect that carbon would respond in the same way. It is quite unlikely that the "detecting levels" in carbon would be coincident with the "absorbing levels" in oxygen if the levels are narrow compared to their separation. Consequently, the detector would not see any nuclear absorption and the experimental values of *R* would decrease smoothly with increasing energy owing to the decrease of electronic absorption coefficients for oxygen with increasing energy in the range considered. In fact, calculations show that the expected values of *R* would follow closely the calculated electronic curve (dotted, *A*) for any assumption concerning the level structure of the detecting reaction consistent with activation curve measurement. It is not certain that similar discontinuities occur in the activation curve of the ( $\gamma, d$ ) reaction in sulphur. If nuclear absorption in sulphur takes place only into discrete levels which do not occur at the same energies as the absorption levels in oxygen, a similar argument applies. The *R* value for electronic absorption using sulphur as a threshold detector, independent of detector response characteristics, is 5.33 at 20 Mev; a figure in good agreement with the value that would be obtained by extrapolating the electronic curve based on smooth absorption. Again, since electronic coefficients decrease smoothly with increasing energy, *R* could not be larger than the value 5.33 on the assumption of narrow level absorption in the oxygen and sulphur.

There might, of course, be some degree of overlapping of "absorbing" and "detecting" levels. The amount of nuclear effect shown by the detector would depend on the extent of overlapping. However, unless this were much larger than one would expect from the assumed width of the levels, the response of the detector into discrete levels would depress the experimental values of *R*.

However, Figs. 3 and 4 show that the experimental points do not lie below the theoretical curves calculated on the basis of smooth detector response. Thus we are led to the conclusion that considerable continuous nuclear absorption takes place.

#### Oxygen Detector

As seen in Fig. 5 the experimental results, which are shown with their probable errors, are for the most part in agreement with the solid curve, *B*, which is based on continuous absorption, and are definitely lower than the broken-line curve, *D*, which is calculated on assumed absorption into levels only, for both the  $(\gamma, n)$  and  $(\gamma, p)$  reactions. The experimental points up to 22 Mev appear to agree with the center-line curve, *C*, and thus indicate partial contribution from level absorption; however, in this region the accuracy of the experimental results does not allow a clear-cut decision as to which curve (solid or center-line) is in better agreement with experiment. Above 22 Mev the experimental points deviate from the center-line curve, and follow the course of the solid curve, which represents continuous nuclear absorption.

#### SUMMARY

It was hoped that the measurement of absorption coefficients for X-rays by oxygen in the energy region 15–25 Mev would provide a sensitive test as to whether the nuclear part of the absorption takes place continuously over this energy region or into sharply defined energy levels. As a basis for calculation the level structure proposed by Penfold (1955) for the  $(\gamma, n)$  reaction in  $O^{16}$  has been used. The results of the experiments described here are not as clear-cut as might be desired.

The values of the total nuclear absorption are well represented by summing up the  $(\gamma, n)$  and  $(\gamma, p)$  cross-sectional values, with a giant resonance in the region between 21 and 25 Mev. This is the case for detectors of material other than oxygen, as well as for the oxygen detector. In view of the occurrence of sharp breaks in the activation curve for the  $(\gamma, n)$  reaction it is clear that a certain amount of photon absorption does take place into levels. But it seems certain that Penfold has over-estimated the integrated cross sections of the levels, or else that the levels are much lower and hence broader than he has suggested. This would correspond more and more nearly to the continuous case as the levels become broader. The best description of the absorption process appears to be continuous absorption on which is superimposed relatively small absorption peaks. The exact knowledge of the level structure of suitable detecting reactions, other than  $O^{16}(\gamma, n)O^{15}$ , would provide a better working basis for comparison of the experimental results with values predicted on the assumption of level absorption only.

#### ACKNOWLEDGMENTS

The authors wish to express their thanks to Dr. O. R. Skinner and Dr. L. Katz for helpful discussions. The assistance of Mr. S. B. Kowalski, Mr. J. L. Bergsteinsson, and Mr. J. P. Roalsvig is acknowledged with thanks.

One of the authors (A.K.M.S.) is indebted to the International Economic and Technical Cooperation Division of the Government of Canada for financial assistance in the form of a Colombo Plan award.

## REFERENCES

- ADAMS, G. D. 1948. Phys. Rev. **74**, 1706.  
BERGSTEINSSON, J. L., ROBINSON, L. B., SIDDIQI, A. K. M., HORSLEY, R. J., and HASLAM, R. N. H. 1958. Can. J. Phys. **36**, 140.  
COHEN, L., MANN, A. K., PATTON, R. B., REIBEL, K., STEPHENS, W. E., and WINHOLD, E. J. 1956. Phys. Rev. **104**, 108.  
GRODSTEIN, G. R. W. 1957. N.B.S. Circular No. 583.  
HASLAM, R. N. H., HORSLEY, R. J., JOHNS, H. E., and ROBINSON, L. B. 1953. Can. J. Phys. **31**, 636.  
HASLAM, R. N. H., KATZ, L., HORSLEY, R. J., CAMERON, A. G. W., and MONTALBETTI, R. 1952a. Phys. Rev. **87**, 196A.  
HASLAM, R. N. H., KATZ, L., HORSLEY, R. J., and CAMERON, A. G. W. 1952b. Royal Society of Canada meeting.  
HORSLEY, R. J., HASLAM, R. N. H., and JOHNS, H. E. 1952. Can. J. Phys. **30**, 159.  
JOHANSSON, S. A. E. and FORKMAN, B. 1955. Phys. Rev. **99**, 1031.  
KATZ, L., JOHNS, H. E., BAKER, R. G., HASLAM, R. N. H., and DOUGLAS, R. A. 1951a. Phys. Rev. **82**, 271.  
KATZ, L. and PENFOLD, A. S. 1951b. Phys. Rev. **81**, 815.  
PENFOLD, A. S. and SPICER, B. M. 1955. Phys. Rev. **100**, 1377.  
STEPHENS, W. E. and MANN, A. K. 1955. Phys. Rev. **98**, 839.  
WALKER, R. L. 1949. Phys. Rev. **76**, 527.  
WHITE, G. R. 1952. N.B.S. Report No. 1003.

---

## NOTES

---

### CONTROL OF LINEAGE STRUCTURE IN ALUMINUM CRYSTALS GROWN FROM THE MELT

K. T. AUST\* AND B. CHALMERS†

During the growth of a metallic crystal from its melt, dislocations may align themselves into regular, continuous, straight arrays of low-angle boundaries, as was observed by Teightsoonian and Chalmers (1951, 1952). This structure, which is a macromosaic type of lineage, may result in misorientations up to a few degrees in the "single crystal". In the present note, a technique is described for avoiding this form of lineage in melt-grown crystals by suitable control of the shape and rate of advance of the solid:liquid interface.

#### EXPERIMENTAL

Single crystals of aluminum were grown from the melt in argon atmosphere, in a horizontal graphite boat enclosed in a vycor tube, using the controlled solidification method described by Chalmers (1949). The shape of the solid: liquid interface was revealed by rapidly removing the liquid from the solid during freezing. If the crystal during growth is completely enclosed by a furnace coil which supplies the heat, the resulting shape of the solid:liquid interface is as shown in Fig. 1(a). This shape is obtained with axial heat flow in the crystal and will be referred to as the "normal" interface shape. However, if the heat is supplied to the top surface of the horizontal crystal during solidification, by suitable disposition of the furnace coil, a solid:liquid interface shape, as shown in Fig. 1(b), is obtained. This latter shape will be termed the "inclined" interface.

Two grades of aluminum, reported to be 99.993 and 99.996% Al, were used as starting material. The dimensions of the polycrystalline blanks from which the crystals were grown were generally 5 mm × 5 mm in cross section and 12–18 cm in length. Approximately twenty single crystals were grown having the interface shape shown in Fig. 1(a), and about twenty single crystals with the interface shape depicted in Fig. 1(b). The rate of growth was varied from 0.5 to about 25 mm/min. The extent of lineage was determined from X-ray Laue back-reflection and Berg-Barrett photographs as described by Barrett (1945), and from etching techniques. The etchant described by Metzger and Intrater (1954) was employed, since the reagent is reported to reveal subboundaries in aluminum with angles of tilt of only 5' of arc or possibly less.

#### RESULTS AND DISCUSSION

The results clearly indicated that the use of an "inclined" solid:liquid inter-

\*General Electric Research Laboratory, Schenectady, New York.

†Harvard University, Cambridge, Mass.

face at sufficiently slow rates of growth resulted in crystals free from the macromosaic lineage, which characterized those crystals grown with the "normal" interface shape. A rate of growth of about 2 mm/min or less for the 99.996% Al, and approximately 0.5 mm/min for the 99.993% Al was required together with the inclined interface. For example, a crystal (99.996% Al) was grown at the rate of 2 mm/min under conditions such that an inclined interface was present during the growth of the first half of the crystal and a normal interface during the remainder of crystal growth. Lineage was found only in the region of the crystal which grew with the normal interface. It was also determined that lineage-free crystals having controlled orientations may be grown from seed crystals containing lineage by the inclined interface technique. For example, seed crystals, with and without lineage, were used to grow several crystals from the 99.996% Al, under conditions of inclined solid:liquid interface and at 2 mm/min. These crystals, which had a  $\langle 111 \rangle$  growth axis and a  $\{110\}$  top surface, were found to be free from the macromosaic lineage. However, identically oriented crystals when grown with normal interface shape and at a rate of 2 mm/min displayed lineage.

The previous work of Teightsoonian and Chalmers (1951, 1952) indicated that lineage structure can be detected after an induction distance, and takes the form of continuous, straight, low-angle boundaries; they form normal to the solid:liquid interface at slow growth rates (approximately 1 mm/min). These factors have been utilized here to remove this type of substructure by adjusting the heat flow so that the advancing solid:liquid interface is inclined to the specimen or growth axis (Fig. 1(b)). In this way, the distance normal to the interface, from bottom to top of the crystal (about 1 cm in Fig. 1(b)), may be made shorter than the induction distance. Consequently, the lineage boundaries do not form when the interface is inclined at slow growth rates. In addition, lineage boundaries already present in a seed crystal are forced to "run out" of the crystal. A slow rate of growth is required since the induction distance for the formation of lineage is greater for slowly grown crystals than for rapidly grown crystals, as was determined by Teightsoonian and Chalmers (1951, 1952). For example, the induction distance of aluminum crystals (99.996%) increased from 0.5 to 4 cm as the rate of growth decreased from 8 mm/min to 2 mm/min.

A slow rate of growth is also important, since the work of Teightsoonian and Chalmers (1951, 1952) and Atwater and Chalmers (1957) indicated that at high rates the lineage boundaries approach parallelism with a characteristic crystallographic direction and not with the axis of heat flow. This characteristic direction appears to be the same as that for dendritic growth, i.e.,  $\langle 100 \rangle$  for aluminum of the purity used in the present study. It was found that if a  $\langle 100 \rangle$  direction is inclined favorably to the solid:liquid interface, i.e., a short direction in relation to the crystal dimensions, the lineage boundaries again "run out" of the crystal at fast rates of growth (approximately 25 mm/min).

The experimental observation that a slower rate of growth is required to remove lineage from the less pure aluminum by the inclined interface method

PLATE I

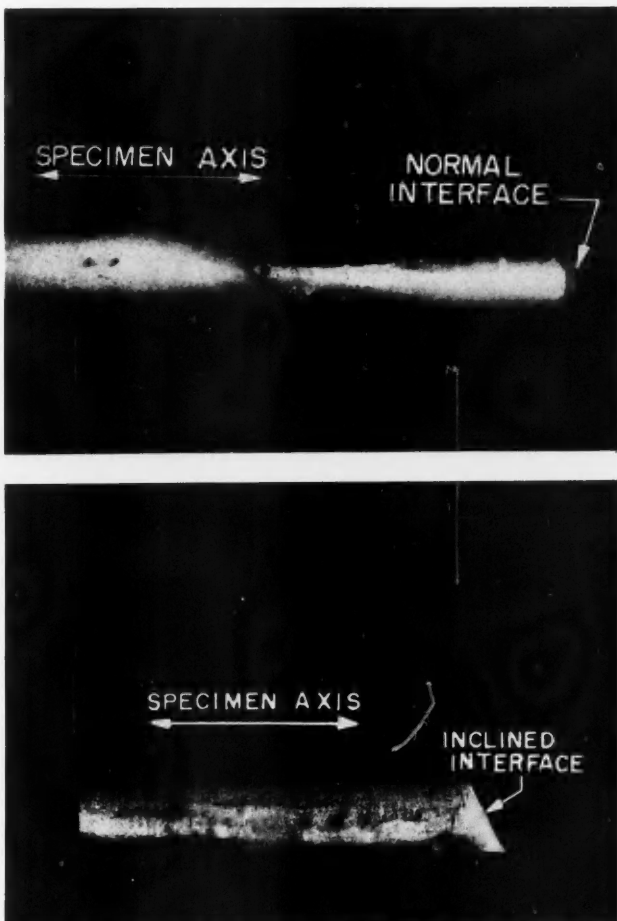


FIG. 1. Shape of (a) "normal" and (b) "inclined" solid:liquid interfaces, after removing the liquid, in aluminum crystals.  $\times 2\frac{1}{4}$ .

PLATE II



FIG. 2. Berg-Barrett X-ray photograph of an aluminum (99.996%) crystal grown with inclined interface at 0.5 mm/min.  $\times 20$ .

may be explained in a similar manner. Atwater and Chalmers (1957) found that for tin and lead crystals grown with constant orientation and growth rate, the direction of lineage boundaries became more closely aligned with the "dendrite" direction with increasing impurity content. The impurity concentration at the solid:liquid interface is probably higher in the 99.993% Al than in the 99.996% Al. Consequently, the attempt to control lineage by a thermal method, i.e., an inclined interface, may be again opposed by a crystallographic condition arising from impurities, similar to the effect of rate of growth previously discussed. The parameters of freezing, namely the rate of advance of the interface and the concentration of impurity in the melt, are interrelated; e.g., an increase in either may lead to increased constitutional supercooling. Therefore, the effect of impurity on the direction of formation of the lineage would be expected to be less at slower rates of growth.

The inclined interface method for avoiding lineage may only be applicable to the type of lineage described by Teghtsoonian and Chalmers (1951, 1952), which grows in a straight, continuous manner, normal to the solid:liquid interface (at slow growth rates). For instance, Berg-Barrett X-ray photographs clearly revealed the absence of such subboundaries, although several irregular subboundaries with misorientations less than a few minutes of arc are evident (Fig. 2). Atwater and Chalmers (1957) found that the subboundaries were non-straight and non-continuous in tin crystals of 99.998% purity grown from the melt. These subboundaries could be made to grow with increasing uniformity with increasing impurity additions, e.g., 0.0003 to 0.006 wt % of lead to tin. Rutter (1957) has also observed irregular subboundaries in zone-refined lead and tin crystals. It appears, therefore, when the impurity content becomes very low that the subboundaries no longer form in a unidirectional manner. The experiments of Rutter and Aust (1958) have shown that this irregular "macromosaic" structure in high purity metal crystals may be removed by the migration of a grain boundary which is motivated by the substructure itself. The latter method is restricted, however, to high purity crystals where sufficient grain boundary mobility exists under a small driving force.

#### SUMMARY

The formation of regular, continuous, straight, low-angle boundaries (striations) during freezing of a metallic crystal may be avoided by inclination of the advancing solid:liquid interface with respect to the direction of freezing.

#### ACKNOWLEDGMENTS

The authors thank J. W. Rutter for several useful discussions, and W. G. Martin for the Berg-Barrett photograph of Fig. 2.

- ATWATER, H. A. and CHALMERS, B. 1957. Can. J. Phys. **35**, 208.  
BARRETT, C. S. 1945. Trans. AIME, **161**, 15.  
CHALMERS, B. 1949. Proc. Roy. Soc. A, **196**, 64.  
METZGER, M. and INTRATER, J. 1954. Nature (London), **174**, 547.

- RUTTER, J. W. 1957. Private communication.  
RUTTER, J. W. and AUST, K. T. 1958. To be published in *Acta Met.*  
TEGHTEESOONIAN, E. and CHALMERS, B. 1951. *Can. J. Phys.* **29**, 370.  
— 1952. *Can. J. Phys.* **30**, 338.

RECEIVED MARCH 24, 1958.  
GENERAL ELECTRIC RESEARCH LABORATORY,  
SCHENECTADY, NEW YORK.

#### FILAMENTARY GROWTH IN IRRADIATED URANIUM<sup>1</sup>

W. M. BARSS,<sup>2</sup> Z. S. BASINSKI,<sup>3</sup> AND F. R. N. NABARRO<sup>4</sup>

Uranium metal fuel elements sometimes break as a result of embrittlement and the recurrent thermal stresses to which they are subjected in a nuclear reactor. When the breakage occurs as a transverse fracture of the uranium, without failure of its ductile protective sheath, subsequent thermal cycles may cause the broken ends to separate. The resulting gap, which might be expected to contain only volatile fission products, sometimes contains dense filaments, of lengths up to 5 cm, projecting from the uranium.

Fig. 1 shows two views of filaments attached to the lower piece of uranium in a broken NRX rod. The views are at right angles to the length of the rod and to each other. The pictures are radiographs, taken by a special technique to overcome the effects of radiation from the uranium itself, and printed so that the uranium appears dark. The filaments project upwards from the lower piece of uranium and are estimated to be 0.3 to 1.0 mm thick. Filaments have not been noted on the upper piece of this or any other rod.

Since the filaments apparently occur on one surface alone they presumably grow as whiskers, rather than being drawn out in tension as the two surfaces separate. A whisker mechanism of growth is favored by the brittleness of irradiated uranium (Konobeevsky *et al.* 1956). Also, it is known (Baker and Koehler 1956) that a whisker may be much longer than the diameter of grains in the substrate. We discuss some reasons for believing that the purely thermal and mechanical conditions in the fuel element will not account for such large whiskers, but that the vacancies or interstitial atoms produced by irradiation may stimulate an adequate rate of whisker growth.

On the other hand, the ductile formation of filaments cannot be excluded with certainty. Roberts and Cottrell (1956) have shown that uranium, while being irradiated, has mechanical properties similar to those of pitch, in that it is brittle under rapid loading but behaves as a Newtonian viscous fluid under very small steady loads. Therefore, we also discuss the conditions required

<sup>1</sup>Issued as A.E.C.L. No. 596 and N.R.C. No. 4785.

<sup>2</sup>Atomic Energy of Canada Limited, Chalk River, Ontario.

<sup>3</sup>Division of Pure Physics, National Research Council, Ottawa, Ontario.

<sup>4</sup>Present address: University of the Witwatersrand, Johannesburg, South Africa. Visiting Professor at the National Research Council when the note was written.

PLATE I

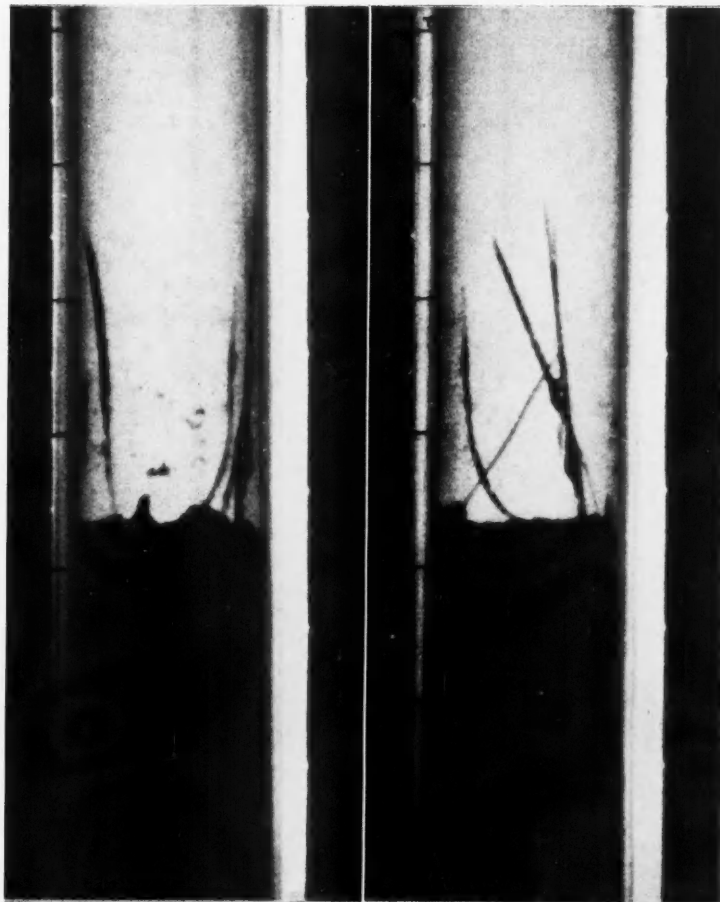
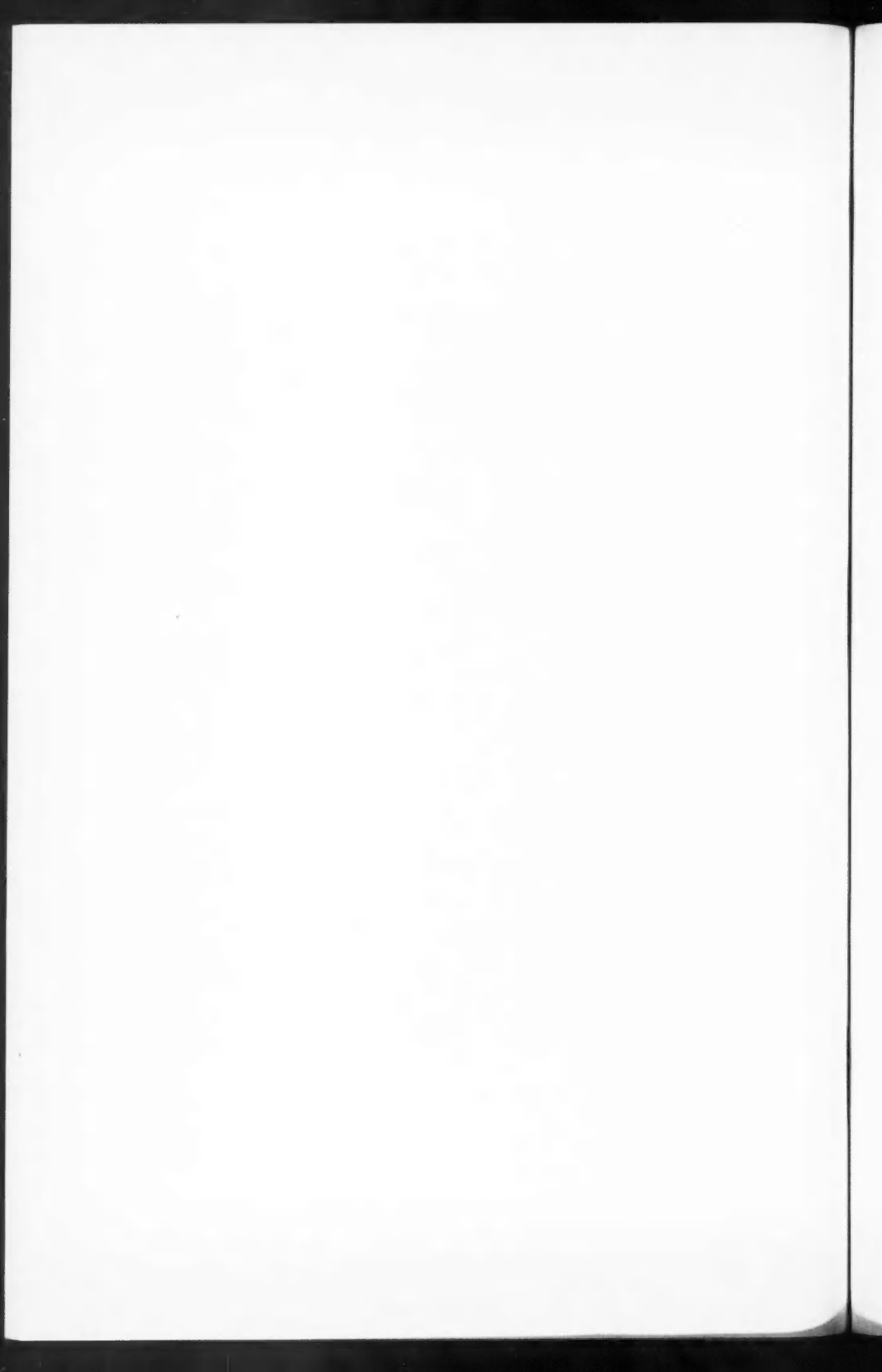


FIG. 1. Two radiographs, taken at right angles to each other, showing filaments on the free surface of a fractured uranium rod inside a thin aluminum sheath. The scale marks are one inch apart.



to produce filaments of this size by a creep mechanism. Unfortunately, it is impossible to tell, at present, whether the growths are polycrystalline, as required for ductile formation, or monocrystalline, as required by the theories of whisker growth.

According to the mechanism of Peach (1952), the whisker might grow from a continuous inserted sheet of atoms bounded by a dislocation. However, a whisker 0.5 mm in diameter and 5 cm long contains about  $5 \times 10^{20}$  atoms which would occupy an area of about  $5 \times 10^6 \text{ cm}^2$  in a monatomic layer. This mechanism is therefore incapable of accounting for whiskers of the observed size.

It appears more likely that whisker growth involves a dislocation source of the type suggested by Frank (1953) or of the type suggested by Eshelby (1953). In either case the source acts as a pump, driven by alternating thermal stresses in the metal. On the forward stroke the dislocation climbs down, ejecting a fresh length of whisker and emitting vacancies which diffuse to the surface. On the back stroke there is no appreciable shortening of the whisker because the dislocation is unable to climb up equally rapidly by the absorption of vacancies or the emission of interstitial atoms. (We use the phrase "climb up" to indicate the motion of an edge dislocation in which the inserted half plane decreases in area, and "climb down" for the opposite process, having in mind the conventional representation of an edge dislocation.)

There are two reasons why the rate of climb is less on the back stroke than on the forward stroke:

(1) Vacancies can be absorbed at a rate that is limited by their equilibrium concentration and diffusion rate but can be emitted more freely.

(2) The rates of emission of interstitial atoms and of vacancies affect the climb of dislocations in almost the same proportions as they contribute to the self-diffusion coefficient (Nabarro 1957). Self-diffusion in alpha-uranium occurs principally by the migration of vacancies, rather than interstitial atoms (Pugh 1956a). It follows that interstitial atoms will not be emitted as rapidly as vacancies under an equal and opposite stress.

The dominant factors in whisker growth are therefore assumed to be the rates of emission and diffusion of vacancies.

Purely thermal activation will probably not account for the observed whisker growth because the activation energy for self-diffusion in uranium is too high, 62.7 kcal. (Pugh 1956b.) At 200°C, the estimated operating temperature where the growth occurs, this energy is equivalent to  $67RT$ . The frequency with which a normal atomic site is visited by a vacancy is, therefore, only about  $10^{13}e^{-67} = 10^{-16} \text{ sec}^{-1}$ . This means that a whisker might elongate by one atomic layer in times of the order of  $10^{16}$  sec, an unreasonably long time.

Irradiation may be expected to increase the rate of whisker growth; possibly by virtue of the intense local heating at fission sites, "thermal spikes," but more likely by producing numerous interstitial atoms, along with an equal number of vacancies. If the dislocations absorb one type of imperfection preferentially, the difference in mobility of the two types may affect the rate of operation of the source that generates the whisker. There is not yet enough

detailed information on the behavior of imperfections in uranium to permit a quantitative calculation, but the following arguments seem capable of accounting for the observed whiskers.

Thermal cycling, under the conditions existing in a broken NRX rod, will produce both hydrostatic and shear stresses approximately equal to the yield strength of the uranium. At 200° C, the maximum hydrostatic stress cannot make a dislocation climb but the maximum shear stress can make it glide. A whisker-producing dislocation must contain jogs that emit vacancies or interstitial atoms as the dislocation glides. Vacancies, having a lower energy of formation, are emitted more readily than interstitial atoms. These vacancies are not very mobile and, as they accumulate around the source that emits them, they oppose its motion. Irradiation provides interstitial atoms throughout the metal. Because of their much higher mobility, a large number of these atoms can be effective in annihilating the accumulated vacancies and thus increasing the rate of whisker growth. The whiskers will grow where the stresses cause a forward stroke of the source while the reactor is operating; i.e., when the motion of the source is enhanced by the low energy of formation for vacancies and the high mobility of interstitial atoms. The source makes its back stroke when the reactor is shut down; i.e., without benefit of the imperfections produced by irradiation. The coupled effects of irradiation and thermal stresses may be sufficient to account for the growth of whiskers of the size observed.

The ductile formation of filaments has been considered as a possible alternative to the growth of whiskers as described above. It is based on the observation of Roberts and Cottrell (1956) that the rate of transient creep in uranium under irradiation increases less than linearly with stress, while the rate of steady-state creep increases more than linearly with stress. Since it is known (Orowan 1949) that a Newtonian fluid (in which strain is proportional to stress) will just draw stably to a filament, it follows that stable filaments could be drawn under transient conditions of irradiation but not under steady conditions where the growth would soon terminate by necking.

At the highest stress they used, Roberts and Cottrell found a creep rate of twice the elastic deflection each week. If we assume that the filaments were under a stress equal to the ultimate tensile strength of uranium, about  $5 \times 10^8$  dyne cm $^{-2}$ , leading to an elastic strain of about  $3 \times 10^{-3}$ , and if we assume that the Newtonian viscosity observed at low stresses will give the creep rate at high stresses correctly in order of magnitude, we obtain a maximum creep rate of  $6 \times 10^{-3}$  per week, or about 0.3 per year, for uranium irradiated in BEPO. The thermal neutron flux in BEPO in the experiments of Roberts and Cottrell was about  $1.3 \times 10^{12}$  cm $^{-2}$  sec $^{-1}$ , while the flux in a fuel element in NRX is about  $2.7 \times 10^{13}$  cm $^{-2}$  sec $^{-1}$ . It is likely that the creep rate will be approximately proportional to the flux, so that a strain of 7 per year can be expected in NRX. This is of the order required to produce the observed filaments.

In favor of the view that the filaments have been pulled out in tension is the fact that they are mainly observed near the outer edges of the broken surfaces

and not near the center, where one might expect to find hydrostatic stresses which would lead to the extrusion of whiskers. Against this view is the argument that if the elongation of the filaments begins under conditions where the strain rate increases more rapidly than the stress, the filaments will neck and break, while if the strain rate increases less rapidly than the stress it is unlikely that filaments as long as 5 cm could be produced within a year. In addition the strain rate for "drawing out" mechanism will only be adequate if the broken ends separate at a reasonably uniform rate. This last condition is almost certainly not satisfied, since the separation is expected to increase when the reactor power falls, and decrease by a slightly smaller amount as the power rises again. The maximum rate of separation may thus be several orders of magnitude larger than the average rate; and the creep mechanism may be too slow to enable the filaments to be drawn. The fact that the filaments are not observed at both ends of the gap also argues against the creep mechanism, since it would be difficult to explain why they should all break at one end.

A clear decision as to whether such growths are fibers or whiskers could be obtained by examination of their structure. The creep mechanism of Roberts and Cottrell can operate only in polycrystalline materials, whereas whiskers are necessarily single crystals.

- BAKER, G. S. and KOEHLER, J. S. 1956. Private communication.  
ESHELBY, J. D. 1953. Phys. Rev. **91**, 755.  
FRANK, F. C. 1953. Phil. Mag. **44**, 854.  
KONOBEEVSKY, S. T., PRAVDYUK, N. F., and KUTAISEV, V. I. 1956. Proceedings of the International Conference on the Peaceful Uses of Atomic Energy, Geneva, Vol. 7 (United Nations, New York), p. 433.  
NABARRO, F. R. N. 1957. Dislocations and mechanical properties of crystals (John Wiley, New York), p. 527.  
OROWAN, E. 1949. Repts. Prog. in Phys. **12**, 185.  
PEACH, M. O. 1952. J. Appl. Phys. **23**, 1401.  
PUGH, S. F. 1956a. Proceedings of the International Conference on the Peaceful Uses of Atomic Energy, Geneva, Vol. 7 (United Nations, New York), p. 441.  
——— 1956b. Bull. Inst. Metals, **3**, 105.  
ROBERTS, A. C. and COTTRELL, A. H. 1956. Phil. Mag. Ser. 8, **1**, 711.

RECEIVED FEBRUARY 10, 1958.

ATOMIC ENERGY OF CANADA LIMITED, CHALK RIVER, ONTARIO,  
NATIONAL RESEARCH COUNCIL OF CANADA, OTTAWA, CANADA,  
AND UNIVERSITY OF WITWATERSRAND, JOHANNESBURG, S.A.

#### THE HALF-LIFE OF $\text{Na}^{24}$ <sup>1</sup>

P. J. CAMPION AND JANET S. MERRITT

In a recent investigation of the corrections applicable to  $4\pi\beta-\gamma$  coincidence counting (Campion 1957), it was necessary to know the half-life of  $\text{Na}^{24}$  to better than 0.1%. The most precise measurement of this quantity reported in the literature is that of Lockett and Thomas (1953), who obtained  $15.00 \pm 0.03$  hours and  $14.97 \pm 0.01$  hours for the decay of two sources, giving a weighted

<sup>1</sup>Issued as A.E.C.L. No. 642.

mean of  $14.97 \pm 0.01$  hours.\* This result is in fair agreement with the value of  $14.90 \pm 0.05$  hours obtained by Tobailem (1955), who followed the decay of two sources for 10 hours. Earlier reported values for this half-life are  $15.0 \pm 0.1$  hours (Sinclair and Holloway 1951),  $15.06 \pm 0.039$  hours (Sreb 1951),  $15.04 \pm 0.1$  hours (Solomon 1950), and  $14.96 \pm 0.1$  hours (Wilson and Bishop 1949; see also Sreb 1951). Chemical purification of the sodium after irradiation is not mentioned in any of the determinations reported to date except in that due to Solomon (1950), who, however, assumed that there was negligible dead time associated with his counting system. Although the intrinsic dead time of a proportional counter can be very small it is difficult to construct an amplifier-discriminator unit which has a resolving time of less than  $2 \mu\text{sec}$ . Such a value would cause a loss of about 0.5% at the highest activities recorded by Solomon.

With the currently available ion exchange techniques it was felt that sources of  $\text{Na}^{24}$  could be prepared which were entirely free of all contaminant activities. Accordingly samples of "spec-pure" sodium carbonate were sealed in quartz tubes and irradiated in the NRX reactor for 20 hours. The sodium carbonate was dissolved in very dilute hydrochloric acid, absorbed on Dowex-50, and eluted with 0.7 N hydrochloric acid. This technique, described by Beaukenkamp and Rieman (1950), separates sodium and potassium from each other and from all other cationic contaminants. Two separate irradiations were made, from which a total of eight sources were prepared, by enclosing the sodium chloride between two gold-coated plastic films of superficial density  $40 \mu\text{g}/\text{cm}^2$ . The use of the sandwich technique prevented possible loss of active material from the sources.

These sources were counted in a  $4\pi$  beta proportional flow type counter using methane gas. The external gain was provided by a non-linear non-overloading amplifier of a type which is in general use in this laboratory. The counter potential was supplied from a chopper stabilized power unit using a standard cell as the reference voltage. The curve of counting rate against counter potential showed plateaux 200 v long and having a slope of less than 0.2% per 100 v. A measurement of the activity consisted in noting the counting rate at two or more different counter potentials to ensure that the observations were made on the counting rate plateau. These readings were corrected for decay during the counting period, for dead time losses, and for background. A half-life of 14.97 hours was assumed for the decay during the counting period.

The timing relied on the 110 v a-c. line frequency and the ability of an observer to switch off a scaler manually after a given interval. In an experiment to observe the variation of the 110 v a-c. line frequency, continuous measurements were made using a pulse generator synchronized to this frequency and a counting rate meter together with a strip chart recorder. About 97% of the voltage output of the counting rate meter was biased off by the use of mercury cells in order to expand the scale. The sensitivity of the apparatus was tested against a General Electric electrodynamic frequency meter. The measurements

\*This is the internal error of the two measurements; it was doubled to give the final value,  $14.97 \pm 0.02$  hours. The external error, however, amounts to  $\pm 0.03$  hours.

were carried out in a temperature controlled room and with a stabilized mains supply. The results indicated that the average frequency differed from 60 cycles/sec by less than 0.1% over periods of time comparable with those taken for counting observations. The human error involved in switching off a scaler after a given time interval was estimated by the use of a crystal-controlled megacycle frequency standard to be less than 0.1% over a 200-second interval, which was the shortest counting period used. The error for longer periods was proportionately less.

By observing the counting rates at 10 and again at 176 half-lives after the last point on the decay curves of two samples selected at random, the activity of any long-lived impurity was found to be less than  $10^{-4}$  of that for the last point. A further check was provided by dividing the time over which the decay of each source was observed in two and calculating the half-lives for both parts. In all cases the two partial half-lives agreed with that calculated from the full data within the experimental errors, and no significant trend was detected.

The dead time of the counting system was measured by the use of a double pulse generator having a continuously variable spacing between the two pulses, and also by the paired source technique. The first method gave dead times which depended somewhat on the relative heights of the two pulses. However, by making these heights equal and observing the dead time as a function of this height, a constant value was obtained over two orders of magnitude of the pulse height. The average value obtained using an oscilloscope sweep to measure the time interval was  $2.9 \pm 0.1 \mu\text{sec}$ . The dead time observed by this method was independent of the repetition rate of the pulse generator over the available range, i.e. 1 to 10 kc/sec. The paired source technique is perhaps more realistic but since it involves the difference of two large rates good statistics are necessary. The value obtained by this method using two sources of about 4000 c.p.s. each was  $2.8 \pm 0.1 \mu\text{sec}$ , in good agreement with that found by the double pulse method. The dead time was shown to be very nearly "non-extendable" by the use of a triple pulse generator.

Each point was assigned an internal error formed by combining in quadrature the statistical counting error, the error due to possible fluctuations in

TABLE I  
SUMMARY OF THE HALF-LIFE DETERMINATIONS

Source No.	No. of points	No. of half-lives followed	Half-life, hours	Internal error, hours	External error, hours
1	14	6	14.952	0.007	0.007
2	15	8	14.960	0.005	0.010
3	13	6	14.965	0.006	0.007
4	18	3	14.950	0.004	0.003
5	16	3	14.959	0.006	0.004
6	9	5	14.964	0.006	0.008
7	10	5	14.969	0.006	0.005
8	10	5	14.967	0.006	0.007
Weighted average:			14.959	0.002	0.003

the mains frequency, the human timing error, and the error caused by uncertainties in the background correction. As a check against gross observational mistakes the data were first plotted on semilogarithmic paper. The half-life of each source was then calculated according to the method of least squares, each point being weighted by the reciprocal of the square of the assigned error. The results of this computation are summarized in Table I, where columns five and six list the internal and external (least squares) errors respectively as calculated from the above mentioned (statistical) errors only. In each case the larger of the two errors quoted in Table I has been used to calculate the weighted mean value, 14.959 hours, of the eight determinations. The internal and external errors of this mean are 0.002 and 0.003 hours respectively and the larger of these was accepted as the final statistical error. In order to determine the systematic error due to the uncertainty in the dead time the half-life was recalculated using a dead time differing from the accepted value by the estimated uncertainty, but with the same statistical errors as before. This yielded a difference in the weighted mean half-life of 0.007 hours. Other systematic errors such as those arising from the possible deliquescence of the source and change in geometry of the source-sandwich were considered to be negligible. Since the known systematic error is random with respect to the final statistical error it is added in quadrature with the latter giving 0.007 hours. This quantity is then increased to allow for any undetected systematic error to give the final value of  $14.959 \pm 0.010$  hours for the half-life of Na<sup>24</sup>.

We should like to thank Mr. J. G. V. Taylor for making the measurements of the 110 v a-c. line frequency variation and Dr. J. M. Kennedy and Mrs. E. A. Okazaki for programing the Chalk River Datatron upon which the computations were carried out.

- BEAUKENKAMP, J. and RIEMAN III, W. 1950. Anal. Chem. **22**, 582.  
CAMPION, P. J. 1958. To be published.  
LOCKETT, E. E. and THOMAS, R. H. 1953. Nucleonics, **11**, No. 3, 14.  
SINCLAIR, W. K. and HOLLOWAY, A. F. 1951. Nature, **167**, 365.  
SOLOMON, A. K. 1950. Phys. Rev. **79**, 403.  
SREB, J. H. 1951. Phys. Rev. **81**, 469.  
TOBAILEM, J. 1955. J. phys. radium, **16**, 48.  
WILSON, R. and BISHOP, G. R. 1949. Proc. Phys. Soc. London, **62**, 457.

RECEIVED MARCH 19, 1958.  
NUCLEAR PHYSICS I,  
ATOMIC ENERGY OF CANADA LIMITED,  
CHALK RIVER, ONTARIO.

#### ATOMIC MASSES OF Kr<sup>84</sup>, Kr<sup>86</sup>, Xe<sup>129</sup>, Xe<sup>132</sup>, Hg<sup>200</sup>, Hg<sup>201</sup>, and Hg<sup>204</sup><sup>1</sup>

JOHN T. KERR<sup>2</sup> AND HENRY E. DUCKWORTH

We have recently determined, with a large semicircular mass spectrometer

<sup>1</sup>This work was supported by the U.S. Air Force through the Air Force Office of Scientific Research of the Air Research and Development Command and by the National Research Council of Canada.

<sup>2</sup>Now with Corning Glass Company, Corning, New York.

(Duckworth, Kerr, and Bainbridge 1958), the masses of Kr<sup>84</sup>, Kr<sup>86</sup>, Xe<sup>129</sup>, Xe<sup>132</sup>, Hg<sup>200</sup>, Hg<sup>201</sup>, and Hg<sup>204</sup>. These mass values can be combined with other existing atomic mass information to compute mass values for the remaining stable isotopes of mercury.

In these experiments the ions were detected with an electron multiplier. The rapid response and high gain of this detector make it possible, when the ion energy is 60-cycle, a-c.-modulated, to present the mass spectral peaks on an oscilloscope screen. When a particular ion group is centered on the collector slit, a distinctive double-peak pattern (Kerr, Bainbridge, Dewdney, and Duckworth 1958) is observed on the screen. In this way the mass spectral peak corresponding to a given ion group can be accurately "located".

As usual, the atomic mass differences were obtained by the doublet method. The doublet spacings were determined by measuring the change in ion energy (i.e., accelerating voltage) necessary to shift from detecting one doublet member to detecting the other. The following mass difference values were found:

<i>Doublet</i>	<i><math>\Delta M</math> in millimass units</i>
N <sub>2</sub> O-CO <sub>2</sub>	11.244±10
CO <sub>2</sub> - $\frac{1}{3}$ Xe <sup>132</sup>	21.762±20
CH <sub>2</sub> Cl <sup>35</sup> <sub>2</sub> -Kr <sup>84</sup>	41.849±33
CHCl <sup>36</sup> F <sub>2</sub> -Kr <sup>86</sup>	62.733±49
$\frac{1}{3}$ Xe <sup>129</sup> - $\frac{1}{2}$ Kr <sup>86</sup>	12.969±17
$\frac{1}{2}$ Hg <sup>200</sup> -COCl <sup>35</sup> Cl <sup>37</sup>	54.196±38
$\frac{1}{3}$ Hg <sup>201</sup> - $\frac{1}{2}$ Xe <sup>134</sup>	37.173±31
$\frac{1}{2}$ Hg <sup>204</sup> -COCl <sup>37</sup>	60.127±45

The first datum given above is to be compared with 11.2355±6 mmu (Scolman, Quisenberry, and Nier 1956). The second of the above data leads to the mass value Xe<sup>132</sup> = 131.94616±6 amu, in good agreement with the accurate Minnesota value (Johnson and Nier 1957) of 131.94615±9 amu. These concordances are taken as evidence that, despite the unorthodoxy of employing a single-, rather than a double-focusing mass spectrometer, the method that we have employed is free from serious systematic error.

The third, fourth, and fifth mass differences given above lead to the following improved atomic mass values: Kr<sup>84</sup> = 83.93820±3 amu (83.93819±5 amu), Kr<sup>86</sup> = 85.93808±5 amu (85.93810±7 amu), and Xe<sup>129</sup> = 128.94603±9 amu (128.94570±11 amu). The values in parentheses are "best" values based on all previous work (Duckworth 1957).

The remaining mass differences not only provide the means of calculating masses for three of the stable isotopes of mercury but, when combined with other information, lead to mass values for Hg<sup>196</sup>, Hg<sup>198</sup>, Hg<sup>199</sup>, and Hg<sup>202</sup> as well. The "other" information required is Hg<sup>199</sup>-Hg<sup>198</sup> = 1.00182±6 amu, Hg<sup>200</sup>-Hg<sup>199</sup> = 1.00031±6 amu, Hg<sup>201</sup>-Hg<sup>200</sup> = 1.00226±6 amu, and Hg<sup>202</sup>-Hg<sup>201</sup> = 1.00064±6 amu (Johnson and Bhanot 1957); Au<sup>196</sup>-Hg<sup>196</sup> = 0.70±0.02 Mev, and Au<sup>198</sup>-Hg<sup>198</sup> = 1.373±0.002 Mev (Lidofsky 1957); the Q's of the Au<sup>197</sup> ( $\gamma$ , n) and Au<sup>197</sup> (d, p) reactions are -7.96±0.07 Mev (Chidley,

Katz, and Kowalski 1958) and  $4.12 \pm 0.15$  Mev (Van Patter and Whaling 1954), respectively. The resulting atomic mass values are the following:

$$\begin{aligned} \text{Hg}^{196} &= 196.02726 \pm 23 \text{ amu} \\ \text{Hg}^{198} &= 198.02914 \pm 12 \text{ amu} \\ \text{Hg}^{199} &= 199.03096 \pm 10 \text{ amu} \\ \text{Hg}^{200} &= 200.03127 \pm 8 \text{ amu} \\ \text{Hg}^{201} &= 201.03351 \pm 12 \text{ amu} \\ \text{Hg}^{202} &= 202.03415 \pm 14 \text{ amu} \\ \text{Hg}^{204} &= 204.03851 \pm 9 \text{ amu} \end{aligned}$$

These values, together with Nier's (1950) isotopic constitution of mercury, give a chemical atomic weight of 200.604. The International value is 200.61. The only previous mass value for any of the isotopes of mercury was an early one given by Aston (1927), namely,  $\text{Hg}^{200} = 200.034$ .

It is also possible, by making use of the mass differences among the heavy elements compiled by Huizenga (1955), to calculate from  $\text{Hg}^{204}$  the masses of all of the heavier stable nuclides. This calculation suggests that the currently accepted mass values for this group are 1–2 Mev too low. For this reason, work is now under way in this laboratory to re-determine the atomic masses of some of the isotopes of lead.

- ASTON, F. W. 1957. Proc. Roy. Soc. A, **115**, 487.  
 DUCKWORTH, H. E. 1957. Progress in nuclear physics, Vol. 6 (The Pergamon Press Ltd., London), 138.  
 DUCKWORTH, H. E., KERR, J. T., and BAINBRIDGE, G. R. 1958. Nuclear masses and their determination (The Pergamon Press, Ltd., London).  
 JOHNSON, W. H. and BHANOT, V. B. 1957. Bull. Am. Phys. Soc. Ser. II, **2**, 224.  
 JOHNSON, W. H. and NIER, A. O. 1957. Phys. Rev. **105**, 1014.  
 KERR, J. T., BAINBRIDGE, G. R., DEWDNEY, J. W., and DUCKWORTH, H. E. 1958. Unpublished. To be presented at Mass Spectrometry Conference in London, Sept. 24, 25, and 26, 1958.  
 LIDOFSKY, L. J. 1957. Revs. Mod. Phys. **29**, 773.  
 NIER, A. O. 1950. Phys. Rev. **79**, 450.  
 SCOLMAN, T. T., QUISENBERY, K. S., and NIER, A. O. 1956. Phys. Rev. **102**, 1076.  
 VAN PATTER, D. M. and WHALING, W. 1954. Revs. Mod. Phys. **26**, 402.

RECEIVED APRIL 22, 1958.  
 DEPARTMENT OF PHYSICS,  
 MCMASTER UNIVERSITY,  
 HAMILTON, ONTARIO.

## THE PHYSICAL SOCIETY

MEMBERSHIP of the Society is open to all who are interested in Physics.

FELLOWS pay an Entrance fee of £1 1s. (\$3.00) and an Annual Subscription of £2 2s. (\$6.00).

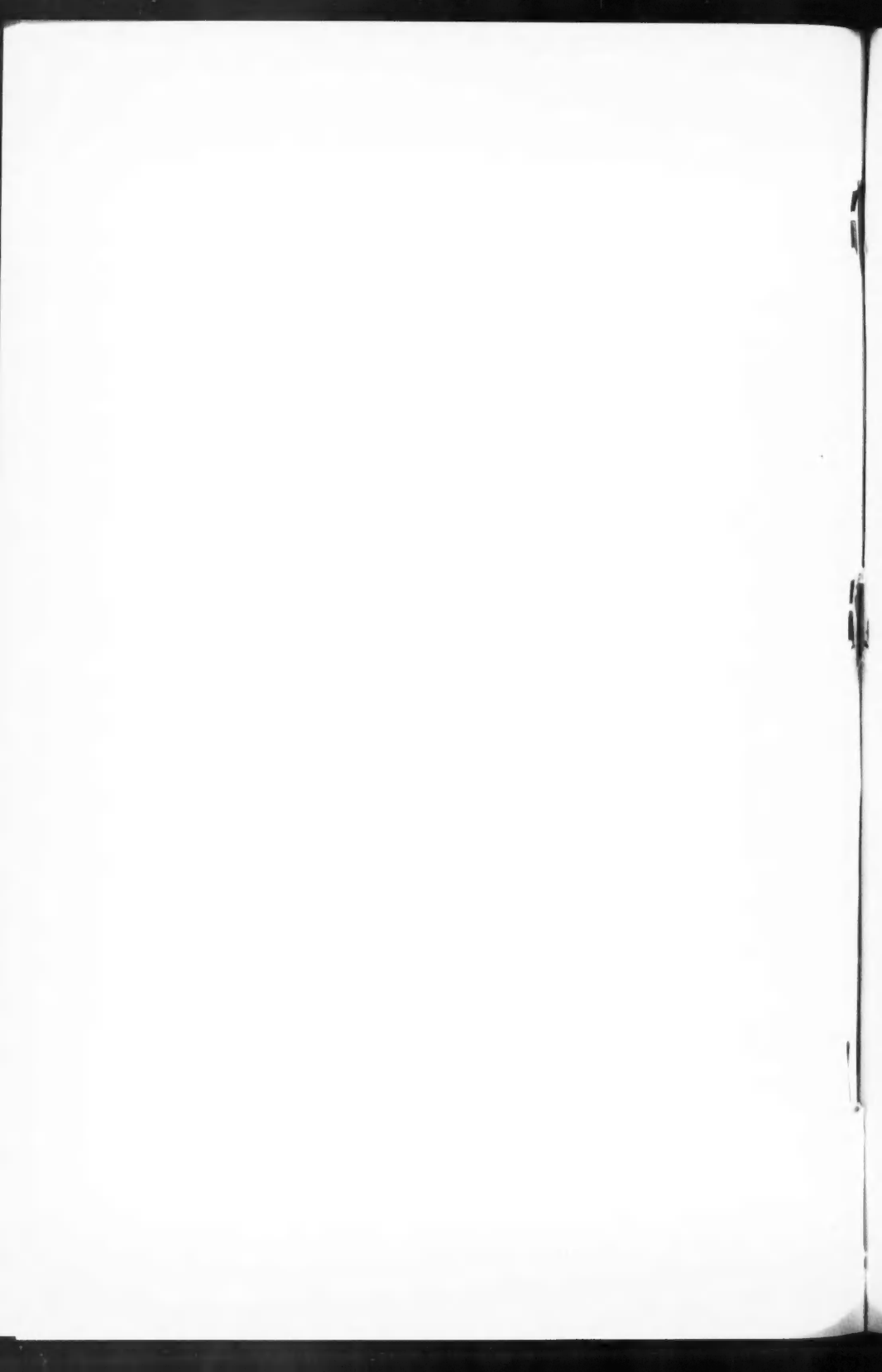
STUDENTS: A candidate for Studentship must be between the ages of 18 and 26, and pays an Annual Subscription of 5s. (\$0.75).

MEETINGS: Fellows and Students may attend all Meetings of the Society including the annual Exhibition of Scientific Instruments and Apparatus.

PUBLICATIONS include the *Proceedings of the Physical Society*, published monthly, and *Reports on Progress in Physics*, published annually. Volume XX, 1957, is now available (price £3 3s. (\$9.00)). Members are entitled to receive any of the Publications at a reduced rate.

Further information can be obtained from:

THE PHYSICAL SOCIETY  
1, LOWTHER GARDENS, PRINCE CONSORT ROAD  
LONDON, S.W.7, ENGLAND



# CANADIAN JOURNAL OF PHYSICS

## Notes to Contributors

### Manuscripts

(i) **General.** Manuscripts, in English or French, should be typewritten, double spaced, on paper  $8\frac{1}{2} \times 11$  in. **The original and one copy are to be submitted.** Tables and captions for the figures should be placed at the end of the manuscript. Every sheet of the manuscript should be numbered.

Style, arrangement, spelling, and abbreviations should conform to the usage of recent numbers of this journal. Names of all simple compounds, rather than their formulas, should be used in the text. Greek letters or unusual signs should be written plainly or explained by marginal notes. Superscripts and subscripts must be legible and carefully placed.

Manuscripts and illustrations should be carefully checked before they are submitted. Authors will be charged for unnecessary deviations from the usual format and for changes made in the proof that are considered excessive or unnecessary.

(ii) **Abstract.** An abstract of not more than about 200 words, indicating the scope of the work and the principal findings, is required, except in Notes.

(iii) **References.** References should be listed **alphabetically by authors' names**, unnumbered, and typed after the text. The form of the citations should be that used in current issues of this journal; in references to papers in periodicals, titles should not be given and only initial page numbers are required. The names of periodicals should be abbreviated in the form given in the most recent *List of Periodicals Abstracted by Chemical Abstracts*. All citations should be checked with the original articles and each one referred to in the text by the authors' names and the year.

(iv) **Tables.** Tables should be numbered in roman numerals and each table referred to in the text. Titles should always be given but should be brief; column headings should be brief and descriptive matter in the tables confined to a minimum. Vertical rules should not be used. Numerous small tables should be avoided.

### Illustrations

(i) **General.** All figures (including each figure of the plates) should be numbered consecutively from 1 up, in arabic numerals, and each figure referred to in the text. The author's name, title of the paper, and figure number should be written in the lower left corner of the sheets on which the illustrations appear. Captions should not be written on the illustrations (see Manuscripts (ii)).

(ii) **Line Drawings.** Drawings should be carefully made with India ink on white drawing paper, blue tracing linen, or co-ordinate paper ruled in blue only; any co-ordinate lines that are to appear in the reproduction should be ruled in black ink. Paper ruled in green, yellow, or red should not be used. All lines should be of sufficient thickness to reproduce well. Decimal points, periods, and stippled dots should be solid black circles large enough to be reduced if necessary. Letters and numerals should be neatly made, preferably with a stencil (**do NOT use typewriting**) and be of such size that the smallest lettering will be not less than 1 mm high when reproduced in a cut 3 in wide.

Many drawings are made too large; originals should not be more than 2 or 3 times the size of the desired reproduction. Whenever possible two or more drawings should be grouped to reduce the number of cuts required. In such groups of drawings, or in large drawings, full use of the space available should be made; the ratio of height to width should conform to that of a journal page ( $4\frac{1}{2} \times 7\frac{1}{2}$  in), but allowance must be made for the captions.

**The original drawings and one set of clear copies (e.g. small photographs) are to be submitted.**

(iii) **Photographs.** Prints should be made on glossy paper, with strong contrasts. They should be trimmed so that essential features only are shown and mounted carefully, with rubber cement, on white cardboard, with no space between them. In mounting, full use of the space available should be made to reduce the number of cuts required (see Illustrations (ii)). Photographs or groups of photographs should not be more than 2 or 3 times the size of the desired reproduction.

**Photographs are to be submitted in duplicate; if they are to be reproduced in groups one set should be mounted, the duplicate set unmounted.**

### Reprints

A total of 50 reprints of each paper, without covers, are supplied free. Additional reprints, with or without covers, may be purchased at the time of publication.

Charges for reprints are based on the number of printed pages, which may be calculated approximately by multiplying by 0.6 the number of manuscript pages (double-spaced type-written sheets,  $8\frac{1}{2} \times 11$  in) and including the space occupied by illustrations. An additional charge is made for illustrations that appear as coated inserts. Prices and instructions for ordinary reprints are sent out with the galley proof.

Any reprints required in addition to those requested on the author's reprint requisition form must be ordered officially as soon as the paper has been accepted for publication.

## Contents

<i>J. Katzman</i> —A cosmic ray increase related to solar activity	807
<i>William Woodside</i> —Calculation of the thermal conductivity of porous media	815
<i>A. G. Fenton, K. B. Fenton, and D. C. Rose</i> —The variation of sea level cosmic ray intensity between 1954 and 1957	824
<i>M. Srirama Rao</i> —Analysis of meteoric body doppler radar records taken during a Geminid shower period	840
<i>J. Y. Wong</i> —Measured self-impedance of a dipole antenna near a conducting cylinder of elliptical cross section	855
<i>A. E. Grün</i> —On the fluorescence of air, excited by fast electrons: light yield as a function of pressure	858
<i>A. P. Baerg, F. Brown, and M. Lounsbury</i> —The cross section for the reaction $\text{Cs}^{135}(n, \gamma)\text{Cs}^{136}$	863
<i>E. Brannen, H. I. S. Ferguson, and W. Wehlau</i> —Photon correlation in coherent light beams	871
<i>G. K. White and S. B. Woods</i> —Low temperature resistivity of the transition elements: ruthenium and osmium	875
<i>M. H. Edwards</i> —Refractive index of $\text{He}^4$ : liquid	884
<i>J. S. Kirkaldy</i> —Diffusion in multicomponent metallic systems. I. Phenomenological theory for substitutional solid solution alloys	899
<i>J. S. Kirkaldy</i> —Diffusion in multicomponent metallic systems. II. Solutions for two-phase systems with applications to transformations in steel	907
<i>J. S. Kirkaldy</i> —Diffusion in multicomponent metallic systems. III. The motion of planar phase interfaces	917
<i>C. Collins</i> —Some observations of aurora using a low-power frequency-modulated radar	926
<i>G. W. Farnell</i> —Measured phase distribution in the image space of a microwave lens	935
<i>E. M. Pennington and M. A. Preston</i> —Alpha decay of spheroidal nuclei	944
<i>A. K. M. Siddiq and R. N. H. Haslam</i> —The nuclear absorption of X-rays by oxygen	963
<b>Notes:</b>	
<i>K. T. Aust and B. Chalmers</i> —Control of lineage structure in aluminum crystals grown from the melt	977
<i>W. M. Barss, Z. S. Basinski, and F. R. N. Nabarro</i> —Filamentary growth in irradiated uranium	980
<i>P. J. Campion and Janet S. Merritt</i> —The half-life of $\text{Na}^{24}$	983
<i>John T. Kerr and Henry E. Duckworth</i> —Atomic masses of $\text{Kr}^{84}$ , $\text{Kr}^{86}$ , $\text{Xe}^{120}$ , $\text{Xe}^{122}$ , $\text{Hg}^{200}$ , $\text{Hg}^{201}$ , and $\text{Hg}^{204}$	986

